Feasibility study of an optical resonator for applications in neutral-beam injection systems for the next generation of nuclear fusion reactors

Donatella Fiorucci

Université Nice Sophia Antipolis - UFR Sciences

Ecole Doctorale de Sciences Fondamentales et Appliquées

THÈSE

pour obtenir le titre de

Docteur en Sciences

de l'Université Nice Sophia Antipolis

Discipline : Physique

présentée et soutenue par

Donatella FIORUCCI

Feasibility study of an optical resonator for applications in Neutral-Beam Injection systems for the next generation of Nuclear Fusion reactors

Etude de faisabilité d'un résonateur optique pour des applications aux systèmes d'injection de neutres pour la prochaine génération de réacteurs á fusion nucléaire

Thèse dirigée par Catherine Nary MAN

soutenue le 12/06/2015

Jury :

Mme.	Viviana Fafone	Professeur	Rapporteur
M.	Carlo Rizzo	Professeur	Rapporteur
M.	Jean Yves Vinet	Directeur de recherches	Examinateur
M.	Christophe Blondel	Directeur de recherches	Examinateur
M.	Frédéric du Burck	Professeur	Examinateur
M.	Walid Chaibi	Chargé de recherches	Encadrant de thèse
Mme.	Chaterine Nary Man	Directeur de recherches	Directeur de thèse
M.	Alain Simonin	Expert Senior NBI	Responsable CEA

To Guillaume

"Oui, mes amis, je crois que l'eau sera un jour employée comme combustible, que l'hydrogène et l'oxygène, qui la constituent, utilisés isolément ou simultanément, fourniront une source de chaleur et de lumière inépuisables et d'une intensité que la houille ne saurait avoir."

Jules Verne - L'île mystérieuse

"Yes, my friends, I believe that water will one day be employed as fuel, that hydrogen and oxygen which constitute it, used singly or together, will furnish an inexhaustible source of heat and light, of an intensity of which coal is not capable."

Jules Verne - The mysterious island

Acknowledgements

I first want to thank Catherine Nary Man, Alain Simonin and Walid Chaibi for their continuous support during my Ph.D and for their kind availability. In particular, I would like to express my gratitude to Walid, who has mostly supervised my work: I really appreciate his expertise and sense of responsibility from which I learned very much.
Besides my advisors, I would like to thank the members of the jury for having kindly accepted to be part of it and for the time they have dedicated to my work.
My sincere thanks goes also to all the people of ARTEMIS laboratory, including the administration staff David Andrieux and Seyna NDiaye, for their warm welcome and support. Particularly, I thank Michel Lintz, Mikhael Pichot, Mourad Merzougui, Gilles Bogaert, Frederic Cleva and Jean Yves Vinet, for their precious help and their availability. I equally thank Jiatai, the master student I have co-supervised during six months. I really thank him for his enthusiasm and his availability. I thank Jacques Millo and Ali Hreibi for their kind help and support. It was a pleasure sharing the office with them. A special thanks goes to Margherita Turconi, for always supporting me, helping me and above all for her friendship.
I wish also to thank the people of the internal services. In particular: Ghislain, Karima, Khaled and Nadia, the amazing restaurant staff; the receptionists Isabelle and Nathalie; and also Christian Capriani, Aziz, Akim, Armand, David Ferrer, Françoise. Thank you all for the nice, small daily chats and for being always very kind and having time for me.
I thank all the nice persons I met at the observatory, who have made this time unforgettable. Especially: Reda, Sarunas, Alvaro, Zeinab, Gaetan, Dario, Lionel, Samriddhi, Masha, Seroga, Elena Lega, Chiara Ferrari, Bertrand Chauvineau, Giulia Macario, Arwa, Kaveh, Gianluca, Judit, Pier Francesco, Gerardo, Gustavo, Sylvie Goletto, Fabien, Dominique Schraen, Laurent Galluccio, Sibilla.
I would like to thank Charles, Genevieve, Claire and Pauline for making me feel like at home, during the last two years. I thank Eric Fossat for all the special moments we shared together in the mountains as well as wherever else. I also thank Seroga, Li-Wei Wei, Farrokh and Guillaume for hiking together to Nasta and Argentera. I will always bring with me the memory of these two days.
I sincerely thank Massimo Granata for his friendship and for his continuous support. Equally, I would like to thank Massimiliano La Neve for his trust in me. A special thanks to Rehab, always kindly close to me. Thanks to all my friends, whether they are now close or far. Particularly: Ada Allegrini, Annamaria Lence, Aurora Ponzi, Valeria Campana and Valerio Paladino.
Finally, I thank all my family for everything. I do thank Stefano, my father, and Maria Tania, my mother. A deep thanks goes to my grandparents: Almerino Fiorucci, Anna Costantini, Elvetra Marchionni, Francesco Pietrarelli, Gino Costantini and Vanda Teti. This thesis is dedicate also to them.

Abstract

This work is part of a larger project called SIPHORE (SIngle gap PHOtoneutralizer energy RE-covery injector), which aims to enhance the overall efficiency of one of the mechanisms through which the plasma is heated, in a nuclear fusion reactor, i.e. the Neutral Beam Injection (NBI) system. An important component of a NBI system is the neutralizer of high energetic ion beams. SIPHORE proposes to substitute the gas cell neutralizer, used in the current NBI systems, with a photo-neutralizer exploiting the photo-detachment process within Fabry Perot cavities. This mechanism should allow a relevant NBI global efficiency of $\eta > 60\%$, significantly higher than the one currently possible ($\eta < 25\%$ for ITER).

The present work concerns the feasibility study of an optical cavity with suitable properties for applications in NBI systems. Within this context, the issue of the determination of an appropriated optical cavity design has been firstly considered and the theoretical and experimental analysis of a particular optical resonator has been carried on. The problems associated with the high levels of intra-cavity optical power ($\sim$3 MW) required for an adequate photo-neutralization rate have then been faced. In this respect, we addressed both the problem of the thermal effects on the cavity mirrors due to their absorption of intra-cavity optical power ($\sim$1 W) and the one associated to the necessity of a high powerful input laser beam ($\sim$1 kW) to feed the optical resonator.

Keywords: nuclear fusion, neutral beam injection, photodetachment of atomic negative ions, high power optical cavity, laser optical systems: design and operation, thermoelastic deformation.

PACs: 28.52.-s, 52.50.Gj, 32.80Gc, 42.60-v, 34.50.-s

Contents

List of Figures

List of Tables

Resumé détaillé

Contexte du travail du doctorat

Depuis ces dernières décennies, la demande énergétique a crucialement augmenté à travers le monde et elle devrait s'intensifier dans un proche avenir. En conséquence, notre besoin de moyens plus sûrs pour produire de l' énergie à grande échelle est de plus en plus pressant. Dans ce contexte, plusieurs projets ont été développés afin de réaliser de la fusion nucléaire contrlée sur Terre. En effet, la chaleur produite par les réactions de fusion nucléaire peut être utilisée pour alimenter les centrales électriques. La raison pour l'utilisation de ces réactions comme source d'énergie pour générer de électricité est basée sur le fait que ces réactions peuvent produire un haut niveau d'énergie en toute sécurité. En particulier, dans les mêmes conditions de poids du carburant, les réactions de fusion fourniraient plus d'énergie que n'importe quelle autre source d'énergie consommatrice de carburant actuellement utilisée dans les centrales électriques. Par exemple, la consommation annuelle de carburant pour produire 1000 MW d'électricité, en une seule centrale électrique de taille typique, est d'environ 2.7 $\times 10^6$ tonnes de charbon, 1.9 $\times 10^6$ tonnes de pétrole, 28 tonnes de UO_2 pour la fission, et 100 kg de deutérium et de 150 kg de tritium pour la fusion [1].

Actuellement, le principal programme de recherche sur la fusion nucléaire est ITER (International Thermonuclear Experimental Reactor), projet international lancé en Novembre 1985. La construction du réacteur de fusion nucléaire ITER est en cours à Cadarache, dans le sud de la France. Les réacteurs de fusion nucléaire sont des machines où les conditions de la matière pour obtenir des réactions de fusion nucléaire sont atteintes. En particulier, dans un réacteur de fusion, la matière est présente à l'état de plasma, et elle doit avoir une température élevée (1.5×10^8 K). Par conséquent, à des fins de fusion, une question cruciale concerne les mécanismes de chauffage du plasma. À cet égard, notons que, dans la chambre à plasma d'un réacteur de fusion, appelée Tokamak, le plasma est chauffé par la puissance ohmique, $P = I^2R$, qui est la combinaison du courant circulant dans le plasma et sa résistance électrique du plasma. Puisque

ce processus n' est pas efficace pour des températures de plasma supérieures à T> 2keV, deux mécanismes de chauffage supplémentaires sont présents: chauffage par Radio-fréquence (RF) et injection de neutres (IDN). Le chauffage par Radio-fréquence est un système impliquant des micro-ondes de haute puissance injectées dans le plasma, qui transfèrent leur énergie aux particules du plasma par des interactions de résonance. Le système IDN concerne l'injection d'un faisceau à haute énergie d'atomes neutres (par exemple deutérium) dans le coeur du plasma de fusion, dont l'énergie est finalement transférée aux particules du plasma, par le biais de collisions. Le système IDN est le seul mécanisme de chauffage placé loin de l'environnement du plasma. Cela le rend particulièrement attrayant pour l'amélioration de son efficacité globale, η, définie comme le rapport entre la puissance neutre à l'entrée du Tokamak et la puissance électrique totale consommée pour la produire. Dans le cas général, les composants d'un système IDN sont les suivants: une source d'ions qui génère un plasma froid de deutérium (T $\sim$ 2eV, n $\sim 10^{18}$ m^3); un accélérateur électrostatique pour accélérer les ions extraits à haute énergie (1 MeV pour ITER); un système pour neutraliser les ions de haute énergie; un système pour se débarrasser des ions restants, laissant le faisceau neutre continuer vers le Tokamak. La construction du réacteur expérimental de fusion nucléaire ITER a soulevé la question de la prochaine étape vers une centrale réelle de fusion, DEMO, qui devrait être le premier réacteur de fusion avec production d'électricité. L'un des principaux objectifs de DEMO est la démonstration de la production d'électricité avec l'approvisionnement auto-suffisante de combustible à un coût modéré. À cet égard, une amélioration du rendement global du réacteur à fusion nucléaire DEMO est nécessaire par rapport à celui du réacteur ITER. Des études de Recherche et développement (R&D) sur DEMO ont déjà commencé.

Mon travail de doctorat fait partie d'un projet plus large appelé Siphore (SIngle gap PHOtoneutralizer energy RE-covery injector), qui est basé sur des collaborations entre le CEA (Commissariatà l'Énergie Atomique) et plusieurs universités françaises. Le but de Siphore est de démontrer la faisabilité d'un système IDN basé sur l'application de cavités de Fabry-Pérot (3MW de puissance lumineuse par cavité) pour la photo-neutralisation d'un faisceau de D^- très énergétique, envoyé par la suite au plasma. Le photo-détachement, qui remplace le système neutralisant à cellule de gaz de ITER, devrait permettre la mise en œuvre d'un système de récupération d'énergie et d'atteindre une efficacité globale pour DEMO de $\eta > 60\%$, nettement plus élevée que celui d'ITER (inférieure à 25%). En particulier, j'ai modélisé une cavité optique avec des propriétés appropriées pour les applications aux systèmes IDN pour la prochaine génération de réacteurs de fusion nucléaire, qui pourrait aussi résoudre des possibles

problèmes d'encombrement. De plus, après avoir réalisé la cavité dans notre laboratoire, j'ai testé expérimentalement la conception de cette cavité. Jusqu'à présent, le problème principal pour la mise en œuvre du principe de la photo-neutralisation de Siphore semble être l'absorption de la puissance optique intra-cavité par les revêtements de miroir. En effet, cela provoque un gradient de température important, avec des déformations conséquentes des surfaces des miroirs. D'une part, les rayons de courbure des miroirs peuvent changer (par exemple, un miroir plat peut assumer un rayon de courbure de plusieurs milliers de mètres) conduisant à des modifications du mode résonant à l'intérieur de la cavité et à des problèmes de stabilité; d'autre part, les écarts de la surface des miroirs d'un profil exactement sphérique génèrent des pertes de diffusion (quelques milliers de ppm). En conséquence, la puissance intra-cavité accessible pour une puissance d'entrée donnée est réduite. À cet égard, dans la deuxième partie de la thèse, nous avons analysé plusieurs systèmes de compensation des effets thermiques, afin de corriger les déformations des surfaces réfléchissantes des miroirs de la cavité.

En outre, des études de faisabilité du processus de la photo-neutralisation pour les systèmes IDN montrent que la cavité optique utilisée pour la neutralisation du faisceau de D^- doit être alimentée par un faisceau laser d'entrée de haute puissance (environ 1kW). En ce qui concerne cet aspect, la dernière partie de la thèse est dédiée à la description des tests expérimentaux que nous avons effectués sur un nouveau concept des fibres optiques LMA (Large Mode Area), appelées fibres Leaky LMA, qui ont été développées pour permettre le fonctionnement monomode, sans augmentation des effets non linéaires. En effet, ces fibres doivent être particulièrement appropriées comme amplificateurs laser. Par conséquence, elles pourraient, en principe, permettre la réalisation de faisceaux laser à haute puissance, tel que celui nécessaire à l'entrée de la cavité optique appliqué pour les systèmes IDN.

Proposition d'une cavité optique pour les applications aux systèmes IDN

Des études récentes sur la faisabilité de la photo-neutralisation dans des systèmes IDN montrent que le compromis optimal entre la finesse de la cavité optique, la puissance laser d'entrée et la nécessité d'une faible charge thermique sur les miroirs de la cavité est donné par une cavité repliée quatre fois avec une taille de faisceau laser intra-cavité de 1 cm, tandis que le faisceau d'ions aura une largeur de 3 cm. En outre, la cavité doit être stable pour permettre la focalisation du faisceau intra-cavité. De plus, elle doit être stable à des petites perturbations du mode laser injecté dans la cavité et de lalignement des miroir, afin d'être moins sensible aux effets thermiques. On observe que pour garantir le chevauchement complet entre le faisceau laser et

le faisceau d'ions, les variations de la section du faisceau de photons intra-cavitaire doivent être aussi petites que possible. De plus, les composants optiques de la cavité doivent être protégés des régions polluées de l'environnement des systèmes IDN, où des radiations (rayons X durs, neutrons), des vibrations mécaniques et le *sputtering* plasma-gaz peuvent réduire leur durée de vie. Une cavité optique stable, de 100 m de long, semble être en mesure d'accueillir toutes les exigences [35] mentionnées. Néanmoins, il a été souligné qu'en raison de la longueur de la cavité il pourrait y avoir des problèmes d'encombrement pour les applications aux systèmes IDN. Ainsi, j'ai ensuite étudié une cavité optique plus courte permettant de garder toutes les conditions mentionnées ci-dessus pour les applications aux systèmes IDN. La cavité proposée est une cavité à trois miroirs où deux des miroirs forment un télescope ayant pour but de contrôler la taille du faisceau intra-cavité et d'assurer la stabilité de la cavité sur une plus petite longueur. Le schéma de la cavité proposée est donné dans l'image (1). Puisque la cavité devra être construite dans notre laboratoire, la longueur L_2 est fixée à 1 m et aussi les rayons de courbure des miroirs sont fixes. Par conséquent la distance L_1 doit être déterminée, de sorte que la conception de la cavité accueille l'ensemble des exigences nécessaires. Dans ce but, les propriétés de la cavité optique en fonction de L_1 ont été théoriquement étudiées avec un programme en Mathematica élaboré à l'aide du formalisme des matrices et loi $ABCD$, pour la propagation d'un faisceau gaussien au travers des systèmes optiques, dans l'approximation paraxiale. Il est possible de démontrer que la cavité déterminée est équivalente à une cavité optique avec la même conception géométrique où L_2 est denviron 31 m et la taille du faisceau sur la même longueur est de 1 cm. Cette dernière conception peut éventuellement accueillir toutes les exigences pour une cavité optique pour les applications aux systèmes IDN. Par conséquent, après la détermination de la valeur optimale pour L_1, la cavité optique a été construite dans notre laboratoire et testée expérimentalement. La réflectivité de la cavité a été mesurée à partir du miroir M_1 à la fréquence de résonance et aux autres fréquences. Le résultat optimal mesuré est de 23 % de la puissance réfléchie par la cavité à la fréquence de résonance. Cependant cette valeur diminue à 15 % lorsque l'on considère la puissance dans les modes d'ordres supérieurs de la cavité, dus à des désalignements résiduels. En raison des caractéristiques des optiques utilisées, la valeur attendue est de 9.2 %, assez proche de la valeur obtenue. En ce qui concerne les dimensions des faisceaux intra-cavité, leurs diamètres sont mesurés avec une caméra et un logiciel dédié, à une distance de 10 cm du miroir M_2. La valeur mesurée est de 4398 μm pour le faisceau le long de L_1 et de 3665 μm pour celui le long de L_2. Une erreur de 5 % peut être associée à ces mesures. En ce qui concerne les valeurs théoriques, elles sont obtenues en utilisant la méthode des matrices $ABCD$

et il en résulte: 4400μm pour le faisceau le long de L_1 et 3686 μm pour celui le long de L_2. Par conséquent, les résultats théoriques et expérimentaux indiquent des valeurs analogues pour les tailles de faisceau intra-cavité. Finalement, la phase de Gouy, Φ_G, accumulée par le faisceau laser lors d'un aller-retour dans la cavité a été mesurée afin de vérifier la stabilité de la cavité. En effet, pour une cavité stable, on doit satisfaire $0 < (\cos\Phi_G + 1)/2 < 1$. La valeur expérimentale de Φ_G est d'obtenue par la relation: $\Phi_G = (2\pi\Delta\nu L)/c$, où L est deux fois la longueur de la cavité, et $\Delta\nu$ est l'espacement en fréquence entre le mode fondamental de la cavité et le premier mode d'ordre supérieur. La dernière quantité a été mesurée expérimentalement afin d'obtenir la valeur Φ_G. Le résultat est $\Phi_G = 3.6\pm0.2$ rad, pour la valeur théorique, et de $\Phi_G = 3.535 \pm 0.021$ rad, pour la valeur expérimentale.

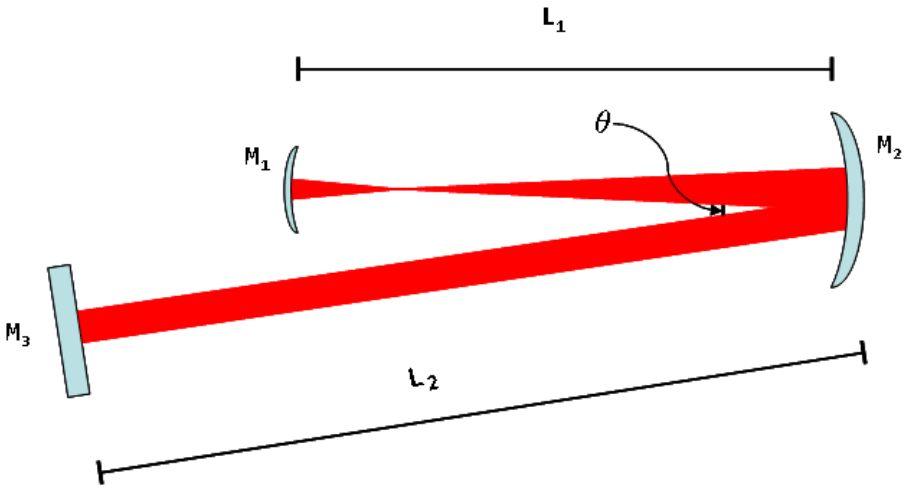

Figure 1: Conception d'une cavité optique avec un télescope - Les miroirs M_1 et M_2 sont utilisés pour composer un télescope permettant d'agrandir la taille du faisceaux et permettent de fixer la phase de Gouy lors d'un trajet aller-retour du faisceau afin de stabiliser la cavité.

Étude des effets thermiques sur les miroirs de la cavité et des systèmes de compensation.

L'étude des effets thermiques sur les miroirs de la cavité et des systèmes de compensation ont été réalisés d'une manière analytique et les résultats ont été vérifiés avec ANSYS et COMSOL, logiciels de simulations numériques basés sur la méthode des éléments finis. Seul le cas des miroirs fins est considéré (5 mm d'épaisseur), de sorte que l'absorption par l'intérieur du miroir peut être négligée par rapport à celle du revêtement. Le formalisme mathématique utilisé

pour calculer analytiquement les effets thermiques sur les miroirs, (en raison de l'absorption du revêtement), et aussi les effets des systèmes de compensation thermique (SCT) est basé sur les fonctions harmoniques pour le champ de température et les fonctions bi-harmoniques pour le champ de déformation. Ce formalisme implique l'utilisation de fonctions de Bessel. En particulier, le champ de température est déterminé par la résolution de l'équation de Fourier, en régime stationnaire, sans source de chaleur interne. Cette solution est utilisée afin d' écrire les équations pour les composantes du vecteur de déplacement décrivent la déformation du miroir. Il est intéressant de remarquer que, comparativement aux simulations aux éléments finis, les calculs analytiques présentent l'avantage d'être plus légers en termes de temps de calcul (jusqu'à 20 fois plus rapides). Cependant, ils montrent aussi des limitations dues aux approximations introduites dans le but de résoudre les équations concernées. Les systèmes de compensation analysés afin de corriger les distorsions de la surface réfléchissante des miroirs, en raison de la puissance optique absorbée par le revêtement, sont de deux types:

- compenser les distorsions des miroirs en appliquant des contraintes mécaniques ;
- compenser la distorsion des miroirs en appliquant des champs de température sur la face arrière du miroir ;

Les solutions mathématiques décrivant la surface réfléchissante des miroirs pour chaque SCT considéré ont été utilisés pour réaliser des programmes MATLAB. Les simulations sont faites pour un miroir de rayon 4 cm, de largeur 5mm et éclairé avec un faisceau de taille 1.0 cm, qui est absorbé à un taux de 0,3 ppm. Une puissance intra-cavité de 3 MW est considérée. Les résultats des simulations montrent que les SCT basés sur l'application de champs de température sont les plus appropriés. En particulier, le meilleur résultat est obtenu lorsqu'une température fixe de $T_c = 690$ K est appliquée sur la partie centrale de la face arrière du miroir, à travers un dispositif de chauffage à disque de rayon 5 mm. Pour donner une idée du facteur de gain en termes de réduction des pertes des miroirs, sans appliquer le SCT mentionné, les pertes d'un miroir, en raison de l'absorption de la puissance optique, par le revêtement des miroirs sont de 2500 ppm et le changement de courbure est de 2.9×10^{-4} m^{-1}, lors du démarrage à partir d'un miroir initialement plat. Si le STC décrit est appliqué, les pertes du miroir sont réduites à 5 ppm et le changement de courbure est maintenant de 8.7×10^{-5} m^{-1}.

Tests expérimentaux sur des fibres optiques LMA Leaky

Un faisceau laser avec une puissance d'environ 1 kW doit être injecté à l'intérieur de la cavité optique pour des applications de système IDN [35]. Un faisceau laser de cette puissance n'est pas facile à réaliser. À cet égard, l'amplification d'un faisceau laser à travers des amplificateurs à fibre optique a été examinée. Dans ce contexte, j'ai testé expérimentalement un nouveau concept de fibres LMA (Large Mode Area), appelées fibres *LMA Leaky*, qui a été développé pour permettre un fonctionnement monomode sans augmentation d'effets non linéaires. Par conséquent, elles devraient être particulièrement indiquées comme amplificateurs laser. Leur fonctionnement monomode est garanti par un profil d'indice de réfraction approprié qui devrait permettre des pertes de puissance élevées pour les modes supérieurs de la fibre et des pertes beaucoup plus bases pour le mode fondamental. Les tests expérimentaux ont démontré que ces fibres sont très sensibles aux flexions : lorsque la fibre est pliée, le mode sortant voit sa forme changer. Les fibres analysées peuvent alors difficilement être utilisées pour l'amplification monomode du faisceau laser.

Introduction

Depuis ces dernières décennies, la demande énergétique a crucialement augmenté à travers le monde et elle devrait s'intensifier dans un proche avenir. En conséquence, notre besoin de moyens plus sûrs pour produire de l' énergie à grande échelle est de plus en plus pressant. Dans ce contexte, plusieurs projets ont été développés afin de réaliser la fusion nucléaire contrôlée sur Terre. En effet, la chaleur produite par les réactions de fusion nucléaire peut être utilisée pour alimenter les centrales électriques. La raison pour l'utilisation de ces réactions comme source d'énergie pour générer de électricité est basée sur le fait que ces réactions peuvent produire un haut niveau d'énergie en toute sécurité. En particulier, dans les mêmes conditions de poids du carburant, les réactions de fusion fourniraient plus d'énergie que toutes les autres sources d'énergie consommantes de carburant utilisé dans les centrales électriques. Par exemple, la consommation annuelle de carburant pour produire 1000 MW d'électricité, en une seule centrale électrique de taille typique, est d'environ 2.7 $\times 10^6$ tonnes de charbon, 1.9×10^6 tonnes de pétrole, 28 tonnes de UO_2 pour fission, et 100 kg de deutérium et de 150 kg de tritium pour la fusion [1]. En outre, le combustible des réactions de fusion nucléaire, sur la Terre, peut être facilement obtenu, étant composé de deutérium et de tritium. Le deutérium est largement présent dans l'eau de mer, et le tritium, en dépit de ne pas être présent dans nature, peut être produit à partir des réactions entre lithium et neutrons. Comme il a été mentionné, les centrales qui exploitent les réactions de fusion nucléaire comme source d'énergie seraient sûres pour l'environnement. En effet, elles n'émettraient aucun gaz à effet de serre, et les éléments radioactifs produits auraient une durée de vie plus courte par rapport à celle des déchets de fission, ce qui rend le processus de fusion très attrayant. De plus, les réactions de fusion ne continuent pas une fois que les dispositifs utilisés pour obtenir les conditions de réactions de fusion nucléaire sont éteints, à la différence des centrales à fission , où des réactions en chaîne peuvent avoir lieu. Actuellement, le principal programme de recherche sur la fusion nucléaire est ITER (International Thermonuclear Experimental Reactor), un projet international lancé en novembre 1985. Le réacteur de fusion

nucléaire ITER est en cours de construction à Cadarache, dans le sud de la France. Les réacteurs de fusion nucléaire sont des machines où les conditions de la matière pour obtenir des réactions de fusion nucléaire sont atteintes. En particulier, dans un réacteur de fusion, la matière est présente à l'état de plasma, et elle doit avoir une température élevée ($1{,}5\times10^8$ K). Par conséquent, afin de la fusion, une question cruciale concerne les mécanismes de chauffage du plasma. À cet égard, notons que, dans la chambre à plasma d'un réacteur de fusion, appelée Tokamak, le plasma est chauffé par la puissance de chauffage ohmique, $P = I^2R$, qui est la combinaison du courant circulant dans le plasma et de sa résistance électrique. Puisque ce processus n' est pas efficace pour des températures de plasma supérieures à T> 2keV, deux mécanismes de chauffage supplémentaires sont présents: chauffage par Radio-fréquence (RF) et injection de neutres (IDN). Le premier système implique des micro-ondes de haute puissance injectées dans le plasma, qui transfèrent leur énergie aux particules du plasma par des interactions de résonance. Le système IDN concerne l'injection d'un faisceau à haute énergie d'atomes neutres (par exemple deutérium) dans le coeur du plasma de fusion, dont l'énergie est finalement transférée aux particules du plasma, par le biais de collisions.

Le système IDN est le seul mécanisme de chauffage placé loin de l'environnement du plasma. Cela le rend particulièrement attrayant pour l'amélioration de son efficacité globale, η , définie comme le rapport entre la puissance neutre à l'entrée du Tokamak et la puissance électrique totale consommée pour la produire. Dans le cas général, les composants d'un système IDN sont les suivants: une source d'ions qui génère un plasma froid de deutérium (T $\sim$ 2eV, n $\sim$ 10^{18} m^3) un accélérateur électrostatique pour accélérer les ions extraits à haute énergie (1 MeV pour ITER); un système pour neutraliser les ions de haute énergie; un système pour retirer les ions restants. La construction du réacteur expérimental de fusion nucléaire ITER a soulevé la question de la prochaine étape vers une centrale réelle de fusion, DEMO, qui devrait être le premier réacteur de fusion avec production d'électricité. L'un des principaux objectifs de DEMO est la démonstration de la production d'électricité avec l'approvisionnement auto-suffisant de combustibile à un coût modéré. À cet égard, une amélioration du rendement global du réacteur à fusion nucléaire DEMO est nécessaire par rapport à celui du réacteur ITER. Des études de Recherche et développement (R & D) sur DEMO ont déjà commencé. Le travail présenté dans cette thèse fait partie d'un projet plus large appelé Siphore (SIngle gap PHOtoneutralizer energy RE-covery injector), qui a commencé par des collaborations entre le CEA (Commissariat à l'énergie atomique) et plusieurs universités françaises. Le but de Siphore est de démontrer la faisabilité d'un système IDN basé sur l'application de cavités de Fabry-Pérot (3MW de puissance

lumineuse par cavité) pour la photo-neutralisation du faisceau très énergétique de D^-, qui est ensuite envoyé dans le plasma. Le photo-détachement, qui remplace le système neutralisant à cellule de gaz de ITER, devrait permettre la mise en œuvre d'un système de récupération d'énergie et d'atteindre une efficacité globale pour DEMO de $\eta > 60\%$, nettement plus élevée que celle d'ITER, qui est inférieure à 25%.

En particulier, la première partie du travail que nous avons réalisé porte sur la détermination d'une cavité optique avec des propriétés appropriées pour les applications dans les systèmes IDN pour la prochaine génération de réacteurs à fusion nucléaire et la construction de la cavité dans notre laboratoire pour la tester expérimentalement. Jusqu'à présent, le problème principal pour la mise en œuvre du principe de la photo-neutralisation de Siphore semble être l'absorption de la puissance optique intra-cavité par les revêtements de miroir. En effet, cela provoque un gradient de température important, avec des déformations conséquentes des surfaces des miroirs. D'une part, les rayons de courbure des miroirs peuvent changer (par exemple, un miroir plat peut prendre un rayon de courbure de plusieurs milliers de mètres) conduisant à des modifications du mode résonant à l'intérieur de la cavité et à des problèmes de stabilité; d'autre part, les écarts de la surface des miroirs d'un profil exactement sphérique génèrent des pertes de diffusion (quelques milliers de ppm). En conséquence, la puissance intra-cavité accessible pour une puissance d'entrée donnée est réduite. À cet égard, dans la deuxième partie de la thèse, nous avons considéré les problèmes des effets thermiques sur les miroirs et nous avons analysé plusieurs systèmes de compensation, afin de corriger les déformations des surfaces réfléchissantes des miroirs de la cavité.

En outre, des études de faisabilité du processus de la photo-neutralisation pour les systèmes IDN montrent que la cavité optique utilisée pour la neutralisation du faisceau de D^- doit être alimentée par un faisceau laser d'entrée de haute puissance (environ 1kW). En ce qui concerne cet aspect, la dernière partie de la thèse est dédiée à la description des tests expérimentaux que nous avons effectués sur un nouveau concept des fibres optiques LMA (Large Mode Area), appelées fibres Leaky LMA, qui ont été développés pour permettre le fonctionnement monomode, sans augmentation des effets non linéaires. En effet, ces fibres doivent être particulièrement appropriées comme amplificateurs laser. Par conséquence, elles pourraient, en principe, permettre la réalisation des faisceaux laser à haute puissance, tel que celui nécessaire à l'entrée de la cavité optique appliqué pour les systèmes IDN.

Aperçu de la thèse

- Le chapitre 1 est un chapitre d'introduction où les conditions pour réaliser des réactions de fusions nucléaires sur la Terre sont décrits, pour la technique basée sur le confinement magnétique du plasma. En outre, une introduction concernant l'application du photodétachement dans les systèmes IDN est donnée. Les principaux résultats obtenus, à ce jour sur le domaine de la fusion nucléaire sont également signalés, ainsi qu'une description des principaux projets de recherche actuels et futurs sur la fusion nucléaire (comme ITER et DEMO).

- Le chapitre 2 développe, en détail, une proposition pour un résonateur optique avec des propriétés appropriées pour l'application dans les systèmes IDN de future génération de réacteurs de fusion nucléaire, comme DEMO, qui permettrait aussi de résoudre les possibles problèmes d'encombrement. En particulier, une cavité optique avec télescope sera étudiée et la détermination de sa conception géométrique sera décrite d'un point de vue théorique. Les résultats des tests expérimentaux, réalisés après la construction de la cavité optique dans notre laboratoire, seront également rapportés.

- Le chapitre 3 est dédié à l'étude analytique des effets thermiques sur les miroirs de la cavité et des systèmes de compensation adoptés. La description mathématique de chaque système de compensation est ensuite utilisée pour réaliser un programme MATLAB pour simuler la déformation de la surface réfléchissante des miroirs.

- Le Chapitre 4 vise à valider les calculs mathématiques sur lesquels les simulations MATLAB sont fondées, en comparant les résultats analytiques avec ceux obtenus par les simulations numériques faites avec ANSYS et COMSOL, deux logiciels basés sur la méthode des éléments finis.

- Le chapitre 5 décrit les résultats des pertes des miroirs de la cavité et leurs changements de courbures obtenus pour chaque système de compensation des effets thermiques considéré. Le but est la détermination d'une technique de compensation optimale pour les distorsions des surfaces réfléchissantes des miroirs de la cavité.

- Le chapitre 6 décrit les tests expérimentaux effectués sur un nouveau concept de fibres optiques LMA (Large Mode Area), appelées fibres Leaky LMA, qui a été développé pour permettre le fonctionnement monomode, sans augmentation des effets non linéaires. Ces fibres doivent être particulièrement appropriées comme amplificateurs laser. Par conséquent, elles peuvent représenter une possibilité pour l'obtention dun faisceau laser de puissance

élevée nécessaire pour alimenter la cavité optique pour les applications dans des systèmes IDN.

Introduction

In the last decades, the energetic request is crucially increased across the world and it is expected to intensify in the near future. As a consequence, our need for clearer ways of energy production on a large scale is getting more and more pressing. Within this context, several projects have been developed at the purpose of realizing controlled nuclear fusion on Earth. Indeed, the heat produced by nuclear fusion reactions can be used to supply power plants for the production of electric power. The reason for using nuclear fusion reactions as energy source to generate electricity is based on the fact that these reactions can safely produce high level of energy. Particularly, at the same conditions of weight of fuel, fusion reactions would provide more energy than any other fuel consuming energy source currently in use in power plants. For instance, the annual fuel consumption for producing 1000MW of electricity, in a single electric power plant of typical size, is of about 2.7×10^6 tonnes of coal, 1.9×10^6 tonnes of oil, 28 tonnes of UO_2 for fission, and 100 kg of Deuterium and 150 kg of Tritium for fusion [1]. Furthermore, the nuclear fusion reaction fuel can be easily obtained, on Earth, being compounded of deuterium and tritium. Deuterium is largely present in seawater, while tritium, in spite of not being present in nature, can be produced from reactions between Lithium and neutrons. As it has be mentioned, power stations harnessing nuclear fusion reactions as energy source would be secure and safe for the environment. Indeed, they would emit no greenhouse gases, while the produced radioactive elements would have a shorter life time, compared to the one of the fission wastes, which make the fusion process very attractive. In addition, fusion reactions do not continue, once the devices used to get to nuclear fusion reaction conditions are switched off, differently from power plant based on nuclear fission, where chain reactions can take place.

Currently, the main research program on nuclear fusion is ITER (International Thermonuclear Experimental Reactor), an international project, which started in November 1985. The building of the ITER nuclear fusion reactor is under way in Cadarache, in the south of France. Nuclear fusion reactors are machines where material conditions for nuclear fusion reactions to

take place are reached. In particular, in a fusion reactor, matter is present in its plasma state, and it must have high temperature ($\sim$1.5 $\times 10^8$ K). Therefore, for fusion purpose, a crucial issue concerns the plasma heating mechanisms. In this respect, it is pointed out that, in the plasma chamber of a fusion reactor, called Tokamak, plasma is heated by Ohmic heating power, $P = I^2R$, which is the combination of the current flowing in the plasma and of the plasma electrical resistance. As this process is not efficient for plasma temperatures higher than $T > 2$keV, two classes of additional heating mechanisms are present: Radio-Frequency (RF) heating and Neutral Beam Injection (NBI). The former system implies high power microwaves injected into the plasma which transfer energy by resonant interactions with plasma particles, whilst the NBI system concerns the injection of a high-energy beam of neutral atoms (e.g. deuterium) into the core of the fusion plasma, whose energy is eventually transferred to the plasma particles, through collisions.

The NBI system is the only heating mechanism placed far away from the plasma environment. This makes it particularly attractive for the improvement of its global efficiency, η, defined as the ratio of the neutral power at the entrance of the Tokamak to the total electric power consumed to produce it. In the general case, the NBI system components are: an ion source generating cold deuterium plasma (T $\sim$ 2eV, n $\sim 10^{18}$ m^3); an electrostatic accelerator to accelerate the extracted ions to high energy (1Mev for ITER); a neutralizer to neutralize the high energetic ions; a system to get rid of the remaining ions, leaving the neutral beam to continue towards the Tokamak.

The construction of the experimental nuclear fusion reactor ITER has raised the question of the next step toward a real Fusion power plant, DEMO, which should be the first fusion reactor with electricity production. One of the main targets of DEMO is the demonstration of electricity generation with self-sufficient fuel supply at a moderate cost. In this respect, an enhancement of the DEMO overall nuclear fusion reactor efficiency is required with respect to the one of ITER. Research and development (R&D) studies on DEMO have been already started.

The work presented in this thesis is part of a larger project called Siphore (SIngle gap PHOtoneutralizer energy RE-covery injector), which has been started by collaborations between CEA (Commissariat à l'énergie atomique) and several French universities. The aim of Siphore is to demonstrate the feasibility of a NBI system based on the implementation of Fabry-Perot cavities ($\sim$ 3MW of light power per cavity) to photo-neutralize the high energetic beam of D^- which is then sent to the plasma. The photo-detachment, which substitutes the ITER gas cell neutralizer, should allow the implementation of an energy recovery system and reach a DEMO relevant NBI

global efficiency of $\eta > 60\%$, significantly higher than the one of ITER, which is less than 25%. Particularly, the first part of the work we carried on concerns the determination of an optical cavity with suitable properties for applications in NBI systems of future generations of nuclear fusion reactors and the building of the cavity in our laboratory for experimentally testing it. So far, the main issue for the implementation of the Siphore photo-neutralization principle appears to be the absorption of the intracavity optical power by the mirror coatings. Indeed, this causes important temperature gradient, with consequent deformations of the mirror surfaces. On one hand, the mirror curvature radii can change (e.g. a flat mirror can assume a curvature radius of few thousands meters) leading to modifications of the mode resonating inside the cavity and to stability issues; on the other hand, mirror surface deviations from a spherical profile generate scattering losses (few thousand of ppm). As a consequence, the reachable intracavity power for a given input power is reduced. In this respect, in the second part of the thesis, we faced the problems of the thermal effects on the cavity mirrors and we analyzed several thermal compensation systems, in order to correct the deformations of the cavity mirror reflecting surfaces. Furthermore, feasibility studies of the photo-neutralization process application for NBI systems show that the optical cavity used for the neutralization of the D^- beam has to be fed by a high power input laser beam ($\sim$ 1kW). In regard to this aspect, the last part of the thesis is dedicated to the description of the experimental tests we performed on a new concept of Large Mode Area (LMA) optical fibers, called Leaky LMA fibers, which have been developed for allowing single mode operation without enhancement of nonlinear effects. Indeed, these fibers should be particularly appropriated as laser amplifiers, hence they could, in principle, allow the realization of high power laser beams, such as the one required at the input of the optical cavity applied in NBI systems.

Outline of the thesis

- Chapter 1 is an introductory chapter where the requirements for realizing nuclear fusions reactions on Earth are described together with the technique based on the magnetic confinement of plasma for obtaining nuclear fusion reaction conditions. In addition, an introduction concerning the photo-detachment application in NBI systems is provided. The main results reached, so far, on the field of nuclear fusion are also reported as well as a description of the principle current and future nuclear fusion research projects (i.e. ITER and DEMO).

- Chapter 2 concerns, in detail, a proposal for an optical resonator with suitable properties for application in NBI systems of future generation of nuclear fusion reactors, such as DEMO, which also would solve possible encumbrance issues. In particular, an optical cavity with telescope will be addressed and its geometrical design determination will be described from a theoretical point of view. The results of the experimental tests, performed after building the modeled optical cavity in our laboratory, will be also reported.

- Chapter 3 is dedicated to the analytical study of the thermal effects on the cavity mirrors and of the considered compensation systems. The mathematical description of each compensation system is then used to realize a MATLAB program for simulating the mirror surface deformations.

- Chapter 4 aims to validate the mathematical calculations on which the MATLAB simulations are based, by comparing the analytical results with the ones obtained by numerical simulations carried on with ANSYS and COMSOL, softwares based on the finite elements method.

- Chapter 5 describes the results obtained for each considered thermal effect compensation systems, as far as cavity mirror losses and curvature changes are concerned. The aim is the determination of an optimum compensation technique for the distortion of the reflecting surface of the cavity mirrors.

- Chapter 6 describes the experimental tests performed on a new concept of Large Mode Area (LMA) optical fibers, called Leaky LMA fibers, which have been developed for allowing single mode operation without enhancement of nonlinear effects. These fibers should be particularly appropriated as laser amplifiers. Hence, they might be a possibility for obtaining the high power laser beam required for feeding the optical cavity for applications in NBI systems.

Chapter 1

Nuclear Fusion on Earth

In this chapter, the problem of obtaining nuclear fusion reactions on Earth will be addressed. It is known that nuclear fusion reactions take place in the core of the stars, where gravity provide the suitable physical conditions of matter which guarantee the production of these reactions. On Earth, there are not similar gravity conditions as in the core of the stars, but it is still possible to obtain appropriate matter characteristics to allow nuclear fusion reactions. The suitable conditions are realized in dedicated machines indicated as nuclear fusion reactors. In this work, only the case of nuclear fusion reactors based on the principles of the magnetic confinement of the plasma involved in the nuclear fusion reactions will be presented [2]-[7]. It is worth noticing that, in these reactors, the role of gravity, as far the plasma confinement is concerned, is played by the magnetic field which constrains the plasma in a delimited space within the reactor, which is called tokamak.

In particular, in the following sections, the constrains to obtain nuclear fusion reactions on Earth will be presented as well as the main working principles of a nuclear fusion reactor. The attention will be focused on the possibility of improving the ratio between the nuclear fusion power produced by a reactor and the power required to make the reactor to work. A high level of this ratio makes interesting to connect the reactor to the electric grid, in order to use it as power supplier. The last part of the chapter is dedicated to the presentation of the main achievements in the field of nuclear fusion reactions on Earth and to the introduction of the principal projects currently under realization and design, i.e. ITER and DEMO.

1.1 Nuclear fusion and Nuclear fusion reactors

Nuclear fusion reactions consist in fusioning two light nuclei to form a heavier nucleus, the mass of which is smaller than the sum of the interacting nucleus masses. Indeed, together with the new nucleus also energy is produced, in agreement with the Einstein law $E = mc^2$. In particular, the produced energy, E_f, depends on the mass difference, Δm, before and after the fusion reaction, i.e. $E_f = \Delta mc^2$. In order to obtain a fusion reaction the nuclei involved in the process need to have enough energy to overcome the coulomb potential barrier due to their positive charge. As a consequence, the interacting nuclei can get close enough to allow the nuclear strong force to become important. The realization of nuclear fusion on Earth requires then specific characteristics for the state of the material involved in the reaction, as it happens in the stellar fusion as well. Particularly, a nuclear fusion reactor based on the magnetic confinement principle, which is the category of nuclear fusion reactors addressed in this work, requires high temperatures, of order of 10^8 K ($\sim$ 10 keV), to increase the reaction rate. At this temperature levels, matter is in the plasma state [8]. It is observed that the temperature required by fusion reactor on Earth is higher than the one of the Sun's core [9]. This is due to the fact that the nuclear fusion conditions of the matter are maintained, in the stars, by the gravitational force, solution which is not possible on the Earth, where higher temperatures become then necessary. Currently, the reaction considered for realizing nuclear fusion on Earth is the one between deuterium and tritium:

$$ {}^{2}_{1}D + {}^{3}_{1}T \rightarrow {}^{4}_{2}He + {}^{1}_{0}n + 17.6MeV, \tag{1.1} $$

indeed, this reaction presents the largest cross section, hence the highest probability to happen, and the atomic number of the species interacting is $Z = 1$, which minimizes the losses for Bremsstrahlung [10]. Furthermore, as it has been already pointed out, the fusion of less than one kilo per day of deuterium and tritium produces the required heat to generate 1000 MW of continuous electricity. In a thermal power plant, this result is obtained by consuming about 5000 tons of fossil fuel. In addition, even if there are not natural sources of tritium, this can be obtained from the interaction of lithium ($^{6}_{3}$Li) with a neutron, while deuterium is largely present on Earth. It is worth recalling the lithium reaction used to produce the tritium involved in nuclear fusion reactor [10], i.e.:

$$ {}^{6}_{3}Li + {}^{1}_{0}n \rightarrow {}^{3}_{1}T + {}^{4}_{2}He + ...4.8MeV. \tag{1.2} $$

The neutron appearing in the previous relation comes from the fusion reactions produced within the reactor, while the lithium is applied to realize the internal reactor walls. As neutron are not confined by the strong magnetic fields, they can reach the first internal reactor wall by generating the required amount of tritium, through interactions with the Lithium of the reactor walls. With reference to the nuclear fusion reactor design, it is important to know how the energy produced in the fusion reaction is divided between the α particle and the neutron. To this aim, it is possible to assume that the momentum is equally divided between the α particle and the neutron:

$$m_\alpha v_\alpha = m_n v_n, \tag{1.3}$$

with m_α and v_α the mass and the velocity of the α particle and m_n, v_n the mass and the velocity of the neutron. This equation can then be combined together with the one for the energy:

$$\frac{1}{2}m_\alpha v_\alpha^2 + \frac{1}{2}m_n v_n^2 = W = W_\alpha + W_n, \tag{1.4}$$

where W indicates the energy released by the fusion of the reacting nuclei, and W_α and W_n are the kinetic energies of the α particle and of the neutron respectively. By solving the system of the two equations, it is found:

$$W_\alpha = \frac{W}{\frac{m_\alpha}{m_n} + 1}, \tag{1.5}$$

$$W_n = \frac{W}{\frac{m_n}{m_\alpha} + 1}. \tag{1.6}$$

As $m_\alpha = 3727 MeV$ and $m_n = 939.4 MeV$, the produced neutron carries the 80% of the energy released, i.e. 14 MeV, and the α particle the 20%, i.e. 3.5 MeV. The high temperature condition is not the only constraint required for realizing convenient nuclear fusion reactors producing an amount of fusion energy which is higher than the energy used to produce it. The nuclear fusion reactors under consideration utilize magnetic fields to contain the plasma involved in the reaction. As the neutrons have no charge, they cannot be trapped by the magnetic fields, then only the energy of the α particles is used to maintain the plasma. Because of the loss mechanisms, this energy could be not sufficient to keep the conditions for a plasma status of matter and external heating techniques have to be applied to warm up the plasma. It is then introduced the ratio between the fusion power, P_{fusion}, produced by the nuclear fusion reactor and the external power, $P_{external}$ required to maintain the plasma, which is called, the

amplification factor [11]:

$$Q = P_{fusion}/P_{external}. \tag{1.7}$$

In order to be convenient, a nuclear fusion reactor must have a Q factor well above 1. Another important parameter is the characteristic time for the plasma to loss its energy, once its energy sources are turned off, τ_e. If P_{losses} is the power lost by the plasma and W its total energy, it is:

$$P_{losses} = W/\tau_e. \tag{1.8}$$

In a steady state, the plasma energy does not vary, hence the power given to the plasma has to be equivalent to the power it looses [11]:

$$P_\alpha + P_{external} = P_{losses} = W/\tau_e, \tag{1.9}$$

with P_α the power supplied by the α particles to the plasma, through collisions. Because of the amplification factor definition, it is possible to write:

$$P_{external} = P_{fusion}/Q, \tag{1.10}$$

thus, the power balance equation reads:

$$P_{fusion}\left(\frac{P_\alpha}{P_{fusion}} + \frac{1}{Q}\right) = P_{losses} = W/\tau_e. \tag{1.11}$$

The plasma thermal energy can be expressed as [11]:

$$W = \int_V \frac{3}{2} k \left(n_e T_e + (n_D + n_T) T_i\right) dV, \tag{1.12}$$

where n_e, n_D, n_T are the numerical density of electron, deuterium ions and tritium ions respectively, and k is the Boltzmann constant. By assuming that $n_D = n_T = n/2$ and remembering the plasma property of being nearly neutral, for a uniform temperature $T_e = T_i = T$, it results:

$$W = 3nkTV. \tag{1.13}$$

As far as the fusion power is concerned, this is obtained by multiplying the energy of one fusion reaction, E_{fusion}, for the number of fusion reaction in the unit of time, N, [11] i.e.:

$$N = \int_V n_D n_T \overline{\sigma\nu}(T) dV, \tag{1.14}$$

with $\overline{\sigma\nu}(T)$ the mean reaction rate. For 10 keV$\leq T \leq$ 20 keV, it turns out $\overline{\sigma\nu}(T) = 1.18 \times 10^{-24}$ T^2 m^3 s^{-1} (T expressed in keV) [12]. Hence:

$$N = \frac{n^2}{4} \overline{\sigma\nu}(T) V, \tag{1.15}$$

and:

$$P_{fusion} = \frac{n^2}{4} \overline{\sigma\nu}(T) V E_{fusion}. \tag{1.16}$$

By considering the balance equation, as given by equation (1.11), and replacing W with its expression (1.13) and P_{fusion} with relation (1.16), it is found:

$$n\tau_e = \frac{12k}{E_{fusion}\left(\frac{E_\alpha}{E_{fusion}} + \frac{1}{Q}\right)} \times \frac{T}{\overline{\sigma\nu}(T)}. \tag{1.17}$$

For the considered range of temperature, i.e. 10 keV$\leq T \leq$ 20 keV, the previous equation can be written as:

$$n\tau_e T = \frac{12}{E_{fusion}\left(\frac{E_\alpha}{E_{fusion}} + \frac{1}{Q}\right)} \times \frac{1}{1.18 \times 10^{-24}}, \tag{1.18}$$

where it has been set k equal to 1, by assuming that the temperatures are expressed in keV. It is then possible to check that, in order to have a nuclear fusion reactor which produces more fusion energy than the energy it uses to produce it, i.e. for Q to be well above 1, it must be:

$$n\tau_e T > 10^{21} \text{ keV m}^{-3}\text{s}. \tag{1.19}$$

The previous relation is known as criterion of the triple product, which derives from the Lawson criterion [13] for obtaining productive nuclear fusion reactor. The realization of condition (1.19) is not trivial. To this aim, dedicated machine have been thought, since late 1960, which can allow both to reach the plasma high temperature required to obtain fusion reactions and to confine the plasma itself [14]. These machines are called tokamak (Toroidalnaya Kamera Magnitnymi Katushkami). In a tokamak the plasma particles are confined through the application of different magnetic fields, whose resultant is a magnetic field of helix shape. Thus the plasma, which

follows the magnetic field lines, is modeled to form a ring or a torus. In picture (1.1), the different magnetic coil systems are illustrated. Particularly, the magnetic fields are [15], [16]:

- a toroidal magnetic field produced by toroidal magnetic coils, whose intensity is about 10T ($\sim$ 100000 times the one of the Earth);
- a poloidal magnetic field generated by means of the central magnetic coil which induces a current of several millions of ampere passing through the plasma;
- A set of horizontal magnets which controls the balance, the shape and the position of the plasma together with the current which passes through it.

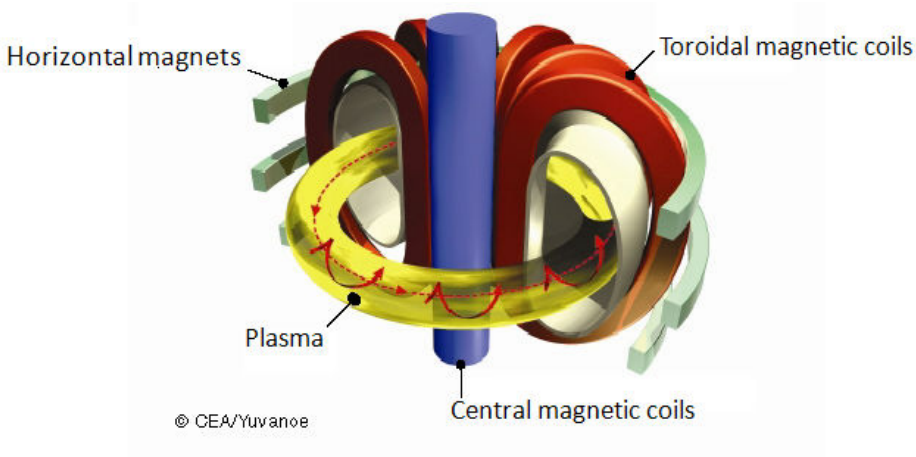

Figure 1.1: Magnetic fields in a tokamak - Description of the magnetic field configurations in a tokamak [15].

Plasma heating mechanisms in a tokamak

As it has been already pointed out, one of the main requirement to realize nuclear fusion reactions on Earth is to warm up the plasma particles at high temperature ($\sim$ 100000000 K). This is done by using several heating mechanisms. One of them is the plasma heating through the Ohmic heating power, P_{OH}. This power is due to the high intensity poloidal current, I_p, which circulates through the plasma, whose resistance, R, is different from zero, because of the collisions between high energetic electrons and ions. Hence, $P_{OH} = I_p^2 R$, and it results P_{OH} $\sim$1 MW. Nevertheless, for temperature of order of $T > 2$ keV, the plasma resistance decreases so that the Ohmic power as well decreases. As a consequence, additional heating methods have to be applied to reach

temperature of the order of $10 - 20$keV. Two further mechanisms are customary used: the neutral beam injection (NBI) system and the radio frequency (RF) heating. As far as the last technique is concerned, this process is based on the injection into the plasma of high power microwaves which transfer their energy to the plasma particles, by resonant interactions with them. Particularly, the ion RF heating system operates customary at the frequency range 35-55 MHz, while the electron RF heating system operate usually at frequency 170 GHz. The neutral beam injection system will be illustrated in more details in the following section. Briefly, it consists in injecting a high energetic beam of neutral particles, usually a hydrogen isotope such as deuterium, into the plasma. As neutral particles are not affected by the strong magnetic fields present in a tokamak, they can penetrate the plasma and transfer their energy to it by means of collisions. The described heating mechanisms are schematically represented in picture (1.2).

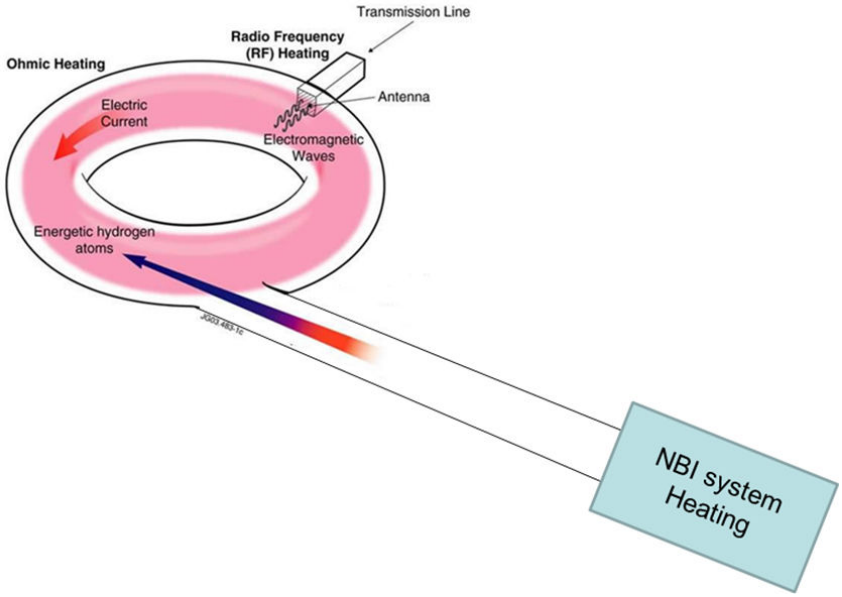

Figure 1.2: Heating systems in a tokamak, inspired by [17] - Schematic representation of the heating mechanisms used in nuclear fusion reactors based on magnetic confinement to warm up the plasma to the required temperatures for realizing nuclear fusion reactions.

1.2 NBI system generalities

In the previous section, the neutral beam injection system has been introduced as one of the mechanism applied for reaching the high temperatures required in nuclear fusion reactors based

on magnetic confinement. As it is possible to realize by looking to picture (1.2), this mechanism, unlike the other two, is developed far from the area of the plasma confinement. For this reason, it turns out to be easier to work on its amelioration than on the betterment of the other two mechanisms, for which the closeness to the region where high energetic neutrons are produced can be a significant problem. Thus, NBI system is of primary importance to improve the amplification factor, Q, of the nuclear fusion reactor. Indeed, if the efficiency of the NBI system, defined as the ratio between the NBI system power at the entrance of the tokamak and the power required to produce it, is increased, the overall efficiency of the nuclear fusion reactor will be enhanced. In this respect, it is worth pointing out that the work presented in the following chapters concerns feasibility studies for an enhancement of the NBI system, which should allow significant higher efficiencies with respect to the ones currently realizable.
As it is shown in figure (1.3), the principal components of typical NBI systems are [18], [19]:

- an ion source which generates a cold hydrogen plasma (or deuterium plasma), with temperature and density of order of $T \sim 2 - 20$ eV, $n \sim 10^{18} - 10^{19}$ m^{-3} respectively;
- an accelerator which significantly makes to increase the energy of the ions exacted from the source (up to about 1 MeV in current nuclear fusion reactors, such as ITER) ;
- a neutralizer which is a gas cell, in conventional NBI system, where the ion beam is partially neutralized by inelastic collisions with the gas injected into the cell (e.g. D_2);
- a residual ion dump, where the residual ions, which escape the neutralization, are magnetically or electrically deflected, to be separated by the neutral beam, which continues towards the tokamak torus at the end of the NBI system duct.

At energies higher than 100 keV, negative ions only can be efficiently neutralized, they are then considered for applications in nowadays NBI systems. It is worth noticing that, for negative ions the neutralization efficiency is about 55% for a gas target at 1 MeV. The inconvenient in using negative ions is that the low binding energy of the extra electron also makes higher the ion destruction rate along the beam line. Indeed, in the case of usual NBI systems, about 30% of the negative ions are lost during acceleration, because of stripping reactions with the gas injected in the ion source and, above all, with the gas injected in the neutralizer which diffuses toward the accelerator. Hence, the overall efficiency of the NBI system is sensibly reduced, being less than 25%. In conventional NBI systems, the amount of gas injected into the neutralizer cannot be reduced, with the aim of improving the performances of the injector. For this reason, it has

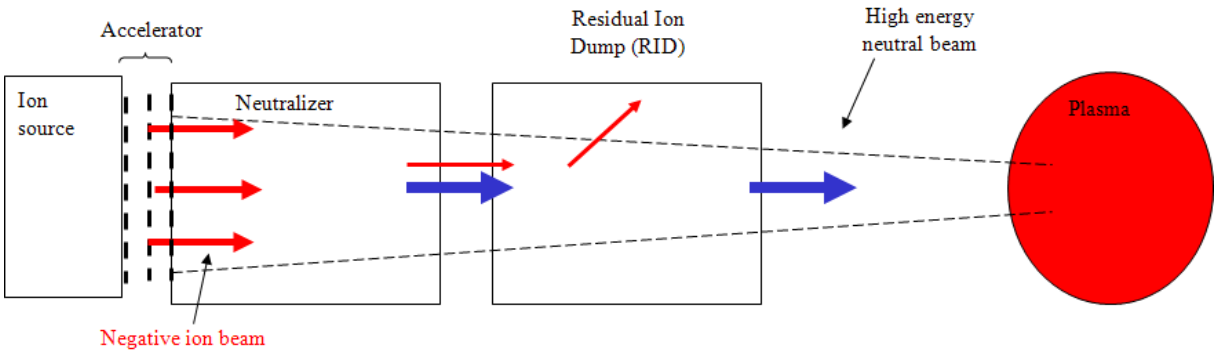

Figure 1.3: NBI system components [19] - Schematic representation of the components of a NBI system.

been proposed to substitute the gas cell neutralizer with a photo-neutralizer, which does not requires any gas injection and which could then significantly enhance the overall NBI system efficiency. In the next sections, the work principles of a photo-neutralizer are presented.

1.3 Photo-Neutralization principles

The photo-neutralization or photo-detachment process is the mechanism through which the extra electron of a negative ion is detached by electromagnetic waves. It is a precess happening only if the photon involved in the interaction with the ion has sufficiently high energy, i.e. higher than the electron affinity (EA) of the neutral atom. In the present contest, the deuterium negative ions are the most interesting ones, because they can eventually supply the deuterium directly involved in the tokamak nuclear fusion reactions. As far as the EA of the hydrogen is concerned, this has been experimentally found to be equal to 0.754 eV and, with respect to this value, the deuterium EA turns out to be about 0.4 meV higher [20]. Several studies have been also carried on to determine the behavior of the photo-neutralization cross section as function of the photon energy, both for the deuterium and for the hydrogen. It was then possible to point out that the photo-detachment cross section has a similar trend for both the considered species [21]. Particularly, the results presented in Ref. [22] and Ref. [23] show that the maximum of the photo-neutralization cross section is substantially flat for the photon energy range between 1.2 eV and 2 eV, that is between the photon wavelengths 1100 nm and 650 nm [24]. In order to stress this important feature, picture (1.4) is reported, which illustrates the photo-detachment cross section as function of the photon energy, for the hydrogen. The

consequence of this experimental result is that the choice of laser wavelengths which could be applied for the photo-neutralization process is quite large. Furthermore, it is possible to assume the deuterium ion photo-detachment cross section at its maximum equal to about $4 \times 10^{-21}\mathrm{m}^2$ [22]. It is also worth noticing that recent studies have been carried on to measure the photo-neutralization cross section concerning hydrogen, as it is shown in Ref. [25] and Ref. [26]. With

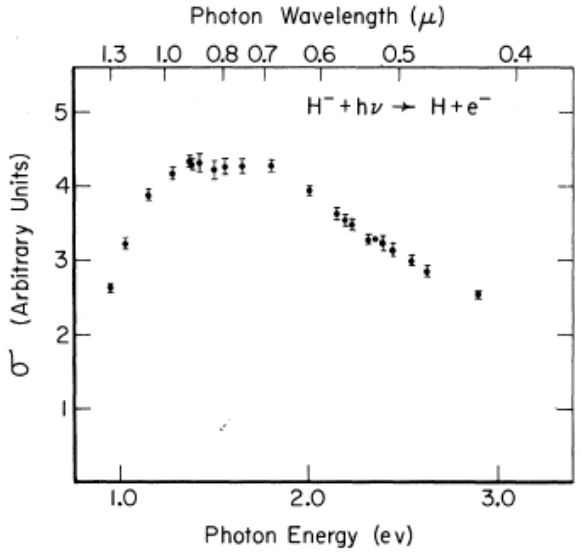

Figure 1.4: Relative photo-detachment cross section measurements for hydrogen - The shape of the cross section is determined relative to the value at 5280 A with an accuracy of about 2 %, as it is described in Ref. [22].

the aim of applying photo-neutralization for neutral beam injection systems of future generation nuclear fusion reactors, it is important to estimate the laser power required to reach a suitable neutralization efficiency. It is assumed that both the ion beam and the laser beam have a rectangular shape and the laser beam completely overlaps the ion beam on a surface $S = d \times l$, see picture (1.5). Moreover, if the deuterium ions are accelerated at 1 MeV, they have a mean velocity of about 10^7 m/s. Consequently, as the velocity of the photons is $c = 3 \times 10^8$ m/s, deuterium ions can be considered static, with respect to the laser beam photons. Let σ be the cross section of the photo-detachment process, then, from Ref. [24], the following relation holds:

$$\frac{\mathrm{d}n}{\mathrm{d}t} = -\frac{\sigma}{dl}\frac{P_L}{h\nu} \times n, \tag{1.20}$$

where n is the negative ion population, $P_L/h\nu$ is the number of photons per unit of time, P_L being the laser power, while d and l are introduced in picture (1.5). Equation (1.20) describes an

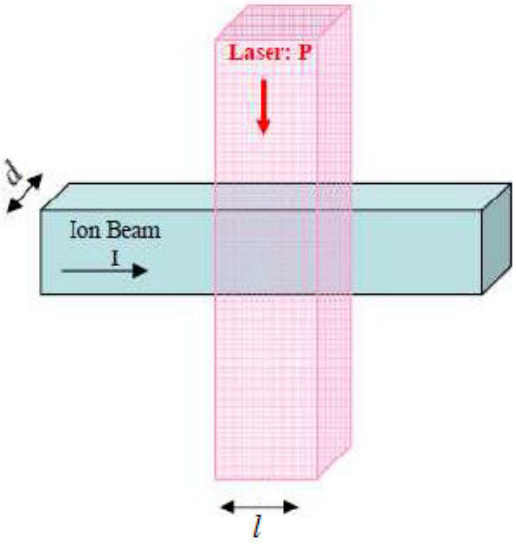

Figure 1.5: Overlap between laser beam and ion beam - Schematic illustration of the overlap between laser beam and ion beam, as described in Ref. [19]. It is worth noticing that the time necessary to the ions to cross the laser beam is $t = l/v$, where v is the ion velocity.

exponential decrease of the ion population, so that, if at the beginning, t=0, the ion population is n_0, at any following time, it becomes:

$$n(t) = n_0 e^{-\frac{\sigma P t}{dlh\nu}}. \tag{1.21}$$

Hence, if t is the time needed for the ion beam to cross the laser beam, i.e. $t = l/v$, with v the ion velocity, it results:

$$n(t) = n_0 e^{-\frac{\sigma P}{dhv\nu}}, \tag{1.22}$$

and the neutralization rate is:

$$\tau = 1 - e^{-\frac{\sigma P}{dhv\nu}}. \tag{1.23}$$

Of particular interest is the laser power at which the photo-detachment process will enter the saturation regime, that is the saturation power, P_s, beyond which the photo-neutralization rate does not increase anymore significantly, so that it is not convenient to augment further the laser power (see picucture 1.6). In particular, P_s is defined by the laser power which produces a photo-detachment rate of $1 - 1/e \sim 63\%$, i.e., by considering equation (1.23), it is:

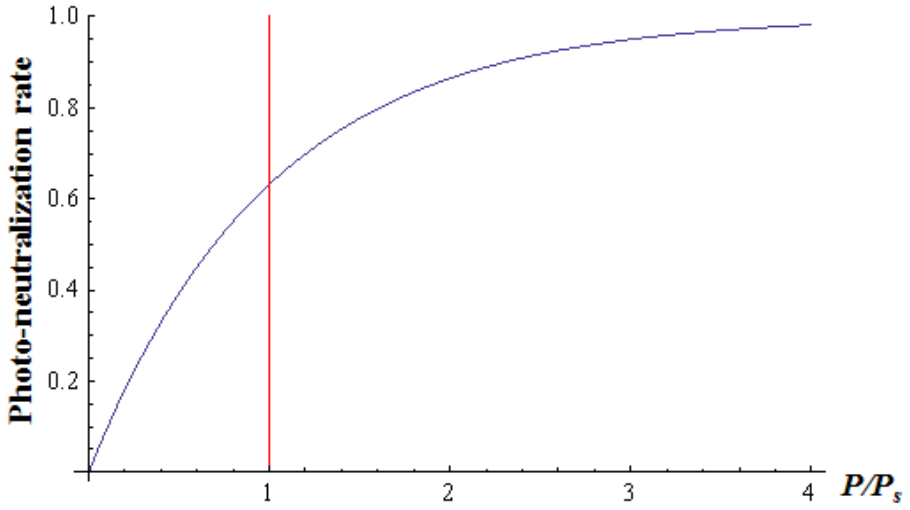

Figure 1.6: Rate of photo-neutralization, τ. - Photo-neutralization rate as function of the ration between laser beam power, P, and saturation power, P_s.

$$P_s = \frac{h\ c\ v\ d}{\sigma\ \lambda}, \tag{1.24}$$

with λ the laser wavelength. From the mathematical definition of the saturation power, it is possible to point out that, on one hand the high velocity of the negative ions are responsible for the high laser power required to get to a suitable level of photo-neutralization rate; on the other hand, equation (1.24) makes clear that it is possible to decrease the saturation laser power by choosing the highest possible value of the laser wavelength and the smallest possible ion beam width. To have an idea of the order of magnitude of the required laser power for obtaining the saturation regime of photo-detachment, it is possible to fix typical numerical values for experimental nuclear fusion reactor, such as ITER. Particularly, in this case, an ion beam at 40 A 1 MeV exits the NBI system accelerator and it is then divided in 4 independent columns 7 cm width and 1.5 m high. For the laser frequency corresponding to $\lambda = 1064$ nm, by considering equation (1.24), it is possible to verify that a laser power of about 30 MW, for each ion segments, is necessary to reach the saturation region of photo-neutralization, when assuming $\sigma = 4. \times 10^{-21} \mathrm{m}^2$ [24], [19]. It is well known that there are no laser so powerful. Nevertheless the laser technology is quite developed on the wavelength 1064 nm, so that it is possible to assume that laser of few hundred of Watts can be realized. This power is still significantly below the required one for getting to suitable values of photo-detachment, but there is still the possibility to apply an optical cavity where the input laser power can be stored in order to reach higher

laser beam power within the cavity. It is remarked that, in this design, the photo-neutralization of the negative ion beam takes place inside the cavity. Hence, it is worth estimate the laser power lost because of the photo-detachment process. By assuming that the laser beam power is less than or equal to the laser saturation power, the fraction of photons which interact with the ions in a photo-detachment process, within the time interval $t = l/v$, is given by:

$$\eta = \frac{I\ \sigma}{e\ v\ d}, \tag{1.25}$$

with I the ion current, e the charge of the deuterium ion and $\sigma/(v\Delta t d)$ the probability for a photon to photo-neutralize an ion on a length $l = v\Delta t$. Hence, for the values introduced above, i.e. I=40 A, $v = 10^7$ m/s, $d = 7$ cm, $\sigma = 4. \times 10^{-21}\mathrm{m}^2$, and $|e| = 1.6 \times 10^{-19}$ C, it is found:

$$\eta \simeq 1.4 \times 10^{-6}. \tag{1.26}$$

The previous results states that only one photon on about one million takes part on the photo-detachment process. If the saturation power is $P_s = 30$MW, this means that the laser power lost by the photo-detachment process is:

$$P_{lost} = \eta \times P_s \simeq 42W. \tag{1.27}$$

The last value is quite lower than the saturation power, so the laser beam power can be considered unchanged after the interaction with deuterium ions.
Another important point to consider is that the coatings of the mirrors used to realize the optical cavity have an electromagnetic wave intensity damage threshold I_{th}. If the laser beam is gaussian, the power it carries reads:

$$P = \frac{1}{2}\pi I_L w^2, \tag{1.28}$$

where I_L is its intensity and w its radius. In terms of the dimension d, introduced above, the following approximation is possible:

$$P \simeq I_L \times d^2. \tag{1.29}$$

At the threshold, it is:

$$P_{th} \simeq I_{th} \times d_{th}^2, \tag{1.30}$$

hence, from equation (1.24), it results:

$$d_{th} = \frac{h\ c\ v}{\sigma \lambda I_{th}}. \tag{1.31}$$

By assuming $I_{th} \sim 10$ MW/cm^2 at $\lambda = 1.06\mu$m, it turns out that the minimum value for d is d_{th}=4.7 mm, and the corresponding value for the power indicates that the minimum power for saturation of photo-detachment has to be higher than or equal to 2 MW, indeed P_{th}=2 MW. Furthermore, the mirrors have to be protected from the environment where the high energetic ions propagate. Indeed, mechanical vibrations, radiations and sputtering processes [19] can reduce the optic lifetime. Consequently, the mirrors have to be kept far from the ion beam line, so that the cavity should be a multi-metric optical resonator and vacuum chambers should be used to maintain clean the environment where the optics are placed. Another important aspect to evaluate is the change of the cavity length, which leads to changes of the laser beam characteristics resonating within the cavity. A treatment of this issue can be found in Ref. [19]. The optical length of the cavity, for unperturbed conditions, is $L = nL_0$, where n here represents the index of refraction of the medium within the cavity and L_0 is the geometrical length of the cavity. A variation of the optical length of the resonator can then be:

$$\frac{\delta(nL)}{nL} = \frac{\delta n}{n} + \frac{\delta L}{L}, \tag{1.32}$$

with $\delta L/L$ the seismic noise, which is about 10^{-8}, and $\delta n/n$ is the variation of the refractive index within the cavity due to the presence of the ion beam, which amounts to about 3×10^{-8}. The value obtained for the total variation of the optical path of the photons inside the resonator is within a range commonly considered in laser stabilization issues, thus the cavity length fluctuations should not represent a problem for the application of an optical resonator in the design of the photo-neutralization for NBI systems.

Another important observation concerns the fact that by refolding the cavity it is possible to completely overlap the ion beam width, with the application of a thiner laser beam, as it is showed in picture (1.7). Hence, from equation (1.24), it is easy to see that the laser power for the saturation regime of the photo-detachment is reduced. The lowering of the minimum laser power required for suitable levels of phot-neutralization efficiency means that a lower laser power injected into the cavity is necessary. Furthermore, the thermal load on each mirrors compounding the resonator is reduced, when the intracavity laser power decreases. This is an important feature as high thermal loads on the cavity mirrors lead to mirror deformations. In

turn, the cavity mirror distortions can cause diffusions of the impinging laser beam, which can result in losses of the intracavity laser beam power, i.e. a reduced capability of the cavity to store optical power. However, it has to be kept in mind that the increase of the cavity mirror number will enhance the cavity losses due to the mirror manufacturing defects, which are not erasable. As a consequence, a suitable optical cavity for application in NBI systems can be a refolded cavity where the refolding number is the most convenient in terms of total cavity losses. It might be worth noticing here that, as it has been already showed above, the laser power lost because of the deuterium ion photo-neutralization is quite low, so that, if the laser beam is made to cross the ion beam several times, like in the case of a refolded cavity, the intracavity laser power would not change appreciably.

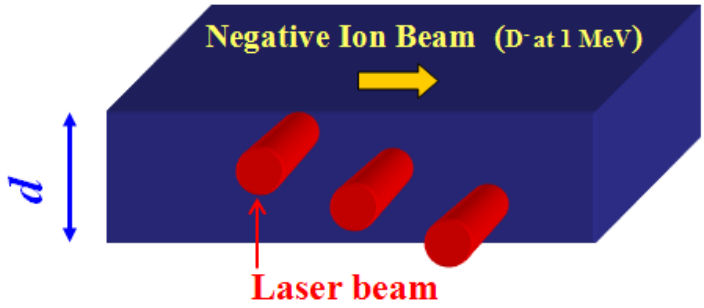

Figure 1.7: deuterium ion beam and laser beam overlap in a refolded cavity [19] - The picture show the overlap between the negative deuterium ion beam and the laser beam. The quantity d is the ion beam width, while the yellow arrow represent the propagation direction of the negative ion beam. The drawn cavity has three refoldings, as it is possible to see from the fact the beam cross three times the ion beam

1.4 Nuclear fusion reactor results and projects

So far, the main results concerning nuclear fusion have been reached with the JET (Joint European Torus) experimental reactor [27], [28]. The tokamak of JET presents a plasma volume of 100 m^3, its magnetic system is compounded of 32 coils producing a magnetic field of 3.4 T at the plasma center. The JET tokamak has also been a test for the technologies concerning the tritium treatment (mainly storage and injection within the plasma). In 1997, the JET reactor achieved the world record for the production of 16 MW of nuclear fusion, with a corresponding amplification factor of $Q = 0.65$. Another important experiment to improve the technology used in the fusion reactors is the French tokamak Tore Supra [11], [14]. Its principal aim is to

demonstrate the possibility of realizing a plasma of long duration. The plasma volume in Tore Supra is about five times less than the one of the JET experiment and its magnetic field is 4.2 T. The optimum results was obtained in 2003, when a plasma discharge lasted 6.5 minutes, by fixing the world record for the plasma duration. After these first encouraging results an international collaboration begun in 1980 for demonstrating the possibility of using the power produced through fusion as energy source. Hence, the ITER (International Thermonuclear Experimental Reactor) project was started with cooperation of USA, Europe, Canada, Japan and Soviet Union [29]. The ITER tokamak will have a plasma volume of about 800 m^3 and the magnetic field will be around 5.3 T. The main task is the production of 500 MW of nuclear fusion power for about 500 seconds, with an amplification factor of $Q \sim 10$. This value for the Q factor is still too low to allow the connection of the reactor to the electric grid, as it is not advantageous. For this reason, another project is already under study, which concerns the realization of the first reactor for a demonstrative power plant based on the production of nuclear fusion energy. This is the next step to ITER and it is know as DEMO (DEMOnstration Power Plant) [30], [31]. The DEMO nuclear fusion power production should be of about 2.4 GW, on a continual basis, with an amplification factor of $Q = 25$. With this values, the electrical power generated by DEMO is expected to be around 1 GW. The power lost in the conversion of the produced fusion power in electrical power does not add, in principle, further costs; this explains why it is important to increase the Q factor. The enhancement of the amplification factor in DEMO rests mainly on the possibility of improving the technique concerning the plasma heating systems. As it has been already pointed out in the previous section, in this respect, the NBI system, which is the only heating mechanism placed far from the plasma confinement region, appears to be the most interesting for operating convenient ameliorations. In particular, in order to pass from the ITER amplification factor to a suitable Q factor for DEMO, the overall NBI system efficiency must become higher than at least 25%. The most promising idea to improve the NBI system efficiency seems to be the replacement of the neutralizer gas cell, which is used in the case of the ITER NBI system [32], [19], [33], with a neutralizer based on the photo detachment, as it has been illustrated previously. Indeed, feasibility study have demonstrated that the application of the photo-neutralization can allow to reach overall NBI system efficiency up to 80%. In this respect, a project called SIPHORE (SIngle gap PHOtoneutralizer energy RE-covery injector) has been elaborated, which appears to be an appropriate model for the NBI system of the DEMO reactor [19], [34]. In the SIPHORE scheme, the negative deuterium ions extracted from the source are pre-accelerated in a multi-aperture system which brings the ions to the energy of 100 keV. Hence,

the ion beams which exit the pre-accelerator are collected in a single beam which is accelerated to the energy of 1 MeV, by applying a single stage electrostatic accelerator. This is why the expression *single gap* is present in the name of the project, it is referred to the characteristics of the ion accelerator. In this respect, it is noticed that this kind of accelerators cannot be applied in the ITER NBI system, due to the large amount of stripping reactions caused mainly by the gas injected into the neutralization cell. After the acceleration, the resulting high energetic negative deuterium ions are neutralized by using the photo-detachment principles, realized with the implementation of a suitable optical cavity, that is why the name of the project also contains the term *photoneutralizer*. Eventually, the energy of the ions which are not neutralized, after passing through the photo-neutralizer, is recovered by applying a dedicated system, this is the reason for the expression *energy re-covery* to be present in the project name. It is observed that such a recovery system could not be used in the ITER NBI system, because of the presence of a secondary plasma, generated by the interaction of the high energetic deuterium ion beam with the gas of the neutralizer, which diffuse within and outside the neutralization cell. A possible design for the SIPHORE NBI system [19], proposed for the DEMO reactor, is illustrated in figure (1.8).

The work presented in the following chapters is part of the SIPHORE project. In particular, its aim is to demonstrate the possibility of realizing an optical cavity with suitable properties for applications in the neutralizer of SIPHORE and, more generally, for the photo-neutralization of negative deuterium ion beams within the context of the NBI systems of the future generation of nuclear fusion reactors, such as DEMO. The issue of the optical cavity losses due to the high thermal load on the cavity mirror will be also addressed, in order to find an effective solution to the problem.

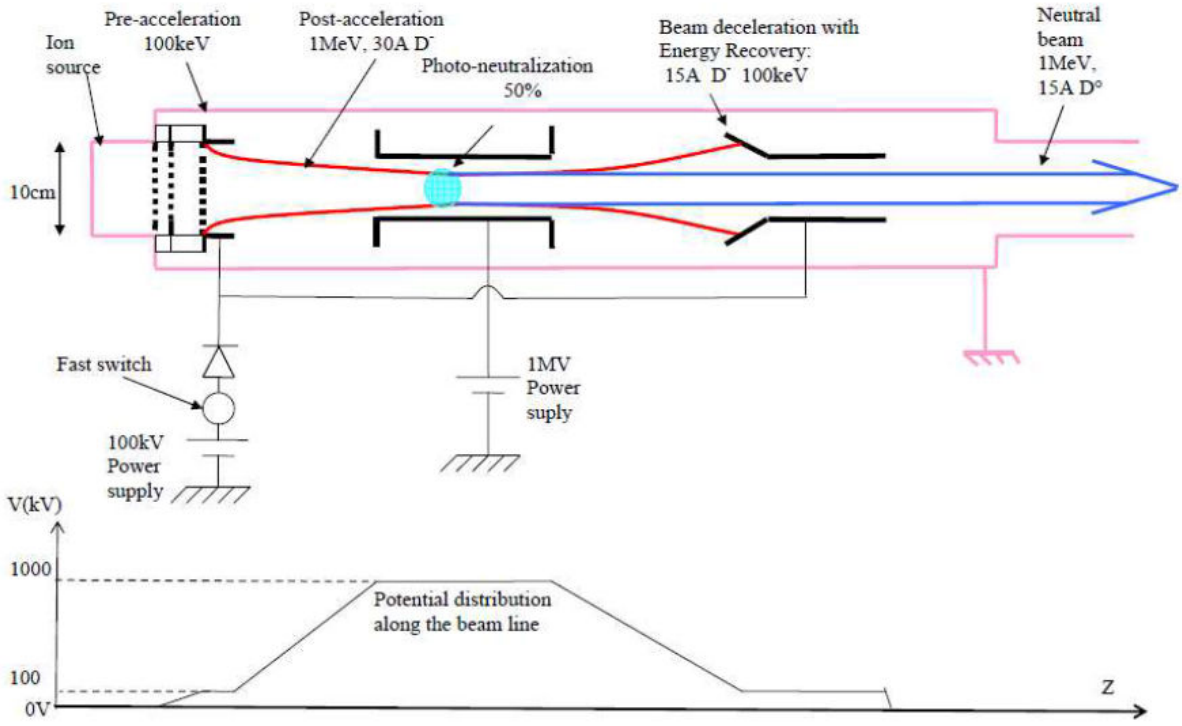

Figure 1.8: Scheme of the SIPHORE NBI system [19] - The explication of the different parts of the injector can be found within the text.

Chapter 2

Optical Cavity Design Proposal

In this chapter, it is reported on the design of an optical cavity with properties suitable for applications in NBI systems of the next generation of nuclear fusion reactors. In particular, it has been found that the requirements for NBI system applications would be accommodated by a two mirror cavity, with length of 100m [19], [35]. However, an optical cavity with this dimensions could lead to deal with encumbrance problems, if there is not enough space availability. Hence, a proposal for an optical resonator, which satisfies all the requisites for the photo-neutralization applications on a smaller length, will be presented, with respect to the theoretical determination of its design, its realization in our laboratory and the experimental tests on it.

It is worth noticing that the first section of the current chapter is dedicated to the recall of the main aspects of an optical resonator. Furthermore, in appendix (A) the mathematical description of laser beams is reported, where definitions useful to the comprehension of the chapter are introduced.

2.1 Optical cavities

An optical cavity is a system of optical components, such as mirrors, allowing the formation of a light standing wave in a path defined through the optical components. In the simplest configuration, an optical cavity is compounded of two mirrors, M_1 and M_2, with reflection coefficients r_1 and r_2, respectively, facing each others and separated by a distance L. The balance equation for M_1 and M_2 can then be written as [48]:

$$r_1^2 + t_1^2 = 1 - p_1, \tag{2.1}$$

$$r_2^2 + t_2^2 = 1 - p_2. \tag{2.2}$$

where t_1, p_1 and t_2, p_2 are the transmission coefficient and the losses for M_1 and M_2, respectively. It is assumed that a steady state optical signal, E_{inc}, is incident on M_1, while the electromagnetic wave amplitude circulating within the resonator, as taken inside M_1, is denoted as E_{cir}, see picture (2.1). The latter quantity is obtained by the sum of the transmitted signal through M_1, it_1E_{inc}, and the circulating signal which has left the point just after M_1, one round trip earlier, multiplied for the gain factor of the cavity, for each round trip, $g(\omega) = r_2r_1e^{-i\frac{2\omega L}{c}}$ [49], i.e.:

$$E_{cir} = it_1E_{inc} + r_2r_1e^{-i\frac{2\omega L}{c}}E_{cir}. \tag{2.3}$$

It is worth noticing that, in the assumed convention, the reflection and transmission coefficients are purely real, and the transmission coefficients have an additional factor i associated with them. From equation (2.3), it is obtained:

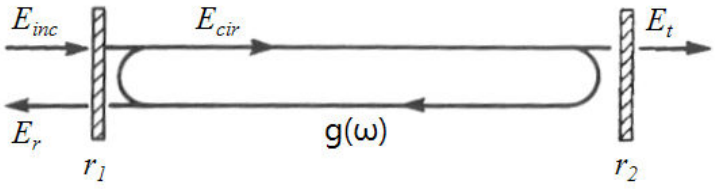

Figure 2.1: Two mirror optical cavity scheme, from [49] - Scheme of the two mirror cavity, where r_1 is the reflection coefficient of the mirror M_1 and r_2 is the reflection coefficient of the mirror M_2. The incident beam is indicated as E_{inc}, E_r represents the reflected field, E_t is the transmitted field and the circulating wave amplitude is labeled as E_{cir}, while $g(\omega)$ is the cavity gain factor for each round trip, i.e. $g(\omega) = r_2r_1e^{-i\frac{2\omega L}{c}}$.

$$E_{cir} = \frac{it_1E_{inc}}{1 - r_2r_1e^{-i\frac{2\omega L}{c}}}, \tag{2.4}$$

where the ratio E_{cir}/E_{inc} is the enhancement factor, S, which describes the power gain of the optical cavity, namely:

$$|S|^2 = \frac{|E_{cir}|^2}{|E_{inc}|^2} = \frac{t_1^2}{1 + (r_2r_1)^2 - 2r_2r_1\cos\left(\frac{2\omega L}{c}\right)}, \tag{2.5}$$

hence:

$$|S|^2 = \frac{|E_{cir}|^2}{|E_{inc}|^2} = \frac{t_1^2}{(1 - r_2r_1)^2 + 4r_2r_1\sin^2\left(\frac{2\omega L}{2c}\right)}. \tag{2.6}$$

Equation (2.6) shows that the maximum cavity gain is obtain when $\omega \equiv \omega_{res}$, where $\omega_{res} = [c/(2L)]2n\pi$ is the resonance frequency, with n an integer number, so that:

$$|S_{max}|^2 = \frac{t_1^2}{(1 - r_2 r_1)^2}, \tag{2.7}$$

with $|S_{max}|^2$ the power gain of the optical cavity at the resonance. Furthermore, from equation (2.6):

$$|S|^2 = \frac{|E_{cir}|^2}{|E_{inc}|^2} = \frac{t_1^2}{(1 - r_2 r_1)^2} \frac{1}{1 + 4\frac{r_2 r_1}{(1 - r_2 r_1)^2} \sin^2\left(\frac{2\omega L}{2c}\right)} = \frac{|S_{max}|^2}{1 + \left(2\frac{\mathcal{F}}{\pi} \sin\left(\frac{2\omega L}{2c}\right)\right)^2}, \tag{2.8}$$

where the quantity $\mathcal{F}$ is the Finesse of the cavity, i.e.:

$$\mathcal{F} = \frac{\pi\sqrt{r_2 r_1}}{1 - r_2 r_1}. \tag{2.9}$$

The finesse of an optical cavity can be interpreted as the number of round-trips of a photon before escaping from the cavity. To make clear this point, it is observed that the frequency separation between two consecutive cavity resonances, i.e. the *free spectral range*, is:

$$\Delta\nu_{FSR} = \frac{c}{2L}, \tag{2.10}$$

while equation (2.8) defines the following full width of the resonance at half maximum (FWHM), $\delta\nu_{FWHM}$:

$$\delta\nu_{FWHM} = \frac{\Delta\nu_{FSR}}{\mathcal{F}}. \tag{2.11}$$

The lifetime of the photon within the cavity, τ_p, is defined through the relation below [50], [51], [52] [53]:

$$\delta\nu_{FWHM} = \frac{1}{2\pi\tau_p}, \tag{2.12}$$

hence:

$$\tau_p = \frac{\sqrt{r_2 r_1}}{1 - r_2 r_1} \frac{L}{c} \tag{2.13}$$

and the number of round trips a photon can do within the cavity is [54]:

$$\frac{\tau_p}{2L/c} = \frac{\mathcal{F}}{2\pi}, \tag{2.14}$$

which is proportional to the cavity finesse.

In what follow, the expressions for the power circulating within the cavity at resonance, the transmitted and reflected power by the cavity are evaluated.
As far as the power circulating within the cavity at the resonance is concerned, from equation (2.7), it is:

$$P_{res} = P_{inc}|S_{max}|^2 = P_{inc}\frac{t_1^2}{(1-r_2r_1)^2}. \tag{2.15}$$

The field transmitted by the cavity is:

$$E_t = it_2e^{-i\frac{\omega L}{c}}E_{cir} = -e^{-i\frac{\omega L}{c}}\frac{t_1t_2E_{inc}}{1-r_2r_1e^{-i\frac{2\omega L}{c}}}, \tag{2.16}$$

therefore, the transmitted power is:

$$P_t = P_{inc}\left|\frac{E_t}{E_{inc}}\right|^2 = P_{inc}\frac{(t_1t_2)^2}{(1-r_2r_1)^2}\frac{1}{1+4\frac{r_2r_1}{(1-r_2r_1)^2}\sin^2\left(\frac{\omega L}{c}\right)}. \tag{2.17}$$

For the field reflected by the cavity, one has:

$$E_r = r_1E_{inc} + it_1r_2e^{-i\frac{2\omega L}{c}}E_{cir} = r_1E_{inc} - e^{-i\frac{2\omega L}{c}}\frac{r_2t_1^2E_{inc}}{1-r_2r_1e^{-i\frac{2\omega L}{c}}}. \tag{2.18}$$

Analogously to the transmitted power, the reflected power expression is:

$$P_r = P_{inc}\left|\frac{E_r}{E_{inc}}\right|^2 = P_{inc}\frac{r_1^2+r_2^2(1-p_1)^2-2r_1r_2(1-p_1)\cos\left(\frac{2L\omega}{c}\right)}{(1-r_2r_1)^2+4r_2r_1\sin^2\left(\frac{2\omega L}{2c}\right)}, \tag{2.19}$$

with $|E_r/E_{inc}|^2$ obtained from equation (2.18).

An optical cavity is said stable if the intracavity laser beam is periodically refocused, so that it can be trapped inside the cavity. For a two mirror resonator, the stability condition is defined through the introduction of the so called mirror *g-factors*. Particularly, if R_1 is the curvature radius of M_1, R_2 is the curvature radius of M_2 and L, as usual, is the distance between the two mirrors, the g-factor for M_1 is:

$$g_1 = 1 - \frac{L}{R_1}, \tag{2.20}$$

while, for M_2:

$$g_2 = 1 - \frac{L}{R_2}. \tag{2.21}$$

The stability criterion reads then:

$$0 < g_1 g_2 < 1. \tag{2.22}$$

The trapped gaussian beam has a unique waist, which can be expressed by using g_1 and g_2, namely:

$$w_0^2 = \frac{L\lambda}{\pi}\sqrt{\frac{g_1 g_2(1-g_1 g_2)}{(g_1+g_2-2g_1 g_2)^2}}, \tag{2.23}$$

with λ the laser wavelength.
Furthermore, the w_0 distance from M_1, d_1, can also be calculated through g_1, g_2, indeed:

$$d_1 = \frac{g_2(1-g_1)}{g_1+g_2-2g_1 g_2}L, \tag{2.24}$$

analogously, for the distance of w_0 from M_2, d_2, it is:

$$d_2 = \frac{g_1(1-g_2)}{g_1+g_2-2g_1 g_2}L. \tag{2.25}$$

The stability criterion (2.22) can also be written in terms of the Gouy phase. Indeed, the Gouy phase accumulated in one round trip within the cavity by the laser beam can be written as [49]:

$$\Phi_G = 2\arccos(\pm\sqrt{g_1 g_2}), \tag{2.26}$$

hence:

$$\cos\Phi_G = \cos\left(2\arccos\left(\pm\sqrt{g_1 g_2}\right)\right) = 2\cos^2\left(\arccos\left(\pm\sqrt{g_1 g_2}\right)\right) - 1 = 2g_1 g_2 - 1. \tag{2.27}$$

Relation (2.22) gives then constraints on the Gouy phase values for stable optical cavities, namely:

$$0 < \frac{\cos\Phi_G + 1}{2} < 1. \tag{2.28}$$

To conclude this section, it is observed that the total round trip on-axis longitudinal phase shift of the laser beam is:

$$\Psi = 2kL - (N+1)\times\Phi_G, \tag{2.29}$$

where $k = 2\pi/\lambda$, with λ the laser wavelength, N is the order of the mode taken into account, i.e. $N = n+m$ for Hermite-Gaussian beam and $N = 2p+|m|$ for Laguerre-Gaussian beam, and Φ_G is the total Gouy phase shift in one round trip. A laser beam resonating within the cavity

if its total on axis phase shift after one round trip is $2\pi q$, with q integer, hence [52]:

$$\nu = \Delta\nu_{FSR}\left(q + \frac{(N+1)}{2\pi} \times \Phi_G,\right), \tag{2.30}$$

where ν is the resonance frequency of the mode N and $\Delta\nu_{FSR}$ has been introduced above. The previous relation illustrates that the resonance frequency depends on the order of the considered propagation mode. Modes with the same value of N and different q are known as *longitudinal modes* and they have identical intensity distributions. Modes with different N values have different transverse intensity profiles. In particular, through equation (2.30), it is possible to check that the resonance frequencies of two transverse modes N, N' with same longitudinal mode, namely with the same value of q, are spaced by:

$$\nu_N - \nu_{N'} = [N - N']\frac{\Phi_G}{2\pi}\Delta\nu_{FSR}. \tag{2.31}$$

The previous relation makes clear that in order to have a unique transverse mode resonating within the cavity, the Gouy phase accumulated in one round trip within the resonator must have appropriate values. Indeed, if Φ_G is too small, all the transverse modes can in principle resonate inside the cavity, at the same time, as it can be checked from equation (2.31), by setting $\Phi_G \sim 0$. Analogously, if $\Phi_G \sim 2n\pi$, with n=$\pm1, \pm2$..., all the modes have resonance frequencies spaced by about a multiple of $\Delta\nu_{FSR}$, and they have then resonance frequencies close to the ones of the fundamental mode, with the same effect described above that all the transverse modes could resonate at the same time. A cavity where all the transverse modes resonate is referred to as *degenerate optical cavity*. It is worth noticing that a degenerate cavity is not stable, as it can be easily checked by imposing $\Phi_G = 0$ or $\Phi_G = 2n\pi$, with n=$\pm1, \pm2$..., in equation (2.28). Nevertheless, if $\Phi_G \sim 0$ or $\Phi_G \sim 2n\pi$, with n=$\pm1, \pm2$..., the cavity can allows the contemporaneous resonance of several transverse modes and it is said *marginally stable optical cavity*.

2.2 Optical cavity design for NBI system applications

As it has been pointed out in chapter (1), an optical cavity dedicated to the photo-neutralization of negative deuterium ion beams, in the context of NBI systems, must be able to store a high level of intracavity power. Therefore, the cavity mirrors will undergo thermal effects, such as distortions of their reflecting surface. It has been showed, (see Ref. [55], [56]), that a degenerate

cavity would enhance thermal effect issues, indeed, perturbations of the cavity geometry can easily lead to power transfer from the fundamental mode to higher-order modes. In turns, the contamination of higher-order modes on one hand reduces the coupling of the field resonating within the cavity, with the consequence of decreasing its optical gain, on the other hand it changes its spatial distribution. A suitable optical cavity for application in NBI system must then be a non-degenerated optical cavity, which allows an efficient suppression of the higher order mode resonance [55]. As it has been shown in the previous section, this means that the Gouy phase accumulated in one round trip within the resonator, Φ_G, must have a suitable value, neither too small nor too large, so that the cavity will be stable. Further properties for an optical cavity for applications in NBI systems have been discussed in section (1.3). They are synthesized in the following:

- *constant intracavity laser beam section*, within a percent error of about 5%, to guarantee the complete overlap of the ion beam;
- *cavity refoldings* to decrease the thermal load on the cavity mirrors, by reducing the intracavity beam section, and to allows the complete overlap of the ion beam;
- *high quality optics* with low loss level to allow of reaching the required intracavity power;
- *multi-metric cavity* in order to keep the optics well outside the polluted (because of radiations, gas, vibrations...) region, which could reduces their lifetime, and for the stabilization of the cavity.

The appropriate number of cavity refoldings is obtained by a compromise, indeed, on one hand the higher the number of the refoldings the lower can be the thermal load on the mirrors, hence the thermal effects, on the other hand, the higher the refolding number the larger is the number of cavity mirrors, hence the total cavity losses. For the SIPHORE injector a possible configuration (Ref.[35]) corresponds to a four times refolded cavity with a total length of 100 m. In this respect, picture (2.2) is reported, where the overlap between laser beam and ion beam is also showed. The mirrors are all flat, but the end mirror, which is curve, with curvature radius $R_f = 1000$m. The cavity is then equivalent to a stable two mirror cavity, whose g-factors are $g_1 = 1$ and $g_2 = 0.9$, with waist on the flat mirror equal to 1cm. It is possible to check (see Ref.[49]) that the maximum variation of the beam size inside the cavity is of about 5%. With a laser input power of 1kW, this optical resonator can allow to reach an intracavity power of 3 MW, when choosing opportunely the mirror optical properties (reflection and transmission coefficients, as

it is showed in equations (2.15)) and by assuming to be able of correcting the mirror thermal effects. It is important to point out that the saturation power, introduced in section (1.3) through equation (1.24), is of $\sim$ 12 MW, when assuming $v = 10^7 ms^{-1}$, $\lambda = 1064$nm, $d = 3$cm and $\sigma = 4.5 \times 10^{-21}\text{m}^2$. In this respect, it is observed that, because of the four cavity refoldings and of the laser beam diameter of 2 cm, the laser power experimented by the ion beam is about 3 MW $\times$ 4= 12 MW. However, it might be possible that there will be encumbrance problems to implement such a long cavity in NBI systems. Hence, in the following sections, a design for an optical cavity of reduced size whose properties allow to maintain all the requirements mentioned in this section, will be presented. In particular, the addressed optical resonator is compounded of three mirrors, where two of them are used to form a telescope which has the aim of stabilizing the cavity, through the definition of an appropriate value for the Gouy phase accumulated in one cavity round trip, and to control the intracavity beam size (see Ref. [57], [58], [59]).

2.3 Optical resonator with telescope

An optical resonator incorporating a telescope is taken into account, in the current section, to the aim of demonstrating the possibility of realizing an optical cavity with suitable properties for application in NBI systems and with reduced size with respect to the 100m long optical cavity described in the previous section. Indeed, the telescope, on one hand, consents to control the beam size, on the other hand, allows to accumulate an appropriate value for the Gouy phase shift on one complete round trip, so that the cavity results stable. In particular, the optical resonator of picture (2.3) is addressed, where mirrors M_1 and M_2 are used to form the telescope, and one flat mirror, M_3, constitutes the end mirror of the cavity. Nevertheless, the considered optical system would have analogous properties, if more flat mirrors are added, after the telescope, to refold the cavity. With reference to picture (2.3), it is assumed that M_1 has curvature radius $R_1 = 15$cm, while for M_2 it is $R_2 = 100$ cm and M_3 has infinitive curvature radius. In addition, it is possible to set the distance between M_2 and M_3, L_2, equal to 100cm. It is worth noticing that the chosen value for L_2 is based on the consideration that the determined cavity must be reproduced in our laboratory to test it, hence its dimensions must fit the space availability. Analogously, quite common values for R_1 and R_2 have been chosen, in order to ensure their availability at the moment of the cavity building in our laboratory. The design determined for the considered optical cavity can then be scaled in order to find a resonator length suitable for NBI system applications. The length L_1 is the quantity we have to determine so that the

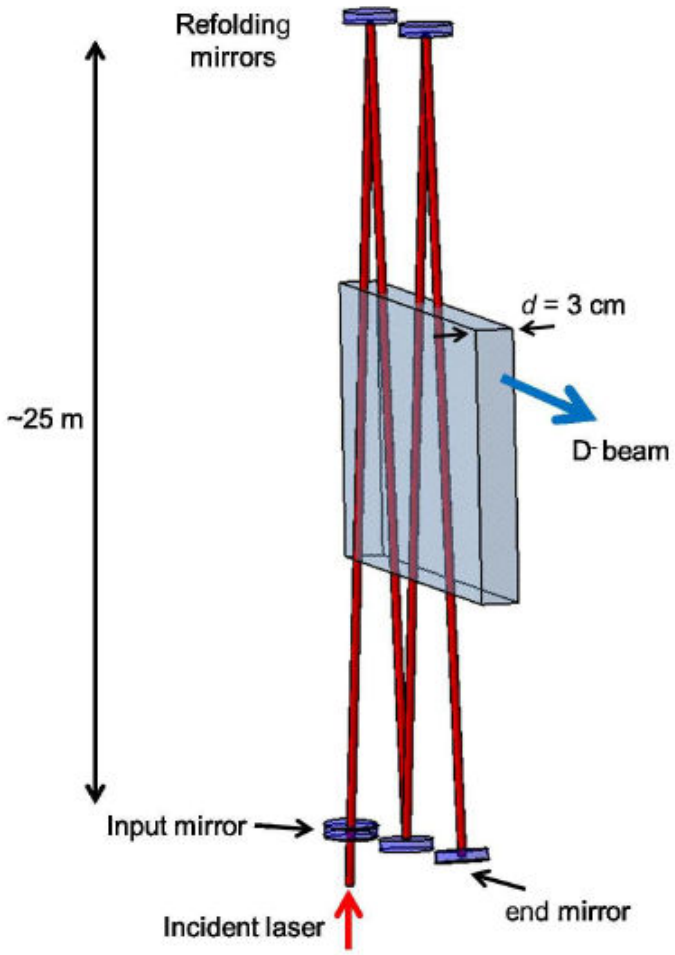

Figure 2.2: Optimum geometry of the cavity for the Siphore injector - The intracavity beam is refolded four times to cover the whole ion beam width of 3 cm.

optical cavity has appropriate characteristics for applications in NBI systems. In this respect, relation (2.27) can be used to write the stability condition for a multi-mirror resonator. Indeed, in analogy with the two mirror cavity theory, it is possible to write:

$$\cos \Phi_G = 2g - 1, \tag{2.32}$$

where Φ_G is the Gouy phase cumulated within the considered resonator, on one complete round trip, and g can be considered as the *generalized g-factor* of the multi-mirror cavity. In order to be well inside the stability region, it is imposed: $0.02 \leq g \leq 0.98$, therefore, from equation (2.32), it results:

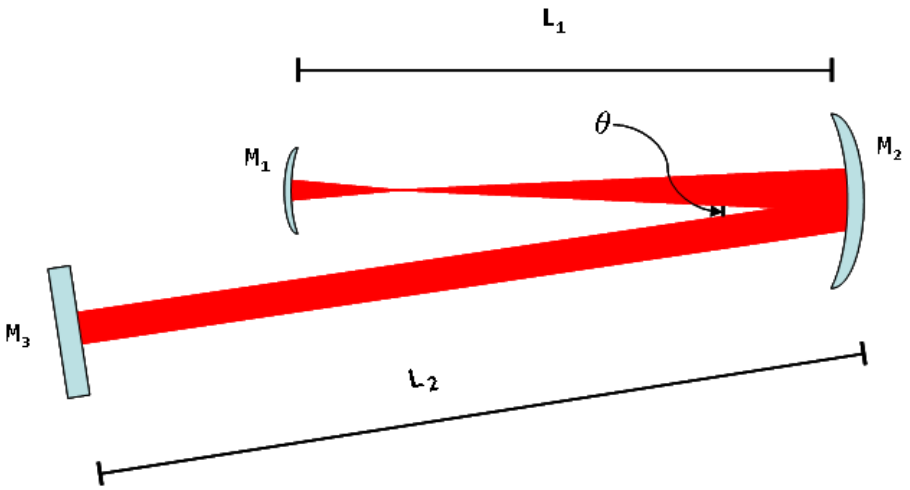

Figure 2.3: Design of an optical cavity with telescope - The mirror M_1 and M_2 are used to compound a telescope which magnifies the beam size and allow to fix a round trip Gouy phase shift appropriate to stabilize the cavity.

$$-0.96 \leq \cos \Phi_G \leq 0.96. \tag{2.33}$$

In addition to the stability requirement, along the length L_2 the laser beam size must be constant, as this part of the cavity should be involved in the photo-detachment process. This condition can be translated in a mathematical form by imposing:

$$\frac{\mid w_3 - w'_3 \mid}{w_3} < 5\%, \tag{2.34}$$

where w_3 and w'_3 correspond to the beam spot on M_3 and on M_2, respectively. Another condition to impose concerns the beam size on the length between M_2 and M_3. It is set:

$$w_3 \sim 2 \text{ mm}. \tag{2.35}$$

Indeed, the Gouy phase is defined through equation (A.17) and, as it has been already showed, it expresses the cavity stability. As a consequence, if the beam waist of the cavity, along L_2, w_3, is scaled of a factor ρ, because of the Rayleigh length dependence on the beam waist (see appendix (A)), the length L_2 must be changed of a factor ρ^2 to maintain the same stability conditions, for the scaled resonator. In this respect, if a beam waist of 1 cm is required, as for the case of the cavity for applications in NBI systems, condition (2.35) leads to cavity lengths significantly smaller than 100 m. Particularly, if a solution for L_1 is found so that $w_3 \equiv 2$mm, the scale factor to obtain a waist of 1 cm is 5, then L_2 for the scaled cavity would be $5^2 \times 1$m =25 m. The properties of the telescope compounded by M_1 and M_2 can be adapted in order to match the scaled cavity beam mode, along L_2, as it is showed in section (2.3.14). Furthermore, because of the chosen values for the mirror curvature radii and for the beam size along L_2, the waist between M_1 and M_2 is of about few hundred μm. Indeed, in the condition of small focal length of M_2, $f = R_2/2$, with respect to the Raleigh length associated with the w_3 size, as given in relation (2.35), the expression for the waist between M_1 and M_2 can be approximated as:

$$w_{01} = \frac{\lambda R_2}{2\pi w_3} \sim 85\mu\text{m}. \tag{2.36}$$

In order to verify that the region of the cavity delimited by M_1 and M_2 magnifies the beam size, the ratio w_3/w_1, with w_1 the beam radius on M_1, is evaluated, to check if it is:

$$\frac{w_3}{w_1} > \text{few units}. \tag{2.37}$$

To determine the appropriate value of L_1, which satisfies all the introduced conditions (2.33), (2.34), (2.35), (2.37), the *ABCD matrix formalism* is used. In addition, it is observed that the design of the cavity shows the presence of astigmatism issues due to the presence of the θ angle [60]. However, it is assumed $\theta << 1$. Hence, the L_1 distance is determined when assuming $\theta \equiv 0$, then the results obtained for the case without astigmatism are corrected, for a particular value of the θ angle.

2.3.1 ABCD Matrix formalism

In the paraxial approximation, the propagation of Gaussian beams through an optical system can be described by the $ABCD$ matrix formalism or *ray transfer matrix formalism*, where the effect of each optical element on the laser beam is given by a 2×2 matrix. Particularly, the matrices for the propagation through a lens, with focal length f is:

$$L = \begin{pmatrix} 1 & 0 \\ -\frac{1}{f} & 1 \end{pmatrix}, \tag{2.38}$$

which also give the propagation through a mirror of curvature radius R, by substituting the focal length f, with R, knowing that $f = R/2$. It is assumed f positive for converging lenses and R positive for concave mirror. As far as the $ABCD$ matrix for the propagation in the free space is concerned, for a length d, this is:

$$D = \begin{pmatrix} 1 & d \\ 0 & 1 \end{pmatrix}. \tag{2.39}$$

The passage of a laser beam through a system of optical elements is described by the $ABCD$ matrix product. For example, for a beam which passes through a lens of focal length f and then propagates over a distance d, the complete $ABCD$ matrix for the system, M, is obtained by:

$$M = \begin{pmatrix} 1 - \frac{d}{f} & d \\ -\frac{1}{f} & 1 \end{pmatrix} = DL = \begin{pmatrix} 1 & d \\ 0 & 1 \end{pmatrix} \begin{pmatrix} 1 & 0 \\ -\frac{1}{f} & 1 \end{pmatrix}. \tag{2.40}$$

The so called *ABCD law* links the q-parameter of a Gaussian beam before passing through an optical system described by an $ABCD$ matrix, and its q-parameter after passing through the optical system, q'. If q_0 is the initial q-parameter of the Gaussian beam, the $ABCD$ law reads:

$$q' = \frac{Aq_0 + B}{Cq_0 + D}. \tag{2.41}$$

It is worth observing that if M is the $ABCD$ matrix, with all real elements, which describes a complete round trip within an optical resonator, the existence of a confined and stable Gaussian mode solution of the cavity is guaranteed by the following condition [49], [61]:

$$\left| \frac{A + D}{2} \right| < 1. \tag{2.42}$$

An optical resonator for which the previous condition holds is stable both in the sense that it is a focusing system and in the sense that small perturbations of the mode injected into the resonator, with respect to the cavity mode, and of the mirror alignment are suppressed (see Ref.[49]).

2.3.2 Optical cavity analysis through $ABCD$ matrix formalism

In order to analyze the properties of the cavity under study, in the current section, the $ABCD$ matrix method introduced above is applied. With reference to figure (2.3), by fixing as initial point the one just before the reflection on M_1, the matrix elements for a complete round trip within the resonator are given by the matrix product:

$$\begin{aligned} M_{rt} = \begin{pmatrix} A_{rt} & B_{rt} \\ C_{rt} & D_{rt} \end{pmatrix} = \begin{pmatrix} 1 & L_1 \\ 0 & 1 \end{pmatrix} \begin{pmatrix} 1 & 0 \\ -\frac{2}{R_2} & 1 \end{pmatrix} \begin{pmatrix} 1 & L_2 \\ 0 & 1 \end{pmatrix} \begin{pmatrix} 1 & 0 \\ 0 & 1 \end{pmatrix} \begin{pmatrix} 1 & L_2 \\ 0 & 1 \end{pmatrix} \times \\ \times \begin{pmatrix} 1 & 0 \\ -\frac{2}{R_2} & 1 \end{pmatrix} \begin{pmatrix} 1 & L_1 \\ 0 & 1 \end{pmatrix} \begin{pmatrix} 1 & 0 \\ -\frac{2}{R_1} & 1 \end{pmatrix}, \end{aligned} \tag{2.43}$$

therefore:

$$\begin{aligned} A_{rt} &= \tfrac{L_1^2(8R_2-16L_2)}{R_1R_2^2} + \tfrac{L_1\left(16L_2R_2+8L_2R_1-4R_2^2-4R_1R_2\right)}{R_1R_2^2} + \tfrac{-4L_2R_2^2-4L_2R_1R_2+R_1R_2^2}{R_1R_2^2}, \\ B_{rt} &= L_1^2\left(\tfrac{8L_2}{R_2^2} - \tfrac{4}{R_2}\right) + L_1\left(2 - \tfrac{8L_2}{R_2}\right) + 2L_2, \\ C_{rt} &= \tfrac{8L_1(R_2-2L_2)}{R_1R_2^2} + \tfrac{8L_2(R_1+R_2)-2R_2(2R_1+R_2)}{R_1R_2^2}, \\ D_{rt} &= 1 - \tfrac{4L_2}{R_2} + L_1\left(\tfrac{8L_2}{R_2^2} - \tfrac{4}{R_2}\right). \end{aligned} \tag{2.44}$$

For the chosen values of R_1, R_2 and L_2, it is found:

$$M_{rt} = \begin{pmatrix} A_{rt} = -\frac{89}{3} + \frac{21L_1}{25} - \frac{2L_1^2}{375} & B_{rt} = 200 - 6L_1 + \frac{L_1^2}{25} \\ C_{rt} = \frac{11}{25} - \frac{2L_1}{375} & D_{rt} = -3 + \frac{L_1}{25} \end{pmatrix} \tag{2.45}$$

It is possible to obtain the q parameter on the mirror M_1, $q_1 = z_1 + iz_{1R}$, through the M_{rt}

matrix by using the $ABCD$ law:

$$q' = \frac{A_{rt}q_0 + B_{rt}}{C_{rt}q_0 + D_{rt}}. \tag{2.46}$$

Indeed, for a complete round trip of the laser beam within the resonator, the consistency condition for the q parameter must be verified, i.e. it has to be $q' = q_0 = q$. Hence, q_1 can be determined by solving the following equation:

$$q_1 = \frac{A_{rt}q_1 + B_{rt}}{C_{rt}q_1 + D_{rt}}. \tag{2.47}$$

Onces q_1 is obtained, the value of the q parameter in any other position of the optical cavity can be calculated. The solutions of equation (2.47) are given by:

$$\frac{1}{q_{1a,1b}} = \frac{A_{rt} - D_{rt}}{2B_{rt}} \mp \frac{1}{B_{rt}}\sqrt{\left(\frac{A_{rt} + D_{rt}}{2}\right)^2 - 1}. \tag{2.48}$$

Only one between the previous two results represents a physical solution carrying finite power. Between $\frac{1}{q_{1a}}$ and $\frac{1}{q_{1b}}$, the one which has a negative imaginary part has to be chosen [49]. Hence the solution can be written as:

$$\frac{1}{q_1} = \frac{A_{rt} - D_{rt}}{2B_{rt}} - \frac{i}{|B_{rt}|}\sqrt{1 - \left(\frac{A_{rt} + D_{rt}}{2}\right)^2}, \tag{2.49}$$

where it must be:

$$1 - \left(\frac{A_{rt} + D_{rt}}{2}\right)^2 > 0, \tag{2.50}$$

indeed, if, in the last relation, the opposite inequality holds, no confined modes exist for the considered resonator. It is observed that relation (2.50) implies the stability of the resonator, in agreement with equation (2.42), and it gives an additional condition to determine L_1. From equation (2.49), it results:

$$q_1 = \frac{2B_{rt}(D_{rt} - A_{rt})}{(D_{rt} - A_{rt})^2 + 4\left(1 - \left(\frac{A_{rt}+D_{rt}}{2}\right)^2\right)} + \frac{i4|B_{rt}|\sqrt{1 - \left(\frac{A_{rt}+D_{rt}}{2}\right)^2}}{(D_{rt} - A_{rt})^2 + 4\left(1 - \left(\frac{A_{rt}+D_{rt}}{2}\right)^2\right)}, \tag{2.51}$$

so:

$$z_1 = \frac{2B_{rt}(D_{rt} - A_{rt})}{(D_{rt} - A_{rt})^2 + 4\left(1 - \left(\frac{A_{rt}+D_{rt}}{2}\right)^2\right)}, \tag{2.52}$$

and:

$$z_{1R} = \frac{4|B_{rt}|\sqrt{1-\left(\frac{A_{rt}+D_{rt}}{2}\right)^2}}{(D_{rt}-A_{rt})^2+4\left(1-\left(\frac{A_{rt}+D_{rt}}{2}\right)^2\right)}. \tag{2.53}$$

It is worth noticing that z_1 gives the distance of M_1 from the beam waist which is between M_1 and M_2. As far as the Gouy phase in the M_1 position is concerned, it reads:

$$\phi_1 = \arctan\left(\frac{z_1}{z_{1R}}\right). \tag{2.54}$$

As q_1 can now be calculated, the q-parameter in any other position inside the cavity can be evaluated, by using the correct $ABCD$ matrix elements and relation (2.46). As a consequence, if $q' = z' + iz'_R$ is the q-parameter in a generic position inside the cavity, and $A'B'C'D'$ is the matrix of the appropriated optical system, the following relations are obtained:

$$z' = \frac{A'C'(z_1^2+z_{1R}^2)+(A'D'+B'C')z_1+B'D'}{(C'z_1+D')^2+z_{1R}^2C'^2}, \tag{2.55}$$

$$z'_R = \frac{z_{1R}^2}{(C'z_1+D')^2+z_{1R}^2C'^2} \tag{2.56}$$

In order to calculate the Gouy phase accumulated within the resonator, the knowledge of the q-parameter in the M_3 position, $q_3 = z'_3 + iz'_{3R}$, is required. So, the appropriate matrix elements have to be evaluated and they are obtained through the following matrix product:

$$M_3 = \begin{pmatrix} 1 & L_2 \\ 0 & 1 \end{pmatrix}\begin{pmatrix} 1 & 0 \\ -\frac{2}{R_2} & 1 \end{pmatrix}\begin{pmatrix} 1 & L_1 \\ 0 & 1 \end{pmatrix}\begin{pmatrix} 1 & 0 \\ -\frac{2}{R_1} & 1 \end{pmatrix},$$

hence, for the values introduced before for R_1, R_2, L_2, it results:

$$M_3 = \begin{pmatrix} A_3 = -\frac{43}{3}+\frac{2L_1}{15} & B_3 = 100-L_1 \\ \\ C_3 = -\frac{23}{150}+\frac{L_1}{375} & D_3 = 1-\frac{L_1}{50} \end{pmatrix}. \tag{2.57}$$

It is observed that, by using the last matrix elements together with equation (2.55) and equation (2.56), the quantities z'_3 and z'_{3R}, entering the definition of the q-parameter on M_3, that is

$q_3 = z'_3 + iz'_{3R}$, can be written as function of L_1.

2.3.3 Determination of L_1

As it has been already pointed out, the case without astigmatism is firstly taken into account. Therefore, once the distance between M_1 and M_2, L_1, is determined, the design of the optical cavity in figure (2.3) is completely known. To obtain possible values of L_1, firstly condition (2.50) is solved, by considering the A_{rt} and D_{rt} matrix elements reported in equation (2.45). Then, it results:

$$50 < L_1 < 65 \ \cup \ 100 < L_1 < 115. \tag{2.58}$$

To restrict L_1 inside a smaller range, the other conditions introduced at the beginning of section (2.3) are taken into account to verify for which L_1 values they are better satisfied.

2.3.4 Gouy phase calculation

The Gouy phase accumulated inside the optical cavity has to be calculated in order to verify if condition (2.33) is satisfied. In what follows, figure (2.4) will be addressed. When the $ABCD$

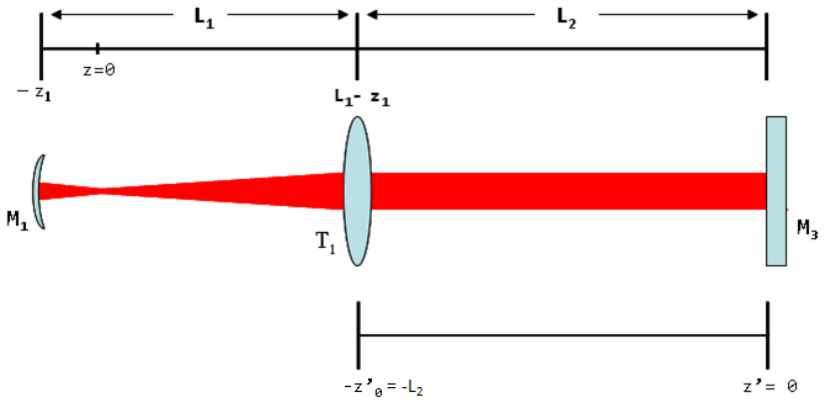

Figure 2.4: Optical system equivalent to the cavity in figure (2.3). - Equivalent optical system compounded of lenses for the optical cavity of picture (2.3).

law is applied to calculate the q-parameter in a generic position, the obtained z value is the considered generic position in a reference frame with origin on the beam waist position. The presence of the lens T_1 changes the reference point along the z axis, as a second waist in the position indicated as $z' = 0$ is present. Therefore, for the Gouy phase shift, it is possible to

write:

$$\begin{cases} \phi(z) = \arctan\left(\frac{z}{z_{1R}}\right) & \text{if } -z_1 < z < L_1 - z_1 \\ \\ \phi(z') = const + \arctan\left(\frac{z'}{z'_{3R}}\right) & \text{if } -L_2 < z' < 0 \end{cases} \tag{2.59}$$

where z_1 and z_{1R} are given by equations (2.52), (2.53) respectively, and z'_{3R} is obtained by using equations (2.56), (2.57). The constant in relation (2.59) is due to the fact that the Gouy phase must be continuum.

As:

$$z = (L_1 - z_1) + z'_0 + z', \tag{2.60}$$

it is possible to write the second of relations (2.59) as a function of z, i.e.:

$$const + \arctan\left(\frac{z - (L_1 - z_1) - z'_0}{z'_{3R}}\right), \tag{2.61}$$

so that, in order to have the continuity of the Gouy phase in the position $z = L_1 - z_1$, the following equation must hold:

$$\arctan\left(\frac{L_1 - z_1}{z_{1R}}\right) = const + \arctan\left(\frac{-L_2}{z'_{3R}}\right), \tag{2.62}$$

then:

$$const = \arctan\left(\frac{L_1 - z_1}{z_{1R}}\right) + \arctan\left(\frac{L_2}{z'_{3R}}\right), \tag{2.63}$$

where it has been considered that $z'_0 = L_2$. The Gouy phase accumulated inside the cavity is:

$$\Phi_G = 2[\phi(L_1 - z_1 + L_2) - \phi(-z_1)]. \tag{2.64}$$

By using the formulas obtained above, it is possible to check the last relation reads:

$$\Phi_G = 2\left[\arctan\left(\frac{L_1 - z_1}{z_{1R}}\right) + \arctan\left(\frac{L_2}{z'_{3R}}\right) + \arctan\left(\frac{z_1}{z_{1R}}\right)\right]. \tag{2.65}$$

Hence, equation (2.65) has to be calculated as function of L_1 to obtain the range of L_1 values for which condition (2.33) is satisfied. For the sake of completeness, it is observed that the Gouy phase shift for one complete round trip in a multi-mirror optical resonator can also be obtained

from the following relation (see Ref. [49]):

$$\cos\Phi_G = \frac{A+D}{2} \implies \Phi_G = \arctan\left(\frac{\pm\sqrt{1-\left(\frac{A+D}{2}\right)^2}}{\frac{A+D}{2}}\right), \tag{2.66}$$

where A and D are the $ABCD$ matrix elements for one round trip within the optical cavity. It is possible to check that the last equation and relation (2.65) give the same results. However, for the presented theoretical determination of the cavity design, equation (2.65) is used.

2.3.5 Calculations of the intracavity beam conditions

In addition to the constraint (2.33), the range of possible L_1 values is determined by requiring the validity of conditions (2.34), (2.35), (2.37). In order to verify for which values of L_1 condition (2.34) is satisfied, w_3 and w_3' are expressed as function of L_1 by using the results for z_{3R}' and z_3', as obtained from the application of equations (2.55), (2.56), (2.57), and by applying the following law for the free propagation:

$$w(z) = w_0\sqrt{1+\left(\frac{z}{z_R}\right)^2}, \tag{2.67}$$

which is written for the more general case. As the beam waist position along L_2 is on M_3, it is:

$$w_3 = w_{03}\sqrt{1+\left(\frac{z_3'}{z_{3R}'}\right)^2} \equiv w_{03}, \tag{2.68}$$

where:

$$w_{03} = \sqrt{\left(\frac{z_{3R}'\,\lambda}{\pi}\right)}, \tag{2.69}$$

$$\lambda = 1.064\times10^{-4}\ \text{cm}, \tag{2.70}$$

and:

$$w_3' = w_{03}\sqrt{1+\left(\frac{-L_2}{z_{3R}'}\right)^2}. \tag{2.71}$$

To check for which values of L_1 the condition given in equation (2.37) is satisfied, w_1 as well has to be expressed as a function of L_1. This can be done, by using equations (2.52), (2.53), (2.67),

hence:

$$w_1 = w_{01}\sqrt{1+\left(\frac{z_1}{z_{1R}}\right)^2}, \tag{2.72}$$

where:

$$w_{01} = \sqrt{\left(\frac{z_{1R}\ \lambda}{\pi}\right)}, \tag{2.73}$$

with the same value assumed above for λ. As it has been already clarified how to express w_3 as function of L_1, condition (2.35) can now be written in terms of L_1 as well.

2.3.6 Results for 100 cm $< L_1 <$ 115 cm

As it is shown in figure (2.5), there are no values of L_1 between 100 cm and 115 cm, for which all the conditions (2.33), (2.34), (2.35), (2.37) can be satisfied at the same time. So the range 50 cm $< L_1 <$ 65 cm has to be taken into account.

2.3.7 Results for 50 cm $< L_1 <$ 65 cm

In the case 50 cm $< L_1 <$ 65 cm, it is possible to find values of L_1 which satisfy all the properties required for the cavity in figure (2.3). This can be seen in figure (2.6).

2.3.8 Results for L_1= 50.7 cm

With reference to the results reported in picture (2.6), it is decided to set $L_1 = 50.7$ cm. Indeed, in this case, on one hand w_3 is quite close to 2 mm; on the other hand, conditions (2.33), (2.34), (2.37) are properly satisfied. Nevertheless, it is worth noticing that other values for L_1 might be possible. In what follows, the results for the specific case of $L_1 = 50.7$ cm are reported:

$$\Phi_G = 3.637 \text{ rad}; \tag{2.74}$$

$$w_3 = 1.74 \text{ mm}; \tag{2.75}$$

$$\frac{w_3}{w_1} = 17.5; \tag{2.76}$$

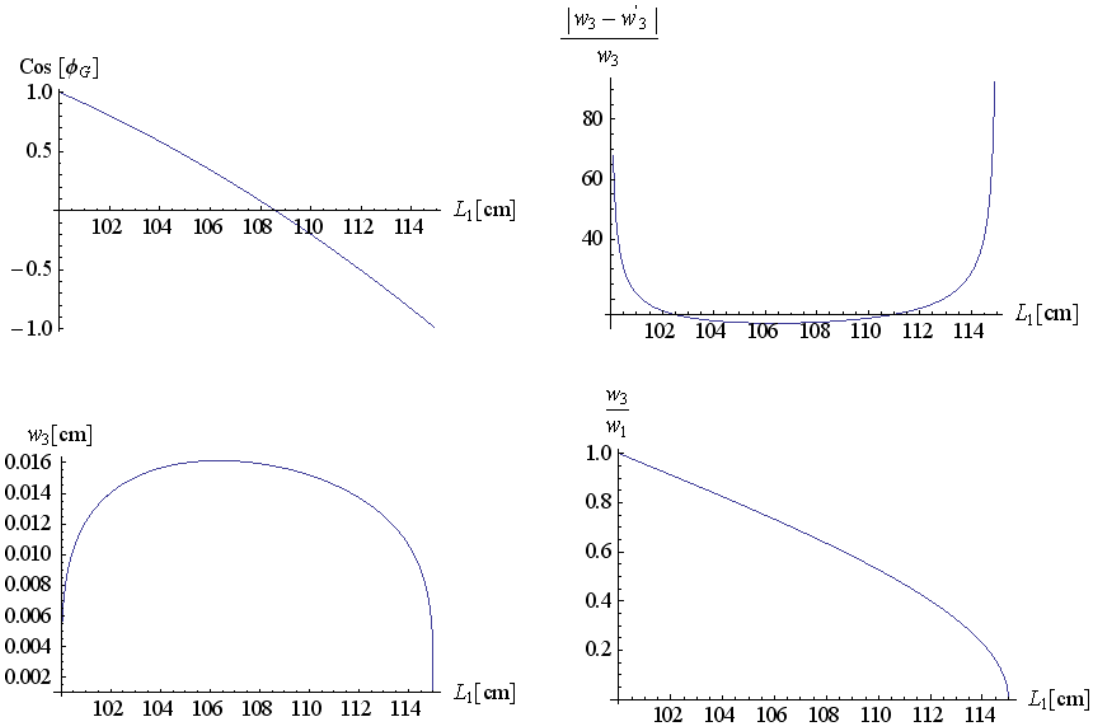

Figure 2.5: Results for the conditions required for the optical cavity for the case 100 cm $< L_1 <$ 115 cm. - **Left-hand side of the picture:** on the top, plot of cosine of the Gouy phase, as obtained by applying equation (2.65), vs. L_1; on the bottom, condition (2.35) vs. L_1. **Right-hand side of the picture:** on the top, plot of condition (2.34) vs. L_1; on the bottom, plot of condition (2.37) vs. L_1.

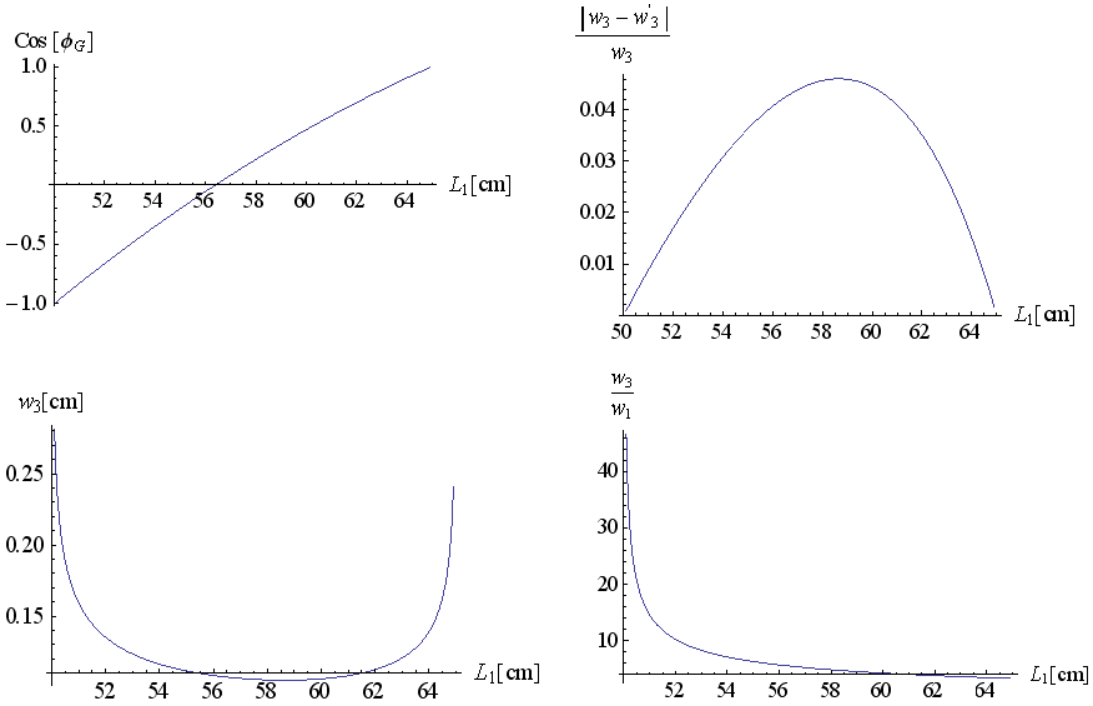

Figure 2.6: Results for the conditions required for the optical cavity for the case 50 cm $< L_1 <$ 65 cm. - **Left-hand side of the picture:** on the top, plot of cosine of the Gouy phase, as obtained by applying equation (2.65), vs. L_1; on the bottom, condition (2.35) vs. L_1. **Right-hand side of the picture:** on the top, plot of condition (2.34) vs. L_1; on the bottom, plot of condition (2.37) vs. L_1.

$$\frac{|w_3 - w_3'|}{w_3} = 0.006. \tag{2.77}$$

For this specific value of L_1, it is possible to plot the behavior of the Gouy phase along the optical cavity. If it is set (see equations (2.59), (2.60), (2.61), (2.63)):

$$\begin{cases} \phi(z) = \arctan\left(\frac{z}{z_{1R}}\right) & -z_1 < z < L_1 - z_1 \\ \\ \phi(z) = const + \arctan\left(\frac{z-(L_1-z_1)-L_2}{z'_{3R}}\right) & L_1 - z_1 < z < L_2 + L_1 - z_1 \end{cases} \tag{2.78}$$

where:

$$const = \arctan\left(\frac{L_1 - z_1}{z_{1R}}\right) + \arctan\left(\frac{L_2}{z'_{3R}}\right), \tag{2.79}$$

the behavior showed in figure (2.7) is obtained for relations (2.78).

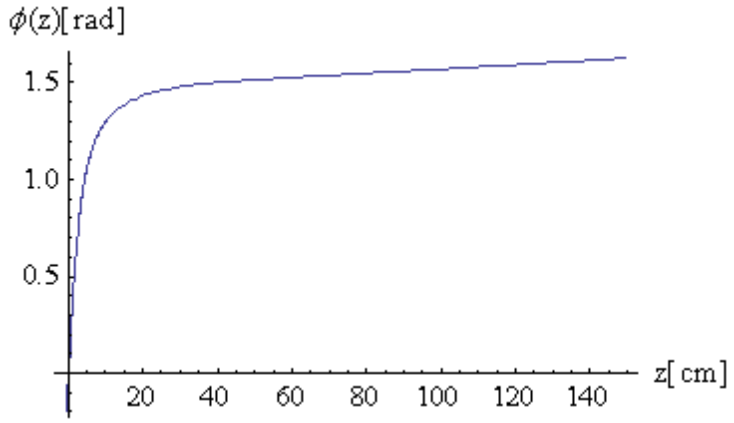

Figure 2.7: Gouy phase shift from one end to the other of the cavity - Behaviour of the Gouy phase as given by relation (2.78) vs. the z-coordinate.

2.3.9 Astigmatism

The astigmatism issue for the cavity in figure (2.3) is now taken into account. In this respect, it is observed that an angle, θ, is present between the incident beam on M_2 and the beam reflected by the same mirror. As a consequence, the $ABCD$ matrix for the curved mirror, M_2, changes. Particularly, it is:

$$M_t = \begin{pmatrix} 1 & 0 \\ -\frac{2}{R_2 \cos\theta} & 1 \end{pmatrix}, \tag{2.80}$$

and:

$$M_s = \begin{pmatrix} 1 & 0 \\ -\frac{2\cos\theta}{R_2} & 1 \end{pmatrix}, \tag{2.81}$$

where t and s refer to the tangential and sagittal planes, with respect to the incidence one, respectively, and θ is shown in figure (2.3).
The beam mode is different in the tangential and sagittal plane, indeed, for instance, equation (2.43) divides in two relations, one for the tangential and one for the sagittal plane (Ref. [60]):

$$\begin{aligned} M_{rtt} = &\begin{pmatrix} 1 & L_1 \\ 0 & 1 \end{pmatrix} \begin{pmatrix} 1 & 0 \\ -\frac{2}{R_2\cos\theta} & 1 \end{pmatrix} \begin{pmatrix} 1 & L_2 \\ 0 & 1 \end{pmatrix} \begin{pmatrix} 1 & 0 \\ 0 & 1 \end{pmatrix} \begin{pmatrix} 1 & L_2 \\ 0 & 1 \end{pmatrix} \times \\ &\times \begin{pmatrix} 1 & 0 \\ -\frac{2}{R_2\cos\theta} & 1 \end{pmatrix} \begin{pmatrix} 1 & L_1 \\ 0 & 1 \end{pmatrix} \begin{pmatrix} 1 & 0 \\ -\frac{2}{R_1} & 1 \end{pmatrix}, \end{aligned} \tag{2.82}$$

$$\begin{aligned} M_{rts} = &\begin{pmatrix} 1 & L_1 \\ 0 & 1 \end{pmatrix} \begin{pmatrix} 1 & 0 \\ -\frac{2\cos\theta}{R_2} & 1 \end{pmatrix} \begin{pmatrix} 1 & L_2 \\ 0 & 1 \end{pmatrix} \begin{pmatrix} 1 & 0 \\ 0 & 1 \end{pmatrix} \begin{pmatrix} 1 & L_2 \\ 0 & 1 \end{pmatrix} \times \\ &\times \begin{pmatrix} 1 & 0 \\ -\frac{2\cos\theta}{R_2} & 1 \end{pmatrix} \begin{pmatrix} 1 & L_1 \\ 0 & 1 \end{pmatrix} \begin{pmatrix} 1 & 0 \\ -\frac{2}{R_1} & 1 \end{pmatrix}. \end{aligned} \tag{2.83}$$

2.3.10 Estimate of the minimum angle on M_2

An estimate of the minimum angle θ, illustrated in picture (2.3), is now carried on. To this aim, the case of $L_1 = 50.7$ cm is considered and the diameter of the mirror M_1 is fixed to 1.27 cm. Figure (2.8) is now addressed, where the quantity R is introduced. As θ is small, the following relation holds:

$$R\cos\theta = w_3 \rightarrow R \sim w_3, \tag{2.84}$$

as a consequence, the smallest distance, d, between the center of the mirror M_1 and the center of the beam along L_2 can be defined in the following way:

$$d = 0.635\text{cm} + 2.63 w_3, \tag{2.85}$$

where 2.63 is the parameter corresponding to 1 ppm of clipping losses [55]. Particularly, in this case, 2.63 corresponds to the ratio between the distance from the end of the mirror M_1 to the center of the beam and the Gaussian beam radius. Eventually, by setting $w_3 \sim 0.17$cm, it

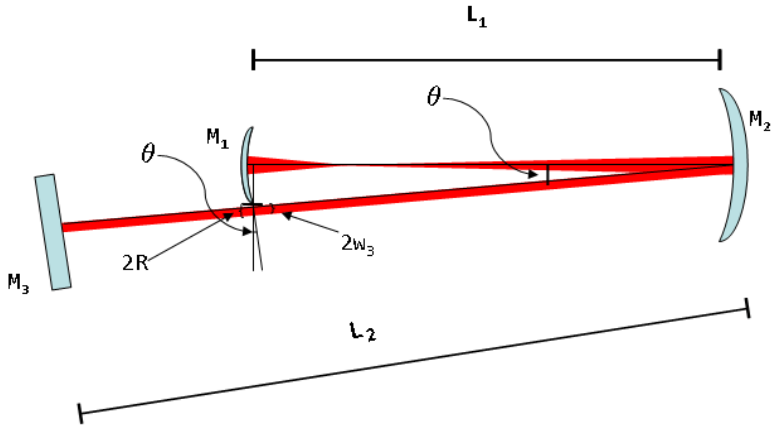

Figure 2.8: Estimate of the minimum angle on M_2. - Estimate of minimum angle θ between the incident beam on M_2 and the reflected beam, for $L_1 = 50.7$cm.

results:

$$L_1 \tan\theta = d \rightarrow \ \theta = \arctan\frac{d}{L_1} \approx 0.02 \text{ rad}. \tag{2.86}$$

2.3.11 Results for $L_1 = 50.7$ cm with astigmatism

In order to calculate conditions (2.33), (2.34), (2.37), (2.35), when considering astigmatism, the same procedure introduced in the previous sections is applied. However, in this case, two different results are obtained: one for the sagittal plane and one for the tangential one. It is stressed that the formulas to calculate the Gouy phase accumulated inside the cavity and the other conditions are the same. It is also observed that the experimental value of θ will be larger than the one reported in equation (2.86). Particularly, it will be set $\theta \simeq 0.05$ rad, therefore the calculation results presented below take into account this θ value and $L_1 = 50.7$cm. In addition, the reported value for the Gouy phase is the average between the tangential one and the sagittal one.

$$\Phi_G = 3.636 \text{ rad}; \tag{2.87}$$

$$w_{3t} = 1.70 \text{ mm}; \tag{2.88}$$

$$w_{3s} = 1.78 \text{ mm}; \tag{2.89}$$

$$\left[\frac{w_3}{w_1}\right]_t = 16.7; \tag{2.90}$$

$$\left[\frac{w_3}{w_1}\right]_s = 18.4; \tag{2.91}$$

$$\left[\frac{|w_3 - w_3'|}{w_3}\right]_t = 0.007, \tag{2.92}$$

$$\left[\frac{|w_3 - w_3'|}{w_3}\right]_s = 0.006. \tag{2.93}$$

2.3.12 Analysis of the ellipticity

As it has been already pointed out in section (2.3.2), ones q_1 is known, it is possible to find the q-parameter in any other position. Therefore, the ellipticity of the beam, due to the cavity astigmatism, can be evaluated, for different positions inside the resonator. To this aim, it is always assumed $\theta \simeq 0.05$ rad and $L_1 = 50.7$cm. In particular, on mirror M_1, it is :

$$\frac{w_{1t}}{w_{1s}} = 1.047; \tag{2.94}$$

the position of the beam waist from the mirror M_1, as described by the matrix for the tangential plane, is:

$$z_{w_{1t}} = 0.59 \text{ cm}; \tag{2.95}$$

the same quantity calculated with the matrix for the sagittal plane reads:

$$z_{w_{1s}} = 0.49 \text{ cm} \tag{2.96}$$

Just before the reflection on the mirror M_2, it results:

$$\frac{w_{2pt}}{w_{2ps}} = 0.956; \tag{2.97}$$

the position of the beam waist from the mirror M_2, when considering the matrix for the tangential plane, is:

$$z_{w_{2pt}} = 50.1 \text{ cm}; \tag{2.98}$$

and, when using the matrix for the sagittal plane, is:

$$z_{w_{2ps}} = 50.2 \text{ cm}. \tag{2.99}$$

Just after the reflection on the mirror M_2, it is again:

$$\frac{w_{2dt}}{w_{2ds}} = 0.956; \tag{2.100}$$

the distance of the second beam waist from the mirror M_2, as described by the matrix for the tangential plane and by the one of the sagittal plane is:

$$z_{w_{2dt}} = z_{w_{2ds}} = 100 \text{ cm}. \tag{2.101}$$

As far as the ellipticity on the mirror M_3 is concerned, it is obtained:

$$\frac{w_{3t}}{w_{3s}} = 0.956. \tag{2.102}$$

The second beam waist is on the mirror M_3 itself. In conclusion, the ellipticity of the beam inside the cavity can be considered of about 4.5%. Because of this, it might be possible to see higher order modes within the cavity.

2.3.13 Experimental Results for the determined optical cavity with telescope

In order to experimentally verify the results of the theoretical calculations carried on in the previous sections, the described optical cavity has been built in our laboratory (see picture (2.9)). For this purpose, we considered the intermediate values between the sagittal ones and the tangential ones. The theoretical cavity waist along the length L_1 is then assumed to be 97.3 μm. We worked with a fiber laser [62] whose wavelength is λ= 1064 nm and the waist, measured with the Beam Scan and the dedicated software, after the collimator, is of 650 μm, with an associated error equal to $\pm$5% of its measured value. So, to inject the laser beam inside the resonator, we realized an optical system before the first mirror of the cavity, M_1, in order to fit the laser beam waist to the cavity waist along L_1. It is worth noticing that the fine alignment of the cavity mirrors and the correct injection of the laser beam into the cavity have represented the main difficulties in the optical cavity realization.
After building the cavity, experimental tests have been carried on in order to verify that the

determined cavity was working as expected. In this respect, the cavity contrast for the fundamental mode, assumed to be resonating within the cavity, has been measured, as well as the intracavity beam dimensions and the Gouy phase.

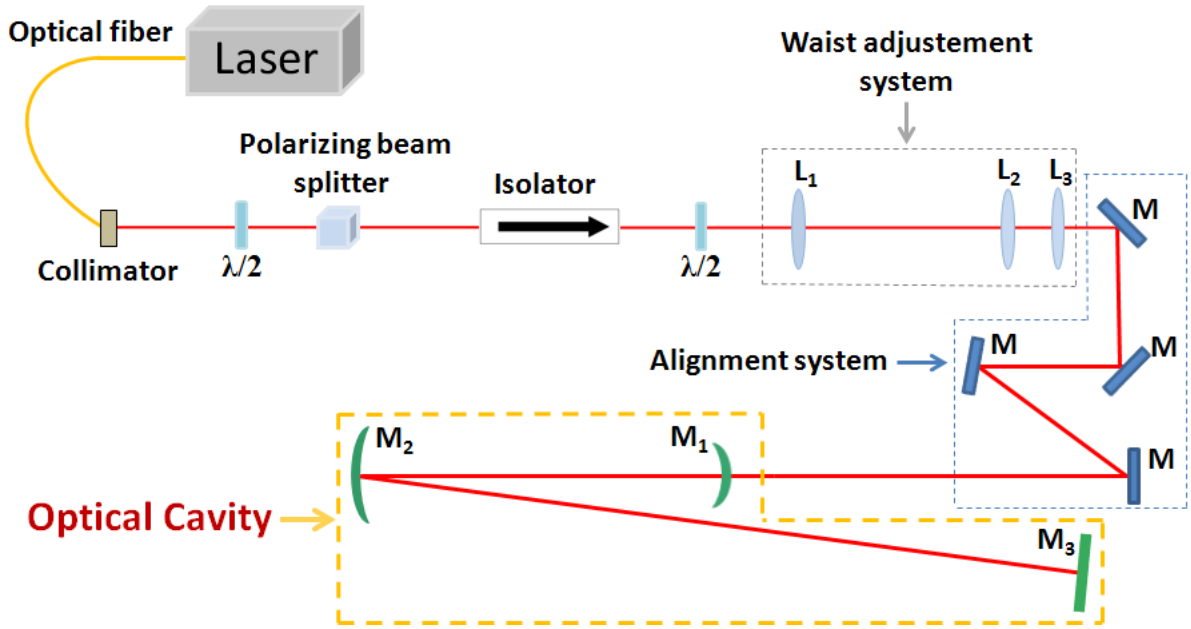

Figure 2.9: Scheme of the optical cavity - The complete scheme of the optical system before the resonator and of the optical cavity is showed. It is pointed out that the label $\lambda/2$ stands for half-wave plate; the index M indicates mirrors and L denotes lenses.

Measurement of the cavity contrast

The cavity contrast, C, has been evaluated by measuring the power reflected by the cavity from mirror M_1, (see picture 2.3), through the following formula:

$$C = \frac{V_{in} - V_{00}}{V_{in}}, \tag{2.103}$$

where V_{00} is the reflected power at the fundamental mode frequency and V_{in} is the one reflected at different frequencies, as it is shown in picture (2.10). The optimum observed result is:

$$C = \frac{V_{in} - V_{00}}{V_{in}} = 77\%. \tag{2.104}$$

When considering the power in the higher-order modes of the cavity due to residual misalignment issues, which, in principle, could be eliminated with a consequent increase of the power in the

fundamental mode of the cavity, the previous results rises to 85%. In order to interpret the last

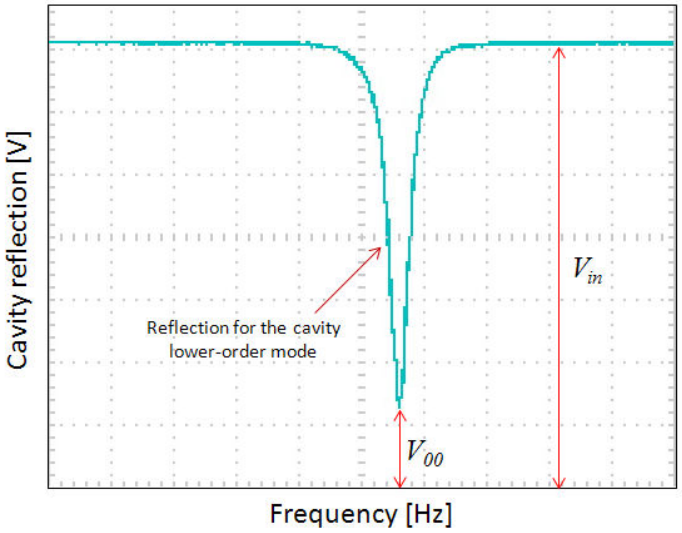

Figure 2.10: Optical cavity reflection - Reflection of the determined optical cavity, as measured from mirror M_1 (see picture 2.3). The power reflected by the cavity is measured through a photodiode connected to the oscilloscope, so that the quantity measured is actually the voltage associated to the power reflected by the cavity at the resonance frequency and at any other frequency.

result, a theoretical calculation of the cavity contrast is now carried on, by taking into account picture (2.3) and by evaluating the cavity reflectivity from M_1. In the following analysis the mirror losses are neglected, the reflection coefficients for mirrors M_1 and mirror M_2 are r_1, r_2, respectively, while for M_3 it is assumed $r_3 \equiv 1$. The field circulating within the cavity is indicated as E_{cir}, while the incident optical signal is E_{inc}. By considering section (2.1), it is possible to verify that E_{cir} is obtained by the sum:

$$E_{cir} = it_1 E_{inc} + r_1 r_2^2 e^{i2k(L_1+L_2)} E_{cir}, \tag{2.105}$$

hence:

$$E_{cir} = \frac{it_1 E_{inc}}{1 - r_1 r_2^2 e^{i2k(L_1+L_2)}}. \tag{2.106}$$

The last result is used to determine the reflected power from mirror M_1, E_r. Indeed, this quantity reads:

$$E_r = r_1 E_{inc} + it_1 r_2^2 e^{i2k(L_1+L_2)} E_{cir}, \tag{2.107}$$

therefore:

$$E_r = r_1 E_{inc} - \frac{t_1^2 r_2^2 e^{i2k(L_1+L_2)} E_{inc}}{1 - r_1 r_2^2 e^{i2k(L_1+L_2)}}. \tag{2.108}$$

The cavity reflectivity, R, is then:

$$R = \left|\frac{E_r}{E_{inc}}\right|^2 = \frac{(r_1 - r_2^2)^2}{(1 - r_1 r_2^2)^2} \times \left[\frac{1 + \frac{4r_1 r_2^2 \sin^2(k(L_1+L_2))}{(r_1 - r_2^2)^2}}{1 + \frac{4r_1 r_2^2 \sin^2(k(L_1+L_2))}{(1 - r_1 r_2^2)^2}}\right], \tag{2.109}$$

hence:

$$R = \left|\frac{E_r}{E_{inc}}\right|^2 = R_0 \times \left[\frac{1 + \frac{4\mathcal{F}^2}{\pi^2 R_0} \sin^2\left(k(L_1 + L_2)\right)}{1 + \frac{4\mathcal{F}^2}{\pi^2} \sin^2\left(k(L_1 + L_2)\right)}\right], \tag{2.110}$$

with:

$$R_0 = \frac{(r_1 - r_2^2)^2}{(1 - r_1 r_2^2)^2}, \tag{2.111}$$

while the cavity finesse, $\mathcal{F}$ is:

$$\mathcal{F} = \frac{\pi r_2 \sqrt{r_1}}{(1 - r_1 r_2^2)}. \tag{2.112}$$

At the cavity resonance, equation (2.110) reads:

$$R = \left|\frac{E_r}{E_{inc}}\right|^2 = R_0 = \frac{(r_1 - r_2^2)^2}{(1 - r_1 r_2^2)^2}. \tag{2.113}$$

The mirror specifications, given by the constructor [63], which concern the reflection coefficients are:

$$r_1 = r_2 = 99\% \pm 0.5\%. \tag{2.114}$$

However, r_1 and r_2 have been also measured in our laboratory and it results:

$$r_1 \simeq 0.9938, \qquad r_2 \simeq 0.9942. \tag{2.115}$$

By using the last values for the reflection coefficients, the cavity finesse, expressed in equation (2.112), results of about 176 and the cavity reflectivity at the resonance frequency, given in relation (2.111), is $R_0 = 9.197\%$. The contrast between the reflected power at the frequency of the cavity fundamental mode, which is assumed as the resonating mode, and the reflected power at different frequencies, can then be theoretically calculated as: $C = 1 - R_0$, thus: $C = 90.8\%$. The difference between the experimental and the theoretical cavity contrast is of about 6%, with the theoretical value higher than the experimental one. Nevertheless, the obtained result is quite common, when a laser beam coming out from an optical fiber and passing through a collimator is injected into an optical cavity. Indeed, because of the beam propagation within the fiber and the aberrations introduced by the passage through the small focal length of the

collimator, the injected beam presents departures from a perfect Gaussian beam. This can lead to a lower coupling between the cavity fundamental mode and the injected beam.

Measurements of the intracavity beam dimensions

In order to compare the actual intracavity beam dimensions with the theoretical values, we have measured the beam diameters, by using the transmission part of the cavity. With reference to figure (2.11), we took the measurements of the widths for Beam 1 and Beam 2, in a position 10 cm away from M_2, and we confronted them with their theoretical values, in the same position.

As far as the beam width experimental measures are concerned, they are performed by using

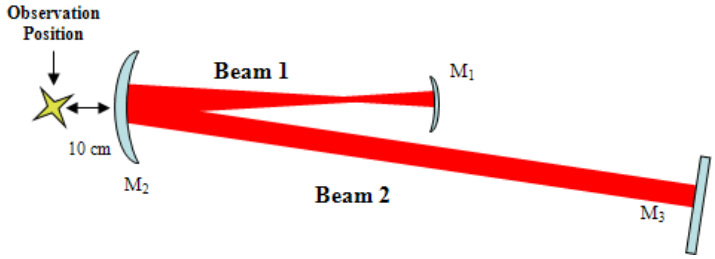

Figure 2.11: Intracavity beam representation - Schematic representation of the intracavity beams, Beam 1 and Beam 2, and of the measurement position.

the camera WinCamD^{TM} Series Cameras [64]. An example of the beam diameter measurement outcome is reported in figure (2.12), together with a picture of the two beams after passing through a 2.5 cm focal length lens. The theoretical beam widths are calculated through the $ABCD$ matrices for the beam propagation up to the measurement position. In particular, by knowing the beam waist position and its dimension both along L_1 and L_2, the total propagation matrix up to the observation point has an analogous form for the two beams, i.e.:

$$M_{b_{1,2}} = \begin{pmatrix} A_{b_{1,2}} & B_{b_{1,2}} \\ C_{b_{1,2}} & D_{b_{1,2}} \end{pmatrix} = \begin{pmatrix} 1 & d \\ 0 & 1 \end{pmatrix} \begin{pmatrix} 1 & 0 \\ 0 & 1 \end{pmatrix} \begin{pmatrix} 1 & \frac{w_{M_2}}{n_2} \\ 0 & 1 \end{pmatrix} \begin{pmatrix} 1 & 0 \\ \frac{n_2-n_1}{R_2} & 1 \end{pmatrix} \begin{pmatrix} 1 & L_{b_{1,2}} \\ 0 & 1 \end{pmatrix} \quad , \quad (2.116)$$

where $n_1 \sim 1$, $n_2 \sim 1.5$ are the refractive index of the air and of the mirror M_2 material (BK7), respectively, $w_{M_2} = 0.98 \pm 0.01$cm [65] is the width of M_2, $d = 10\text{cm} \pm 0.5\text{cm}$ is the distance between M_2 and the observation position, while $L_{b_{1,2}}$ can be either the distance between the waist position along L_1 and the mirror M_2, or the distance between the waist position along L_2 and the mirror M_2, depending on which one between Beam 1 and Beam 2 is considered, respectively. It is worth noticing that the matrix containing the element $(\frac{n_2-n_1}{R_2})$ represents the

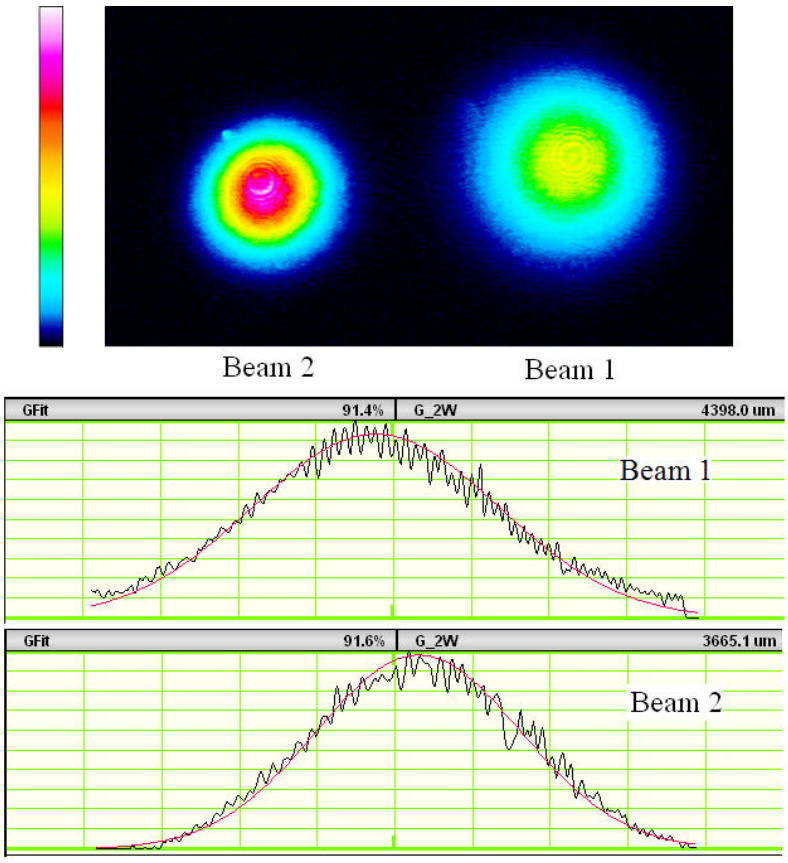

Figure 2.12: Intracavity beam picture and diameter measurements. - **Upper panel:** Beam 1 and Beam 2 picture after a 2.5 cm focal length lens. It is worth noting that the colors refer to the Gaussian beam intensity distribution. **Lower panel:** Beam 1 and Beam 2 size measurements.

Beam 1	Beam 2
Theoretical diameter= 4400 μm	Theoretical diameter= 3685 μm
Measured diameter = 4398 $\pm$ 220 μm	Measured diameter = 3665 $\pm$ 183 μm

Table 2.1: Comparison between theoretical and experimental results for the intracavity beam diameters. The definition of the quantities Beam 1 and Beam 2 is illustrated in picture (2.11).

$ABCD$ matrix at the interface between the free space and the curved surface of M_2 [62]; the matrix which involves the element w_{M_2}/n_2 gives the beam propagation within M_2 [62]; while the identity matrix is the $ABCD$ matrix for the interface between the flat rear-side surface of M_2 and the free propagation in the air. In table (2.1), both the theoretical values and the experimental values are reported for both the beams, where an error of $\pm 5\%$ for the beam measurements as been settled. However, this is an underestimate of the effective errors, indeed the error on the camera position has been neglected. Furthermore, the measure of one single beam diameter is complicated by the simultaneous presence of the two beams, in the observation point. Because of this, there might be possible systematic errors in the Gaussian beam fit performed by the dedicated software of the camera, which gives the beam diameter dimensions. An accurate study of the error is then quite tricky, nevertheless, the theoretical and the experimental values for the diameters of both the beams show a good agreement.

Gouy phase experimental measurement

The last experimental test on the determined optical cavity concerns the measurement of the Gouy phase shift, Φ_G, of the laser beam on a complete round trip within the optical resonator. As it possible to check from relation (2.31), the lower-order mode and the first higher-order mode of the cavity are connected by the following relation:

$$\Phi_G = \frac{4\pi\Delta\nu L}{c} \tag{2.117}$$

where $\Delta\nu$ is the frequency spacing between the fundamental mode and the first higher-order mode, c is the light speed, and L is the length of the cavity from one end to the other, $L = 150.7$cm. Relation (2.117) makes clear that a measurement of $\Delta\nu$ allows to get to the experimental value of Φ_G. Nevertheless, an accurate measurement of $\Delta\nu$ turned out to be not trivial. Indeed, we used a piezo-modulation of the laser frequency to follow the cavity resonance frequency, which changes because of the cavity length fluctuations, but the laser response to the

modulation is not linear, as it should be. Moreover, we observe that the laser frequency presents a drift due to noises (temperature changes, mechanical vibrations, air flow) whose frequencies are usually low, then, if we modulate the laser at high frequencies, we should be able to eliminate the noise effect from our measurements. So, for increasing values of the modulation frequency, we took several measurements of the voltages corresponding to the fundamental mode and to the first higher-order mode, in order to verify that the laser stability increases at higher modulation frequency. In picture (2.13), an example of the oscilloscope output is reported. Regarding picture (2.13), it is also observed that the modulation signal is amplified through a 100 V amplifier, which allows to properly adjust the laser frequency to the resonance frequency of the analyzed optical cavity, and the voltages are measured by considering the amplified signal.
The measurements of the voltages corresponding to the cavity fundamental mode are used to

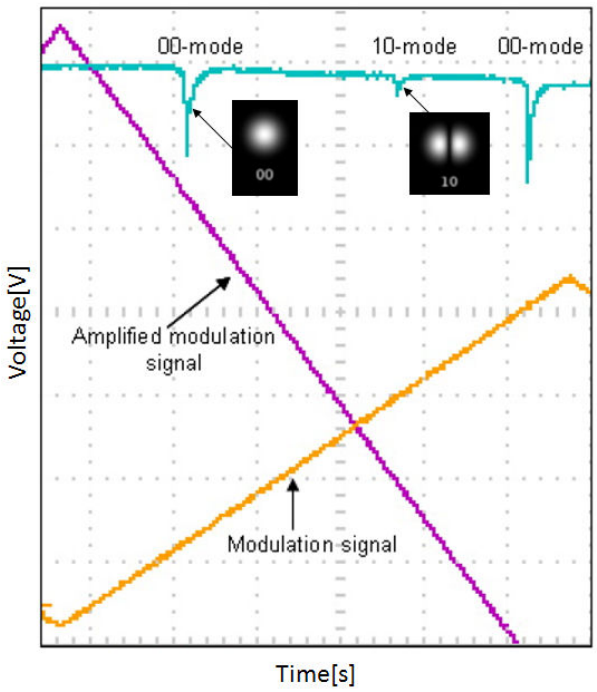

Figure 2.13: Cavity fundamental mode and first-higher order mode as seen on the oscilloscope screen - The cavity fundamental mode (00-mode), the first-higher order mode (10-mode), the modulation signal (yellow line) and the amplified modulation signal (purple line) are showed. Modulation frequency of 300 Hz.

carry on a data analysis, involving a χ^2 test, at the aim of reconstructing the curve of the laser frequency response to the modulation signal, for correctly calculating the introduced $\Delta\nu$ quantity. In effect, an accurate measure of the Gouy phase is required to be sure of the cavity

stability. In this respect, it is observed that, when a modulation signal is applied to the laser, the resonance frequency of order q, for the fundamental mode of the cavity, at a given time t, can be written as:

$$\nu_{00,Laser}(t) + f(V(t)) = \frac{qc}{2L(t)} + \frac{c\Phi_G}{4\pi L(t)}, \tag{2.118}$$

where $\nu_{00,Laser}(t)$ is the proper laser frequency for the fundamental mode, which varies with time; the function $f(V(t))$ describes the modulation signal, $V(t)$, contribution to the laser frequency, as function of time; $L(t)$ is the one trip length of the cavity, which slightly depends on time. Let us evaluate relation (2.118) at the time $t = t_0$, corresponding to the resonance frequency q, and at the time $t_0 + \Delta t$, corresponding to the resonance frequency of order $q+1$, and let us perform the difference between the two obtained expressions. It is possible to verify that, if the laser is modulated at high frequency, the mentioned difference reduces to:

$$f(V(t_0 + \Delta t)) - f(V(t_0)) = \frac{c}{2L(t_0)}, \tag{2.119}$$

where $V(t_0+\Delta t)$ and $V(t_0)$ are the voltages associated to the resonance frequencies of the orders $q+1$ and q, respectively, for the fundamental mode of the cavity. Furthermore, as the cavity length variations are small (about 1μm), it is possible to set: $L(t_0) = L_0 = L = 150.7$cm.
To determine the form of the function $f(V(t))$, an hypotheses is made about it and a χ^2 test is then performed to evaluate the accuracy of the assumption. A polynomial form is considered, i.e.:

$$f(V(t)) = A + BV(t) + CV(t)^2 + DV(t)^3 + ..., \tag{2.120}$$

where $V(t)$ is the applied voltage to the laser piezoelectric actuator. By taking into account equation (2.119), the following random variable is introduced:

$$\begin{aligned} &y_{i+1,i} = f(V_{i+1}) - f(V_i) - \tfrac{c}{2L(t_0)} = \\ &= B(V_{i+1} - V_i) + C(V_{i+1}^2 - V_i^2) + D(V_{i+1}^3 - V_i^3) + ... - \tfrac{c}{2L(t_0)}, \end{aligned} \tag{2.121}$$

whose average value must be equal to zero, and the index i and $i+1$ are used to indicate the voltages associated with two adjacent resonances. In particular, as far as our data are concerned, for each measurement, the voltage associated with three or four resonances were taken, at the same time, hence the index i can assume the values $i = 1, 2$ or $i = 1, 2, 3$, depending on the set of measurement. Picture (2.14) is reported to clarify what has been just said. The variables $y_{i+1,i}$

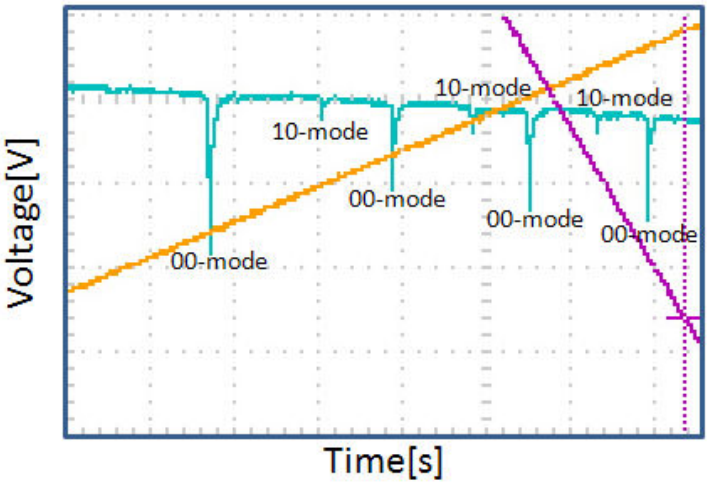

Figure 2.14: Example of one measurement set for a fixed frequency. - Measurements of the voltages for the cavity fundamental mode (00-mode) and for the first-higher order mode (10-mode), for the modulation frequency of 100 Hz. Several sets of measures, analogous to the one showed in the current picture, are taken for this frequency and at higher modulation signal frequencies.

of the same set of measurements present correlations, however they are not correlated with the $y_{i+1,i}$ belonging to different set of measurements, for the same modulation frequency. In order to verify the assumption on $f(V(t))$, a χ^2 test is performed for each considered frequency of the modulation signal. Because of the data correlation, the χ^2 has been evaluated through the following relation:

$$\chi^2 = \mathbf{y}^T \Sigma^{-1} \mathbf{y}, \tag{2.122}$$

where $\mathbf{y}$ is the column vector compounded of all the $y_{i+1,i}$ quantities, for a given frequency of the modulation signal, while $\mathbf{y}^T$ is its transpose, and Σ is the variance-covariance matrix associated to the vector $\mathbf{y}$. If, for a given frequency, $\bar{\nu}$, N set of measures are taken and for each of them two variable $y_{i+1,i}$ can be written, i.e. $y_{2,1}$ and $y_{3,2}$, the Σ matrix reads:

$$\Sigma = \begin{pmatrix} \sigma_{11} & 0 & \cdots & 0 \\ 0 & \sigma_{22} & \cdots & 0 \\ \vdots & \vdots & \ddots & \vdots \\ 0 & 0 & \cdots & \sigma_{NN} \end{pmatrix}, \tag{2.123}$$

with:

$$\sigma_{kk} = \begin{pmatrix} \mathrm{var}_k & \mathrm{cov}_k \\ \mathrm{cov}_k & \mathrm{var}_k \end{pmatrix}, \quad k = 1, ..., N \tag{2.124}$$

hence, Σ is a $2N \times 2N$ matrix, whose elements are the variance and covariance of the $y_{2,1}$ and $y_{3,2}$ quantities, for each data set, that is var_k and cov_k. As fas as the vector $\mathbf{y}$ is concerned, this is then a $2N$ column vector. In order to find the parameters of the fit, a system of equations is defined, which is obtained by deriving the χ^2 expression with respect to the fit parameters, and by equating these derivatives to zero. In this respect, it is worth noticing that the Σ matrix is evaluated by neglecting the terms higher than the linear one in the voltage, i.e. by keeping only the term $B(V_{i+1} - V_i)$, where as a first estimate of the B value is assumed the one reported on the laser specification book [62], i.e. 0.08 pm/V. This choice is mainly based on the necessity of writing a system of equations whose solution can be calculated and on the consideration that the terms $C(V_{i+1}^2 - V_i^2) + D(V_{i+1}^3 - V_i^3) + ...$ are corrections to the linear behavior, hence they are smaller than the term involving the parameter B. It has been checked, during the analysis, that this condition is verified. It is worth noticing that, because of this approximation, the terms var_k and cov_k, entering the Σ matrix, are the same for each data set, k, of a given frequency, that is:

$$\text{var}_k = \text{var} = \frac{c^2}{4L^4}\sigma_L^2 + 2B^2\sigma_V^2, \qquad k = 1, ..., N \tag{2.125}$$

$$\text{cov}_k = \text{cov} = \frac{c^2}{4L^4}\sigma_L^2 - B^2\sigma_V^2, \qquad k = 1, ..., N \tag{2.126}$$

with N indicating the number of data sets for the considered frequency. In the previous equations, σ_L represents the error on the cavity length, which is assumed equal to $\sqrt{2}\times 0.25$ cm, being the error on L_1 and on L_2 equal to 0.25cm, while σ_V is the error on the voltage measurements, which is always the same, for a fixed frequency. The parameter B has been already introduced above. Once the systems of equations compounded of the χ^2 derivatives with respect to the fit parameters is solved, so that the fit parameters are completely determined, the new value of B is used to evaluate again the Σ matrix and to obtain new values of the fit parameters. The procedure is repeated until the variance (calculated through equation (2.125)) does not vary anymore. Hence, the final result of the χ^2, for a given frequency, is evaluated by using the fit parameter values obtained from the last iterative step.

For starting the analysis, a parabolic form is assumed, i.e.:

$$\begin{aligned} y_{i+1,i} &= f(V_{i+1}) - f(V_i) - \tfrac{c}{2L(t_0)} = \\ &= B(V_{i+1} - V_i) + C(V_{i+1}^2 - V_i^2) - \tfrac{c}{2L(t_0)}. \end{aligned} \tag{2.127}$$

Frequency[Hz]	$\bar{\chi}^2$
100	4.5 ± 0.4
200	2.1 ± 0.5
300	1.4 ± 0.5
400	1.4 ± 0.5
500	1.02± 0.5
600	1.2± 0.5
700	1.1(5)± 0.5
800	0.99± 0.5
900	1.5± 0.5
1000	2.9± 0.5

Table 2.2: $\bar{\chi}^2$ test for a second order polynomial. The normalized χ^2, $\bar{\chi}^2$, is reported for each considered frequency.

The χ^2 has been evaluated for several modulation frequencies, the results are reported in table (2.2), where the χ^2 has been normalized to the degrees of freedom, i.e. the number of measurements for each frequencies, n, minus the number of the fit parameters, k, (two, in the current case). As it possible to see, with the exception of the frequencies 100Hz, 200Hz and 1000Hz, the normalized χ^2, indicated as $\bar{\chi}^2$, is acceptable, within its associated error, which is estimated through relation:

$$\sigma_{\bar{\chi}^2} = \sqrt{\frac{2}{n-k}}. \tag{2.128}$$

However, the same calculations are carried on for a cubic polynomial as well to see if it could be a suitable description of the laser frequency response to the modulation. So, it is set:

$$\begin{aligned} y_{i+1,i} &= f(V_{i+1}) - f(V_i) - \tfrac{c}{2L(t_0)} = \\ &= B(V_{i+1} - V_i) + C(V_{i+1}^2 - V_i^2) + D(V_{i+1}^3 - V_i^3) - \tfrac{c}{2L(t_0)}, \end{aligned} \tag{2.129}$$

the results for $\bar{\chi}^2$ are reported in table (2.3). With the exception of the frequencies 100Hz and 1000Hz, the model described by function (2.129) turns out to be valid as well. It is noticed that both table (2.2) and table (2.3) show lower $\bar{\chi}^2$ values at high modulation frequencies, up to 800Hz, as a result of the enhancement of the laser stability. The increase of the $\bar{\chi}^2$ at high modulation frequencies (900Hz, 1000Hz) is instead due to a decrease of the accuracy in the reading of the voltage values, as it can be seen from picture (2.15), where the fundamental mode and the first higher order mode of the cavity are showed, for the modulation frequency of 1kHz.

The estimate of the gouy phase experimental value and of its associated error is carried on by

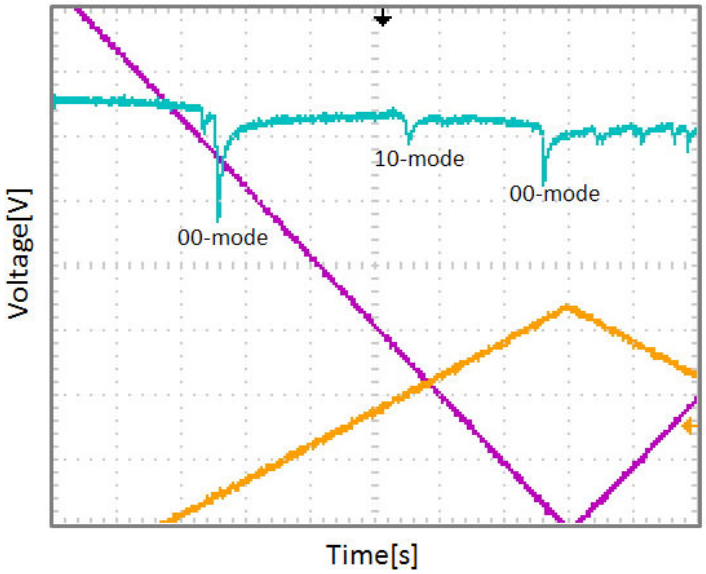

Figure 2.15: Example of oscilloscope output for the modulation frequency of 1kHz. - Cavity fundamental mode (00-mode) and first-higher order mode (10-mode), for the modulation frequency of 1kHz. It is possible to see that the accuracy in reading the voltages associated with the 00-mode and with the 10-mode is quite low, for the considered modulation frequency.

Frequency[Hz]	$\bar{\chi}^2$
100	6.4 ± 0.4
200	0.57 ± 0.5
300	0.98 ± 0.5
400	0.1 ± 0.5
500	0.16 ± 0.5
600	0.3 ± 0.5
700	0.3(4)± 0.5
800	1.0(1)± 0.5
900	1.17± 0.5
1000	2.6± 0.5

Table 2.3: $\bar{\chi}^2$ test for a third order polynomial. The normalized χ^2, $\bar{\chi}^2$, is reported for each considered frequency.

considering the result of the cubic fit, as it seems to describe slightly better the behavior of our data sets. So, the laser frequency response to the modulation signal is written as:

$$f(V(t)) = BV(t) + CV^2(t) + DV^3(t), \tag{2.130}$$

where B, C, D are determined by the fit, as described above, and their values differ at each considered modulation frequency. Moreover, it is pointed out that, because of the χ^2 values, the data corresponding to the frequencies 100Hz and 1000Hz, are not taken into account in the following analysis. As a consequence, the index i, introduced in equation (2.121), can only assume the value 1 or 2, as the measure sets with four resonances visible, at the same time, are present for the frequency 100 Hz only. For each data set, k, of each frequencies, two values for the gouy phase are then obtained:

$$\Phi_{G,ik} = \frac{4\pi L(f(V_{10,ik}) - f(V_{ik}))}{c}, \qquad i = 1, 2 \tag{2.131}$$

with $k = 1, ..., N$, where N indicates the number of measurement sets for each frequency. Particularly, for the case of 200 Hz, N=6, while for all the other frequencies $N = 5$. Furthermore, in equation (2.131), the quantity $V_{10,ik}$ is the measured voltage for the first higher order mode of the cavity corresponding to the k-th set of measurements, with either $i = 1$, if it is the first 10-mode observed on the oscilloscope screen, or $i = 2$ if it is the second one visible on the oscilloscope. As far as the quantity V_{ik} is concerned, this is the measured voltage for the fundamental mode of the cavity, used for the determination of the fit parameters as well, where k and i have the same meaning introduced above, except for the fact that i is now referred to the 00-mode. It is worth remarking that L is the length between one end to the other of the cavity, i.e. $L = 150.7$cm, and the function f is reported in equation (2.130). To determine an average value of the gouy phase for each considered frequency, $\bar{\nu}$, the following formulas are applied:

$$\Phi_{G,\bar{\nu}} = \frac{\sum_{k=1}^{N}\sum_{i=1}^{2} p_{ik}\Phi_{G,ik}}{\sum_{k=1}^{N}\sum_{i=1}^{2} p_{ik}}, \quad p_{ik} = \frac{1}{\sigma^2_{\Phi_{G,ik}}}, \tag{2.132}$$

$$\sigma_{\Phi_{G,\bar{\nu}}} = \sqrt{\frac{1}{\sum_{k=1}^{N}\sum_{i=1}^{2} p_{ik}}}, \tag{2.133}$$

it is then clear that the error, $\sigma_{\Phi_{G,ik}}$, associated with each obtained gouy phase value, $\Phi_{G,ik}$, for the considered frequency, is necessary to calculate the previous equations. Because of relation

(2.131) and of the already discussed data correlation, the variance of the Gouy phase, $\Phi_{G,ik}$, must be calculated from the following expression:

$$\begin{aligned}
&\sigma^2_{\Phi_{G,ik}} = \mathrm{var}(\Phi_{G,ik}) = \left(\frac{\partial\Phi_{G,ik}}{\partial D}\right)^2 \mathrm{var}(D) + \left(\frac{\partial\Phi_{G,ik}}{\partial C}\right)^2 \mathrm{var}(C) + \left(\frac{\partial\Phi_{G,ik}}{\partial B}\right)^2 \mathrm{var}(B) + \\
&\left(\frac{\partial\Phi_{G,ik}}{\partial L}\right)^2 \sigma^2_L + \left(\frac{\partial\Phi_{G,ik}}{\partial V_{10,ik}}\right)^2 \sigma^2_{V_{10,ik}} + \left(\frac{\partial\Phi_{G,ik}}{\partial V_{ik}}\right)^2 \sigma^2_{V_{ik}} + 2\left(\frac{\partial\Phi_{G,ik}}{\partial D}\right)\left(\frac{\partial\Phi_{G,ik}}{\partial B}\right)\mathrm{cov}(D,B) + \\
&2\left(\frac{\partial\Phi_{G,ik}}{\partial D}\right)\left(\frac{\partial\Phi_{G,ik}}{\partial C}\right)\mathrm{cov}(D,C) + 2\left(\frac{\partial\Phi_{G,ik}}{\partial C}\right)\left(\frac{\partial\Phi_{G,ik}}{\partial B}\right)\mathrm{cov}(C,B) + \\
&2\left(\frac{\partial\Phi_{G,ik}}{\partial D}\right)\left(\frac{\partial\Phi_{G,ik}}{\partial V_{ik}}\right)\mathrm{cov}(D,V_{ik}) + 2\left(\frac{\partial\Phi_{G,ik}}{\partial C}\right)\left(\frac{\partial\Phi_{G,ik}}{\partial V_{ik}}\right)\mathrm{cov}(C,V_{ik}) + \\
&2\left(\frac{\partial\Phi_{G,ik}}{\partial B}\right)\left(\frac{\partial\Phi_{G,ik}}{\partial V_{ik}}\right)\mathrm{cov}(B,V_{ik}) + 2\left(\frac{\partial\Phi_{G,ik}}{\partial D}\right)\left(\frac{\partial\Phi_{G,ik}}{\partial L}\right)\mathrm{cov}(D,L) + \\
&2\left(\frac{\partial\Phi_{G,ik}}{\partial C}\right)\left(\frac{\partial\Phi_{G,ik}}{\partial L}\right)\mathrm{cov}(C,L) + 2\left(\frac{\partial\Phi_{G,ik}}{\partial B}\right)\left(\frac{\partial\Phi_{G,ik}}{\partial L}\right)\mathrm{cov}(B,L),
\end{aligned} \tag{2.134}$$

with $i = 1, 2$. In the previous relation, it is $\sigma^2_{V_{10,ik}} = \sigma^2_{V_{ik}} = \sigma^2_V$ and it changes from one frequency to another; the error on the length of the cavity is always equal to $\sqrt{2}\times$ 0.5cm, so that $\sigma^2_L \sim (\sqrt{2}\times 0.5)^2$ cm^2, while the variance, *var*, and covariance, *cov*, terms are obtained from the variance-covariance matrix of the coefficient vector $\vec{\alpha} = (D, C, B)$ and from its covariance with V_{ik} and L. In the following it is showed how these quantities have been obtained. Firstly, the variance-covariance matrix of the vector $\vec{\alpha}$ is calculated. By taking into account relation (2.129), for each frequency, the analytical expression of the χ^2, calculated through relation (2.122), reads:

$$\begin{aligned}
&\chi^2 = \textstyle\sum_{k=1}^{N} \frac{\mathrm{var}}{\mathrm{var}^2-\mathrm{cov}^2}\left[\left(D\delta''_{1,k} + C\delta'_{1,k} + B\delta_{1,k} - \frac{c}{2L}\right)^2 + \left(D\delta''_{2,k} + C\delta'_{2,k} + B\delta_{2,k} - \frac{c}{2L}\right)^2\right] - \\
&\textstyle\sum_{k=1}^{N} \frac{2\mathrm{cov}}{\mathrm{var}^2-\mathrm{cov}^2}\left[\left(D\delta''_{1,k} + C\delta'_{1,k} + B\delta_{1,k} - \frac{c}{2L}\right)\left(D\delta''_{2,k} + C(\delta'_{2,k} + B\delta_{2,k}) - \frac{c}{2L}\right)\right] = \\
&\textstyle\sum_{k=1}^{N} \frac{\mathrm{var}}{\mathrm{var}^2-\mathrm{cov}^2}\left[\left(y^2_{2,1,k} + y^2_{3,2,k}\right) - \frac{2\mathrm{cov}}{\mathrm{var}^2-\mathrm{cov}^2}\left(y_{2,1,k}y_{3,2,k}\right)\right].
\end{aligned} \tag{2.135}$$

In the last equation, *var* and *cov* are the variances and covariances, respectively, associated to the quantities $y_{i+1,i}$, they are given in relations (2.125) and (2.126). As far as the other terms in equation (2.135) are concerned, these are:

$$\delta''_{1,k} = (V^3_{2k} - V^3_{1k}), \quad \delta'_{1,k} = (V^2_{2k} - V^2_{1k}), \quad \delta_{1,k} = (V_{2k} - V_{1k}), \tag{2.136}$$

$$\delta''_{2,k} = (V^3_{3k} - V^3_{2k}), \quad \delta'_{2,k} = (V^2_{3k} - V^2_{2k}), \quad \delta_{2,k} = (V_{3k} - V_{2k}), \tag{2.137}$$

where V_{1k}, V_{2k}, V_{3k} are the voltages corresponding to the fundamental mode of the cavity, obtained from a single set of measurements, k, of a given frequency, $\bar{\nu}$. For the sake of clearness

it is pointed out that V_{1k} and V_{2k} enter the calculation of the Gouy phase through equation (2.131), while all the three values V_{1k}, V_{2k}, V_{3k} are involved in the determination of the fit parameters D, C, B, for a given modulation frequency. By deriving the χ^2 expression of equation (2.135), with respect to the parameters D, C, B, and equating each derivative to zero, a system of three equations is obtained, whose solution gives the values of the mentioned parameters, as it is already described above. However, in this case we are interested in finding the variance-covariance matrix for the parameter vector, $\vec{\alpha} = (D, C, B)$. With this aim, the system of the three equations is rewritten in a matrix form as follows:

$$S\vec{\alpha} = \frac{c(\text{var} - \text{cov})}{2L}\vec{\Delta}, \tag{2.138}$$

where:

$$S = \begin{pmatrix} s_{11} & s_{12} & s_{13} \\ s_{21} & s_{22} & s_{23} \\ s_{31} & s_{32} & s_{33} \end{pmatrix}, \tag{2.139}$$

$$s_{11} = \text{var}\sum_{k=1}^{N}(\delta''^2_{1,k} + \delta''^2_{2,k}) - 2\text{cov}\sum_{k=1}^{N}\delta''_{1,k}\delta''_{2,k}, \tag{2.140}$$

$$s_{22} = \text{var}\sum_{k=1}^{N}(\delta'^2_{1,k} + \delta'^2_{2,k}) - 2\text{cov}\sum_{k=1}^{N}\delta'_{1,k}\delta'_{2,k}, \tag{2.141}$$

$$s_{33} = \text{var}\sum_{k=1}^{N}(\delta^2_{1,k} + \delta^2_{2,k}) - 2\text{cov}\sum_{k=1}^{N}\delta_{1,k}\delta_{2,k}, \tag{2.142}$$

$$s_{12} = \text{var}\sum_{k=1}^{N}(\delta''_{1,k}\delta'_{1,k} + \delta''_{2,k}\delta'_{2,k}) - \text{cov}\sum_{k=1}^{N}(\delta''_{1,k}\delta'_{2,k} + \delta''_{2,k}\delta'_{1,k}) \equiv s_{21}, \tag{2.143}$$

$$s_{13} = \text{var}\sum_{k=1}^{N}(\delta''_{1,k}\delta_{1,k} + \delta''_{2,k}\delta_{2,k}) - \text{cov}\sum_{k=1}^{N}(\delta''_{1,k}\delta_{2,k} + \delta''_{2,k}\delta_{1,k}) \equiv s_{31}, \tag{2.144}$$

$$s_{23} = \text{var}\sum_{k=1}^{N}(\delta'_{1,k}\delta_{1,k} + \delta'_{2,k}\delta_{2,k}) - \text{cov}\sum_{k=1}^{N}(\delta'_{1,k}\delta_{2,k} + \delta'_{2,k}\delta_{1,k}) \equiv s_{32}, \tag{2.145}$$

$$\vec{\Delta} = \frac{c(\text{var} - \text{cov})}{2L}\begin{pmatrix} \delta''_{1,k} + \delta''_{2,k} \\ \delta'_{1,k} + \delta'_{2,k} \\ \delta_{1,k} + \delta_{2,k} \end{pmatrix}. \tag{2.146}$$

From equation (2.138), it results:

$$\vec{\alpha} = \frac{c(\text{var} - \text{cov})}{2L} S^{-1} \vec{\Delta}. \tag{2.147}$$

It is then possible to verify that the derivatives of $\vec{\alpha}$ with respect to the voltages V_{1k}, V_{2k}, V_{3k}, defined above, have the following form:

$$\left.\frac{\partial \vec{\alpha}}{\partial V_{jk}}\right|_{\bar{V}_{jk}} = -S_0^{-1} \left.\frac{\partial S}{\partial V_{jk}}\right|_{\bar{V}_{jk}} \vec{\alpha}_0 + \frac{c(\text{var} - \text{cov})}{2L} S_0^{-1} \left.\frac{\partial \vec{\Delta}}{\partial V_{jk}}\right|_{\bar{V}_{jk}} \vec{\alpha}_0, \qquad j = 1, 2, 3 \tag{2.148}$$

where S_0 indicates the S matrix evaluated by considering the values of the parameters obtained by the fit, labeled as $\vec{\alpha}_0$ in the previous equation, and the measured voltages. Furthermore, it is:

$$\left.\frac{\partial \vec{\alpha}}{\partial L}\right|_{L_0} = \frac{c(\text{var} - \text{cov})}{2L_0} \left.\frac{\partial S^{-1}}{\partial L}\right|_{L_0} \vec{\Delta} - \frac{c(\text{var} - \text{cov})}{2L_0^2} S^{-1} \vec{\Delta}, \tag{2.149}$$

with L_0 the length of the cavity from one end to the other one, $L_0 = 150.7$cm. The variance-covariance matrix for the parameter vector $\vec{\alpha}$, for a given frequency, $\bar{\nu}$, can then be calculated, by using the following relation:

$$\begin{aligned} var(\vec{\alpha}) =& < (\vec{\alpha} - \vec{\alpha}_0)^T (\vec{\alpha} - \vec{\alpha}_0) > = \sigma_V^2 \sum_{k=1}^{N} \left[\left.\frac{\partial \vec{\alpha}}{\partial V_{1k}}\right|_{\bar{V}_{1k}} \times \left.\frac{\partial^T \vec{\alpha}}{\partial V_{1k}}\right|_{\bar{V}_{1k}} \right] + \\ & \sigma_V^2 \sum_{k=1}^{N} \left[\left.\frac{\partial \vec{\alpha}}{\partial V_{2k}}\right|_{\bar{V}_{2k}} \times \left.\frac{\partial^T \vec{\alpha}}{\partial V_{2k}}\right|_{\bar{V}_{2k}} \right] + \sigma_V^2 \sum_{k=1}^{N} \left[\left.\frac{\partial \vec{\alpha}}{\partial V_{3k}}\right|_{\bar{V}_{3k}} \times \left.\frac{\partial^T \vec{\alpha}}{\partial V_{3k}}\right|_{\bar{V}_{3k}} \right] + \sigma_L^2 \left.\frac{\partial \vec{\alpha}}{\partial L}\right|_{L_0} \times \left.\frac{\partial^T \vec{\alpha}}{\partial L}\right|_{L_0}, \end{aligned} \tag{2.150}$$

where the symbol T stands for *transverse*. As far as the covariances of the vector $\vec{\alpha}$ with V_{ik}, where i=1,2, and L are concerned, these can be evaluated by using the results of equations (2.148) and (2.149), respectively. Indeed, it is:

$$cov(\vec{\alpha}, V_{ik}) = \left.\frac{\partial \vec{\alpha}}{\partial V_{ik}}\right|_{\bar{V}_{ik}} \sigma_V^2, \qquad i = 1, 2 \tag{2.151}$$

and:

$$cov(\vec{\alpha}, L) = \left.\frac{\partial \vec{\alpha}}{\partial L}\right|_{L_0} \sigma_L^2. \tag{2.152}$$

With the formulas (2.150), (2.151), (2.152), equation (2.134), for the errors $\sigma_{\Phi_{G,ik}}$, can be calculated, so that all the quantities entering relations (2.132), (2.133) are known and it is then possible to evaluate the average value of the Gouy phase and its associated error, for each considered modulation frequency, i.e. $\Phi_{G,\bar{\nu}} \pm \sigma_{\Phi_{G,\bar{\nu}}}$. The results are reported in table (2.4). In

Frequency[Hz]	Gouy phase [rad]
200	3.49 ± 0.04
300	3.57± 0.05
400	3.54 ± 0.05
500	3.51 ± 0.05
600	3.44 ± 0.07
700	3.53± 0.08
800	3.56± 0.08
900	3.54± 0.09

Table 2.4: Average value of the Gouy phase at different modulation frequencies.

addition, by using formulas analogues to equations (2.132), (2.133), the value of the Gouy phase, averaged over all the modulation frequencies taken into account, can be obtained, and it results:

$$\Phi_G = 3.52 \pm 0.02 \text{ rad.} \tag{2.153}$$

For the sake of completeness, a plot of the data in table (2.4) is showed in picture (2.16), where the average value of the Gouy phase, over all the modulation frequencies, is also underlined. A χ^2 is evaluated as well for verifying the agreement of the Gouy phase average value of equation (2.153), with the values reported in table (2.4). Particularly, the χ^2 is now calculated through the following formula:

$$\chi^2_G = \sum_{\bar{\nu}} \frac{(\Phi_{G,\bar{\nu}} - \Phi_G)^2}{\sigma^2_{\Phi_{G,\bar{\nu}}}}, \tag{2.154}$$

where the quantities $\Phi_{G,\bar{\nu}}$ and $\sigma_{\Phi_{G,\bar{\nu}}}$ are given in table (2.4), Φ_G is the one of relation (2.153), and the sum is performed over all the modulation frequencies of table (2.4). The χ^2_G result has to be divided for the degrees of freedom, in order to get to the normalized χ^2, $\bar{\chi}^2_G$. In the present analysis, the degrees of freedom are eight, equal to the number of modulation frequencies taken into account. Eventually, the normalized χ^2 results:

$$\bar{\chi}^2_G = 0.4 \pm 0.5, \tag{2.155}$$

which confirms the agreement between the average value of the Gouy phase, in equation (2.153), and the values reported in table (2.4).

It is necessary to correct the the Gouy phase value of equation (2.153) for the effects introduced by the astigmatism. As this is a systematic error, the correction can be applied directly to the value showed in relation (2.153). By considering the fact that our measurements concern the

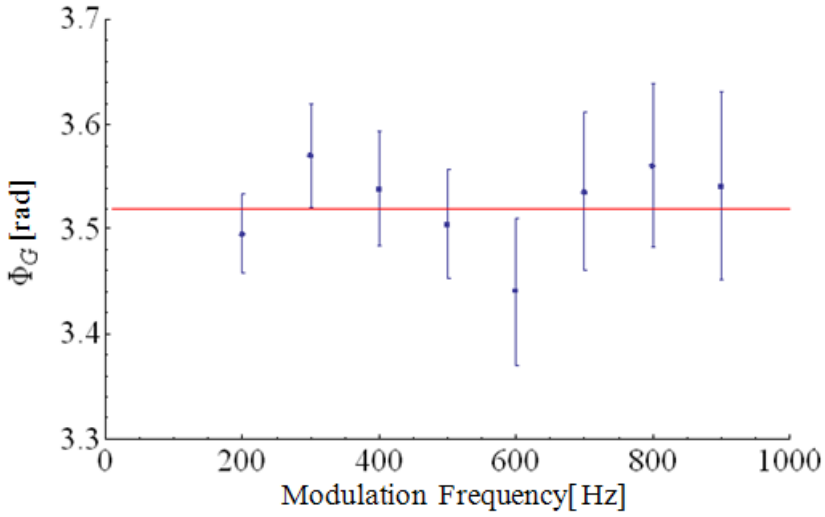

Figure 2.16: Gouy phase average values vs. the considered modulation frequencies. - Plot of the values reported in table 2.4. The red line represents the average value of the Gouy phase, calculated over all the considered modulation frequencies, namely the value given in equation (2.153).

10-mode and the 00-mode, it can be checked that we have actually measured the following quantity:

$$\Delta\nu_{measured} = \frac{c}{4\pi L}\Phi_{G_{00}} + \frac{c}{8\pi L}\left[\arctan\left(\frac{\sqrt{1-m_t^2}}{m_t}\right) - \arctan\left(\frac{\sqrt{1-m_s^2}}{m_s}\right)\right], \tag{2.156}$$

where the indexes t and s stand for tangential and sagittal and it is:

$$m_i = \left(\frac{A_i + D_i}{2}\right), \qquad i = t, s, \tag{2.157}$$

with A_t, D_t elements of the tangential matrix for one round trip within the resonator, given in equation (2.82), and A_s, D_s have the same meaning for the sagittal matrix of equation (2.83). It is worth noticing that, in order to obtain equation (2.156), the gouy phase definition of relation (2.66) has been used. The effective gouy phase shift for the fundamental mode of the cavity, after one round trip, is then:

$$\Phi_{G_{00}} = \Phi_G - \frac{1}{2}\left[\arctan\left(\frac{\sqrt{1-m_t^2}}{m_t}\right) - \arctan\left(\frac{\sqrt{1-m_s^2}}{m_s}\right)\right]. \tag{2.158}$$

For the optical cavity realized in our laboratory, the second term of the right hand side of the previous equation results:

$$\Delta\Phi_{G_{00}} = \frac{1}{2}\left[\arctan\left(\frac{\sqrt{1-m_t^2}}{m_t}\right) - \arctan\left(\frac{\sqrt{1-m_s^2}}{m_s}\right)\right] = -0.015\text{rad}. \tag{2.159}$$

As far as the error associated to $\Delta\Phi_{G_{00}}$ is concerned, this is calculates through the error propagation formula, by considering that $m_i = m_i(R_1, R_2, L_1, L_2, \theta)$, with $i = t, s$. Correlations between the error on Φ_G, as given in equation (2.153), and the error on $\Delta\Phi_{G_{00}}$ are present, because both the quantities depend on L_1 and L_2. However, the contributions of the errors on the lengths to the overall uncertainty on $\Delta\Phi_{G_{00}}$ is small, so that the correlation with the error on Φ_G is neglected. It is noticed that for both L_1 and L_2 we assumed an error of ± 0.25 cm, while for the mirror curvature radii the error is $\pm 0.5\%$ [63]. Furthermore, it is:

$$\left|\frac{\partial\Delta\Phi_{G_{00}}}{\partial\theta}\right|\sigma_\theta = 6\times 10^{-3}, \tag{2.160}$$

where the measured value of θ is 0.05 ± 0.01rad. The overall uncertainty on $\Delta\Phi_{G_{00}}$ results to be of 0.006 rad. Eventually, the experimental value of the Gouy phase shift for the fundamental mode of the cavity is:

$$\Phi_{G_{exp.}} = \Phi_{G_{00}} = 3.535 \pm 0.021\text{rad}. \tag{2.161}$$

To interpret the last result, we have evaluated the error on the gouy phase shift theoretically calculated, $\Phi_{G_{theor.}}$, by applying the uncertainty propagation formula to the Gouy phase shift expression (2.65). The errors on L_1 and L_2 are always equal to 0.25 cm, and, from [63], the error on R_1 and R_2 are set again to $\pm 0.5\%$. Then, the theoretical result for the Gouy phase shift is:

$$\Phi_{G_{theor.}} = 3.6 \pm 0.1 \text{ rad}, \tag{2.162}$$

so that the experimental value of gouy phase, given in relation (2.161) is well inside the theoretical error bar. In conclusion, through relation (2.32) and the Gouy phase experimental value of equation (2.161), the *generalize g-factor* of the cavity is:

$$g = 0.038 \pm 0.004, \tag{2.163}$$

where the error on g has been evaluated with the error propagation formula.

2.3.14 Scaled optical cavity with telescope for NBI system applications

It has been already said that the determined optical cavity, with telescope, can be scaled to get to an optical resonator with the same stability properties and the same geometrical design, but with beam width between M_2 and M_3 of 1cm and L_2 smaller than 100m. This is showed in what follows. Indeed, by scaling of a same factor the quantity R_1, R_2, L_1, L_2, the matrix elements A_{rt} and D_{rt}, expressed in section (2.3.2), do not change. As a consequence, the Gouy phase as well does not vary, as it is possible to check, by using its definition given in equation (2.66). In order to find the scaling factor, the results concerning the cavity we have realized in our laboratory are considered. Particularly, the measured value of the beam diameter along L_2 is taken into account. For the sake of clearness, it is observed that this value is reported in table (2.1) and, by rounding the error value to 200μm, it is $2w_m = 3665 \pm 200\mu$m. The beam size does not vary significantly along L_2 and on the 10 cm of propagation distance between M_2 and the observation point. Indeed, it has been checked through simulations that the beam size variations on the mentioned distances are lower than the error associated to w_m. Hence, for the waist along L_2, it is possible to set $w_{3m} = w_m = 1800 \pm 100\mu$m. As a consequence, in order to obtain a waist of 1 cm along L_2, w_{3m} has to be multiplied for a scale factor of 1/0.18. In turn, for guaranteeing the same stability condition on L_2, this length has to be multiplied for a factor $(1/0.18)^2$. Hence:

$$L_{2,scaled} = \left(\frac{w_{3,scaled}}{w_{3m}}\right)^2 L_2 = 31\text{m} \pm 3\text{m}, \tag{2.164}$$

with $w_{3,scaled} = 1$cm. By scaling for the same factor, $(1/0.18)^2$, the quantities R_1, R_2 and L_1, a cavity with the same stability conditions of the one we realized in our laboratory, but with a distance between M_2 and M_3 of 31m and a waist, on the same length, of 1 cm, is determined. In conclusion, it is worth observing that, calculations analogous to the ones carried on to get to the results reported in section (2.3.8) lead to the values presented below, which are obtained when setting: $R_{1,scaled} \simeq 4.65$m, $R_{2,scaled} \simeq 31$m, $L_{1,scaled} \simeq 15.65$m, $L_{2,scaled} \simeq 31$m.

$$\Phi_{G,scaled} = 3.637 \text{ rad}; \tag{2.165}$$

$$w_{3,scaled} = 1.0 \text{ cm}; \tag{2.166}$$

$$\frac{w_{3,scaled}}{w_{1,scaled}} = 17.8; \tag{2.167}$$

$$\frac{|w_{3,scaled} - w'_{3,scaled}|}{w_{3,scaled}} = 0.004. \tag{2.168}$$

Regarding the last results, we remark that the Gouy phase value does not change.

Chapter 3

Thermal Effect Compensation Systems

In this chapter, the issue of the optical power absorbed by the cavity mirrors [71]-[76] will be addressed and several possible compensation systems, which aim to decrease the effects associated with this phenomenon, will be investigated. It is worth recalling that the mentioned problem has been already faced in different contexts, such as the ground-based gravitational wave interferometers [77]- [81]. In the most general case, both effects due to the mirror coating absorption and the mirror substrate absorption should be taken into account. However, the mirror coating absorption, on one hand, causes the formation of a temperature gradient which distorts the mirror surface; on the other hand, it makes the overall temperature of the mirror to increase, by enhancing the mirror expansion. As the larger the mirror thickness is, the greater is its expansion, only thin mirror (5 mm) will be considered. As a consequence of this choice and because of the characteristics of silica, which is the bulk material of the mirror, the power absorbed by the substrate is very low, so that the effects due to it can be neglected. Only the absorption by the mirror coating will be then taken into account in the present study. The performed research of compensation techniques for the effects associated with the mirror coating absorption grounds on two main concepts: the application of known temperature fields on the rear side of the cavity mirrors, in order to compensate for the mirror deformation, and the use of mechanical constrains (e.g. suitable fixations of the mirror edges and/or borders and the setting up of pressure fields), with the same aim of reducing the mirror distortions. This chapter is thus separated in two principle sections corresponding to these two main concepts, while the validity of the analytical calculations exposed in the following sections will be discussed in chapter (4).

With the aim of making clearer the meaning of the quantities that will be used in the analytic analysis and for a better comprehension of the mathematical tools applied, the two mirror optical cavity of figure (3.1) will be addressed. Furthermore, only cylindrical mirrors will be considered of radius a and thickness h, so that the useful coordinates are the radial one $0 \leq r \leq a$, the azimuthal one $0 \leq \phi \leq 2\pi$ and the longitudinal one $-h/2 \leq z \leq h/2$. With reference to figure (3.1), it is worth noticing that the mirror considered in the following calculations is M_1, so that the surface internal to the optical cavity is the one at $z = -h/2$.

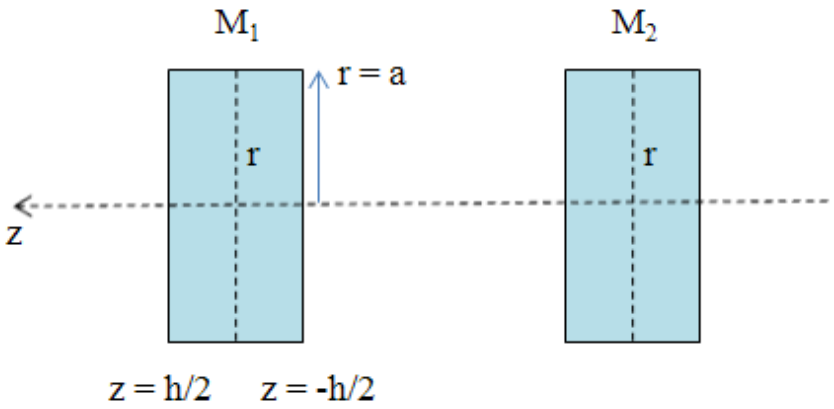

Figure 3.1: Scheme of the optical cavity mirrors - A two mirror cavity is considered in order to introduce the quantities defining the mirror geometrical parameters and the conventions on the coordinate system.

3.1 Mathematical description of the mirror temperature field

The mathematical description of the mirror temperature field will be determined by assuming equilibrium beween the optical power absorbed by the mirror, which makes it to warm up, and the exchanges through thermal radiation between the mirror and its environment, whose temperature is considered constantly equal to T_0. The heat equation, or Fourier equation, in steady state conditions [71], [72], without internal source of heat, and by assuming cylindrical symmetry, reads:

$$\left(\partial_r^2 + \frac{1}{r}\partial_r + \partial_z^2\right) T(r,z) = 0, \tag{3.1}$$

which means that the temperature has to be a harmonic function (see appendix (B) and Ref.[82], [83], [84]). It is then possible to write it as a constant term, $\bar{T}$, plus an harmonic function of r

and z, $\tau = \tau(r, z)$, giving the excess of temperature with respect to $\bar{T}$, i.e.:

$$T(r, z) = \bar{T} + \tau(r, z). \tag{3.2}$$

A possible form for the function $\tau(r, z)$ is:

$$F_{H,\nu}(r, z) = (Ae^{-kz} + Be^{kz})J_\nu(kr), \tag{3.3}$$

where $\nu = 0, 1, 2...$ is an arbitrary integer, J_ν are Bessel functions of the first kind and order ν, and k is an arbitrary constant. As a consequence, the excess of temperature can be expressed by a development on an appropriate base of Bessel functions, depending on the boundary conditions describing the heat flows on the cavity mirror faces and edges, which in general change for the different thermal effect compensation systems (TCS) considered. It is worth noticing that to solve the equations regulating the physical problems faced in this chapter, all the functions entering the calculations will be then expressed through a suitable Bessel function base. Furthermore, the choice of describing the cavity mirror temperature through equation (3.2) has the important feature to allow the linearization of the equations that will have to be solved, if the condition $\tau(r, z) << \bar{T}$ holds. In the calculations presented in this chapter, it is assumed that this condition is always verified, but when analyzing the results of each TCS, it will be necessary to check if the condition holds and to quantify the errors introduced in the physical and mathematical results, when it is not verified.

3.2 TCS based on temperature field application

In this section, the mathematical description of the TCS realized by imposing a suitable field of temperature on the cavity mirror is exposed. The aim of the applied temperature is to generate an overall mirror temperature distribution field which compensates for the deformation associated with the coating absorption of optical power. In this respect, several configurations for the imposed temperature field have been considered, and for each of them the mathematical description is reported in the following subsections.

3.2.1 TCS with fixed temperature on the cavity mirror edges

The first method that will be analyzed, among the ones based on a temperature field application, concerns the fixing of a constant temperature on the mirror edges, as it is shown on figure (3.2).

The idea of such configuration is supported by two reasons: on one hand, to fix the temperature on the mirror edges at the same value of the one of the environment could allow to uniform the mirror overall temperature and then to decrease the mirror deformation due to the optical power absorbed; on the other hand, for fixed temperature values higher with respect to the one of the environment, it could be possible to distort the mirror in a way which compensates for the deformation associated with the absorbed optical power. With reference to figure 3.2, T_1 plays the role of the quantity $\bar{T}$, which is defined above, being the constant temperature imposed on the mirror edges, in order to decrease the thermal effects. So, the mirror temperature field is $T(r,z) = T_1 + \tau(r,z)$, where $\tau(r,z)$ is the temperature excess, which in terms of the Fourier-Bessel series reads:

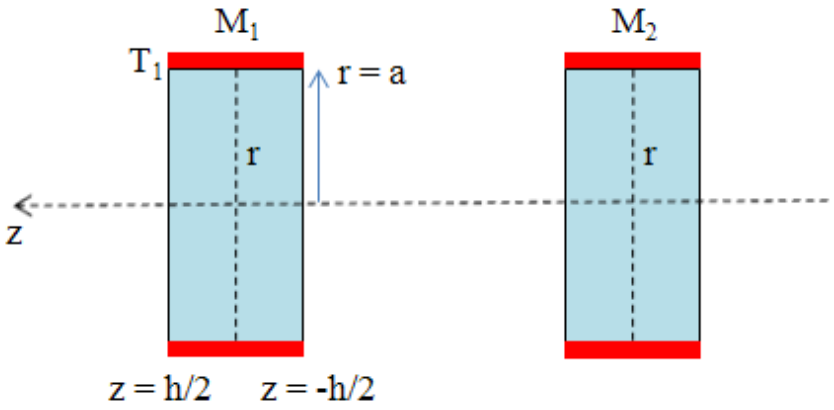

Figure 3.2: Scheme of the TCS treated in section (3.2.1) - The cavity mirrors together with the applied TCS are shown, for the TCS configuration with fixed temperature on the cavity mirror edges.

$$\tau = \sum_{n=1}^{\infty} \tau_n(z) J_0\left(k_n \frac{r}{a}\right), \quad \tau_n(z) = A_n \mathrm{e}^{-k_n \frac{z}{a}} + B_n \mathrm{e}^{k_n \frac{z}{a}}, \tag{3.4}$$

where k_n, $n = 1, 2...$ are the solutions of the equation $J_0(k_n) = 0$, indeed in $r = a$ it has to be $T(a,z) = T_1$. In order to determine the coefficients A_n and B_n, the following boundary conditions are taken into account:

$$-K \left[\frac{\partial \tau(r,z)}{\partial z}\right]_{z=-h/2} = -\sigma\left((T_1 + \tau(r,z))^4 - {T_0}^4\right) + \epsilon I(r), \tag{3.5}$$

$$-K\left[\frac{\partial\tau(r,z)}{\partial z}\right]_{z=h/2} = \sigma\left((T_1+\tau(r,z))^4 - {T_0}^4\right), \tag{3.6}$$

where T_0 is the environment temperature, K the conductivity of the mirror material, σ the Stefan Boltzmann constant, ϵ the mirror absorption coefficient, and $I(r)$ is the laser beam intensity. Particularly, in this work, it is assumed a radial intensity variation of a gaussian beam with spot size w and total carried power, P, i.e.:

$$I(r) = \frac{2P}{\pi w^2}\mathrm{e}^{-\frac{2r^2}{w^2}}. \tag{3.7}$$

Furthermore, in equations (3.5), (3.6), the left side terms represent the power lost by the mirror bulk through the surfaces in $z=-h/2$ and in $z=h/2$ respectively, the terms containing the Stefan-Boltzmann constant give the power flow of thermal radiation, when setting the emissivity of the silica equal to 1, and the term $\epsilon I(r)$, in equation (3.5), describes the mirror absorption of laser power. By considering $\tau \ll T_1$, equations (3.5) and 3.6 can be linearized with respect to the quantity $\tau(r,z)$:

$$-K\tau_{,z}|_{-h/2} = -4\sigma {T_1}^3\tau - \sigma\left({T_1}^4 - {T_0}^4\right)H_a(r) + \epsilon I(r), \tag{3.8}$$

$$-K\tau_{,z}|_{h/2} = 4\sigma {T_1}^3\tau + \sigma\left({T_1}^4 - {T_0}^4\right)H_a(r), \tag{3.9}$$

with:

$$H_a(r) = \begin{cases} 0 & \text{if } r > a \\ 1 & \text{if } r < a \end{cases} \tag{3.10}$$

For solving the system of equations compounded of relation (3.8) and relation (3.9) to find A_n and B_n, the function $I(r)$ and $H_a(r)$ are expressed in terms of a Furier-Bessel series analogue to the one used for the temperature excess, τ, i.e.:

$$I(r) = \sum_{n=1}^{\infty} I_n J_0\left(k_n\frac{r}{a}\right), \tag{3.11}$$

$$\sigma\left({T_1}^4 - {T_0}^4\right)Ha(r) = \sum_{n=1}^{\infty} C_n J_0\left(k_n\frac{r}{a}\right), \tag{3.12}$$

where I_n and C_n are the constant coefficients of the considered developments.
It is worth recalling here that if f is a function of the real variable r, its development in terms

of Fourier Bessel series is [66], [67]:

$$\begin{aligned} f(r) &= \textstyle\sum_{n=1}^{\infty} D_n J_\nu(k_n^\nu \frac{r}{\alpha}), \\ D_n &= \textstyle\frac{2}{\alpha^2 J_{\nu+1}^2(k_n^\nu)} \int_0^\alpha r f(r) J_\nu(k_n^\nu \frac{r}{\alpha}) dr, \end{aligned} \tag{3.13}$$

where k_n^ν are positive zeros of J_ν, and $\nu \geq 0$. Indeed, when the last two conditions are verified, the following orthogonality property holds:

$$\int_0^\alpha r J_\nu\left(\frac{r}{\alpha} a_l\right) J_\nu\left(\frac{r}{\alpha} a_m\right) dr = \frac{\alpha^2}{2} \delta_{lm} (J_{\nu+1}(a_m))^2. \tag{3.14}$$

Then, by using equation (3.7) and (3.13) with $\nu = 0$, for I_n, in (3.11), it results:

$$I_n = \frac{2}{a^2 J_1^2(k_n)} \int_0^a r \frac{2P}{\pi w^2} \mathrm{e}^{-\frac{2r^2}{w^2}} J_0\left(k_n \frac{r}{a}\right) dr. \tag{3.15}$$

By applying the following relation [69]:

$$\int_0^\infty t \mathrm{e}^{-a^2 t^2} J_0(bt) dt = \frac{1}{2a^2} \mathrm{e}^{-\frac{b^2}{4a^2}}, \tag{3.16}$$

we get to:

$$I_n = \frac{P}{\pi a^2 J_1^2(k_n)} \mathrm{e}^{-\frac{k_n^2 w^2}{8a^2}}, \tag{3.17}$$

so:

$$I(r) = \sum_{n=1}^{\infty} \frac{P}{\pi a^2 J_1^2(k_n)} \mathrm{e}^{-\frac{k_n^2 w^2}{8a^2}} J_0\left(k_n \frac{r}{a}\right). \tag{3.18}$$

As far as equation 3.12 is concerned, by performing the integration in equation 3.13 with $\nu = 0$, it is found:

$$C_n = \frac{2\sigma\left({T_1}^4 - {T_0}^4\right)}{a^2 J_1^2(k_n)} \int_0^a r J_0(k_n \frac{r}{a}) dr = \frac{2\sigma\left({T_1}^4 - {T_0}^4\right)}{a^2 J_1^2(k_n)} \frac{a^2 J_1(k_n)}{k_n}, \tag{3.19}$$

hence:

$$\sigma\left({T_1}^4 - {T_0}^4\right) Ha(r) = \sum_{n=1}^{\infty} \frac{2\sigma\left({T_1}^4 - {T_0}^4\right)}{J_1(k_n) k_n} J_0\left(k_n \frac{r}{a}\right) \tag{3.20}$$

As it has been already pointed out, the determination of the coefficient A_n and B_n, which will allow to complete the description of the mirror temperature field, it is obtained by resolving the system of the two equations (3.8), (3.9). To this aim, firstly, equations (3.4), (3.18) and (3.20) are substituted in equation (3.8), while equations (3.4) and 3.20 are substituted in equation

(3.9). Then, both the sides of equations (3.8) and (3.9), as obtained after the substitutions mentioned above, are multiplied by:

$$J_0\left(k_m\frac{r}{a}\right)r \tag{3.21}$$

and the integration on r from 0 to a is performed, by using the orthogonality property of the Bessel functions (3.14), for $\nu = 0$. Hence, equation (3.8) reads:

$$-K\left(\frac{-k_nA_n}{a}\mathrm{e}^{\frac{k_nh}{2a}}+\frac{k_nB_n}{a}\mathrm{e}^{-\frac{k_nh}{2a}}\right)=-4\sigma T_1^3\left(A_n\mathrm{e}^{\frac{k_nh}{2a}}+B_n\mathrm{e}^{-\frac{k_nh}{2a}}\right)- \frac{2\sigma\left({T_1}^4-{T_0}^4\right)}{J_1(k_n)k_n}+\frac{\epsilon P\mathrm{e}^{-\frac{k_n^2w^2}{8a^2}}}{a^2\pi J_1^2(k_n)}, \tag{3.22}$$

and, equation 3.9 becomes:

$$-K\left(\frac{-k_nA_n}{a}\mathrm{e}^{-\frac{k_nh}{2a}}+\frac{k_nB_n}{a}\mathrm{e}^{\frac{k_nh}{2a}}\right)=4\sigma T_1^3\left(A_n\mathrm{e}^{\frac{-k_nh}{2a}}+B_n\mathrm{e}^{\frac{k_nh}{2a}}\right)+ \frac{2\sigma\left({T_1}^4-{T_0}^4\right)}{J_1(k_n)k_n}. \tag{3.23}$$

The system compounded of the last two equations gives the following result, for A_n and B_n:

$$A_n=\frac{P\epsilon\exp\left(\frac{k_n\left(8ah-w^2k_n\right)}{8a^2}+\frac{hk_n}{2a}\right)\left(4a\sigma T_1^3+Kk_n\right)}{\pi aJ_1(k_n)^2\left(e^{\frac{2hk_n}{a}}\left(4a\sigma T_1^3+Kk_n\right)^2-\left(Kk_n-4a\sigma T_1^3\right)^2\right)}- \frac{2a\sigma\left(T_1^4-T_0^4\right)e^{\frac{hk_n}{2a}}\left(e^{\frac{hk_n}{a}}\left(4a\sigma T_1^3+Kk_n\right)-4a\sigma T_1^3+Kk_n\right)}{k_nJ_1(k_n)\left(e^{\frac{2hk_n}{a}}\left(4a\sigma T_1^3+Kk_n\right)^2-\left(Kk_n-4a\sigma T_1^3\right)^2\right)}, \tag{3.24}$$

$$B_n=\frac{P\epsilon e\frac{k_n\left(4ah-w^2k_n\right)}{8a^2}\left(Kk_n-4a\sigma T_1^3\right)}{\pi aJ_1(k_n)^2\left(e^{\frac{2hk_n}{a}}\left(4a\sigma T_1^3+Kk_n\right)^2-\left(Kk_n-4a\sigma T_1^3\right)^2\right)}- \frac{2a\sigma\left(T_1^4-T_0^4\right)\exp\left(\frac{k_n\left(4ah-w^2k_n\right)}{8a^2}+\frac{w^2k_n^2}{8a^2}\right)\left(e^{\frac{hk_n}{a}}\left(4a\sigma T_1^3+Kk_n\right)-4a\sigma T_1^3+Kk_n\right)}{k_nJ_1(k_n)\left(e^{\frac{2hk_n}{a}}\left(4a\sigma T_1^3+Kk_n\right)^2-\left(Kk_n-4a\sigma T_1^3\right)^2\right)}. \tag{3.25}$$

To conclude this section, it is worth stressing that the cavity mirror field of temperature, $T(r,z) = T_1 + \tau(r,z)$, is now completely determined, for the case where the described TCS is applied on the cavity mirrors.

3.2.2 Fixed temperature on the edges and on the rear side of total reflective cavity mirrors

In this section, a TCS applicable only on totally reflective mirrors of the optical cavity will be considered. Indeed, this thermal effect compensation system concerns the edges and the overall rear side of a mirror, then it cannot be applied on the input cavity mirror (see figure (3.3)). The

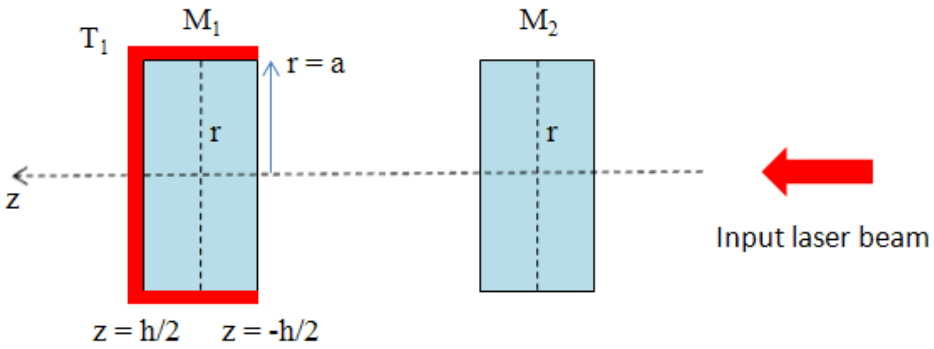

Figure 3.3: TCS configuration studied on section (3.2.2) - Scheme of the TCS with fixed temperature on the mirror edges and on the overall mirror rear face. TCS applicable only on total reflective cavity mirror

reason motivating the study of this TCS configuration is based on the fact that, by applying a fixed temperature on the rear side of the mirror and on its edges, it should be possible to reach a higher level of mirror temperature uniformity with respect to the one obtained by using the TCS described in section (3.2.1). As far as the mathematical treatment of this TCS is concerned, this is not so different with respect to the one of the TCS analyzed in the previous section. Indeed, it is sufficient to substitute equation (3.9) describing the boundary condition of the heat flow on the external surface of the mirror, with the condition on the excess of temperature, $\tau(r, z)$, in $z = h/2$, i.e. $\tau(r, h/2) = 0$. In this way, the temperature in $z = h/2$ is simply equal to T_1, for each value of the mirror radius. So, to determine the coefficients A_n and B_n, which enter the $\tau(r, z)$ expression given in equation (3.4), it is necessary to solve the system formed by equation (3.22) and the equation:

$$\tau_n(h/2) = 0 \implies A_n e^{-k_n \frac{h}{2a}} + B_n e^{k_n \frac{h}{2a}} = 0. \tag{3.26}$$

The solution of the system above mentioned leads to the following expression for A_n and B_n:

$$A_n = \frac{P\epsilon \exp\left(\frac{k_n\left(8ah-w^2k_n\right)}{8a^2}+\frac{hk_n}{2a}\right)\left(4a\sigma T_1^3+Kk_n\right)}{\pi a J_1(k_n)^2\left(e^{\frac{2hk_n}{a}}\left(4a\sigma T_1^3+Kk_n\right)^2-\left(Kk_n-4a\sigma T_1^3\right)^2\right)}- \\ \frac{2a\sigma\left(T_1^4-T_0^4\right)e^{\frac{hk_n}{2a}}\left(e^{\frac{hk_n}{a}}\left(4a\sigma T_1^3+Kk_n\right)-4a\sigma T_1^3+Kk_n\right)}{k_n J_1(k_n)\left(e^{\frac{2hk_n}{a}}\left(4a\sigma T_1^3+Kk_n\right)^2-\left(Kk_n-4a\sigma T_1^3\right)^2\right)}, \tag{3.27}$$

$$B_n = \frac{P\epsilon e^{\frac{k_n\left(4ah-w^2k_n\right)}{8a^2}}\left(Kk_n-4a\sigma T_1^3\right)}{\pi a J_1(k_n)^2\left(e^{\frac{2hk_n}{a}}\left(4a\sigma T_1^3+Kk_n\right)^2-\left(Kk_n-4a\sigma T_1^3\right)^2\right)}- \\ \frac{2a\sigma\left(T_1^4-T_0^4\right)\exp\left(\frac{k_n\left(4ah-w^2k_n\right)}{8a^2}+\frac{w^2k_n^2}{8a^2}\right)\left(e^{\frac{hk_n}{a}}\left(4a\sigma T_1^3+Kk_n\right)-4a\sigma T_1^3+Kk_n\right)}{k_n J_1(k_n)\left(e^{\frac{2hk_n}{a}}\left(4a\sigma T_1^3+Kk_n\right)^2-\left(Kk_n-4a\sigma T_1^3\right)^2\right)}. \tag{3.28}$$

T_1 is a known quantity, and A_n and B_n have now an explicit expression, hence the mirror temperature field $T(r,z) = T_1 + \tau(r,z)$ is completely determined.

3.2.3 Free cavity mirror

In this section, the mathematical description of a TCS which aims to uniform the mirror temperature by fixing an appropriate temperature of the environment where the mirror cavity is placed will be presented. It is worth remarking that the mirror is free, in this case, which means that there are no temperature fields applied on it, its temperature depends on the exchanges with the environment and on the optical power absorbed in the coating. The mirror temperature field solutions reported in this section can be found in Ref. [71]. As customary, the cylindrical symmetry is assumed, hence the heat equation (3.1) still holds. Consequently, the mirror temperature is described with formulas similar to the ones used in section (3.2.1), i.e. $T_0 + \tau(r,z)$, where T_0 is the fixed environment temperature and $\tau(r,z)$ is a harmonic function describing the excess of temperature with respect to T_0. As it has been already said, a possible solution for τ has the form:

$$\tau(r,z) = \left(A\mathrm{e}^{-\eta z} + B\mathrm{e}^{\eta z}\right) J_0(\eta r). \tag{3.29}$$

The heat flows on the mirror surfaces are given by the boundary conditions, which, after the linearization obtained by considering $\tau \ll T_0$, take the form:

$$-K\left[\frac{\partial\tau(r,z)}{\partial z}\right]_{z=-h/2} = -4\sigma {T_0}^3\tau(r,-h/2) + \epsilon I(r), \tag{3.30}$$

$$-K\left[\frac{\partial\tau(r,z)}{\partial z}\right]_{z=h/2} = 4\sigma {T_0}^3\tau(r,h/2), \tag{3.31}$$

where K is always the conductivity of the mirror material and $I(r)$ the laser beam intensity distribution, described with formula (3.7). Furthermore, the boundary condition on the mirror edges has also to be considered, i.e.:

$$-K\left[\frac{\partial\tau(r,z)}{\partial r}\right]_{r=a} = 4\sigma {T_0}^3\tau. \tag{3.32}$$

This last equation can be rewritten as :

$$\zeta J_0'(\zeta) + \chi_e J_0(\zeta) = 0, \tag{3.33}$$

where $\zeta = \eta a$ and $\chi_e = 4\sigma {T_0}^3 a/K$. Equation (3.33) has an infinite number of discrete solutions $\zeta_n = \eta_n a,\ n = 1,\ 2\ 3\ ...$, hence a general solution of the heat equation (3.1) is:

$$\tau(r,z) = \sum_{n=1}^{\infty} \tau_n(z) J_0(\zeta_n r), \quad \tau_n(z) = A_n \mathrm{e}^{-\frac{\zeta_n}{a}z} + B_n \mathrm{e}^{\frac{\zeta_n}{a}z}. \tag{3.34}$$

From the Sturm-Liouville theorem, the family of functions $J_0(\zeta_n r/a), n = 1, 2, ...$ is orthogonal and complete in the interval $[0, a]$ with normalization factor given by:

$$\int_0^1 x J_0(x\zeta_n) J_0(x\zeta_{n'}) dx = \frac{1}{2\zeta_n^2}\delta_{nn'}(\chi_e^2 + \zeta_n^2)(J_0(\zeta_n))^2. \tag{3.35}$$

By using the previous relation, the intensity function of the laser beam, $I(r)$, can be developed as follow:

$$I(r) = \frac{P}{\pi a^2}\sum_{n>0} p_n J_0(\zeta_n r/a), \tag{3.36}$$

with P the integrated power, and:

$$p_n = \frac{2\pi\zeta_n^2}{P(\chi_e^2 + \zeta_n^2)J_0^2(\zeta_n)}\int_0^a I(r) J_0(\zeta_n r/a) r dr. \tag{3.37}$$

From equations (3.30), (3.31) and (3.36), the coefficient A_n and B_n, which are present in equation (3.34), are found, so that:

$$\tau_n(z) = \frac{\epsilon P}{\pi K a} p_n \mathrm{e}^{(-\zeta_n h/2a)} \frac{(\zeta_n - \chi_e)\mathrm{e}^{-\zeta_n \frac{h-z}{a}} + (\zeta_n + \chi_e)\mathrm{e}^{-\zeta_n \frac{z}{a}}}{(\zeta_n + \chi_e)^2 - (\zeta_n - \chi_e)^2 \mathrm{e}^{-2\zeta_n h/a}}. \tag{3.38}$$

The total mirror temperature field is then determined, as it is: $T_0 + \tau(r, z)$, where $\tau(r, z)$ is now a known quantity, indeed:

$$\tau(r, z) = \sum_{n=1}^{\infty} \tau_n(z) J_0 \left(\zeta_n \frac{r}{a}\right) \tag{3.39}$$

with $\tau_n(z)$ given in equation (3.38).

3.2.4 Fixed temperature on the cavity mirror edges and one ring heater

Another method which has been analyzed with the aim of compensating for the mirror distortion due to the laser power absorption by the mirror coating, concerns the application of a constant temperature, T_1, on the mirror edges, and the heating of the mirror rear face with a chosen temperature field. In particular, the temperature field imposed on the back side of the mirror can be described as the sum of the fixed temperature, T_1, plus an excess of temperature, $\theta(r)$. With reference to figure 3.4, it can be checked that the quantity $\theta(r)$ is known for mirror radii $b < r < a$, but it is unknown for $r < b$. Then, it is useful to define the following function:

$$\theta_<(r) = H_b(r)\theta(r), \tag{3.40}$$

where:

$$H_b(r) = \begin{cases} 0 & \text{if } r > b \\ 1 & \text{if } r < b \end{cases} \tag{3.41}$$

while $\theta_>(r)$ is the excess of temperature, for $b < r < a$, so that $\theta(r) = \theta_<(r) + \theta_>(r)$. In terms of a Bessel function base, for $\theta(r)$ it is obtained:

$$\theta(r) = \sum_{n=1}^{\infty} \theta_n J_0(k_n \frac{r}{a}) = \sum_{n=1}^{\infty} (\theta_{<n} + \theta_{>n}) J_0(k_n \frac{r}{a}), \tag{3.42}$$

where $\theta_{>n}$ and $\theta_{>n}$ are the coefficients of the following developments:

$$\theta_<(r) = \sum_{n=1}^{\infty} \theta_{<n} J_0(k_n \frac{r}{a}), \quad \theta_>(r) = \sum_{n=1}^{\infty} \theta_{>n} J_0(k_n \frac{r}{a}), \tag{3.43}$$

and k_n, $n = 1,\ 2$ ... are the zeros of the equation $J_0(k_n) = 0$. It is worth noticing that $\theta_>(a) = 0$. In particular, in what follows it is assumed $\theta_>(r) \equiv 0$, so that the applied field of temperature, on the back side of the mirror, corresponds to the fixing of the mirror temperature at T_1, on a ring of internal radius b and external radius a. As far as the mirror surface in $z = -h/2$ is concerned, the flux balance is yet:

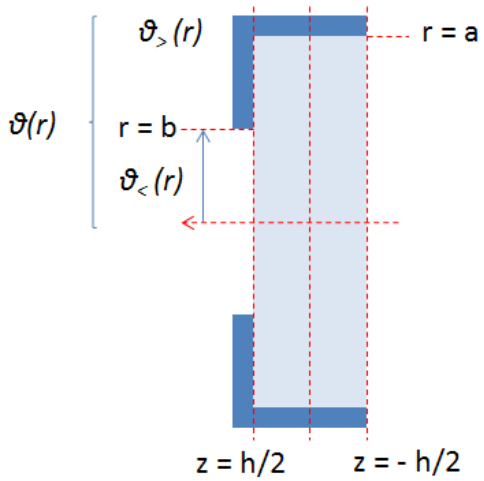

Figure 3.4: Scheme of the TCS described in section (3.2.4). - Mirror rear face heating through a given temperature field, $T_1 + \theta(r)$, where T_1 is a chosen constant temperature and $\theta(r)$ is the excess of temperature compounds of $\theta_>(r)$ and $\theta_<(r)$, with $\theta_>(r)$ known function and $\theta_<(r)$ unknown.

$$-K\left[\frac{\partial\tau(r,z)}{\partial z}\right]_{z=-h/2} = -4\sigma {T_1}^3\tau - \sigma\left({T_1}^4 - {T_0}^4\right)H_a(r) + \epsilon I(r). \tag{3.44}$$

For obtaining the previous equation, the total temperature of the mirror has to be described as $T_1+\tau(r,z)$, where τ is the excess of temperature with respect to the constant temperature T_1, and $T_1 >> \tau$. The function $H_a(r)$ is the same as given in equation (3.10) and the mirror absorption of optical power is described, as usual, by the term $\epsilon I(r)$, with $I(r)$ as in equation(3.7). By assuming for the excess of temperature, τ, the same developement as given in equation (3.4) and by expressing $H_a(r)$ and $I(r)$ in terms of Fourier-Bessel series, equation (3.44) becomes:

$$-K\left(\frac{-k_n A_n}{a}\mathrm{e}^{\frac{k_n h}{2a}} + \frac{k_n B_n}{a}\mathrm{e}^{-\frac{k_n h}{2a}}\right) = -4\sigma T_1^3\left(A_n\mathrm{e}^{\frac{k_n h}{2a}} + B_n\mathrm{e}^{-\frac{k_n h}{2a}}\right) + \tag{3.45}$$

$$-\frac{2\sigma\left({T_1}^4-{T_0}^4\right)}{J_1(k_n)k_n} + \frac{\epsilon P\mathrm{e}^{-\frac{k_n^2 w^2}{8a^2}}}{a^2\pi J_1^2(k_n)}.$$

Another condition is determined by the requirement of the equality between the mirror temperature and the imposed field of temperature, in $z = h/2$, i.e: $\tau(r, h/2) = \theta(r)$. In the Bessel function base, it is:

$$A_n e^{(\frac{-k_n h}{2a})} + B_n e^{(\frac{k_n h}{2a})} = \theta_n = \theta_{>n} + \theta_{<n} \equiv \theta_{>n}, \tag{3.46}$$

where the coefficients $\theta_{<n}$ are unknown. The flux in $z = h/2$ can be written as:

$$\phi(r, h/2) = \phi(r)H_b(r) + \phi(r)(1 - H_b(r)) = \phi_<(r) + \phi_>(r), \tag{3.47}$$

with $H_b(r)$ as given in equation (3.41). $\phi(r, h/2)$ can be expressed as function of $\theta_<(r)$, for $r < b$, indeed:

$$\begin{aligned} \phi_<(r) &= \left(4\sigma {T_1}^3 \tau(r, h/2) + \sigma({T_1}^4 - {T_0}^4)\right) H_b(r) = \\ &= 4\sigma {T_1}^3 \theta_<(r) + \left(\sigma({T_1}^4 - {T_0}^4)\right) H_b(r). \end{aligned} \tag{3.48}$$

However $\phi(r, h/2)$ is unknown for $r > b$. Hence, for the boundary condition on the mirror surface at $z = h/2$, it is:

$$-K \left[\frac{\partial \tau(r, z)}{\partial z}\right]_{z=h/2} = 4\sigma {T_1}^3 \theta_<(r) + \sigma \left({T_1}^4 - {T_0}^4\right) H_b(r) + \phi_>(r). \tag{3.49}$$

In terms of the Bessel series, the previous equation becomes:

$$-K \left(\frac{-k_n A_n}{a} \mathrm{e}^{-\frac{k_n h}{2a}} + \frac{k_n B_n}{a} \mathrm{e}^{\frac{k_n h}{2a}}\right) = 4\sigma T_1^3 \theta_{<n} + \sigma \left({T_1}^4 - {T_0}^4\right) c_{<n} + \phi_{>n}. \tag{3.50}$$

In equation (3.50), the quantities $\phi_{>n}$ indicate the coefficients for the development of $\phi_>(r)$ in terms of Bessel function base, while the coefficients $c_{<n}$ can be obtained from relation (3.13), where $f(r) = H_b(r)$:

$$c_{<n} = \frac{2}{J_1^2(k_n)a^2} \int_0^b r J_0(k_n \frac{r}{a}) dr = \frac{2}{J_1^2(k_n)a^2} \frac{ab J_1\left(\frac{k_n b}{a}\right)}{k_n}. \tag{3.51}$$

So far, three equations in four unknowns are present. The four unknowns are: $A_n,\ B_n,\ \theta_{<n},\ \phi_{>n}$ and the equations are: (3.45), (3.46), (3.50). It is observed that, by using equations (3.45), (3.46), (3.50), the coefficients $A_n,\ B_n,\ \theta_{<n}$ can be written as functions of $\phi_{>n}$, by solving the system of the three equations, where $\phi_{>n}$ has the role of a parameter. As the function $\phi_>(r)$ is not known, an assumption about it is required in order to solve the problem. The following approximation

is established:

$$\phi_{>}(r) = \sum_{m=0}^{M-1} \phi_m H_m(r), \tag{3.52}$$

where M can be arbitrary chosen and:

$$H_m(r) = \begin{cases} 1 & \text{if } b + \frac{(a-b)(m)}{M} \leq r \leq b + \left(\frac{(a-b)(m+1)}{M}\right) \\ 0 & \text{if } r \notin \left[b + \frac{(a-b)(m)}{M}, b + \frac{(a-b)(m+1)}{M}\right] \end{cases}. \tag{3.53}$$

$H_m(r)$, on a Bessel function base, becomes:

$$H_m(r) = \sum_{n=1}^{\infty} H_m^n J_0\left(\frac{k_n r}{a}\right), \tag{3.54}$$

where H_m^n are the coefficients of the expansion in terms of Bessel function base, which are found by using relation (3.13), with $f(r) = H_m(r)$. Then:

$$\phi_{>}(r) = \sum_{m=0}^{M-1} \phi_m \sum_{n=1}^{\infty} H_m^n J_0\left(\frac{k_n r}{a}\right) = \sum_{n=1}^{\infty} \phi_{>n} J_0\left(\frac{k_n r}{a}\right), \tag{3.55}$$

so that:

$$\phi_{>n} = \sum_{m=0}^{M-1} \phi_m H_m^n. \tag{3.56}$$

As it is possible to calculate H_m^n, once the quantities ϕ_m are determined as well, the problem of three equations and four unknowns is reduced to a problem with three equations, three unknowns and one parameter, which is $\phi_{>n}$. By assuming the possibility of obtaining ϕ_m, the system of three equations and three unknowns is solved through Mathematica and the result is reported in the following:

$$\begin{aligned} A_n = & \frac{e^{\frac{k_n\left(4ah - w^2 k_n\right)}{8a^2} + \frac{hk_n}{a}}\left(4a\sigma T_1^3 + Kk_n\right)\left(2\pi a^2\sigma\left(T_0^4 - T_1^4\right)J_1(k_n)e^{\frac{w^2 k_n^2}{8a^2}} + P\epsilon k_n\right)}{\pi a k_n J_1(k_n)^2\left(e^{\frac{2hk_n}{a}}\left(4a\sigma T_1^3 + Kk_n\right)^2 - \left(Kk_n - 4a\sigma T_1^3\right)^2\right)} + \\ & \frac{e^{\frac{hk_n}{2a}}\left(4a\sigma T_1^3 - Kk_n\right)\left(2b\sigma\left(-T_0^4 + T_1^4\right)J_1\left(\frac{bk_n}{a}\right)\right)}{k_n J_1(k_n)^2\left(e^{\frac{2hk_n}{a}}\left(4a\sigma T_1^3 + Kk_n\right)^2 - \left(Kk_n - 4a\sigma T_1^3\right)^2\right)} + \\ & \frac{e^{\frac{hk_n}{2a}}\left(4a\sigma T_1^3 - Kk_n\right)\left(ak_n J_1(k_n)^2\right)}{k_n J_1(k_n)^2\left(e^{\frac{2hk_n}{a}}\left(4a\sigma T_1^3 + Kk_n\right)^2 - \left(Kk_n - 4a\sigma T_1^3\right)^2\right)}\phi_{>n}, \end{aligned} \tag{3.57}$$

$$B_n = \frac{P\epsilon e^{\frac{k_n\left(4ah-w^2k_n\right)}{8a^2}}\left(Kk_n-4\mathrm{aT}_1^3\sigma\right)}{\pi aJ_1(k_n)^2\left(e^{\frac{2hk_n}{a}}\left(4\mathrm{aT}_1^3\sigma+Kk_n\right)^2-\left(Kk_n-4\mathrm{aT}_1^3\sigma\right)^2\right)}+$$
$$\frac{2\sigma\left(T_0^4-T_1^4\right)e^{\frac{hk_n}{2a}}\left(bJ_1\left(\frac{\mathrm{bk}_n}{a}\right)e^{\frac{hk_n}{a}}\left(4\mathrm{aT}_1^3\sigma+Kk_n\right)+aJ_1(k_n)\left(Kk_n-4\mathrm{aT}_1^3\sigma\right)\right)}{k_nJ_1(k_n)^2\left(e^{\frac{2hk_n}{a}}\left(4\mathrm{aT}_1^3\sigma+Kk_n\right)^2-\left(Kk_n-4\mathrm{aT}_1^3\sigma\right)^2\right)}- \tag{3.58}$$
$$\frac{e^{\frac{3hk_n}{2a}}\left(4\mathrm{aT}_1^3\sigma+Kk_n\right)\left(ak_nJ_1(k_n)^2\right)}{k_nJ_1(k_n)^2\left(e^{\frac{2hk_n}{a}}\left(4\mathrm{aT}_1^3\sigma+Kk_n\right)^2-\left(Kk_n-4\mathrm{aT}_1^3\sigma\right)^2\right)}\phi_{>n},$$

$$\theta_{<n} = \frac{2e^{\frac{hk_n}{a}-\frac{w^2k_n^2}{8a^2}}\left(2\pi a^2K\sigma\left(T_0^4-T_1^4\right)k_nJ_1(k_n)e^{\frac{w^2k_n^2}{8a^2}}+KP\epsilon k_n^2\right)}{\pi ak_nJ_1(k_n)^2\left(e^{\frac{2hk_n}{a}}\left(4a\sigma T_1^3+Kk_n\right)^2-\left(Kk_n-4a\sigma T_1^3\right)^2\right)}+$$
$$\frac{4b\sigma\left(T_0^4-T_1^4\right)e^{\frac{hk_n}{a}}J_1\left(\frac{bk_n}{a}\right)\left(Kk_n\cosh\left(\frac{hk_n}{a}\right)+4a\sigma T_1^3\sinh\left(\frac{hk_n}{a}\right)\right)}{k_nJ_1(k_n)^2\left(e^{\frac{2hk_n}{a}}\left(4a\sigma T_1^3+Kk_n\right)^2-\left(Kk_n-4a\sigma T_1^3\right)^2\right)}- \tag{3.59}$$
$$-\frac{2ae^{\frac{hk_n}{a}}\left(e^{\frac{2hk_n}{a}}\left(4a\sigma T_1^3+Kk_n\right)-4a\sigma T_1^3+Kk_n\right)}{e^{\frac{2hk_n}{a}}\left(4a\sigma T_1^3+Kk_n\right)^2-\left(Kk_n-4a\sigma T_1^3\right)^2}\phi_{>n}.$$

However, the problem will be really solved only when an expression for ϕ_m will be found. With this aim in mind, it is observed that the obtained results for A_n and B_n show a linear behavior with $\phi_{>n}$, so that it is possible to write them as:

$$A_n = \alpha_n + \beta_n\phi_{>n}, \qquad B_n = \gamma_n + \delta_n\phi_{>n}, \tag{3.60}$$

where α_n, γ_n are intercepts and β_n, δ_n are the angular coefficients of the linear dependence. Then, for $\tau(r, h/2)$, it is:

$$\tau(r,h/2) = \sum_{n=1}^{\infty}\left[\left(\alpha_n+\beta_n\phi_{>n}\right)e^{\left(\frac{-k_nh}{2a}\right)}+\left(\gamma_n+\delta_n\phi_{>n}\right)e^{\left(\frac{k_nh}{2a}\right)}\right]J_0\left(k_n\frac{r}{a}\right), \tag{3.61}$$

and, by remembering that $\phi_{>n} \simeq \sum_{m=0}^{M-1}\phi_m H_m^n$:

$$\tau(r,h/2) = \sum_{n=1}^{\infty}\left(\alpha_ne^{\frac{-k_nh}{2a}}+\gamma_ne^{\frac{k_nh}{2a}}\right)J_0\left(k_n\frac{r}{a}\right)+$$
$$+\sum_{m=0}^{M-1}\phi_m\sum_{n=1}^{\infty}\left(\beta_ne^{\frac{-k_nh}{2a}}+\delta_ne^{\frac{k_nh}{2a}}\right)H_m^nJ_0\left(\frac{k_nr}{a}\right) \tag{3.62}$$

For obtaining a relation to determine the quantity ϕ_m, the average of the function $\tau(r,z)$, in the interval $b \leq r \leq a$, is defined as follow:

$$T_p = \frac{1}{\frac{a-b}{M}} \int_{b+\frac{(a-b)p}{M}}^{b+\frac{(a-b)(p+1)}{M}} \tau(r, h/2)dr \tag{3.63}$$

where $[p = 0, 1, ..., M-1]$. Furthermore, it is set:

$$J_n^p = \frac{1}{\frac{a-b}{M}} \int_{p+\frac{(a-b)p}{M}}^{b+\frac{(a-b)(p+1)}{M}} J_0(k_n \frac{r}{a})dr, \tag{3.64}$$

so that:

$$\begin{aligned} T_p = \textstyle\sum_{n=1}^{\infty} \left(\alpha_n e^{\frac{-k_n h}{2a}} + \gamma_n e^{\frac{k_n h}{2a}}\right) J_n^p + \\ + \textstyle\sum_{m=0}^{M-1} \phi_m \sum_{n=1}^{\infty} \left(\beta_n e^{\frac{-k_n h}{2a}} + \delta_n e^{\frac{k_n h}{2a}}\right) H_m^n J_n^p. \end{aligned} \tag{3.65}$$

Two further quantities are then introduced:

$$D_p = \sum_{n=0}^{\infty} \left(\alpha_n e^{\frac{-k_n h}{2a}} + \gamma_n e^{\frac{k_n h}{2a}}\right) J_n^p; \tag{3.66}$$

$$E_{p,m} = \sum_{n=1}^{\infty} \left(\beta_n e^{\frac{-k_n h}{2a}} + \delta_n e^{\frac{k_n h}{2a}}\right) H_m^n J_n^p, \tag{3.67}$$

hence:

$$T_p = D_p + \sum_{m=0}^{M-1} E_{p,m}\phi_m. \tag{3.68}$$

It is possible to write the previous equation in terms of matrices. To this purpose, J_n^p is considered as a $M \times n_{max}$ matrix and the quantity H_m^n is treated as a $n_{max} \times M$ matrix. Here n_{max} indicates the last zero of J_0 which enters the sum of the Bessel function development. Moreover, the $M \times M$ matrix is defined :

$$E = E_{p,m} = \sum_{n=1}^{\infty} J_n^p \left(\beta_n e^{\frac{-k_n h}{2a}} + \delta_n e^{\frac{k_n h}{2a}}\right) H_m^n \tag{3.69}$$

together with the two column vectors, ϕ_m and:

$$V_p = T_p - D_p. \tag{3.70}$$

As a consequence, the inversion of the relation $E\phi = V$ gives the quantities ϕ_m, as:

$$\phi = E^{-1}V. \tag{3.71}$$

To show how $E_{p,m}$ is calculated, it is useful to introduce the coefficients:

$$coef(n) = \left(\beta_n e^{\frac{-k_n h}{2a}} + \delta_n e^{\frac{k_n h}{2a}}\right), \tag{3.72}$$

indeed they are present in equation (3.69) and they enter the evaluation of the following matrix:

$$\widetilde{H}_m^n = \begin{pmatrix} coef(1)H_0^1 & coef(1)H_1^1 & \cdots & coef(1)H_{M-1}^1 \\ coef(2)H_0^2 & coef(2)H_1^2 & \cdots & coef(2)H_{M-1}^2 \\ \vdots & \vdots & \ddots & \vdots \\ coef(n)H_0^{n_{max}} & coef(n)H_1^{n_{max}} & \cdots & coef(n)H_{M-1}^{n_{max}} \end{pmatrix} \tag{3.73}$$

Hence, $E_{p,m}$ is determined, by the simple application of the matrix multiplication formula $\sum_{n=1}^{n_{max}} J_n^p \times \widetilde{H}_m^n$. As far as equation (3.73) is concerned, it is worth stressing that the m index range is $m = 0, ...M-1$, while the n index range is $n = 1, ...n_{max}$. To find the quantity V, given in (3.70), the vectors T_p and D_p are separately calculated and after the vector subtraction is made. For $b \leq r \leq a$, it is:

$$\tau(r, h/2) = \theta_>(r) \equiv 0, \tag{3.74}$$

and it results:

$$T_p = \frac{1}{\frac{a-b}{M}} \int_{b+\frac{(a-b)p}{M}}^{b+\frac{(a-b)(p+1)}{M}} \theta_>(r)dr = 0, \tag{3.75}$$

so that, the quantities T_p compounds a column vector with M rows and all the components equal to zero. As far as D_p is concerned, firstly, the following coefficients are introduced:

$$\text{Inter}(n) = \left(\alpha_n e^{-\frac{k_n h}{2a}} + \gamma_n e^{\frac{k_n h}{2a}}\right), \tag{3.76}$$

as they enter the definition of D_p, given in equation (3.66). A column vector with n_{max} rows is then generated, by using relation (3.76):

$$\text{Icoe} = \begin{pmatrix} \text{Inter}(1) \\ \text{Inter}(2) \\ \vdots \\ \text{Inter}(n_{max}) \end{pmatrix} \tag{3.77}$$

The quantity introduced above, Icoe, together with the matrix J_n^p are applied to calculate D_p, through the following matrix-vector multiplication:

$$D_p = \sum_{n=1}^{n_{max}} J_n^p \ \mathrm{Icoe}(n). \tag{3.78}$$

It is worth pointing out that the inversion of the matrix M is made by using the MATLAB formula $M^{-1} = inv(M)$. Then, from relation $\phi = M^{-1}V$, the components of the column vector ϕ, i.e. ϕ_m, are found and the coefficients $\phi_{>n}$ are calculated with the vector-matrix multiplication:

$$\phi_{>n} = \sum_{m=0}^{M-1} H_m^n \ \phi_m, \tag{3.79}$$

where H_m^n are introduced in equation (3.54). The $\phi_{>n}$ coefficients are then used to evaluate A_n and B_n, which will allow to determine the temperature field, through the formula $T = T_1 + \tau(r, z)$, with:

$$\tau = \sum_{n=1}^{n_{max}} \tau_n(z) J_0(k_n \frac{r}{a}), \quad \tau_n(z) = A_n \mathrm{e}^{-k_n \frac{z}{a}} + B_n \mathrm{e}^{k_n \frac{z}{a}}. \tag{3.80}$$

For the sake of completeness, it is shown here how the matrix J_n^p and H_m^n are calculated. As far as the matrix H_m^n is concerned, by considering equations (3.53) and (3.13), the following relation is obtained:

$$H_m^n = \frac{2}{a^2 J_1^2(k_n)} \int_{b+\frac{(a-b)m}{M}}^{b+\frac{(a-b)(m+1)}{M}} r J_0(k_n \frac{r}{a}) dr. \tag{3.81}$$

The result of the integration is:

$$\begin{aligned} H_m^n = & \frac{2(a(m+1)+b(-m+M-1))J_1\left(\frac{(a(m+1)+b(-m+M-1))k_n}{aM}\right)}{aMk_nJ_1(k_n)^2} - \\ & - \frac{2(am+b(M-m))J_1\left(\frac{(am+b(M-m))k_n}{aM}\right)}{aMk_nJ_1(k_n)^2} \end{aligned} \tag{3.82}$$

and it is used within the MATLAB program calculating the mirror temperature field. As far as the matrix J_n^p is concerned, it is required to calculate:

$$J_n^p = \frac{1}{\frac{a-b}{M}} \int_{b+\frac{(a-b)p}{M}}^{b+\frac{(a-b)(p+1)}{M}} J_0(k_n \frac{r}{a}) dr, \tag{3.83}$$

which is an integration not analytically calculable. So, two different methods are used to obtain the elements of the J_n^p matrix. One method is based on the application of the MATLAB function

quad[1], to estimate:

$$\int_{b+\frac{(a-b)p}{M}}^{b+\frac{(a-b)(p+1)}{M}} J_0(k_n\frac{r}{a})dr. \tag{3.85}$$

The other method grounds on the following approximation:

$$\begin{aligned} J_n^p = \frac{1}{\frac{a-b}{M}} \int_{b+\frac{(a-b)p}{M}}^{b+\frac{(a-b)(p+1)}{M}} J_0(k_n\tfrac{r}{a})dr \sim \\ \frac{1}{\left(b+\frac{(a-b)p}{M}\right)\frac{a-b}{M}} \int_{b+\frac{(a-b)p}{M}}^{b+\frac{(a-b)(p+1)}{M}} rJ_0(k_n\tfrac{r}{a})dr. \end{aligned} \tag{3.86}$$

The last integration in equation (3.86) can be analytically calculated and the result for the J_n^p matrix elements is:

$$\begin{aligned} J_n^p \simeq \frac{\left(-\frac{p(a-b)}{M}-b\right)J_1\left(\sqrt{\frac{1}{a^2}}\left(b+\frac{(a-b)p}{M}\right)k_n\right)}{\sqrt{\frac{1}{a^2}}k_n\left(\frac{p(a-b)^2}{M^2}+\frac{b(a-b)}{M}\right)} + \\ + \frac{\left(\frac{(p+1)(a-b)}{M}+b\right)J_1\left(\sqrt{\frac{1}{a^2}}\left(b+\frac{(a-b)(p+1)}{M}\right)k_n\right)}{\sqrt{\frac{1}{a^2}}k_n\left(\frac{p(a-b)^2}{M^2}+\frac{b(a-b)}{M}\right)}. \end{aligned} \tag{3.87}$$

It is found out that the application of the two different methods, for the calculation of J_n^p, does not give results significantly different in term of the mirror temperature field. Particularly, the maximum difference between the temperature values calculated through the analytical formula for J_n^p, and the ones calculated with the numerical formula for J_n^p, amount at 0.02 K. As the temperature considered are bigger than 300 K, an error of 0.02 K is not significant. Then, both the methods could be applied within the MATLAB program, without appreciable modifications of the results. For the sake of completeness, it is noticed that the results that will be presented, about the TCS currently analyzed, are obtained by using formula (3.87).

[1] *quad* is a method to numerically evaluate a finite integral, i.e.:

$$q = \int_a^b f(x)dx. \tag{3.84}$$

Its syntax is *q=quad(fun,a,b)* [70], where *fun* is the function which has to be integrated and a and b are the extremes of the integration interval. The *quad* method approximates the integral of *fun* from a to b within an error of 10^{-6} using recursive adaptive Simpson quadrature. It is stressed that the quantities a and b have to be finite.

3.2.5 Fixed temperature on the mirror edges, one external ring heater and a separated central disk heater

In order to compensating for the mirror distortion due to the absorption of the optical power in the mirror coating, another TCS configuration is analyzed, which consists in applying, in the rear side of the mirror, a temperature field as described in figure 3.5: fixed temperature T_3 in a central circular section of radius b_1; fixed temperature T_1 in an external ring of internal radius b; and fixed temperature, equal to T_1, on the mirror edges.

As already done in sections (3.2.1), (3.2.2) and (3.2.4), the total mirror temperature is described

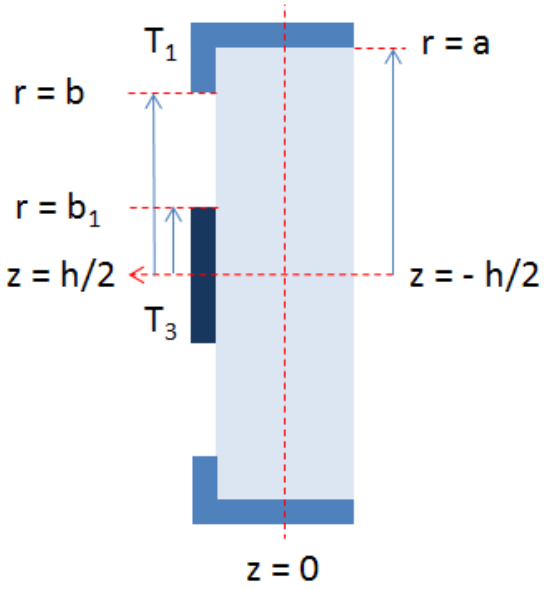

Figure 3.5: TCS with one ring heater, one disk heater and space to freely exchange heat with the environment at temperature $T_0 = 300K$ - fixed temperature T_3 in a central circular section of radius b_1, fixed temperature T_1 in an external ring of internal radius b and fixed temperature, equal to T_1, on the mirror edges.

as $T_1 + \tau(r, z)$, where $\tau(r, z)$ is the excess of temperature with respect to the known constant temperature T_1, as expressed in equation (3.4). By assuming that the linearization condition, $T_1 >> \tau$, is satisfied, the boundary condition for the heat flow, through the mirror surface in $z = -h/2$, is again:

$$-K\tau_{,z}|_{-h/2} = -4\sigma {T_1}^3 \tau(r, -h/2) - \sigma \left({T_1}^4 - {T_0}^4\right) H_a(r) + \epsilon I(r). \tag{3.88}$$

It is worth stressing that all the quantities in the previous equation have been already introduced, in the previous sections, and they keep the same meaning. The mathematical analysis of the considered TCS is carried on, as customary, by expressing the functions in equation (3.88) in terms of a Bessel function base, it is then obtained:

$$-K\left(\frac{-k_n A_n}{a}\mathrm{e}^{\frac{k_n h}{2a}}+\frac{k_n B_n}{a}\mathrm{e}^{-\frac{k_n h}{2a}}\right)=-4\sigma T_1^3\left(A_n\mathrm{e}^{\frac{k_n h}{2a}}+B_n\mathrm{e}^{-\frac{k_n h}{2a}}\right)+$$
$$-\frac{2\sigma\left({T_1}^4-{T_0}^4\right)}{J_1(k_n)k_n}+\frac{\epsilon P\mathrm{e}^{-\frac{k_n^2 w^2}{8a^2}}}{a^2\pi J_1^2(k_n)} \tag{3.89}$$

In the rear side of the mirror, the temperature is given by $T_1+\tau(r,h/2)$. The following relation must hold:

$$T_1+\tau(r,h/2)=T_1+\theta_1 H_1(r)+\theta_2(r)+\theta_3 H_3(r), \tag{3.90}$$

where:

$$H_1(r)=\begin{cases}0 & \text{if } r<b\\ 1 & \text{if } b\le r\le a\end{cases}, \tag{3.91}$$

$$H_3(r)=\begin{cases}0 & \text{if } r>b_1\\ 1 & \text{if } 0\le r\le b_1\end{cases}, \tag{3.92}$$

$$\theta_2(r)=\begin{cases}0 & \text{if } r\notin[b_1,b]\\ \theta_2(r) & \text{if } b_1\le r\le b\end{cases}. \tag{3.93}$$

θ_1 and θ_3 are constant quantities depending on the temperatures imposed on the rear side of the cavity mirror, in the two regions $b\le r\le a$ and $0\le r\le b_1$ respectively. In particular, as it is shown in figure 3.5, by considering T_1 as reference temperature, it is: $\theta_1\equiv 0$, while $\theta_3=T_3-T_1$, hence, because of the linearization condition $T_1>>\tau$, it must be $|\theta_3|<<T_1$. As far as $\theta_2(r)$ is concerned, this is an unknown function of r, giving the difference between the temperature on the mirror back side, in the region $b_1\le r\le b$, and the reference mirror temperature T_1 (figure 3.5). By developing the functions in equation (3.90) in terms of a Bessel function base, for the coefficients of the excess of temperature in the back side of the cavity mirror, it is found:

$$A_n e^{(\frac{-k_n h}{2a})}+B_n e^{(\frac{k_n h}{2a})}=\theta_{2,n}+\theta_3 H_{3,n}, \tag{3.94}$$

In agreement with equation (3.13), $H_{3,n}$ is defined by the following relations:

$$\begin{aligned} H_3(r) &= \textstyle\sum_{n=1}^{\infty} H_{3,n} J_0(k_n \frac{r}{a}), \\ H_{3,n} &= \frac{2b_1 J_1\left(k_n \frac{b_1}{a}\right)}{a k_n J_1^2(k_n)}; \end{aligned} \tag{3.95}$$

while $\theta_{2,n}$ are the unknown coefficients of the following development:

$$\theta_2(r) = \sum_{n=1}^{\infty} \theta_{2,n} J_0(k_n \frac{r}{a}). \tag{3.96}$$

For the sake of completeness, it is also worth pointing out that, as far as the function $H_1(r)$ is concerned, in terms of Fourier-Bessel series, it is:

$$\begin{aligned} H_1(r) &= \textstyle\sum_{n=1}^{\infty} H_{1,n} J_0(k_n \frac{r}{a}), \\ H_{1,n} &= \frac{2\left(aJ_1(k_n) - bJ_1\left(\frac{bk_n}{a}\right)\right)}{a k_n J_1^2(k_n)}. \end{aligned} \tag{3.97}$$

By using the development on a Bessel function base, the boundary condition in $z = h/2$ has the form:

$$-K\left(\frac{-k_n A_n}{a} \mathrm{e}^{-\frac{k_n h}{2a}} + \frac{k_n B_n}{a} \mathrm{e}^{\frac{k_n h}{2a}}\right) = \phi_{1,n} + \phi_{2,n} + \phi_{3,n}, \tag{3.98}$$

where the coefficients $\phi_{1,n}$, $\phi_{3,n}$ are unknown quantities, as they describe the heat flows, in the regions of the mirror $b \leq r \leq a$ and $0 \leq r \leq b_1$, which are unknown. As far as the coefficients $\phi_{2,n}$ are concerned, they are known as function of $\theta_{2,n}$, because the heat flow, in the mirror region $b_1 \leq r \leq b$, is:

$$\phi_{2,n} = 4\sigma T_1^3 \theta_{2,n} + \sigma\left({T_1}^4 - {T_0}^4\right) H_{2,n}, \tag{3.99}$$

with:

$$H_2(r) = \begin{cases} 0 & \text{if } r < b_1 \cup r > b \\ 1 & \text{if } b_1 \leq r \leq b \end{cases} \tag{3.100}$$

so that:

$$\begin{aligned} H_2(r) &= \textstyle\sum_{n=1}^{\infty} H_{2,n} J_0(k_n \frac{r}{a}), \\ H_{2,n} &= \frac{2\left[bJ_1\left(k_n \frac{b}{a}\right) - b_1 J_1\left(k_n \frac{b_1}{a}\right)\right]}{a k_n J_1^2(k_n)}. \end{aligned} \tag{3.101}$$

There are three equations (3.89), (3.94), (3.98) in five unknown quantities: A_n, B_n, $\theta_{2,n}$, $\phi_{1,n}$, $\phi_{3,n}$ and the coefficients A_n and B_n are required in order to describe the temperature field on the mirrors. To determine them, the solutions of the three equations is obtained for A_n, B_n, $\theta_{2,n}$ as functions of $\phi_{1,n}$, $\phi_{3,n}$ and these quantities become parameters that can be evaluated with a similar procedure adopted in section (3.2.4). In particular, for A_n, B_n and $\theta_{2,n}$, it is:

$$
\begin{aligned}
A_n = {} & \frac{e^{\frac{3hk_n}{2a}}\left(4a\sigma T_1^3+Kk_n\right)\left(\frac{P\epsilon e^{-\frac{w^2k_n^2}{8a^2}}}{\pi}+\frac{2a^2\sigma\left(T_0^4-T_1^4\right)J_1(k_n)}{k_n}\right)}{aJ_1(k_n)^2\left(e^{\frac{2hk_n}{a}}\left(4a\sigma T_1^3+Kk_n\right)^2-\left(Kk_n-4a\sigma T_1^3\right)^2\right)}+ \\
& \frac{2\sigma e^{\frac{hk_n}{2a}}\left(b\left(T_1^4-T_0^4\right)J_1\left(\frac{bk_n}{a}\right)+b_1\left(T_0^4+T_1^3(3T_1-4T_3)\right)J_1\left(\frac{b_1k_n}{a}\right)\right)\left(4a\sigma T_1^3-Kk_n\right)}{k_nJ_1(k_n)^2\left(e^{\frac{2hk_n}{a}}\left(4a\sigma T_1^3+Kk_n\right)^2-\left(Kk_n-4a\sigma T_1^3\right)^2\right)}+ \\
& \frac{ae^{\frac{hk_n}{2a}}\left(4a\sigma T_1^3-Kk_n\right)}{e^{\frac{2hk_n}{a}}\left(4a\sigma T_1^3+Kk_n\right)^2-\left(Kk_n-4a\sigma T_1^3\right)^2}\phi_{3,n}+\frac{ae^{\frac{hk_n}{2a}}\left(4a\sigma T_1^3-Kk_n\right)}{e^{\frac{2hk_n}{a}}\left(4a\sigma T_1^3+Kk_n\right)^2-\left(Kk_n-4a\sigma T_1^3\right)^2}\phi_{1,n},
\end{aligned}
\tag{3.102}
$$

$$
\begin{aligned}
B_n = {} & \frac{ae^{\frac{hk_n}{2a}}\left(-\frac{e^{\frac{2hk_n}{a}}\left(\frac{Kk_n}{a}+4\sigma T_1^3\right)\left(4a\sigma T_1^3+Kk_n\right)\left(\frac{P\epsilon e^{-\frac{w^2k_n^2}{8a^2}}}{\pi}+\frac{2a^2\sigma\left(T_0^4-T_1^4\right)J_1(k_n)}{k_n}\right)}{aJ_1(k_n)^2\left(e^{\frac{2hk_n}{a}}\left(4a\sigma T_1^3+Kk_n\right)^2-\left(Kk_n-4a\sigma T_1^3\right)^2\right)}+\frac{P\epsilon e^{-\frac{w^2k_n^2}{8a^2}}}{\pi a^2J_1(k_n)^2}+\frac{2\sigma\left(T_0^4-T_1^4\right)}{k_nJ_1(k_n)}\right)}{4a\sigma T_1^3-Kk_n}- \\
& -\frac{a^2e^{\frac{3hk_n}{2a}}\left(\frac{Kk_n}{a}+4\sigma T_1^3\right)}{e^{\frac{2hk_n}{a}}\left(4a\sigma T_1^3+Kk_n\right)^2-\left(Kk_n-4a\sigma T_1^3\right)^2}\phi_{3,n}-\frac{a^2e^{\frac{3hk_n}{2a}}\left(\frac{Kk_n}{a}+4\sigma T_1^3\right)}{e^{\frac{2hk_n}{a}}\left(4a\sigma T_1^3+Kk_n\right)^2-\left(Kk_n-4a\sigma T_1^3\right)^2}\phi_{1,n}- \\
& -\frac{2a\sigma e^{\frac{3hk_n}{2a}}\left(b\left(T_1^4-T_0^4\right)J_1\left(\frac{bk_n}{a}\right)+b_1\left(T_0^4+T_1^3(3T_1-4T_3)\right)J_1\left(\frac{b_1k_n}{a}\right)\right)\left(\frac{Kk_n}{a}+4\sigma T_1^3\right)}{k_nJ_1(k_n)^2\left(e^{\frac{2hk_n}{a}}\left(4a\sigma T_1^3+Kk_n\right)^2-\left(Kk_n-4a\sigma T_1^3\right)^2\right)},
\end{aligned}
\tag{3.103}
$$

$$\theta_{2,n} = \frac{e^{\frac{hk_n}{a}}\left(P\epsilon k_n e^{-\frac{w^2k_n^2}{8a^2}} + 2\pi a^2\sigma\left(T_0^4 - T_1^4\right)J_1(k_n)\right)}{\pi a k_n J_1(k_n)^2\left(4a\sigma T_1^3 - Kk_n\right)} + \frac{e^{\frac{hk_n}{a}}\left(4a\sigma T_1^3 + Kk_n\right)\left(\frac{e^{\frac{2hk_n}{a}}\left(4a\sigma T_1^3 + Kk_n\right)}{Kk_n - 4a\sigma T_1^3} + 1\right)\left(\frac{P\epsilon e^{-\frac{w^2k_n^2}{8a^2}}}{\pi} + \frac{2a^2\sigma\left(T_0^4 - T_1^4\right)J_1(k_n)}{k_n}\right)}{aJ_1(k_n)^2\left(e^{\frac{2hk_n}{a}}\left(4a\sigma T_1^3 + Kk_n\right)^2 - \left(Kk_n - 4a\sigma T_1^3\right)^2\right)} + \frac{2\sigma\left(b\left(T_1^4 - T_0^4\right)J_1\left(\frac{bk_n}{a}\right) + b_1\left(T_0^4 + T_1^3(3T_1 - 4T_3)\right)J_1\left(\frac{b_1k_n}{a}\right)\right)\left(4a\sigma T_1^3 - Kk_n\right)\left(\frac{e^{\frac{2hk_n}{a}}\left(4a\sigma T_1^3 + Kk_n\right)}{Kk_n - 4a\sigma T_1^3} + 1\right)}{k_n J_1(k_n)^2\left(e^{\frac{2hk_n}{a}}\left(4a\sigma T_1^3 + Kk_n\right)^2 - \left(Kk_n - 4a\sigma T_1^3\right)^2\right)} + \frac{2b_1(T_1 - T_3)J_1\left(\frac{b_1k_n}{a}\right)}{ak_nJ_1(k_n)^2} + \frac{a\left(4a\sigma T_1^3 - Kk_n\right)\left(\frac{e^{\frac{2hk_n}{a}}\left(4a\sigma T_1^3 + Kk_n\right)}{Kk_n - 4a\sigma T_1^3} + 1\right)}{e^{\frac{2hk_n}{a}}\left(4a\sigma T_1^3 + Kk_n\right)^2 - \left(Kk_n - 4a\sigma T_1^3\right)^2}\phi_{3,n} + \frac{a\left(4a\sigma T_1^3 - Kk_n\right)\left(\frac{e^{\frac{2hk_n}{a}}\left(4a\sigma T_1^3 + Kk_n\right)}{Kk_n - 4a\sigma T_1^3} + 1\right)}{e^{\frac{2hk_n}{a}}\left(4a\sigma T_1^3 + Kk_n\right)^2 - \left(Kk_n - 4a\sigma T_1^3\right)^2}\phi_{1,n}. \tag{3.104}$$

As it is possible to see from equations (3.102) and (3.103), the functional form of A_n and B_n with respect to $\phi_{1,n}$ and $\phi_{3,n}$ is:

$$\begin{aligned} A_n &= \alpha_n + \beta_{1,n}\phi_{1,n} + \beta_{3,n}\phi_{3,n}\ , \\ B_n &= \gamma_n + \delta_{1,n}\phi_{1,n} + \delta_{3,n}\phi_{3,n}\ , \end{aligned} \tag{3.105}$$

with $\beta_{1,n} = \beta_{3,n}$ and $\delta_{1,n} = \delta_{3,n}$, which are known coefficients. To the purpose of finding the value of $\phi_{1,n}$ and $\phi_{3,n}$, which will allow to determine A_n and B_n, i.e. the mirror temperature field, a mathematical procedure analogous to the one adopted in section (3.2.4) will be considered. In the following paragraphs, the implemented method to continue the analysis of the currently studied TCS will be presented.

Firstly, both of the two mirror regions delimited by the radii $b \leq r \leq a$ and $0 \leq r \leq b_1$, in the mirror rear side, are mathematically divided in M equal parts and in each part it is imposed that the average of the excess of temperature is equal to θ_1 and θ_3, respectively; i.e. :

$$\theta_{1,p} = \frac{M}{a-b}\int_{b+\frac{a-b}{M}(p)}^{b+\frac{a-b}{M}(p+1)} \tau(r, h/2)\mathrm{d}r, \tag{3.106}$$

$$\theta_{3,p} = \frac{M}{b_1} \int_{\frac{b_1}{M}p}^{\frac{b_1}{M}(p+1)} \tau(r, h/2)\mathrm{d}r, \tag{3.107}$$

where $p = 0, ..., M-1$, whilst $\theta_{1,p}$ and $\theta_{3,p}$ are two column vectors of M rows with constant elements equal to θ_1 and θ_3, respectively. If A_n and B_n are written in terms of equations 3.105, it is obtained:

$$\begin{array}{l} \theta_{1,p} = \frac{M}{a-b} \int_{b+\frac{a-b}{M}(p)}^{b+\frac{a-b}{M}(p+1)} \tau(r, h/2)\mathrm{d}r = \\ \frac{M}{a-b} \int_{b+\frac{a-b}{M}(p)}^{b+\frac{a-b}{M}(p+1)} \sum_{n=1}^{\infty} \left(A_n e^{\frac{-hk_n}{2a}} + B_n e^{\frac{hk_n}{2a}} \right) J_0(k_n \frac{r}{a})\mathrm{d}r = \\ \frac{M}{a-b} \int_{b+\frac{a-b}{M}(p)}^{b+\frac{a-b}{M}(p+1)} \sum_{n=1}^{\infty} \left(\alpha_n e^{-\frac{hk_n}{2a}} + \gamma_n e^{\frac{hk_n}{2a}} \right) J_0(k_n \frac{r}{a})\mathrm{d}r + \\ \frac{M}{a-b} \int_{b+\frac{a-b}{M}(p)}^{b+\frac{a-b}{M}(p+1)} \sum_{n=1}^{\infty} \left(\beta_{1,n} e^{-\frac{hk_n}{2a}} + \delta_{1,n} e^{\frac{hk_n}{2a}} \right) \phi_{1,n} J_0(k_n \frac{r}{a})\mathrm{d}r + \\ \frac{M}{a-b} \int_{b+\frac{a-b}{M}(p)}^{b+\frac{a-b}{M}(p+1)} \sum_{n=1}^{\infty} \left(\beta_{3,n} e^{-\frac{hk_n}{2a}} + \delta_{3,n} e^{\frac{hk_n}{2a}} \right) \phi_{3,n} J_0(k_n \frac{r}{a})\mathrm{d}r, \end{array} \tag{3.108}$$

it is possible to define:

$$J_{0,n}^{p,1} = \frac{M}{a-b} \int_{b+\frac{a-b}{M}(p)}^{b+\frac{a-b}{M}(p+1)} J_0 \left(k_n \frac{r}{a} \right) \mathrm{d}r, \tag{3.109}$$

then:

$$\begin{array}{l} \theta_{1,p} = \sum_{n=1}^{\infty} \left(\alpha_n e^{-\frac{hk_n}{2a}} + \gamma_n e^{\frac{hk_n}{2a}} \right) J_{0,n}^{p,1} + \\ + \left(\beta_{1,n} e^{-\frac{hk_n}{2a}} + \delta_{1,n} e^{\frac{hk_n}{2a}} \right) \phi_{1,n} J_{0,n}^{p,1} + \left(\beta_{3,n} e^{-\frac{hk_n}{2a}} + \delta_{3,n} e^{\frac{hk_n}{2a}} \right) \phi_{3,n} J_{0,n}^{p,1}. \end{array} \tag{3.110}$$

With analogy to what has been done in section (3.2.4), $\phi_{1,n}$ $\phi_{3,n}$ have the same form of $\phi_{>n}$, i.e.:

$$\phi_{1,n} = \sum_{m=0}^{M-1} \phi_{1,m} H_{1,m}^n, \tag{3.111}$$

$$\phi_{3,n} = \sum_{m=0}^{M-1} \phi_{3,m} H_{3,m}^n, \tag{3.112}$$

where:

$$H_{1,m}(r) = \begin{cases} 1 & \text{if } b + \frac{(a-b)(m)}{M} < r < b + \left(\frac{(a-b)(m+1)}{M} \right) \\ 0 & \text{if } r \text{ is outside } \left[b + \frac{(a-b)(m)}{M}, b + \frac{(a-b)(m+1)}{M} \right] \end{cases} \tag{3.113}$$

$$H_{3,m}(r) = \begin{cases} 1 & \text{if } \frac{b_1 m}{M} \leq r \leq \left(\frac{b_1(m+1)}{M} \right) \\ 0 & \text{if } r \text{ is outside } \left[\frac{b_1 m}{M}, \frac{b_1(m+1)}{M} \right] \end{cases} \tag{3.114}$$

$m = 0, ...M-1$. In terms of Fourier-Bessel series, $H_{1,m}(r)$ and $H_{3,m}(r)$ become:

$$H_{1,m}(r) = \sum_{n=1}^{\infty} H_{1,m}^{n} J_0\left(\frac{k_n r}{a}\right), \tag{3.115}$$

$$H_{3,m}(r) = \sum_{n=1}^{\infty} H_{3,m}^{n} J_0\left(\frac{k_n r}{a}\right), \tag{3.116}$$

with $H_{1,m}^{n}$ and $H_{3,m}^{n}$ the coefficients of the series, which are found by using relation (3.13). Hence, equation (3.110) becomes:

$$\begin{array}{l} \theta_{1,p} = \sum_{n=1}^{\infty}\left(\alpha_n e^{-\frac{hk_n}{2a}} + \gamma_n e^{\frac{hk_n}{2a}}\right) J_{0,n}^{p,1} + \\ \sum_{m=0}^{m=M-1}\sum_{n=1}^{\infty}\left(\beta_{1,n} e^{-\frac{hk_n}{2a}} + \delta_{1,n} e^{\frac{hk_n}{2a}}\right)\phi_{1,m} H_{1,m}^{n} J_{0,n}^{p,1} + \\ \sum_{m=0}^{m=M-1}\sum_{n=1}^{\infty}\left(\beta_{3,n} e^{-\frac{hk_n}{2a}} + \delta_{3,n} e^{\frac{hk_n}{2a}}\right)\phi_{3,m} H_{3,m}^{n} J_{0,n}^{p,1} = \\ D_{1,p} + \sum_{m=0}^{m=M-1}\phi_{1,m} E_{1m,p}^{1} + \sum_{m=0}^{m=M-1}\phi_{3,m} E_{3m,p}^{1}, \end{array} \tag{3.117}$$

where it has been set:

$$D_{1,p} = \sum_{n=1}^{\infty}\left(\alpha_n e^{-\frac{hk_n}{2a}} + \gamma_n e^{\frac{hk_n}{2a}}\right) J_{0,n}^{p,1}, \tag{3.118}$$

$$E_{1m,p}^{1} = \sum_{n=1}^{\infty}\left(\beta_{1,n} e^{-\frac{hk_n}{2a}} + \delta_{1,n} e^{\frac{hk_n}{2a}}\right) H_{1,m}^{n} J_{0,n}^{p,1}, \tag{3.119}$$

$$E_{3m,p}^{1} = \sum_{n=1}^{\infty}\left(\beta_{3,n} e^{-\frac{hk_n}{2a}} + \delta_{3,n} e^{\frac{hk_n}{2a}}\right)\phi_{3,m} H_{3,m}^{n} J_{0,n}^{p,1}. \tag{3.120}$$

The last equality, in equation (3.117), can be written in term of matrix as follows:

$$M_{m,p}^{1,1}\phi_{1,m} + M_{m,p}^{1,3}\phi_{3,m} = \theta_{1,p} - D_{1,p}, \tag{3.121}$$

with:

$$M_{m,p}^{1,1} = E_{1m,p}^{1}, \qquad M_{m,p}^{1,3} = E_{3m,p}^{1}. \tag{3.122}$$

If the same procedure is applied also for equation (3.107), another matrix equation is obtained, with the same shape of equation (3.121). In particular:

$$\theta_{3,p} = D_{3,p} + \sum_{m=0}^{m=M-1}\phi_{1,m} E_{1m,p}^{3} + \sum_{m=0}^{m=M-1}\phi_{3,m} E_{3m,p}^{3} \tag{3.123}$$

with:

$$D_{3,p} = \sum_{n=1}^{\infty} \left(\alpha_n e^{-\frac{hk_n}{2a}} + \gamma_n e^{\frac{hk_n}{2a}} \right) J_{0,n}^{p,3}, \tag{3.124}$$

$$E_{1m,p}^{3} = \sum_{n=1}^{\infty} \left(\beta_{1,n} e^{-\frac{hk_n}{2a}} + \delta_{1,n} e^{\frac{hk_n}{2a}} \right) H_{1,m}^{n} J_{0,n}^{p,3}, \tag{3.125}$$

$$E_{3m,p}^{3} = \sum_{n=1}^{\infty} \left(\beta_{3,n} e^{-\frac{hk_n}{2a}} + \delta_{3,n} e^{\frac{hk_n}{2a}} \right) \phi_{3,m} H_{3,m}^{n} J_{0,n}^{p,3}. \tag{3.126}$$

and:

$$J_{0,n}^{p,3} = \frac{M}{b_1} \int_{\frac{b_1}{M}p}^{\frac{b_1}{M}(p+1)} J_0 \left(k_n \frac{r}{a} \right) \mathrm{d}r. \tag{3.127}$$

Eventually:

$$M_{m,p}^{3,1} \phi_{1,m} + M_{m,p}^{3,3} \phi_{3,m} = \theta_{3,p} - D_{3,p}, \tag{3.128}$$

$$M_{m,p}^{3,1} = E_{1m,p}^{3}, \qquad M_{m,p}^{1,3} = E_{3m,p}^{3}. \tag{3.129}$$

By using equation (3.121) and equation (3.128), the coefficients $\phi_{1,m}$ and $\phi_{3,m}$ can be found. Indeed, in analogy to section (3.2.4), the following system can be written:

$$M\phi = V, \tag{3.130}$$

where now it is:

$$M = \begin{pmatrix} M_{m,p}^{1,1} & M_{m,p}^{1,3} \\ M_{m,p}^{3,1} & M_{m,p}^{3,3} \end{pmatrix}, \tag{3.131}$$

$$\phi = \begin{pmatrix} \phi_{1,m} \\ \phi_{3,m} \end{pmatrix}, \tag{3.132}$$

$$V = \begin{pmatrix} \theta_{1,p} - D_{1,p} \\ \theta_{3,p} - D_{3,p} \end{pmatrix}. \tag{3.133}$$

By inverting matrix M, $\phi_{1,m}$ and $\phi_{3,m}$ are determined from the relation: $\phi = M^{-1}V$. After applying (3.111) and (3.112), $\phi_{1,n}$ and $\phi_{3,n}$ are also calculated. So, A_n and B_n result to be

determined, and the mirror temperature field is now known. It is worth remarking that the quantity $J_{0,n}^{p,1}$ and $J_{0,n}^{p,3}$ can be calculated both with an approximation analogue to the one in equation (3.86), and in a numerical way, by using the MATLAB function *quad*, as it is shown in section (3.2.4). As the application of the two different methods does not give significant result differences, in what follows it is chosen to report only the results concerning the application of the formulas similar to equation (3.86), for $J_{0,n}^{p,1}$ and $J_{0,n}^{p,3}$.

3.2.6 Fixed temperature on the mirror edges, one external ring heater and central disk heater

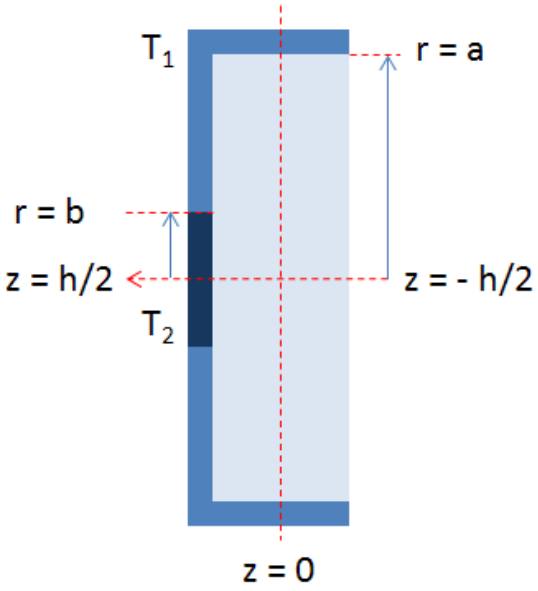

Figure 3.6: TCS with one ring heater and one disk heater - fixed temperature T_2 on a central circular section of radius b; fixed temperature T_1 in an external ring of internal radius b and external radius a; fixed temperature, equal to T_1, on the mirror edges. Environment at temperature $T_0 = 300K$.

The TCS configuration analyzed in this section aims to correct for the mirror distortions due to the coating absorption of optical power. It consists in warming up at a constant temperature T_2 the central part of the mirror, with a disk heater in its rear side, and the adjacent part with a ring heater fixing the mirror temperature at T_1. Furthermore the temperature is kept fixed at T_1 on the mirror edges as well. The TCS discussed here is illustrated in figure (3.6) to better clarify its principle. The mirror temperature field is again described as $T_1 + \tau(r, z)$, where T_1 is the fixed temperature, mentioned above, while $\tau(r, z)$ is the excess of temperature with respect

to T_1. In order to have the linearization condition verified, it has always to be $\tau << T_1$. In the mathematical formalism adopted in this work, as usual, it is:

$$\tau(r,z) = \sum_{n=1}^{\infty} \left(A_n \mathrm{e}^{-k_n \frac{z}{a}} + B_n \mathrm{e}^{k_n \frac{z}{a}} \right) J_0(k_n \frac{r}{a}). \tag{3.134}$$

with $k_n,\ n = 1,\ 2$ ... zeros of equation $J_0(k_n) = 0$. The coefficients A_n and B_n are determined, by using the equation of the boundary condition for the heat flow at the thermal equilibrium on the mirror face internal to the optical cavity (the face at $z = -h/2$) and the equation of the excess of temperature on the rear side of the mirror (the face at $z = h/2$). As far as the former equation is concerned, this is written as equation (3.22), where the linearization with respect to the temperature excess, τ, is considered. The latter equation is instead:

$$\tau(r, h/2) = \theta_1 H_{ab}(r) + \theta_2 H_b(r), \tag{3.135}$$

where θ_1 and θ_2 describe the temperature imposed on the rear side of the mirror. By considering T_1 as reference temperature, it is: $\theta_1 = T_1 - T_1 = 0$, $\theta_2 = T_2 - T_1$ and:

$$H_{ab}(r) = \begin{cases} 1 & \text{if } b \leq r \leq a \\ 0 & \text{if } r < b \cup r > a, \end{cases} \tag{3.136}$$

$$H_b(r) = \begin{cases} 1 & \text{if } 0 \leq r \leq b \\ 0 & \text{if } r > b \end{cases} . \tag{3.137}$$

In terms of Bessel function base, it is:

$$\begin{aligned} H_{ab}(r) &= \textstyle\sum_{n=1}^{n_{max}} H_{ab,n} J_0(k_n \frac{r}{a}), \\ H_{ab,n} &= \frac{2\left(aJ_1(k_n) - bJ_1\left(\frac{bk_n}{a}\right)\right)}{ak_n J_1(k_n)^2}, \end{aligned} \tag{3.138}$$

$$\begin{aligned} H_b(r) &= \textstyle\sum_{n=1}^{n_{max}} H_{b,n} J_0(k_n \frac{r}{a}), \\ H_{b,n} &= \frac{2bJ_1\left(\frac{bk_n}{a}\right)}{ak_n J_1(k_n)^2}, \end{aligned} \tag{3.139}$$

and from equation (3.135), it is obtained:

$$A_n \mathrm{e}^{-k_n \frac{h}{2a}} + B_n \mathrm{e}^{k_n \frac{h}{2a}} = \theta_1 H_{ab,n} + \theta_2 H_{b,n}. \tag{3.140}$$

By solving the system compounded of equation (3.22) and equation (3.140), the solutions for the coefficients A_n and B_n are found, and the mirror temperature field is now known. In particular:

$$A_n = -\frac{e^{\frac{hk_n}{2a}}\left(\frac{2\sigma\left(T_1^4-T_0^4\right)}{k_nJ_1(k_n)} - \frac{\epsilon Pe^{-\frac{w^2k_n^2}{8a^2}}}{\pi a^2 J_1(k_n)^2}\right) + \frac{2b(T_2-T_1)e^{-\frac{hk_n}{2a}}J_1\left(\frac{bk_n}{a}\right)\left(4\sigma T_1^3-\frac{Kk_n}{a}\right)}{ak_nJ_1(k_n)^2}}{e^{\frac{hk_n}{a}}\left(\frac{Kk_n}{a}+4\sigma T_1^3\right) - e^{-\frac{hk_n}{a}}\left(4\sigma T_1^3-\frac{Kk_n}{a}\right)} \tag{3.141}$$

$$B_n = \frac{e^{-\frac{hk_n}{a}}\left(e^{\frac{hk_n}{2a}}\left(\frac{2\sigma\left(T_1^4-T0^4\right)}{k_nJ_1(k_n)} - \frac{Pe\epsilon e^{-\frac{w^2k_n^2}{8a^2}}}{\pi a^2 J_1(k_n)^2}\right) + \frac{2b(T_2-T_1)e^{-\frac{hk_n}{2a}}J_1\left(\frac{bk_n}{a}\right)\left(4\sigma T_1^3-\frac{Kk_n}{a}\right)}{ak_nJ_1(k_n)^2}\right)}{e^{\frac{hk_n}{a}}\left(\frac{Kk_n}{a}+4\sigma T_1^3\right)-e^{-\frac{hk_n}{a}}\left(4\sigma T_1^3-\frac{Kk_n}{a}\right)} - \frac{2e^{-\frac{hk_n}{2a}}\left(bT_1J_1\left(\frac{bk_n}{a}\right)-bT_2J_1\left(\frac{bk_n}{a}\right)\right)}{ak_nJ_1(k_n)^2} \tag{3.142}$$

3.2.7 Fixed temperature on the mirror edges, three external ring heaters and central disk heater

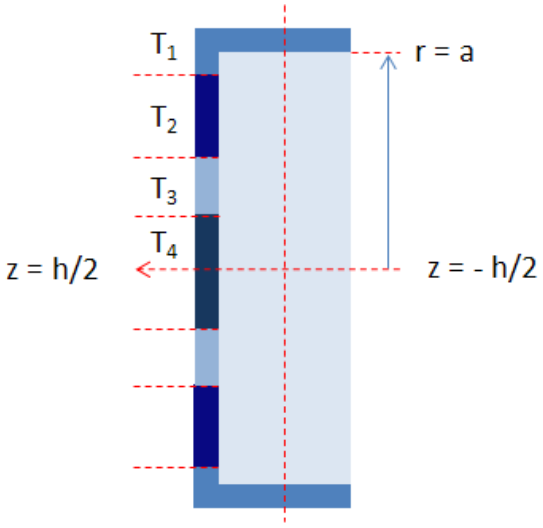

Figure 3.7: TCS with three ring heaters and one disk heater in the mirror rear side - Applied temperature field in the rear side of the mirror: fixed temperature T_4 in a central circular section of radius b_1; fixed temperature T_3 in the adjacent ring of internal radius b_1 and external radius b_2; fixed temperature T_2 an a ring of internal radius b_2 and external radius b_3; fixed temperature T_1 an a ring of internal radius b_3 and external radius a. Fixed temperature, equal to T_1, on the mirror edges. Environment at temperature $T_0 = 300K$.

The TCS studied in this section, similarly to the ones already considered, has the purpose

to correct for the cavity mirrors distortions due to the coating absorption of optical power. Its configuration is described in figure (3.7). From a mathematical point of view, this system is not so different with respect to the one considered in the previous section. Indeed, the mirror temperature field is always written as $T_1 + \tau(r,z)$, where $\tau(r,z)$ is the excess of temperature described as follows:

$$\tau = \sum_{n=1}^{\infty} \tau_n(z) J_0(k_n \frac{r}{a}), \quad \tau_n(z) = A_n \mathrm{e}^{-k_n \frac{z}{a}} + B_n \mathrm{e}^{k_n \frac{z}{a}} \tag{3.143}$$

with $k_n,\ n = 1,\ 2$ ... zeros of equation $J_0(k_n) = 0$. In order to determine the coefficients A_n and B_n, a system of two equations is required. One of these is equation (3.22), which gives the boundary condition for the heat flow on the mirror face at $z = -h/2$. The second equation is obtaining by imposing that the mirror temperature in $z = h/2$ is equal to the temperature field set up in the rear side of the mirror, i.e.:

$$T_1 + \tau(r, h/2) = T_1 + \theta_1 H_1(r) + \theta_2 H_2(r) + \theta_3 H_3(r) + \theta_4 H_4(r), \tag{3.144}$$

where:

$$H_1(r) = \begin{cases} 1 & \text{if } 0 \le r \le b_1 \\ 0 & \text{if } r > b_1 \end{cases}, \tag{3.145}$$

$$H_2(r) = \begin{cases} 1 & \text{if } b_1 \le r \le b_2 \\ 0 & \text{if } r < b_1 \cup r > b_2 \end{cases}, \tag{3.146}$$

$$H_3(r) = \begin{cases} 1 & \text{if } b_2 \le r \le b_3 \\ 0 & \text{if } r < b_2 \cup r > b_3 \end{cases}, \tag{3.147}$$

$$H_4(r) = \begin{cases} 1 & \text{if } b_3 \le r \le a \\ 0 & \text{if } r < b_3 \cup r > a \end{cases}, \tag{3.148}$$

and: $\theta_1 = T_4 - T_1$, $\theta_2 = T_3 - T_1$, $\theta_3 = T_2 - T_1$, $\theta_4 = T_1 - T_1 = 0$. After the development on Bessel function base, for the coefficients of the excess of temperature, in $z = h/2$, it is:

$$A_n \mathrm{e}^{-k_n \frac{h}{2a}} + B_n \mathrm{e}^{k_n \frac{h}{2a}} = \theta_1 H_{1,n} + \theta_2 H_{2,n} + \theta_3 H_{3,n}, \tag{3.149}$$

where $H_{1,n}$, $H_{2,n}$ and $H_{3,n}$ are the coefficients of the expansion on the Bessel function base for

the function: $H_1(r)$, $H_2(r)$ and $H_3(r)$. Hence, by using formulas (3.13):

$$H_{1,n} = \frac{2b_1 J_1\left(\frac{b_1 k_n}{a}\right)}{a k_n J_1\left(k_n\right)^2}, \tag{3.150}$$

$$H_{2,n} = \frac{2\left(a b_2 J_1\left(\frac{b_2 k_n}{a}\right) - a b_1 J_1\left(\frac{b_1 k_n}{a}\right)\right)}{a^2 k_n J_1\left(k_n\right)^2}, \tag{3.151}$$

$$H_{3,n} = \frac{2\left(a b_3 J_1\left(\frac{b_3 k_n}{a}\right) - a b_2 J_1\left(\frac{b_2 k_n}{a}\right)\right)}{a^2 k_n J_1\left(k_n\right)^2}. \tag{3.152}$$

The expression for the coefficients A_n and B_n are then obtained by solving the system made up of equation (3.22) and equation (3.149). It is found:

$$\begin{aligned} A_n = & -\frac{2(T_2-T_1)e^{-\frac{hk_n}{2a}}\left(ab_3J_1\left(\frac{b_3k_n}{a}\right)-ab_2J_1\left(\frac{b_2k_n}{a}\right)\right)\left(4\sigma T_1^3-\frac{Kk_n}{a}\right)}{a^2k_nJ_1(k_n)^2\left(e^{\frac{hk_n}{a}}\left(\frac{Kk_n}{a}+4\sigma T_1^3\right)-e^{-\frac{hk_n}{a}}\left(4\sigma T_1^3-\frac{Kk_n}{a}\right)\right)}+ \\ & \frac{e^{-\frac{hk_n}{2a}}\left(-\frac{2(T_3-T_1)\left(ab_2J_1\left(\frac{b_2k_n}{a}\right)-ab_1J_1\left(\frac{b_1k_n}{a}\right)\right)}{a^2k_nJ_1(k_n)^2}-\frac{2b_1(T_4-T_1)J_1\left(\frac{b_1k_n}{a}\right)}{ak_nJ_1(k_n)^2}\right)\left(4\sigma T_1^3-\frac{Kk_n}{a}\right)}{e^{\frac{hk_n}{a}}\left(\frac{Kk_n}{a}+4\sigma T_1^3\right)-e^{-\frac{hk_n}{a}}\left(4\sigma T_1^3-\frac{Kk_n}{a}\right)}- \\ & \frac{e^{\frac{hk_n}{2a}}\left(\frac{2\sigma\left(T_1^4-T_0^4\right)}{k_nJ_1(k_n)}-\frac{P\epsilon e^{-\frac{w^2k_n^2}{8a^2}}}{\pi a^2J_1(k_n)^2}\right)}{e^{\frac{hk_n}{a}}\left(\frac{Kk_n}{a}+4\sigma T_1^3\right)-e^{-\frac{hk_n}{a}}\left(4\sigma T_1^3-\frac{Kk_n}{a}\right)}, \end{aligned} \tag{3.153}$$

$$\begin{aligned} B_n = & -\frac{2(T_2-T_1)e^{-\frac{3hk_n}{2a}}\left(ab_3J_1\left(\frac{b_3k_n}{a}\right)-ab_2J_1\left(\frac{b_2k_n}{a}\right)\right)\left(4\sigma T_1^3-\frac{Kk_n}{a}\right)}{a^2k_nJ_1(k_n)^2\left(e^{\frac{hk_n}{a}}\left(\frac{Kk_n}{a}+4\sigma T_1^3\right)-e^{-\frac{hk_n}{a}}\left(4\sigma T_1^3-\frac{Kk_n}{a}\right)\right)}- \\ & \frac{e^{-\frac{3hk_n}{2a}}\left(-\frac{2(T_3-T_1)\left(ab_2J_1\left(\frac{b_2k_n}{a}\right)-ab_1J_1\left(\frac{b_1k_n}{a}\right)\right)}{a^2k_nJ_1(k_n)^2}-\frac{2b_1(T_4-T_1)J_1\left(\frac{b_1k_n}{a}\right)}{ak_nJ_1(k_n)^2}\right)\left(4\sigma T_1^3-\frac{Kk_n}{a}\right)}{e^{\frac{hk_n}{a}}\left(\frac{Kk_n}{a}+4\sigma T_1^3\right)-e^{-\frac{hk_n}{a}}\left(4\sigma T_1^3-\frac{Kk_n}{a}\right)}+ \\ & \frac{e^{-\frac{hk_n}{2a}}\left(\frac{2\sigma\left(T_1^4-T_0^4\right)}{k_nJ_1(k_n)}-\frac{\epsilon Pe^{-\frac{w^2k_n^2}{8a^2}}}{\pi a^2J_1(k_n)^2}\right)}{e^{\frac{hk_n}{a}}\left(\frac{Kk_n}{a}+4\sigma T_1^3\right)-e^{-\frac{hk_n}{a}}\left(4\sigma T_1^3-\frac{Kk_n}{a}\right)}- \\ & \frac{2e^{-\frac{hk_n}{2a}}\left(b_3T_1J_1\left(\frac{b_3k_n}{a}\right)+b_2T_2J_1\left(\frac{b_2k_n}{a}\right)-b_3T_2J_1\left(\frac{b_3k_n}{a}\right)+b_1T_3J_1\left(\frac{b_1k_n}{a}\right)-b_2T_3J_1\left(\frac{b_2k_n}{a}\right)-b_1T_4J_1\left(\frac{b_1k_n}{a}\right)\right)}{ak_nJ_1(k_n)^2}. \end{aligned} \tag{3.154}$$

3.3 Mathematical description of the mirror thermal deformations for the considered TCS

This section aims to present the mathematical description of the mirror surface distortions caused by the presence of a temperature field. To this purpose, the displacement vector, $\vec{u}$, is defined to describe the difference between the coordinates of a given mirror atom before and after the heating process [85]. It is observed that, as a cylindrical symmetry is assumed for the mirror, in cylindrical coordinates, the displacement vector has only two components $u_z(r,z)$ and $u_r(r,z)$. Once $\vec{u}$ is found, the mirror deformation is determined. The behavior of an isotropic material under given configurations of stress is predicted by the generalized Hooke law [85], [86], which, in the presence of a temperature field, $T = T(r,z)$, reads:

$$\Theta_{i,j} = \delta_{i,j}(\lambda E - \nu T) + 2\mu E_{i,j}, \tag{3.155}$$

where $\Theta_{i,j}$ and $E_{i,j}$ are the stress tensor and the strain tensor, respectively, ν is the stress temperature modulus, E the trace of the strain tensor, $\delta_{i,j}$ is the Kronecher tensor and λ, μ are the Lamé coefficients. As far as $\Theta_{i,j}$ and $E_{i,j}$ are concerned, they are connected to the displacement vector, $\vec{u}(r,z)$. Particularly, in cylindrical symmetry and in cylindrical coordinates, the strain tensor has the following four components:

$$E_{rr}(r,z) = \frac{\partial u_r}{\partial r}(r,z), \qquad E_{zz}(r,z) = \frac{\partial u_z}{\partial z}(r,z), \tag{3.156}$$

$$E_{\phi\phi}(r,z) = \frac{u_r(r,z)}{r}, \qquad E_{rz}(r,z) = \frac{1}{2}\left\{\frac{\partial u_r}{\partial z}(r,z) + \frac{\partial u_z(r,z)}{\partial r}\right\}, \tag{3.157}$$

and the stress tensor components are:

$$\begin{cases} \Theta_{rr} = -\nu T + \lambda E + 2\mu E_{rr} \\ \Theta_{\phi\phi} = -\nu T + \lambda E + 2\mu E_{\phi\phi} \\ \Theta_{zz} = -\nu T + \lambda E + 2\mu E_{zz} \\ \Theta_{rz} = +2\mu E_{rz} \end{cases}, \tag{3.158}$$

It is worth stressing that the temperature field, $T(r,z)$, entering the Hooke law is the variation of the mirror temperature with respect to a reference temperature, for which there is no deformation. Furthermore, in absence of external applied forces, the stress tensor must obey a

particular case of Navier-Cauchy equations, i.e. :

$$\begin{cases} \partial_r \Theta_{rr} + (\Theta_{rr} - \Theta_{\phi\phi})/r + \partial_z \Theta_{rz} = 0 \\ (\partial_r + 1/r)\Theta_{rz} + \partial_z \Theta_{zz} = 0 \end{cases} . \tag{3.159}$$

If there is not external application of pressures, the following boundary conditions have to be verified as well:

$$\Theta_{rr}(a, z) = 0, \quad \Theta_{rz}(a, z) = 0, \quad \Theta_{rz}(r, \pm h/2) = 0, \quad \Theta_{zz}(r, \pm h/2) = 0. \tag{3.160}$$

The notions introduced in this section are applied to determine the cavity mirror deformations associated to the TCS considered so far. In this respect, exactly the same mathematical solution for $\vec{u}$ will be used for the TCS described in sections (3.2.1), (3.2.2), (3.2.4), (3.2.5), (3.2.6) and (3.2.7), but, according to Ref. [71], for the TCS analyzed in section (3.2.3), another solution for the displacement vector is considered. However, it is possible to check that both the two solutions for $\vec{u}$ can be applied to describe the TCS analyzed in section (3.2.3). To show this point, a comparison between the results obtained with the two calculations methods is reported in appendix (C). For the sake of clearness, it is worth saying that the former solution, used for the TCS of sections (3.2.1), (3.2.2), (3.2.4), (3.2.5), (3.2.6) and (3.2.7), is addressed in what follows as *Displacement vector solution with zeros of the Bessel function of the first kind and first order*; while the latter solution, applied for the TCS of section (3.2.3), is indicated as *Displacement vector solution involving Dini equation (3.33).*

3.3.1 Displacement vector solution with zeros of the Bessel function of the first kind and first order

In this section, the displacement vector, $\vec{u}$, solution is reported, for the TCS studied in sections (3.2.1), (3.2.2), (3.2.4), (3.2.5), (3.2.6) and (3.2.7). In these cases, the cavity mirror temperature is written as $T_1 + \tau(r, z)$, where T_1 is a constant temperature imposed on the mirror and $\tau(r, z)$ is the excess of temperature with respect to T_1, with the same form as given in equation (3.4). If the environment temperature is T_0, it is possible to define it as the reference temperature for which the mirror does not present distortion. Then, for the TCS currently considered, the temperature field entering the generalized Hooke law, can be described as:

$$\tilde{T}(r, z) = \sum_{n=1}^{n_{max}} (A_n e^{-k_n \frac{z}{a}} + B_n e^{k_n \frac{z}{a}}) J_0 \left(k_n \frac{r}{a} \right) + (T_1 - T_0), \tag{3.161}$$

where the coefficients A_n and B_n depends on the particular TCS taken into account among the ones concerned. As it is possible to look for solutions of $\vec{u}$ which involve the zeros of the Bessel function J_1, it is convenient to decompose the field $\tilde{T}(r,z)$ in terms of a Dini series [66], [67], [68]:

$$T(r,z) = \sum_{m\geq 1} T_m(z) J_0\left(l_m \frac{r}{a}\right) + T_{m=0}, \tag{3.162}$$

where l_m are the zeros of the Dini equation:

$$l_m J_0^{'}(l_m) + c J_0(l_m) = 0; \tag{3.163}$$

with $c = 0$, so that l_m are actually the zeros of the function J_1. For a function, $f(y)$, the following development in terms of Dini series holds [66], [67]:

$$f(y) = \sum_{m=0}^{\infty} b_m J_0\left(\frac{l_m y}{a}\right), \tag{3.164}$$

with coefficients:

$$b_m = \frac{2l_m^2}{a^2(c^2+l_m^2)J_0^2(l_m)} \int_0^a J_0\left(\frac{l_m y}{a}\right) f(y) y dy. \tag{3.165}$$

Hence, for equation (3.162), it is obtained:

$$T_m(z) = \frac{2}{a^2 J_0^2(l_m)} \int_0^a \tilde{T}(r,z) J_0\left(l_m \frac{r}{a}\right) r \mathrm{d}r, \tag{3.166}$$

$$T_m(z) = \sum_{n=1}^{\infty} (A_n e^{-k_n \frac{z}{a}} + B_n e^{k_n \frac{z}{a}}) D_{m,n} + (T_1 - T_0) C_m, \tag{3.167}$$

$$D_{m,n} = \frac{2}{a^2 J_0^2(l_m)} \int_0^a J_0\left(l_m \frac{r}{a}\right) J_0\left(k_n \frac{r}{a}\right) r \mathrm{d}r, \tag{3.168}$$

$$C_m = \frac{2}{a^2} \int_0^a J_0\left(l_m \frac{r}{a}\right) r \mathrm{d}r, \tag{3.169}$$

$$\begin{aligned} &T_{m=0} = \tfrac{2}{a^2 J_0^2(l_m)} \textstyle\int_0^a \tilde{T}(r,z) r \mathrm{d}r = \\ &= (T_1 - T_0) + 2 \textstyle\sum_{n=1}^{\infty} (A_n e^{-k_n \frac{z}{a}} + B_n e^{k_n \frac{z}{a}}) \frac{J_1(k_n)}{k_n}. \end{aligned} \tag{3.170}$$

It must be observed that $C_m \equiv 0$, as it is $m \geq 1$. It is possible to look for a solution of equations

(3.159), in terms of displacement vector components, with the following form:

$$u_r(r,z) = \sum_{m=1}^{\infty} U_m^r(z) J_1(l_m r/a), \tag{3.171}$$

$$u_z(r,z) = \sum_{m=0}^{\infty} U_m^z(z) J_0(l_m r/a). \tag{3.172}$$

Then, the first of equations (3.159) reads:

$$-\mu a^2 U_m^r{}''(z) + a l_m(\lambda+\mu) U_m^z{}'(z) + (\lambda+2\mu) l_m^2 U_m^r(z) = a l_m \nu T_m(z), \tag{3.173}$$

and the second one:

$$a^2(\lambda+2\mu) U_m^z{}''(z) + a l_m(\lambda+\mu) U_m^r{}'(z) - \mu l_m^2 U_m^z(z) = a^2 \nu T_m'(z). \tag{3.174}$$

For $m \geq 1$ the previous two equations are solved by functions with the following form:

$$U_m^r(z) = (c_{1,m} + c_{3,m} z) e^{(l_m z/a)} + (c_{2,m} + c_{4,m} z) e^{-(l_m z/a)} + F_m^r(z) + H_m, \tag{3.175}$$

$$\begin{aligned} U_m^z(z) = \; & \left(-c_{1,m} - c_{3,m} z + c_{3,m} \tfrac{a(\mu+\lambda)}{l_m(\lambda+\mu)}\right) e^{(l_m z/a)} + \\ & + \left(c_{2,m} + c_{4,m} z + c_{4,m} \tfrac{a(\mu+\lambda)}{l_m(\lambda+\mu)}\right) e^{-(l_m z/a)} + F_m^z(z) \end{aligned} \tag{3.176}$$

where:

$$F_m^r(z) = \frac{\nu a l_m}{\lambda+2\mu} \sum_{n=1}^{n_{max}} \frac{A_n e^{-k_n z/a} + B_n e^{k_n z/a}}{l_m^2 - k_n^2} D_{m,n}, \tag{3.177}$$

$$F_m^z(z) = \frac{-\nu a}{\lambda+2\mu} \sum_{n=1}^{n_{max}} \frac{k_n(-A_n e^{-k_n z/a} + B_n e^{k_n z/a})}{l_m^2 - k_n^2} D_{m,n}, \tag{3.178}$$

$$H_m = \frac{\nu a}{l_m(\lambda+2\mu)} (T_1 - T_0) C_m \equiv 0. \tag{3.179}$$

For $m = 0$, i.e. $l_0 = 0$ (see Ref. [69]), the Navier-Cauchy equations give:

$$U_0^r{}''(z) = 0, \tag{3.180}$$

$$(\lambda+2\mu) U_0^z{}''(z) = \nu T_{m=0}'(z). \tag{3.181}$$

As $J_1(0) \equiv 0$, a possible solution of equation (3.180) is:

$$U_0^r = 0, \tag{3.182}$$

while a solution of equation (3.181) is:

$$U_0^z = c_5 + c_6 z + 2 \sum_{n=1}^{n_{max}} \frac{\left(-aA_n e^{-k_n z/a} + aB_n e^{k_n z/a}\right)}{k_n} \frac{J_1(k_n)}{k_n} \frac{\nu}{(\lambda + 2\mu)}. \tag{3.183}$$

In order to determine the coefficients entering the expressions of $U_m^z(z)$, $U_m^r(z)$, $U_0^z(z)$, conditions (3.160) are considered. In particular, $c_{1,m},\ c_{2,m}\ c_{3,m},\ c_{4,m},\ c_6$ are obtained by fixing the constrains $\Theta_{zz}(r, \pm h/2) = 0$ and $\Theta_{rz}(r, \pm h/2) = 0$, as follows:

$$\begin{cases} \Theta_{zz,m}(h/2) = 0 \\ \Theta_{zz,m}(-h/2) = 0 \\ \Theta_{rz,m}(-h/2) = 0 \\ \Theta_{rz,m}(h/2) = 0 \end{cases} \tag{3.184}$$

where:

$$\Theta_{zz,m}(r, z) = \frac{J_0(l_m r/a)}{a} \left(l_m \lambda U_m^r(z) - a\nu T_m(z) + a(\lambda + 2\mu) U_m^{z\,\prime}(z)\right), \tag{3.185}$$

$$\Theta_{rz,m}(r, z) = \mu \frac{J_1(l_m r/a)}{a} \left(-l_m U_m^z(z) + a U_m^{r\,\prime}(z)\right). \tag{3.186}$$

Moreover, from the expressions of U_m^z and U_m^r, for $m \geq 1$, it is:

$$\begin{aligned} \Theta_{rz,m}(z) = {} & 2\mu \left(\textstyle\sum_{n=1}^{n_{\max}} \frac{\nu A_n D_{\mathrm{mn}} k_n l_m e^{-\frac{z k_n}{a}}}{(\lambda+2\mu)(k_n^2 - l_m^2)} + \frac{\nu B_n D_{\mathrm{mn}} k_n l_m e^{\frac{z k_n}{a}}}{(\lambda+2\mu)(l_m^2 - k_n^2)} \right) + \\ & 2\mu \left(\frac{e^{-\frac{z l_m}{a}} \left(l_m (z c_{3,m} + c_{1,m}) e^{\frac{2 z l_m}{a}} - l_m (z c_{4,m} + c_{2,m}) \right)}{a} - \frac{\mu e^{-\frac{z l_m}{a}} \left(c_{3,m} e^{\frac{2 z l_m}{a}} + c_{4,m} \right)}{\lambda + \mu} \right), \end{aligned} \tag{3.187}$$

$$\Theta_{zz,m}(z) = \frac{\sum_{n=1}^{n_{\max}} \left(\frac{\nu A_n D_{\mathrm{mn}} e^{-\frac{zk_n}{a}} \left(\lambda k_n^2 + 2\mu k_n^2 - \lambda l_m^2\right)}{k_n^2 - l_m^2} + \frac{\nu B_n D_{\mathrm{mn}} e^{\frac{zk_n}{a}} \left(\lambda k_n^2 + 2\mu k_n^2 - \lambda l_m^2\right)}{k_n^2 - l_m^2} \right)}{\lambda + 2\mu} +$$

$$\frac{2\mu(\lambda+2\mu)c_{3,m}e^{\frac{zl_m}{a}}}{\lambda+\mu} - \frac{2\mu(\lambda+2\mu)c_{4,m}e^{-\frac{zl_m}{a}}}{\lambda+\mu} + \tag{3.188}$$

$$+ \frac{e^{-\frac{zl_m}{a}} \left(-2\mu l_m (z c_{3,m} + c_{1,m}) e^{\frac{2zl_m}{a}} - 2\mu l_m (z c_{4,m} + c_{2,m}) \right)}{a} - \nu T_m.$$

For $m = 0 \implies l_0 = 0$ and by using the definitions of U_0^z and U_0^r, it is found:

$$\Theta_{zz,0} = \text{constant} = c_6(\lambda + 2\mu) + (T_0 - T_1)\nu, \tag{3.189}$$

$$\Theta_{rz,0} = 0. \tag{3.190}$$

The complete expressions of $\Theta_{rz}(r, z)$ and $\Theta_{zz}(r, z)$ are:

$$\Theta_{zz}(r, z) = \sum_{m=0}^{m_{max}} J_0(l_m r/a)\Theta_{zz,m}(z), \tag{3.191}$$

$$\Theta_{rz}(r, z) = \sum_{m=1}^{m_{max}} J_1(l_m r/a)\Theta_{rz,m}(z). \tag{3.192}$$

Hence, it is possible to check that all the boundary conditions (3.160) are satisfied, but $\Theta_{rr}(a, z) = 0$. According to the Saint Venant principle (see Ref. [86]-[94]), a suitable term is then added to the displacement vector, in order to verify it. Indeed, the Saint Venant principle states that if a system of forces with null resultant and moment acts on a portion of a homogeneous, isotropic and elastic body, the effects of the system of forces are negligible, when considering points sufficiently distant from the region of application of the system of forces. The Saint-Venant correction added to the displacement vector reads:

$$\delta u_r(r, z) = \frac{\lambda + 2\mu}{2\mu(3\lambda + 2\mu)}(\omega_0 r + \omega_1 r z), \tag{3.193}$$

$$\delta u_z(r, z) = -\frac{\lambda}{\mu(3\lambda + 2\mu)}(\omega_0 z + \omega_1 z^2/2) - \frac{\lambda + 2\mu}{4\mu(3\lambda + 2\mu)}\omega_1 r^2, \tag{3.194}$$

where ω_0 and ω_1 are arbitrary constants, while λ and μ are the Lamè coefficients. These extra components of the displacement vector firstly satisfy the equilibrium equations, secondly have null stress components Θ_{rz} and Θ_{zz}, thirdly produce a radial edge stress:

$$\delta\Theta_{rr}(az) = \omega_0 + \omega_1 z. \tag{3.195}$$

The constants ω_1 and ω_0 are chosen in order to minimize the quadratic error:

$$Error(\omega_0, \omega_1) = \int_{-h/2}^{h/2} \left[\Theta_{rr}(a,z) + \omega_0 + \omega_1 z\right]^2 dz, \tag{3.196}$$

through the application of the classical mean-squares formulas, which allow to set to zero the mean force and the mean moment. It is then found:

$$\omega_0 = -\frac{1}{h}\int_{h/2}^{h/2} \Theta_{rr}(a,z)dz \tag{3.197}$$

$$\omega_1 = -\frac{12}{h^3}\int_{h/2}^{h/2} \Theta_{rr}(a,z)dz. \tag{3.198}$$

The expression of the $\Theta_{rr,m}$ components, for $m \geq 1$ and $m = 0$, which are used for the determination of ω_0 and ω_1, are:

$$\Theta_{rr,m} = \frac{J_0(l_m)\left(-a\nu\sum_{n=1}^{n_{\max}}\left(A_n D_{m,n} e^{-\frac{zk_n}{a}} + B_n D_{m,n} e^{\frac{zk_n}{a}}\right) + a\lambda F'_{z,m}(z)\right)}{a} +$$

$$\frac{J_0(l_m)\left(\frac{2\mu e^{\frac{zl_m}{a}}\left(a\lambda c_{3,m} + (\lambda+\mu) l_m\left(z c_{3,m} + c_{1,m}\right)\right) + 2\mu e^{-\frac{zl_m}{a}}\left((\lambda+\mu) l_m\left(z c_{4,m} + c_{2,m}\right) - a\lambda c_{4,m}\right)}{\lambda+\mu} + (\lambda+2\mu) l_m F_{r,m}(z)\right)}{a}, \tag{3.199}$$

$$\Theta_{rr,0} = -4\mu\nu\sum_{n=1}^{n_{\max}} \frac{J_1(k_n)\left(A_n e^{-\frac{zk_n}{a}} + B_n e^{\frac{zk_n}{a}}\right)}{(\lambda+2\mu)k_n} + c_6\lambda + \nu\left(T_0 - T_1\right). \tag{3.200}$$

The displacement vector components, by considering the Saint - Venant correction, will have the same form as given through equations (3.171), (3.172), (3.175), (3.176), (3.177), (3.178), (3.179), (3.182), (3.183), plus δu_r and δu_z, for the components along r and z, respectively. To determine c_5 and c_6, a system of two equations is applied. One equation is (3.189), which contains c_6, the second equation is obtained by imposing that the barycenter of the mirror does not moves

because of the deformation, indeed there are not external forces applied on the system, i.e. :

$$2\pi \int_{-h/2}^{h/2} dz \int_0^a u_z(r,z) r dr = 0. \tag{3.201}$$

The previous equation together with equation (3.189) allows to determine the values of c_5 and c_6, which are required to write the z component of the displacement vector for $m = 0$. It is interesting to notice that, as:

$$\int_0^a J_0\left(l_m r/a\right) r dr \equiv 0, \tag{3.202}$$

condition (3.201) becomes:

$$2\pi \int_{-h/2}^{h/2} dz \int_0^a (U_0^z(z) + \delta u_z) r dr = 0. \tag{3.203}$$

In conclusion, the application of conditions (3.184), (3.203) and (3.189) allows to determine all the coefficients entering the definition of the displacement vector components, hence the mirror distortion turns out to be completely described. In this respect, it is worth observing that the displacement vector is in general defined up to a constant value. In the previous calculations, this degree of freedom has been used to introduce condition (3.201).

3.3.2 Displacement vector solution involving the Dini equation (3.33)

The displacement vector solution for the TCS analyzed in section (3.2.3) will be now presented. As it has been already remarked, for this configuration, the calculations both for the temperature field and for the displacement vector have been completely accomplished in Ref. [71], hence here the main results will be reported. Firstly, it is observed that the temperature of the mirror is now $T_0+\tau(r,z)$, with T_0 the environment temperature and τ the excess of temperature with respect to it. There are no temperature fields applied on the mirror, hence the field of temperature entering the generalized Hooke law is exactly $\tau(r,z)$. It is worth recalling that, in this configuration, the coefficients of the temperature excess are described by equation (3.38) were ζ_n are solutions of equation (3.33), so that the complete expression for $\tau(r,z)$ is:

$$\tau(r,z) = \sum_{n=1}^{n_{max}} \tau_n(z) J_0(\zeta_n r/a). \tag{3.204}$$

A solution of the Navier-Cauchy equations (3.159) which satisfies all the boundary conditions (3.160), but $\Theta_{rr}(a,z)=0$, can be written as follows:

$$u_r(r,z)=\frac{\nu}{2(\lambda+\mu)}\frac{1}{r}\int_0^r \tau(r',z)r'dr', \tag{3.205}$$

$$u_z(r,z)=\frac{\nu}{2(\lambda+\mu)}\frac{1}{r}\left[\int_{-h/2}^z \tau(r,z')z'dz'+\Phi(r)\right], \tag{3.206}$$

with $\Phi(r)$ a function to be determined. Because of the expression of u_r and u_z, it results $\Theta_{zz}=0$, and:

$$\partial_r\Theta_{rr}+(\Theta_{rr}-\Theta_{\phi\phi})/r\equiv 0, \tag{3.207}$$

then equations (3.159) reads:

$$\begin{cases} \partial_z\Theta_{rz}=0 \\ (\partial_r+1/r)\Theta_{rz}=0 \end{cases}. \tag{3.208}$$

The function $\Phi(r)$ is determined, by demanding the validity of the second of the previous equations, hence:

$$\Phi(r)=-\int_0^r \frac{dr'}{r'}\int_0^{r'}\frac{\partial\tau}{\partial z}(r'',-h/2)r''dr''+C, \tag{3.209}$$

with C an arbitrary constant. It is now possible to verify that all the conditions (3.160) are satisfied, but $\Theta_{rr}(a,z)=0$, as it has been already stressed. In order to make valid also this last condition, the Saint -Venant correction is added, which is defined by equations (3.193), (3.194), (3.195), (3.196), (3.197), (3.198), with the expression of $\Theta_{rr}(a,z)$ as calculated by using equations (3.205) and (3.206). Eventually, a complete displacement vector solution, for the currently considered TCS, is written as:

$$u_r(r,z)=\alpha(1+\sigma_p)a\sum_{n=1}^{n_{max}}\frac{\tau_n(z)}{\zeta_n}J_1(\zeta_n r/a), \tag{3.210}$$

$$\delta u_r(r,z)=\frac{1-\sigma_p}{Y}(\omega_0+\omega_1 z)r, \tag{3.211}$$

$$\begin{aligned} u_z(r,z)=&\tfrac{\alpha(1+\sigma_p)\epsilon P}{2\pi K}\textstyle\sum_{n=1}^{n_{max}}\frac{p_n}{\zeta_n}\times \\ &\times\left[\tfrac{1}{d_{2,n}}+\left(\tfrac{\sinh(\zeta_n z/a)}{d_{1,n}}-\tfrac{\cosh(\zeta_n z/a)}{d_{2,n}}\right)J_0(\zeta_n r/a)\right], \end{aligned} \tag{3.212}$$

$$\delta u_z(r,z) = -\frac{2\sigma_p}{Y}\left(\omega_0 + \frac{1}{2}\omega_1 z\right) z - \frac{1-\sigma_p}{2Y}\omega_1 r^2, \tag{3.213}$$

where σ_p is the Poisson ratio, Y the Young modulus, α the expansion coefficient, and the following relations with the Lamè coefficients and the stress temperature modulus, ν, hold:

$$\lambda = \frac{Y\sigma_p}{(1+\sigma_p)(1-2\sigma_p)}, \quad \mu = \frac{Y}{2(1+\sigma_p)}, \quad \frac{\nu}{2(\lambda+\mu)} = \alpha(1+\sigma_p). \tag{3.214}$$

As far as the other quantities entering equations (3.210) and (3.212) are concerned, $d_{1,n}$, $d_{2,n}$ are:

$$\begin{aligned} d_{1,n} &= \zeta_n \sinh\gamma_n + \chi_e \cosh\gamma_n, \\ d_{2,n} &= \zeta_n \cosh\gamma_n + \chi_e \sinh\gamma_n, \\ \gamma_n &= \zeta_n h/2a, \end{aligned} \tag{3.215}$$

$\tau_n(z)$ are the same as given in equation (3.38), moreover the coefficient p_n, in equation (3.212), are calculated through relation (3.37), in section (3.2.3), then:

$$p_n = \frac{\zeta_n^2}{(\chi_e^2+\zeta_n^2)J_0^2(\zeta_n)} \exp\left(\frac{\zeta_n^2 w^2}{8a^2}\right) \tag{3.216}$$

w being the spot size of the laser beam. The remaining terms in equations (3.210) and (3.212) have been already introduced in section (3.2.3). In conclusion, it is worth to explicit the expressions for ω_0 and ω_1 as well, which are:

$$\omega_0 = \frac{\alpha Y \chi_e \epsilon P}{\pi K h} \sum_{n=1}^{n_{max}} p_n \frac{J_0(\zeta_n)}{\zeta_n^3} \frac{\sinh\gamma_n}{d_{1,n}}, \tag{3.217}$$

$$\omega_1 = -\frac{12\alpha Y \chi_e \epsilon a P}{\pi K h^3} \sum_{n=1}^{n_{max}} p_n \frac{J_0(\zeta_n)}{\zeta_n^4} \frac{\gamma_n \cosh\gamma_n - \sinh\gamma_n}{d_{2,n}}. \tag{3.218}$$

The cavity mirror deformation can now be completely described, by using the components of the displacement vector given in equations (3.210) - (3.213). However, how it has been pointed out in the previous section, the displacement vector is defined up to a constant value. For the $\vec{u}$ solution, which is given above, this constant value has been chosen in order to have the zero of the displacement vector on the mirror point $z = 0$ and $r = 0$, in analogy to the solution reported in Ref. [71].

3.4 TCS with mechanical constraints and temperature field

In this section, the possibility to correct for the mirror distortion through the application of suitable stresses on the mirror surfaces will be considered. The mathematical tools applied on the following calculations have already been introduced at the beginning of section (3.3), then they will be recalled, when it is necessary. For the sake of clearness, it is worth saying that the procedure adopted in the TCS descriptions below aims to obtain the components of the displacement vector, which solve the Navier-Cauchy equations (3.159) together with appropriated boundary conditions, in general different from equations (3.160), when a known temperature field is present on the mirror.

3.4.1 Thermal Compensation system through mechanical constraints and temperature field application on the cavity mirrors

The TCS presented in this section has the aim to analyze the possibility to correct the mirror distortion due to the coating absorption of optical power, by fixing the mirror borders and edges, as it is showed in picture (3.8). To the aim of writing the equations for determining the displacement vector, $\vec{u}$, of this TCS, firstly, a mirror temperature field has to be fixed. In what follows, it is assumed a mirror temperature field, $\tilde{T}$, as given in (3.161). It is worth to recall that, in this case, the environment temperature, T_0, is assumed as reference temperature, corresponding to the situation without mirror deformation. The next step consists in writing $\tilde{T}$ in terms of Dini series, as it has been done in section (3.3.1). Hence, all the relations from (3.162) to (3.170) are valid, for the current treatment. As it has been already seen, to describe the mirror distortion, the determination of the displacement vector components is required. To this purpose, the equations involved in the calculations are the Navier-Cauchy equation (3.159), with the boundary conditions appropriated to the TCS under study. The solution given in section (3.3.1), through equations (3.171), (3.172), (3.175)-(3.179), (3.182), (3.183) can be used also for the considered TCS. Hence:

$$u_r(r,z) = \sum_{m=1}^{\infty} U_m^r(z) J_1(l_m r/a), \tag{3.219}$$

$$u_z(r,z) = \sum_{m=0}^{\infty} U_m^z(z) J_0(l_m r/a). \tag{3.220}$$

where, for $m \geq 1$, it is:

$$U_m^r(z) = (c_{1,m} + c_{3,m}z)e^{(l_m z/a)} + (c_{2,m} + c_{4,m}z)e^{-(l_m z/a)} + F_m^r(z) + H_m, \tag{3.221}$$

$$\begin{aligned} U_m^z(z) = & \left(-c_{1,m} - c_{3,m}z + c_{3,m}\frac{a(\mu+\lambda)}{l_m(\lambda+\mu)}\right)e^{(l_m z/a)} + \\ & + \left(c_{2,m} + c_{4,m}z + c_{4,m}\frac{a(\mu+\lambda)}{l_m(\lambda+\mu)}\right)e^{-(l_m z/a)} + F_m^z(z) \end{aligned} \tag{3.222}$$

with:

$$F_m^r(z) = \frac{\nu a l_m}{\lambda + 2\mu}\sum_{n=1}^{\infty}\frac{A_n e^{-k_n z/a} + B_n e^{k_n z/a}}{l_m^2 - k_n^2}D_{m,n}, \tag{3.223}$$

$$F_m^z(z) = \frac{-\nu a}{\lambda + 2\mu}\sum_{n=1}^{\infty}\frac{k_n(-A_n e^{-k_n z/a} + B_n e^{k_n z/a})}{l_m^2 - k_n^2}D_{m,n}, \tag{3.224}$$

$$H_m = \frac{\nu a}{l_m(\lambda + 2\mu)}(T_1 - T_0)C_m \equiv 0; \tag{3.225}$$

and, for $m = 0$:

$$U_0^r = 0, \tag{3.226}$$

$$U_0^z = c_5 + c_6 z + 2\sum_{n=1}^{\infty}\frac{\left(-aA_n e^{-k_n z/a} + aB_n e^{k_n z/a}\right)}{k_n}\frac{J_1(k_n)}{k_n}\frac{\nu}{(\lambda + 2\mu)} \tag{3.227}$$

Nevertheless, the boundary conditions associated with the Navier-Cauchy equations are different with respect to the ones given in equation (3.160), as mechanical constrains are imposed on the mirror edges and borders. The configuration of the considered mechanical constrains is showed in figure (3.8). To describe it from a mathematical point of view, the following function of r is introduced:

$$f(r) = \begin{cases} 0 & r < a - d \\ 1 & r \geq a - d \end{cases} \tag{3.228}$$

where d is defined as in figure (3.8) and a is the mirror radius, as customary. In terms of Dini series, the function $f(r)$ becomes:

$$f(r) = \sum_{m=0}^{m_{max}} f_m J_0(l_m r/a), \tag{3.229}$$

with :

$$f_0 = \frac{2}{a^2}\int_{a-d}^{a} r dr, \tag{3.230}$$

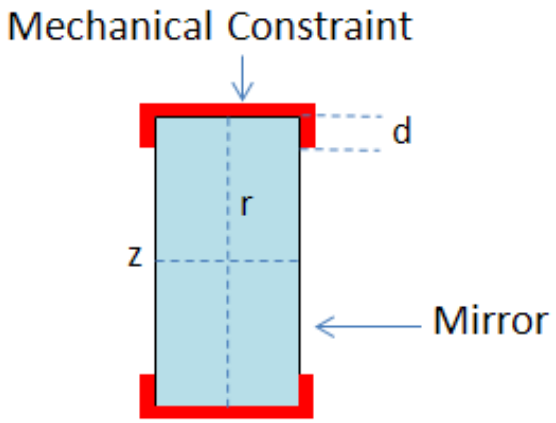

Figure 3.8: Description of the TCS analyzed in section (3.4.1). - Application of mechanical constraints on the mirror edges.

and for $m \geq 1$:

$$f_m = \frac{2}{a^2 J_0^2(l_m)} \int_{a-d}^{a} J_0(l_m r/a) r dr. \tag{3.231}$$

The boundary conditions on the stress tensor Θ_{ij} are now written as:

$$\begin{cases} \Theta_{zz,m}(h/2) = p_+ f_m \\ \Theta_{zz,m}(-h/2) = p_- f_m \\ \Theta_{rz,m}(-h/2) = 0 \\ \Theta_{rz,m}(h/2) = 0 \end{cases}, \tag{3.232}$$

where p_+ and p_- describe uniform stresses and $\Theta_{zz,m}$ and $\Theta_{rz,m}$ are completely defined through equations (3.185)-(3.192). It is worth recalling that, for $m = 0 \implies l_0 = 0$ and from the expressions of U_0^z and U_0^r, it is found:

$$\Theta_{zz,0} = \text{constant} = c_6(\lambda + 2\mu) + (T_0 - T_1)\nu; \tag{3.233}$$

$$\Theta_{rr,0} = 0. \tag{3.234}$$

To determine the components of the displacement vector, the expressions of the unknown quantities $c_{1,m}$, $c_{2,m}$, $c_{3,m}$, $c_{4,m}$, c_6, c_5, p_+ and p_- have to be found. With this aim, firstly, it is

observed that, because of the constance of $\Theta_{zz,0}$, the following relation has to be verified:

$$\Theta_{zz,0}(h/2) = \Theta_{zz,0}(-h/2) \implies p_+ = p_- = p. \tag{3.235}$$

The number of unknowns decreases, but still two equations are missing in order to solve the problem. However, it is possible to describe the constraints present for $a-d \leq r \leq a$, represented in picture (3.8), by introducing the following conditions:

$$\frac{1}{d(a-d)} \int_{a-d}^{a} u_z(r, -h/2) r dr = 0, \tag{3.236}$$

$$\frac{1}{d(a-d)} \int_{a-d}^{a} u_z(r, h/2) r dr = 0. \tag{3.237}$$

The previous two relations are equivalent to demand the cancellation of the average of the u_z component of the displacement vector, on both the mirror surfaces and on the region indicated by the integration in equations (3.236), (3.237). They approximate the condition of null displacement vector for $a - d \leq r \leq a$, on the surfaces internal and external to the optical cavity, showed in picture (3.8). Hence, equations (3.236) and (3.237) are used together with the boundary conditions (3.232) for determining the constants $c_{1,m},\ c_{2,m},\ c_{3,m},\ c_{4,m}, c_5,\ c_6$. Indeed, by considering the conditions on $\Theta_{rz,m}$ and $\Theta_{zz,m}$ for $m \geq 1$, as given in (3.232), the coefficients $c_{1,m}\ c_{2,m}\ c_{3,m}\ c_{4,m}$ are written as functions of p. Once this is done, conditions (3.236), (3.237) and the relation:

$$c_6(\lambda + 2\mu) + (T_0 - T_1)\nu = p f_0, \tag{3.238}$$

are utilized as a system of equations for obtaining the values of $c_5,\ c_6$ and p. As p is now known, it is possible to calculate $c_{1,m}\ c_{2,m}\ c_{3,m}\ c_{4,m}$ and, from the numerical values of c_5 and c_6, also U_0^z can be evaluated. In conclusion, the displacement vector results to be completely known.

3.4.2 TCS with fixation of the cavity mirror edges and temperature field application

The TCS analyzed in this section concerns the application of fixation on the mirror edges, as it is showed in figure (3.9), when an external temperature field is also applied on the mirror. In particular, it is assumed a mirror temperature field, $\tilde{T}$, as given in equation (3.161).
From a mathematical and conceptual point of view, this compensation system is similar to the

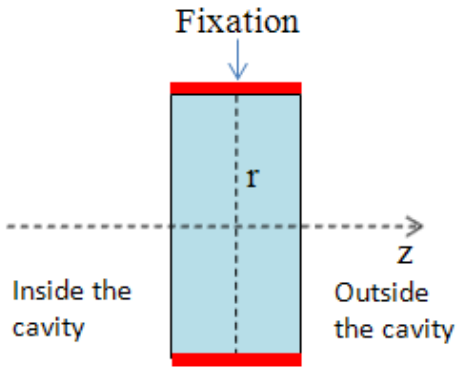

Figure 3.9: Scheme of the TCS studied in section (3.4.2). - A fixation is applied on the edges of the mirror, i.e. on its cylindrical surface, so that the displacement vector component along r is null. A temperature field is also applied on the mirror, hence its temperature is $T_1 + \tau(r, z)$

one analyzed in section (3.4.1), indeed, relations (3.171)-(3.183) are still valid. However, the coefficients $c_{1,m}$, $c_{2,m}$, $c_{3,m}$, $c_{4,m}$, c_5 and c_6, entering the displacement vector components, defined through equations (3.175), (3.176), (3.182) and (3.183), are different, because the conditions to impose in order to determine them are not the same as the ones in section (3.4.1). For the TCS currently under analysis, the boundary conditions on the components Θ_{zz} and Θ_{rr} of the stress tensor, after the development in terms of Dini series, are:

$$\begin{cases} \Theta_{zz,m}(h/2) = 0 \\ \Theta_{zz,m}(-h/2) = 0 \\ \Theta_{rz,m}(-h/2) = 0 \\ \Theta_{rz,m}(h/2) = 0 \end{cases} \tag{3.239}$$

Equations (3.239), for $m \geq 1$, are used to find $c_{1,m}$, $c_{2,m}$, $c_{3,m}$, $c_{4,m}$. As far as c_6 and c_5 are concerned, their determination is obtained, by defining a system of two further equations. One of theses equations is given by the boundary condition $\Theta_{zz,0}$, which reads:

$$c_6(\lambda + 2\mu) + (T_0 - T_1)\nu = 0. \tag{3.240}$$

Another equation is obtained by using the fact that the displacement vector is defined up to a constant vector. Indeed, it is chosen to set to zero the displacement vector $\vec{u} = (u_r(r, z), u_z(r, z))$ at the mirror point $z = -h/2$, $r = 0$, i.e. on the center of the reflecting surface. Mathematically,

from the equation for the z component of $\vec{u}$, it is obtained:

$$U_0^z(-h/2) + \sum_{m=0}^{\infty} U_m^z(-h/2) = 0. \tag{3.241}$$

It is pointed out that the same equation for the radial component of $\vec{u}$ gives the identity $0 = 0$. As equation (3.241) contains c_5 and c_6, the solution of a system compounded of both equation (3.240) and equation (3.241) allows to determine U_0^z, so that the displacement vector is now completely known.

3.4.3 TCS based on pressure applications on the mirror

The possibility of correcting the mirror deformation by opportunely applying a field of pressure on the mirror surfaces is now considered. With this aim, firstly, the mirror thermal condition will be defined. In particular, it is assumed that no external temperature field are implemented on the cavity mirror, so that its temperature is the one already considered in section (3.2.3). However, the results found in section (3.2.3) will be developed on the zeros of the first order Bessel function, J_1, to describe the mirror deformation and temperature with the same formalism. Indeed, the solution for $\vec{u}$ reported in section (3.3.2) cannot be used, when considering stress applications on the mirror surfaces, as it can be checked that the form of the displacement vector, given in section (3.3.2), leads to $\Theta_{zz} \equiv 0$. Consequently, as it has been already pointed out in the previous sections, solutions of the Navier-Cauchy equations (3.159) with the following form can be considered:

$$U_r(r, z) = \sum_{m\geq 1}^{\infty} U_{r,m}(z) J_1\left(\frac{l_m r}{a}\right), \tag{3.242}$$

$$U_z(r, z) = \sum_{m\geq 0}^{\infty} U_{z,m}(z) J_0\left(\frac{l_m r}{a}\right), \tag{3.243}$$

where a is the mirror radius, while l_m is the mth zero of the Dini equation:

$$yJ_0'(y) + cJ_0(y) = 0, \tag{3.244}$$

with c equal to zero. Then, as it has been already seen in section (3.3.1), l_m are, actually, the zeros of the Bessel function, J_1. Furthermore, the development described by equations (3.164), (3.165) holds, so that the temperature field solution given in equation (3.39) can be rewritten,

by using the zeros of J_1, as:

$$T(r,z) = T_0 + \tilde{\tau}(r,z), \tag{3.245}$$

with T_0 the constant environment temperature and $\tau(r,z)$ the excess of temperature, which now reads:

$$\tilde{\tau} = \sum_{m\geq 0}^{\infty} \tilde{\tau}_m(z) J_0\left(l_m \frac{r}{a}\right) \tag{3.246}$$

$$\tilde{\tau}_m(z) = \frac{2}{a^2 J_0^2(l_m)} \int_0^a J_0(l_m r/a)\tau(r,z) r dr. \tag{3.247}$$

It is stressed that $\tau(r,z)$ has the same form as given in equation (3.39), so that, it is possible to write equation (3.247) as:

$$\begin{aligned} &\tilde{\tau}_m(z) = \tfrac{2}{a^2 J_0^2(l_m)} \textstyle\int_0^a J_0(l_m r/a) \sum_{n=1}^{\infty} J_0(k_n r/a) \left(A_n \mathrm{e}^{-k_n \frac{z}{a}} + B_n \mathrm{e}^{k_n \frac{z}{a}}\right) r dr = \\ &= \textstyle\sum_{n=1}^{\infty} \left(A_n \mathrm{e}^{-k_n \frac{z}{a}} + B_n \mathrm{e}^{k_n \frac{z}{a}}\right) D_{m,n} \end{aligned} \tag{3.248}$$

with k_n zeros of the equation (3.33), and $D_{m,n}$ the same integration as given in (3.168).

The Navier et Cauchy equations to solve in order to get to the U_z and U_r components of the displacements vector are similar to (3.173) and (3.174), for $m \geq 1$, and to (3.180) and (3.181), for $m = 0$, so that the solutions are equivalent, even if it has to be considered that the quantities describing the temperature are different, as the temperature field is different. So, for $m \geq 1$, it is:

$$U_m^r(z) = (c_{1,m} + c_{3,m} z) e^{(l_m z/a)} + (c_{2,m} + c_{4,m} z) e^{-(l_m z/a)} + F_m^r(z), \tag{3.249}$$

$$\begin{aligned} U_m^z(z) = \; & \left(-c_{1,m} - c_{3,m} z + c_{3,m} \tfrac{a(\mu+\lambda)}{l_m(\lambda+\mu)}\right) e^{(l_m z/a)} + \\ & + \left(c_{2,m} + c_{4,m} z + c_{4,m} \tfrac{a(\mu+\lambda)}{l_m(\lambda+\mu)}\right) e^{-(l_m z/a)} + F_m^z(z) \end{aligned} \tag{3.250}$$

where the function $F_m^z(z)$ and $F_m^r(z)$ have the same form as the one introduced in the previous section. For $m = 0$, the solutions are equal to the one given in equation (3.182) and (3.183).
The field of pressure can be applied by using the boundary conditions on the stress tensor components Θ_{zz} and Θ_{rz}. Then, by solving the resulting equations for Θ_{zz} and Θ_{rz}, with the applied field of pressure, the coefficients $c_{1,m}$ $c_{2,m}$, $c_{3,m}$, $c_{4,m}$, c_5, c_6 are determined.
For $m \geq 1$, on the mirror reflecting surface, i.e. on $z = -h/2$, the Dini series coefficients of

stress tensor components, Θ_{zz} and Θ_{rz}, have the following expression, respectively:

$$\Theta_{zz,m}(-h/2) = \frac{\mu(\lambda+\mu)e^{-\frac{hl_m}{2a}}\left(2a(\lambda+2\mu)\left(c_{3,m}-c_{4,m}e^{\frac{hl_m}{a}}\right)+(\lambda+\mu)l_m\left(-(2c_{2,m}-hc_{4,m})e^{\frac{hl_m}{a}}+hc_{3,m}-2c_{1,m}\right)\right)}{a}+$$

$$+\frac{(\lambda+\mu)^2\left(a(\lambda+2\mu)F_z'\left[-\frac{h}{2}\right]-a\nu\tilde{\tau}_m\left[-\frac{h}{2}\right]+\lambda l_m F_r\left[-\frac{h}{2}\right]\right)}{a}, \tag{3.251}$$

$$\Theta_{rz,m}(-h/2) = \frac{\mu e^{-\frac{hl_m}{2a}}\left(e^{\frac{hl_m}{a}}(c_{4,m}(h(\lambda+\mu)l_m-2a\mu)-2(\lambda+\mu)l_m c_{2,m})-(\lambda+\mu)e^{\frac{hl_m}{2a}}\left(l_m F_z\left[-\frac{h}{2}\right]-aF_r'\left[-\frac{h}{2}\right]\right)\right)}{a(\lambda+\mu)}+$$

$$+\frac{\mu e^{-\frac{hl_m}{2a}}(2(\lambda+\mu)l_m c_{1,m}-c_{3,m}(2a\mu+h(\lambda+\mu)l_m))}{a(\lambda+\mu)}. \tag{3.252}$$

On the rear side of the mirror, i.e. $z = h/2$, it is:

$$\Theta_{zz,m}(h/2) = \frac{\mu(\lambda+\mu)e^{-\frac{hl_m}{2a}}\left((\lambda+\mu)l_m\left(-(hc_{3,m}+2c_{1,m})e^{\frac{hl_m}{a}}-hc_{4,m}-2c_{2,m}\right)-2a(\lambda+2\mu)\left(c_{4,m}-c_{3,m}e^{\frac{hl_m}{a}}\right)\right)}{a}+$$

$$+\frac{(\lambda+\mu)^2\left(a(\lambda+2\mu)F_z'\left[\frac{h}{2}\right]-a\nu\tau_m\left[\frac{h}{2}\right]+\lambda l_m F_r\left[\frac{h}{2}\right]\right)}{a}, \tag{3.253}$$

$$\Theta_{rz,m}(h/2) = \frac{\mu(\lambda+\mu)e^{-\frac{hl_m}{2a}}\left(e^{\frac{hl_m}{a}}(c_{3,m}(h(\lambda+\mu)l_m-2a\mu)+2(\lambda+\mu)l_m c_{1,m})-(\lambda+\mu)e^{\frac{hl_m}{2a}}\left(l_m F_z\left[\frac{h}{2}\right]-aF_r'\left[\frac{h}{2}\right]\right)\right)}{a}+$$

$$+\frac{\mu(\lambda+\mu)e^{-\frac{hl_m}{2a}}(-c_{4,m}(2a\mu+h(\lambda+\mu)l_m)-2(\lambda+\mu)l_m c_{2,m})}{a}. \tag{3.254}$$

In order to determine $c_{1,m}$ $c_{2,m}$ $c_{3,m}$ $c_{4,m}$, when a pressure field is applied on the mirror, the following equations can be written:

$$\begin{cases} \Theta_{zz,m}(h/2) = P_{+,m} \\ \Theta_{zz,m}(-h/2) = P_{-,m} \\ \Theta_{rz,m}(-h/2) = 0 \\ \Theta_{rz,m}(h/2) = 0 \end{cases} \tag{3.255}$$

where $P_{+,m}$ and $P_{-,m}$ are the coefficients of the development on the Bessel function base of the

field of pressure applied on the mirror. In the easier case:

$$P_+(r) = \begin{cases} 0 & r < d_{out} \\ P_+ & r \geq d_{out} \end{cases} \tag{3.256}$$

$$P_-(r) = \begin{cases} 0 & r < d_{in} \\ P_- & r \geq d_{in} \end{cases} \tag{3.257}$$

where P_+ and P_- are the constant pressure values applied on the mirror outside and inside the optical cavity respectively, as it is shown in figure (3.10).
It is also possible to have a configuration with different pressures applied on the back side of the

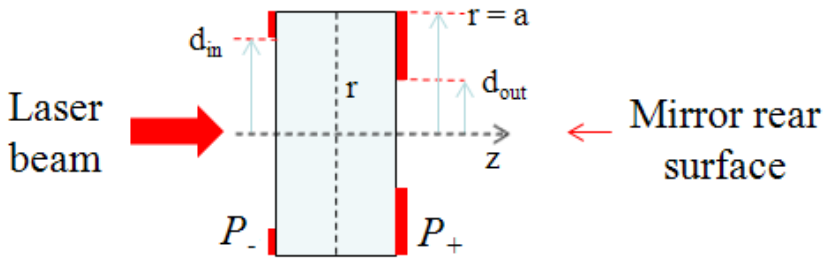

Figure 3.10: Mirror scheme with TCS based on pressure application - Application of pressure P_+ on a ring of internal radius d_{out} and external radius a, on the rear side of the mirror, and of pressure P_- on a ring of internal radius d_{in} and external radius a, on the mirror surface internal to the optical cavity.

mirror. An example of this case is:

$$P_+(r) = \begin{cases} 0 & d_{out,1} < r < d_{out,2} \\ g_+ & 0 \leq r \leq d_{out,1} \\ p_+ & r \geq d_{out,2} \end{cases} \tag{3.258}$$

where a pressure, g_+, is applied on a central disk of radius $d_{out,1}$ and a second pressure, p_+, is set up on a ring of internal radius $d_{out,2}$. The rear side of the mirror surface can also be divided in one central disk and several adjacent rings. In each of these mirror regions, a different value of pressure can be applied. It is worth noticing that a MATLAB program with seven different pressures applicable in the back side of the mirror has been realized, in this work. The cases with one, two, three, four, five and six fixed values of the pressure can be analyzed, by using the program with seven different fixed values of pressure, indeed it is enough to set to zeros the appropriate number of fixed external pressure to recover the desired case.

For the sake of simplicity, the configuration with one fixed value of the pressure in the rear side of the mirror is now considered, in order to show the mathematical procedure used to obtain the complete solution for the displacement vector components, in the case of the TCS under study. However, what will be explain holds even for the case with seven pressure values applied on the mirror.

In terms of Dini series, the functions $P_+(r)$, $P_-(r)$, described in figure (3.10), become:

$$P_+(r) = \sum_{m=0}^{\infty} P_{+,m} J_0(l_m r/a), \tag{3.259}$$

$$P_-(r) = \sum_{m=0}^{\infty} P_{-,m} J_0(l_m r/a), \tag{3.260}$$

with :

$$P_{+,0} = \frac{2P_+}{a^2} \int_{d_{out_1}}^{a} r dr, \tag{3.261}$$

$$P_{-,0} = \frac{2P_-}{a^2} \int_{d_{in}}^{a} r dr, \tag{3.262}$$

and, for $m \geq 1$:

$$P_{+,m} = \frac{2P_+}{a^2 J_0^2(l_m)} \int_{d_{out_1}}^{a} J_0(l_m r/a) r dr, \tag{3.263}$$

$$P_{-,m} = \frac{2P_-}{a^2 J_0^2(l_m)} \int_{d_{in}}^{a} J_0(l_m r/a) r dr. \tag{3.264}$$

As far as the Dini series coefficients of the stress tensor components, Θ_{zz} and Θ_{rz}, for $m = 0$ are concerned, it is:

$$\Theta_{zz,0}(z) = constant = c_6(\lambda + 2\mu), \tag{3.265}$$

$$\Theta_{rz,0}(z) = constant = 0. \tag{3.266}$$

So that the following condition is found:

$$P_{+,0} = P_{-,0}. \tag{3.267}$$

It is possible to show that this condition is equivalent to say that the magnitude of the total force applied on the mirror surface internal to the optical cavity has to be equal to the magnitude of

the total force applied to the rear side of the mirror. Indeed, the magnitude of the total force applied in the external surface of the mirror is:

$$F_+ = 2\pi \int_0^a \left(\sum_{m=0}^{\infty} P_{+,m} J_0(l_m r/a), \right) r dr = 2\pi \int_0^a P_{+,0} r dr = \pi P_{+,0} a^2, \tag{3.268}$$

while the magnitude of the total force applied in the internal surface of the mirror is:

$$F_- = 2\pi \int_0^a \left(\sum_{m=0}^{\infty} P_{-,m} J_0(l_m r/a), \right) r dr = 2\pi \int_0^a P_{-,0} r dr = \pi P_{-,0} a^2. \tag{3.269}$$

By equating equation (3.268) and (3.269), we get to the same condition already given in (3.267), where the expression of $P_{+,0}$ and $P_{-,0}$ are the ones of equations (3.261) and (3.262). As a consequence, it is possible to fix the pressure to apply on the rear side of the mirror, and the pressure on the mirror surface internal to the optical cavity turns out to be determined, i.e. the value of P_+ is a program data and P_- is found by using the last condition (3.267). In order to determine c_5 and c_6, a system of two equations is used. One of the equations compounding the system is:

$$\Theta_{zz,0} = c_6(\lambda + 2\mu) = P_{+,0}. \tag{3.270}$$

The other equation can be obtained by imposing that the barycenter of the mirror does not change its position:

$$2\pi \int_{-h/2}^{h/2} dz \int_0^a u_z(r,z) r dr = 0. \tag{3.271}$$

It is important to notice that the vector $u_z(r,z)$, in equation (3.271), contains also the Saint Venant correction, which has been already introduced in section (3.3.1), and it is defined by equations (3.193)-(3.198). For the sake of clearness, the expressions of the coefficients $\Theta_{rr,m}$, for $m \geq 1$ and $m = 0$, entering the calculations of the Saint-Venant terms, are reported below. In

particular, for $m \geq 1$:

$$\Theta_{rr,m}(a,z) = \frac{\lambda J_0(l_m)\left(\sum_{n=1}^{\infty} \nu D_{\mathrm{mn}}(\lambda+\mu)\left(A_n e^{-\frac{zk_n}{a}}+B_n e^{\frac{zk_n}{a}}\right)+2\mu(\lambda+2\mu)c_{3,m}e^{\frac{zl_m}{a}}-2\mu(\lambda+2\mu)c_{4,m}e^{-\frac{zl_m}{a}}\right)}{(\lambda+\mu)(\lambda+2\mu)}+$$

$$\frac{\mu l_m(J_0(l_m)-J_2(l_m))\left(\sum_{n=1}^{\infty}\frac{a\nu D_{\mathrm{mn}}l_m\left(A_n e^{-\frac{zk_n}{a}}+B_n e^{\frac{zk_n}{a}}\right)}{(\lambda+2\mu)(l_m^2-k_n^2)}+(zc_{3,m}+c_{1,m})e^{\frac{zl_m}{a}}+(zc_{4,m}+c_{2,m})e^{-\frac{zl_m}{a}}\right)}{a}-$$

$$\sum_{n=1}^{\infty}\nu D_{\mathrm{mn}}J_0\left(l_m\right)\left(A_n e^{-\frac{zk_n}{a}}+B_n e^{\frac{zk_n}{a}}\right), \tag{3.272}$$

and for $m = 0$:

$$\Theta_{rr,0}(a,z) = c_6\lambda - \sum_{n=1}^{\infty}\frac{4\mu\nu J_1\left(k_n\right)\left(A_n e^{-\frac{zk_n}{a}}+B_n e^{\frac{zk_n}{a}}\right)}{(\lambda+2\mu)k_n} \tag{3.273}$$

As, even in this case relation (3.202) holds, the integration in equation 3.271 takes the form:

$$2\pi\int_{-h/2}^{h/2}dz\int_0^a(U_0^z(z)+\delta u_z)rdr = 0. \tag{3.274}$$

In conclusion, all the quantities required to determine the mirror displacement vector components can be obtained by implementing the calculations performed in this section, with a MATLAB program.

Chapter 4

TCS Result validation through numerical simulaitons

This chapter has the aim to report on the verification of the results previously shown on the thermal effect compensation systems. The check of the analytical results, concerning mirror temperature field and deformation, is made by comparing the MATLAB solutions, based on the analytical calculations, with the numerical results given by ANSYS [96] and COMSOL [97], [98]. These softwares utilize the finite element method (FEM) to obtain approximated solutions of differential equations with specified boundary conditions, as it is the case of the deferential equations we analytically solved in the previous sections The implementation of a finite element method analysis requires, first of all, the geometrical description of the considered object. This can be done both by using directly the COMSOL and ANSYS software, both by importing the geometry from another software dedicated to design studio (e.g. CATIA [99] or AUTOCAD [100]), if the geometry to consider is complicated. However, the mirror geometry taken into account in this section is quite simple, so that it is better to characterize it within ANSYS and COMSOL. In particular, it is assumed that the mirror are cylinder of radius 4 cm and thickness 5 mm, as it is supposed to be for the mirrors of the SIPHORE optical cavity. After describing the geometry of the considered object, its material has to be defined. For the simulations in the following the fused silica has been chosen whose properties are reported in table (4.1). The next step for a FEM analysis is the subdivision of the modeled object in a suitable number of parts with finite dimension and defined shape, the finite element of the simulation. The so called *meshing* is the process of the modeled object subdivision in elementary parts and the mesh is the net resulting from the meshing process. The reliability of a MEF solution depends strongly

Quantity	Value	Unit
Coefficient of thermal expansion	0.54×10^{-6}	1/K
Heat capacity at constant temperature	745	J/(kg K)
Density	2202	kg/m^3
Thermal conductivity	1.38	W/(m K)
Young's modulus	73×10^{-9}	Pa
Poisson's ratio	0.17	1

Table 4.1: Fused silica parameters

on an appropriate definition of the mesh. On one hand, the finest the mesh, the higher the precisions of the solutions, on the other hand the finest the mesh the longer the computational time. Then, a good mesh results from a compromise between calculation time and precision of the results. The shape of the mesh elements can also be chosen, in order to better describe the considered object. The mesh also define the number of knots, i.e. the points, inside the object, where the physical unknown quantities will be determined by the MEF analysis. A knot belongs to more than one mesh constituent, but the MEF is thought so that in a given knot the value of the determined physical quantity has the same value, in each mesh constituent. In the following sections, the MEF solutions concerning the mirror temperature fields and deformations in the stationary state will be illustrated, for the TCS considered in the previous chapter. These results are compared to the ones based on the calculations of chapter 3 in order to have an estimations of the correctness of the analytical calculation solutions.

4.1 ANSYS COMSOL Software Comparison

It is worth noticing the differences observed between the ANSYS and COMSOL softwares. Firstly, we point out that as far as the chosen mirror geometry is considered, it turned out to be easier handled with COMSOL than with ANSYS. This is due to the fact that, thanks to the assumption of cylindrical symmetry, COMSOL allows to work on a 2D axis-symmetric plan with respect to the variable z, instead of the 3D space required by ANSYS, which demands a thickness specification. The importance of working in a 2D plan rises from the fact that this reduces the computational time and the memory required for the calculations. In spite of this, for the TCSs where the mirror has no constrains and it is considered free in the space, COMSOL takes long time to finalize the calculations (from 6h to 24h), while ANSYS takes just few minutes. This

difference comes from the fact that in the COMSOL case the mirror appears to accelerate in the space and a stationary solution can be obtained only after a quite long computational time. Furthermore, the mirror displacement evaluated in this way with COMSOL is the sum of the mirror spatial displacement and of its deformation. As the deformation is much smaller than the spatial displacement, it is not possible to distinguish it by a numerical error. The calculations has then to be performed in the transitory frame, by limiting the computational time at three hours, as two hours already describe quite properly the stationary state [101]. However, this time remains much longer than the one required by ANSYS. A further difference in the application of the two softwares comes from the fact that a function of r has to be applied as boundary condition on the mirror surface internal to the optical cavity, to describe the fraction of intracavity optical power absorbed by the mirror coating. In ANSYS, the absorbed optical power with gaussian dependence on the radius of the mirror can be easily set as boundary condition, by importing a table of data describing the absorbed optical power as function of r. As far as COMSOL is concerned, it allows to define any function of r as boundary condition [101].

4.2 TCS with fixed temperature on the cavity mirror edges

This section has the aim to show the agreement between the analytical results for the TCS described in section (3.2.1) and the numerical calculations, as far as the mirror temperature field and distortion are concerned. It is worth recalling that this TCS consists in fixing the temperature of the mirror at a known value T_1, on the mirror edges. The validation of the MATLAB code, based on the analytical results, is made by comparing the curves of the temperature and deformation on the mirror surface internal and external to the optical cavity with the same curves, obtained through numerical simulations. Both the COMSOL and ANSYS softwares are used in the analysis. The results are showed in figures (4.1) and (4.2). By assuming an error for the numerical calculations equal to 5%, it is possible to check that the numerical and analytical curves are in good agreement, as their difference is within the software error. To confirm the last statement, a more quantitative analysis can be carried on to evaluate the departure of the analytical results from the numerical ones. As far as the mirror surface deformations, inside and outside the cavity, are concerned, the following quantity can be calculated to have an estimation

of the error of the analytical method with respect to the numerical one:

$$Error = \frac{\sqrt{\int_0^a (U_N^z - U_A^z)^2 r dr}}{\sqrt{\int_0^a (U_N^z - \mathrm{Min}\left[U_N^z\right])^2 r dr}}, \tag{4.1}$$

where U_N^z and U_A^z indicate the z component of the mirror surface displacement vector numerically and analytically calculated, respectively, and $\mathrm{Min}\left[U_N^z\right]$ is the minimum value of U_N^z. It is observed that the same equation (4.1) is applied for evaluating the error of the analytically calculated mirror displacement vector on the surface internal to the optical cavity and on the one external to the optical cavity, i.e. both for $z = -h/2$ and for $z = h/2$. The value of $Error$ has to be smaller than the software error (5%). The results for both the mirror surfaces and for the numerical calculations performed with ANSYS and COMSOL are reported in table (4.2). It is then possible to state the agreement between analytical and numerical calculations for the mirror distortions, indeed, the value of the function $Error$ is always below 5%.
In order to evaluate the differences between the temperature field analytically and numerically calculated, it is convenient to plot the following function:

$$Error_T = \frac{|T_N - T_A|}{T_N}, \tag{4.2}$$

where T_N and T_A are the fields of temperature at the mirror surfaces evaluated by using numerical and analytical calculations, respectively. At each radius value, the function $Error_T$ is obtained and the results for both the mirror surfaces (the one internal and the one external to the optical cavity) are plotted in picture (4.3) and picture (4.4), for the numerical calculations carried on with ANSYS and COMSOL. These pictures show the substantial agreement between the analytical calculated temperature field and the one numerically calculated. Indeed the percent error, $Error_T$, is always below the software error of 5%.

4.3 TCS with fixed temperature on the edges and on the rear side of total reflective cavity mirrors

The validation of the MATLAB code based on the results presented in section (3.2.2) is now taken into account. The TCS currently considered can be applied only on totally reflective mirror, as both the edges of the mirror and the integrity of its rear surface are used by the thermal effect compensation system. Indeed, it is assumed that a temperature T_1 is fixed on

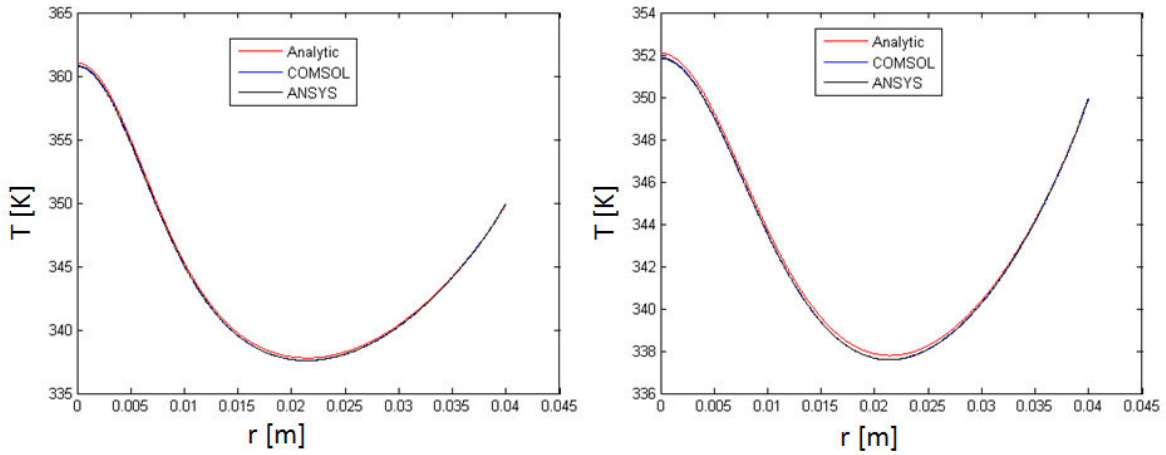

Figure 4.1: Temperature field validation for the TCS in section (4.2) - SIPHORE mirror geometry. Absorption coefficient 0.3ppm. Intracavity power 3MW. Environment temperature T_0=300K. Mirror edge temperature fixed at T_1=350K. **Left panel**: mirror surface temperature inside the optical cavity. **Right panel**: mirror surface temperature outside the optical cavity.

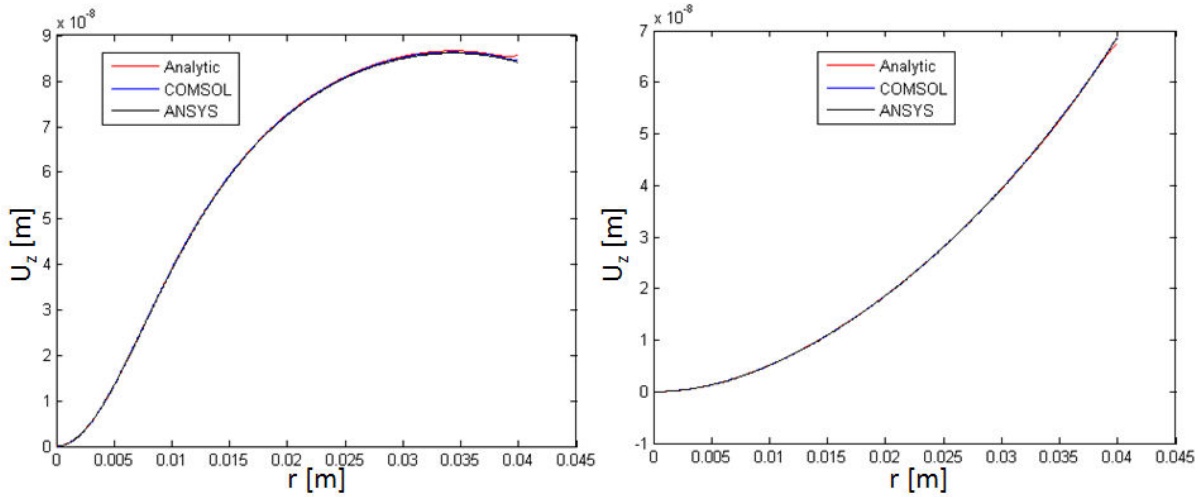

Figure 4.2: Mirror distortion validation for the TCS in section (4.2) - SIPHORE mirror geometry. Absorption coefficient 0.3ppm. Intracavity power 3MW. Environment temperature T_0=300K. Mirror edge temperature fixed at T_1=350K. **Left panel**: mirror surface displacement inside the optical cavity. **Right panel**: mirror surface displacement outside the optical cavity.

	Error
Mirror surface distortion inside the cavity ANSYS-analytic result comparison	5.8×10^{-3}
Mirror surface distortion inside the cavity COMSOL-analytic result comparison	3.2×10^{-3}
Mirror surface distortion outside the cavity ANSYS-analytic result comparison	3.7×10^{-3}
Mirror surface distortion outside the cavity COMSOL-analytic result comparison	5.3×10^{-3}

Table 4.2: Error estimation between analytical and numerical calculations for the TCS of section (4.2) - The values of the reported errors concern the mirror surface displacement vectors of picture (4.2) and they are evaluated by applying equation 4.1.

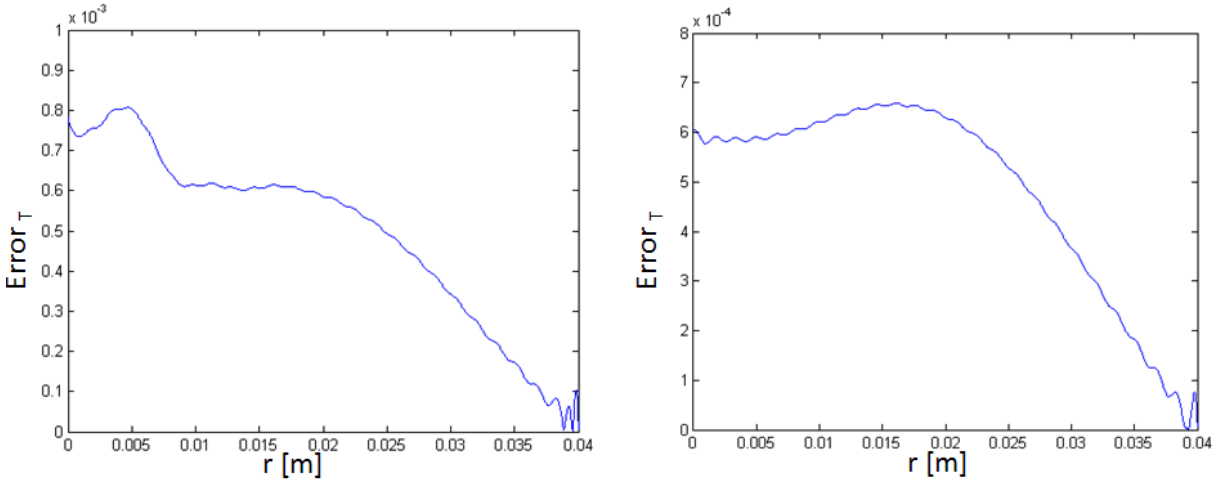

Figure 4.3: Percent error for the analytically calculated temperature field with respect to the numerically calculated one, for the TCS in section (4.2). Mirror front surface. - The reported errors are obtained through the application of equation (4.2) and they concern the data of the left panel of picture (4.1). **Left panel**: percent error of the analytical calculations with respect to the ones performed with ANSYS, as far as the mirror surface temperature inside the optical cavity is concerned. **Right panel**: percent error of the analytical calculations with respect to the ones performed with COMSOL, as far as the mirror surface temperature inside the optical cavity is concerned.

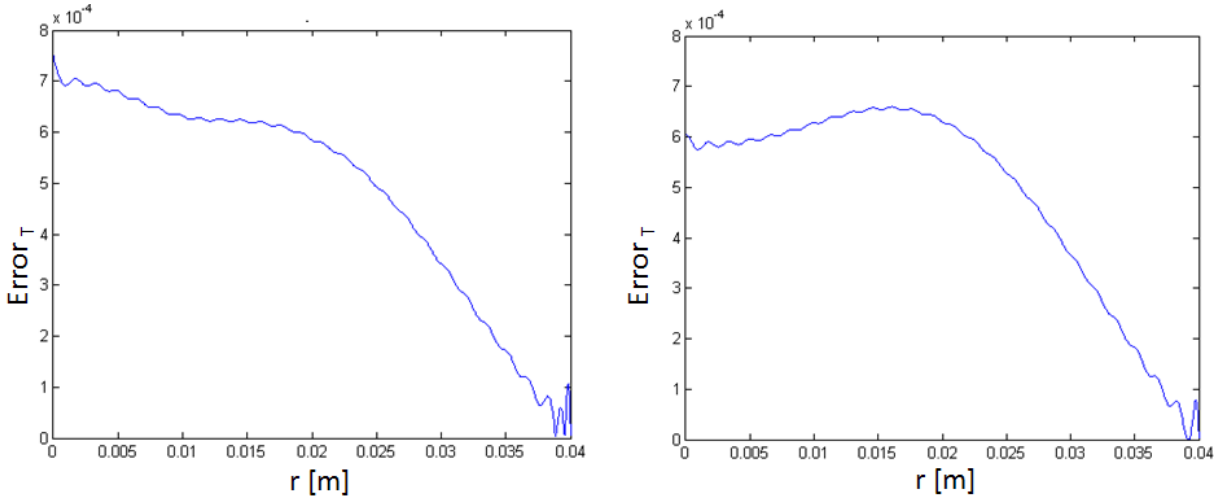

Figure 4.4: Percent error for the analytically calculated temperature field with respect to the numerically calculated one, for TCS in section (4.2). Mirror rear surface. - The reported errors are obtained through the application of equation (4.2) and they concern the data of the right panel of picture (4.1). **Left panel**: percent error of the analytical calculations with respect to the ones performed with ANSYS, as far as the mirror surface temperature outside the optical cavity is concerned. **Right panel**: percent error of the analytical calculations with respect to the ones performed with COMSOL, as far as the mirror surface temperature outside the optical cavity is concerned.

the mirror edges and on its rear surface. The analytically calculated curves of the temperature and deformation on the mirror surface internal and external to the optical cavity are compared with the same curves obtained through numerical simulations, in order to verify the correctness of the analytical calculations. Both the COMSOL ans ANSYS softwares are applied. The results are showed in pictures (4.5), (4.6). By looking to them it is possible to perceive the agreement between analytical and numerical results. However, a more quantitative estimation of the differences between the analytical and the numerical solutions can be carried on, as it has been already done in the previous section. In particular, as far as the mirror surface displacement vector is concerned, equation (4.1) is calculated and the results are reported in table (4.3). For the temperature field, equation (4.2) is taken into account and the plots in figure (4.7) and figure (4.8) are realized. From the error values presented in these last two pictures and in table (4.3), it is eventually possible to state the agreement between analytical and numerical results.

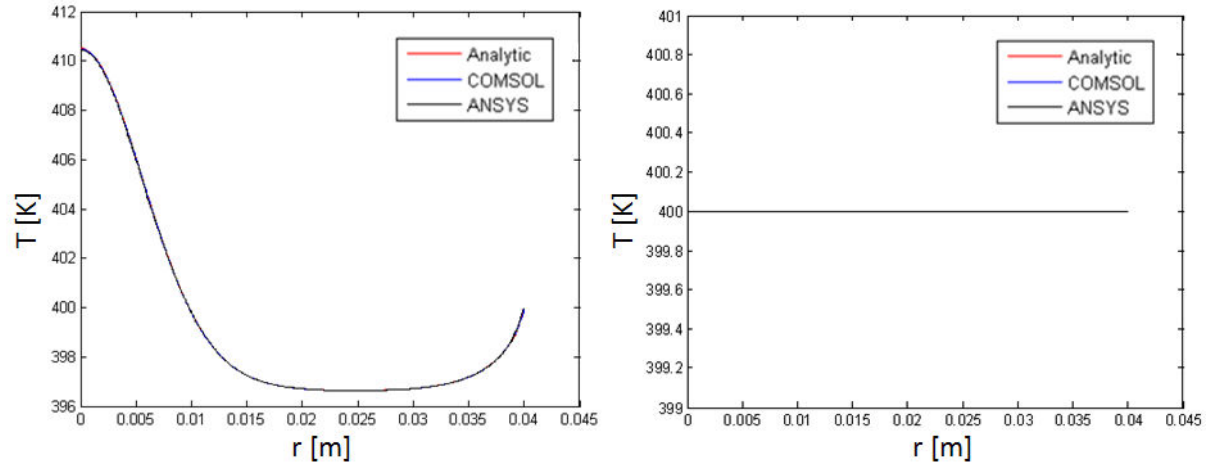

Figure 4.5: Temperature field validation for TCS in section (4.3) - SIPHORE mirror geometry. Absorption coefficient 0.3ppm. Intracavity power 3MW. Environment temperature T_0=300K. Mirror edge temperature fixed at T_1=400K. Temperature fixed on the rear side of the mirror at T_1=400K **Left panel**: mirror surface temperature inside the optical cavity. **Right panel**: mirror surface temperature outside the optical cavity.

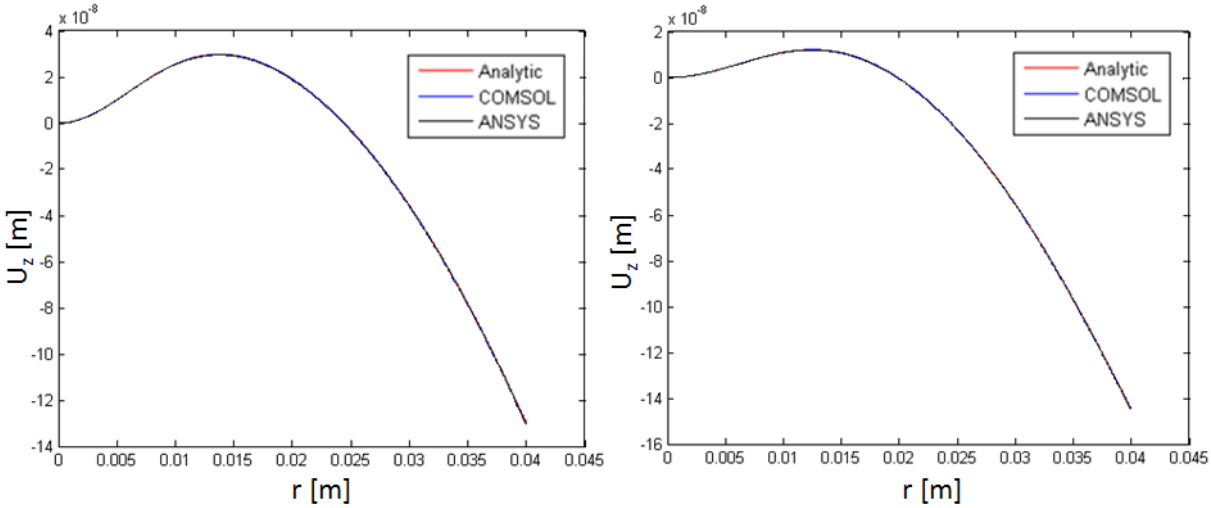

Figure 4.6: Mirror distortion validation for TCS in section (4.3) - SIPHORE mirror geometry. Absorption coefficient 0.3ppm. Intracavity power 3MW. Environment temperature T_0=300K. Mirror edge temperature fixed at T_1=400K. Temperature fixed on the rear side of the mirror at T_1=400K **Left panel**: mirror surface temperature inside the optical cavity. **Right panel**: mirror surface temperature outside the optical cavity.

	Error
Mirror surface distortion inside the cavity ANSYS-analytic result comparison	4.0×10^{-3}
Mirror surface distortion inside the cavity COMSOL-analytic result comparison	1.4×10^{-3}
Mirror surface distortion outside the cavity ANSYS-analytic result comparison	3.3×10^{-3}
Mirror surface distortion outside the cavity COMSOL-analytic result comparison	1.2×10^{-3}

Table 4.3: Error estimation between analytical and numerical calculations for the TCS of section (4.3) - The values of the reported errors concern the mirror surface displacement vectors of picture (4.6) and they are evaluated by applying equation 4.1.

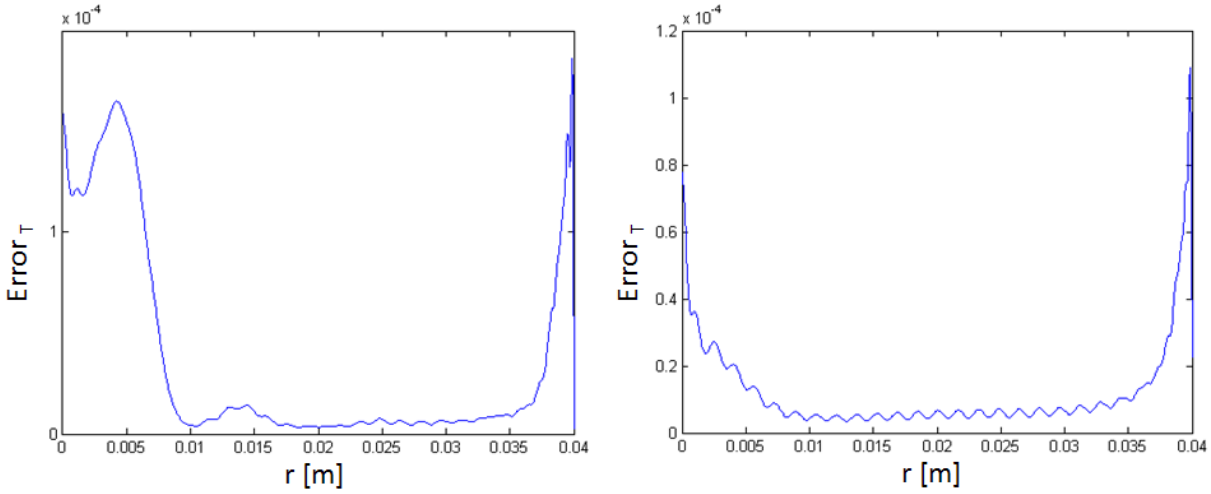

Figure 4.7: Percent error for the analytically calculated temperature field with respect to the numerically calculated one, for the TCS in section (4.3). Mirror front surface. - The reported errors are obtained through the application of equation (4.2) and they concern the data of the left panel of picture (4.5). **Left panel**: percent error of the analytical calculations with respect to the ones performed with ANSYS, as far as the mirror surface temperature inside the optical cavity is concerned. **Right panel**: percent error of the analytical calculations with respect to the ones performed with COMSOL, as far as the mirror surface temperature inside the optical cavity is concerned.

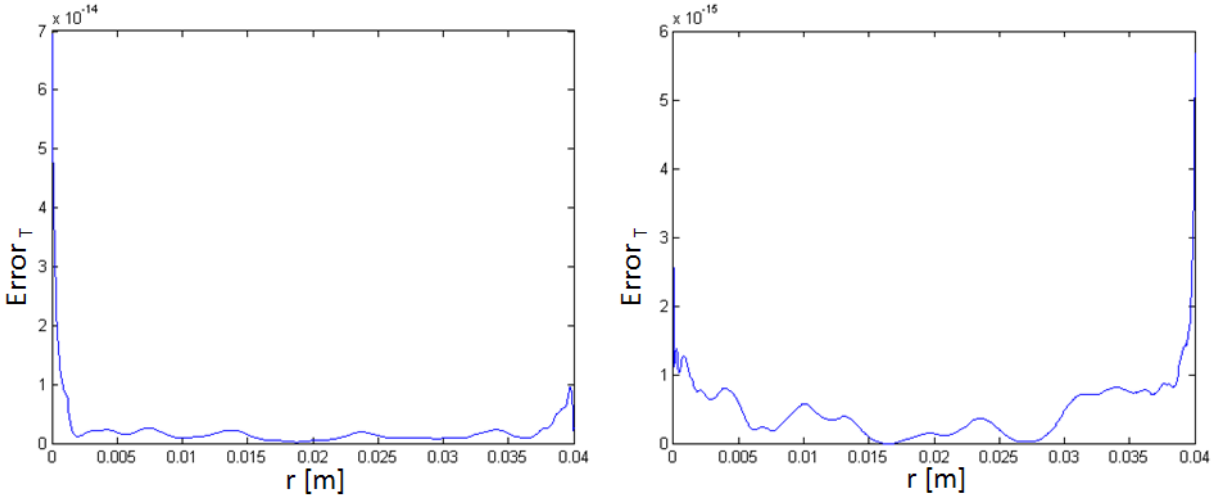

Figure 4.8: Percent error for the analytically calculated temperature field with respect to the numerically calculated one, for TCS in section (4.3). Mirror rear surface. - The reported errors are obtained through the application of equation (4.2) and they concern the data of the right panel of picture (4.6). **Left panel**: percent error of the analytical calculations with respect to the ones performed with ANSYS, as far as the mirror surface temperature outside the optical cavity is concerned. **Right panel**: percent error of the analytical calculations with respect to the ones performed with COMSOL, as far as the mirror surface temperature outside the optical cavity is concerned.

4.4 Free Mirror

As it is shown in section 3.2.3, this case corresponds to the configuration where no temperature fields are applied on the mirror, but the complete environment where the mirror is set is warmed up. To validate the MATLAB code based on the analytical calculations previously discussed for this configuration, the curves relative to the mirror surface deformation and to the mirror surface temperature are plotted for both the analytical and the numerical calculations, obtained by ANSYS and COMSOL. Picture (4.9) and picture (4.10) show a good agreement between the analytical and numerical results. However, for this TCS as well a more accurate analysis is performed, to quantify the differences between the numerical method and analytical one. As far as the mirror surface displacement vectors are concerned, the errors are evaluated, as customary, through equation (4.1). The results are reported in table (4.4). For the comparison of the analytically calculated temperature field with the numerically calculated one, equation (4.2) is applied and the corresponding plots of pictures (4.11), (4.12) are realized. Both the table and the pictures state the agreement between numerical and analytical calculations, as the reported errors are always smaller than the COMSOL and ANSYS softwares error (5%).

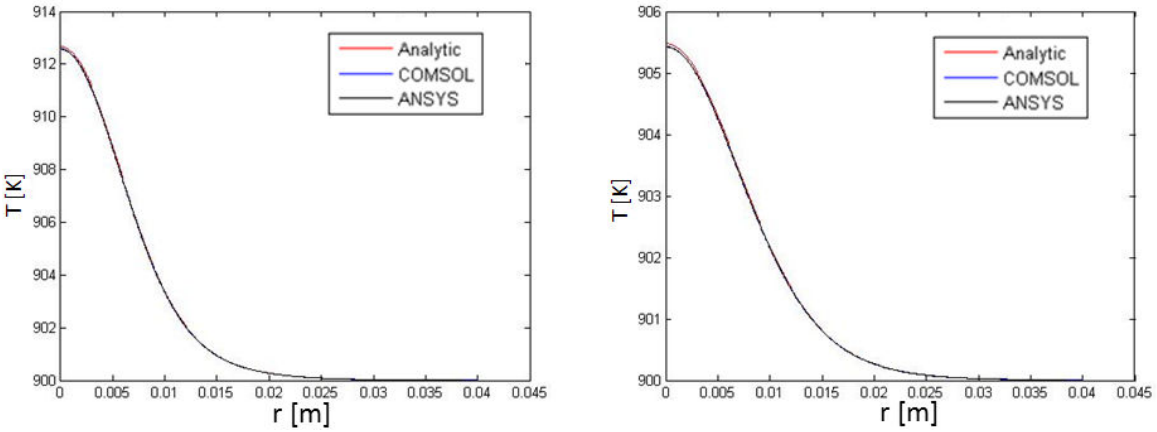

Figure 4.9: Temperature field validation for the TCS of section (4.4) - SIPHORE mirror geometry. Absorption coefficient 0.3ppm. Intracavity power 3MW. Environment temperature T_0=900K. **Left panel**: mirror surface temperature inside the optical cavity. **Right panel**: mirror surface temperature outside the optical cavity.

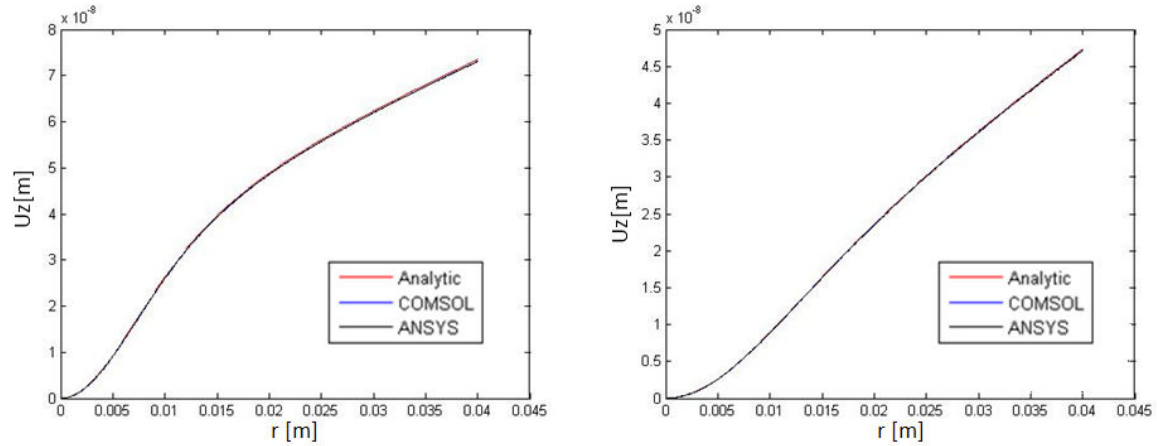

Figure 4.10: Mirror distortion validation for the TCS of section (4.4) - SIPHORE mirror geometry. Absorption coefficient 0.3ppm. Intracavity power 3MW. Environment temperature T_0=900K. **Left panel**: mirror surface displacement inside the optical cavity. **Right panel**: mirror surface displacement outside the optical cavity.

	Error
Mirror surface distortion inside the cavity ANSYS-analytic result comparison	5.8×10^{-3}
Mirror surface distortion inside the cavity COMSOL-analytic result comparison	5.5×10^{-3}
Mirror surface distortion outside the cavity ANSYS-analytic result comparison	3.8×10^{-3}
Mirror surface distortion outside the cavity COMSOL-analytic result comparison	2.6×10^{-3}

Table 4.4: Error estimation between analytical and numerical calculations for the TCS of section (4.4) - The values of the reported errors concern the mirror surface displacement vectors of picture (4.10) and they are evaluated by applying equation 4.1.

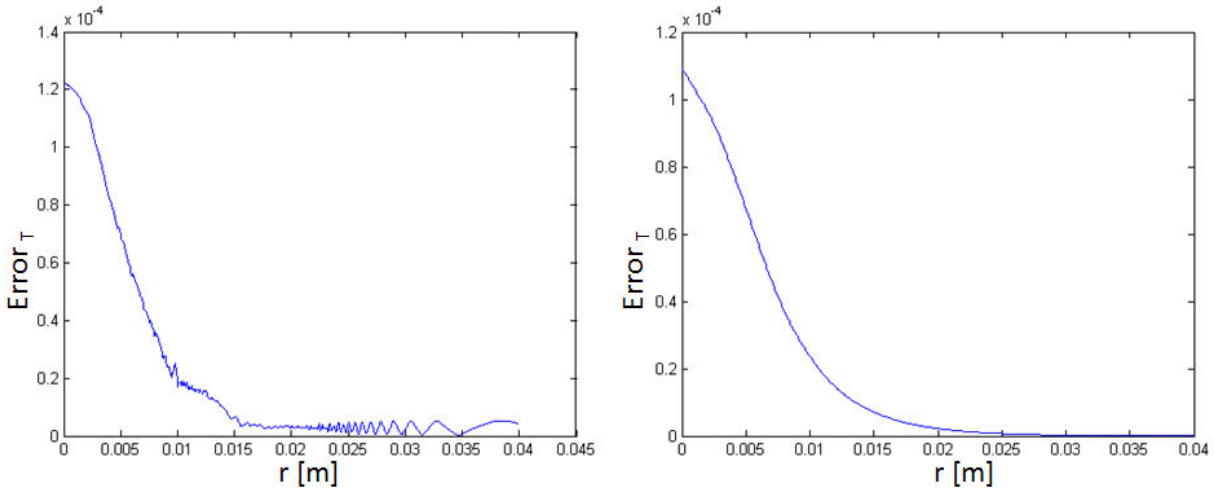

Figure 4.11: Percent error for the analytically calculated temperature field with respect to the numerically calculated one, for the TCS in section (4.4). Mirror front surface. - The reported errors are obtained through the application of equation (4.2) and they concern the data of the left panel of picture (4.9). **Left panel**: percent error of the analytical calculations with respect to the ones performed with ANSYS, as far as the mirror surface temperature inside the optical cavity is concerned. **Right panel**: percent error of the analytical calculations with respect to the ones performed with COMSOL, as far as the mirror surface temperature inside the optical cavity is concerned.

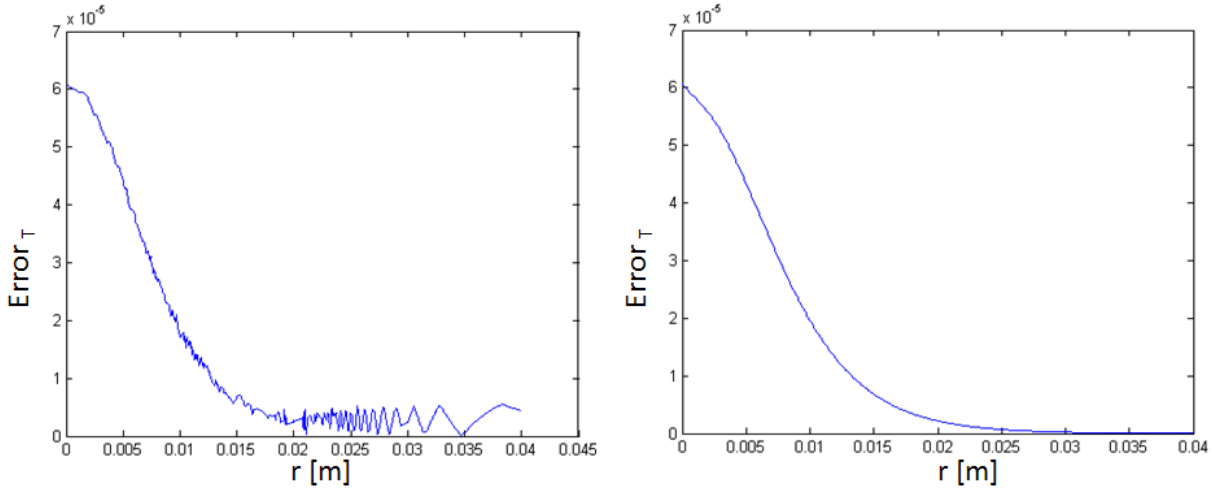

Figure 4.12: Percent error for the analytically calculated temperature field with respect to the numerically calculated one, for TCS in section (4.4). Mirror rear surface. - The reported errors are obtained through the application of equation (4.2) and they concern the data of the right panel of picture (4.9). **Left panel**: percent error of the analytical calculations with respect to the ones performed with ANSYS, as far as the mirror surface temperature outside the optical cavity is concerned. **Right panel**: percent error of the analytical calculations with respect to the ones performed with COMSOL, as far as the mirror surface temperature outside the optical cavity is concerned.

4.5 Edge temperature fixed and one ring heater

This case correspond to the configuration illustrated by figure (3.4), and it has being already described in section (3.2.4). Here, it is reported on the verification of the analytical calculations for this TCS. In figures (4.13), (4.14), it is shown how the curves relative to the mirror deformation and to the mirror temperature, obtained through ANSYS and COMSOL, reproduce the ones analytically calculated for $T_1 = 480$K. For a more quantitative valuation of the differences between analytical and numerical solutions, equation (4.1) is applied for calculating the errors associated with the analytically calculated mirror surface displacement vectors, which are reported in table (4.5), and equation (4.2) is used to realize the plots of pictures (4.15), (4.16), for the percent errors on the analytically calculated temperature fields. The mentioned table together with the pictures state the agreement between the numerical and analytical method results. Nevertheless, for this configuration it is possible to verify that the linearization of the equations, discussed in section (3.2), which allows to write equation (3.44), introduces an error in the analytical calculations, which is not negligible when the excess of temperature τ is not enough smaller than the fixed temperature on the mirror, T_1. To make clear this point, in figures

	Error
Mirror surface distortion inside the cavity ANSYS-analytic result comparison	2.0×10^{-2}
Mirror surface distortion inside the cavity COMSOL-analytic result comparison	2.0×10^{-2}
Mirror surface distortion outside the cavity ANSYS-analytic result comparison	2.0×10^{-2}
Mirror surface distortion outside the cavity COMSOL-analytic result comparison	1.0×10^{-2}

Table 4.5: Error estimation between analytical and numerical calculations for the TCS of section (4.5) and $T_1 = 480$ K - The values of the reported errors concern the mirror surface displacement vectors of picture (4.14) and they are evaluated by applying equation 4.1.

(4.17), (4.18), the results for both the analytical and the numerical simulations are reported, when assuming $T_1 = 600$K. Indeed, as it possible to see from table 4.6, with the increase of the temperature T_1 the effective power radiate by the mirror becomes the more and more different with respect to the one calculated by using the linearization. In particular, for T_1=600K, the error on the mirror radiated power becomes more consistent than the absorbed optical power. Then the effect of the linearization is not anymore negligible and the analytical results show differences with respect to the numerical ones (figures (4.17), (4.18)).

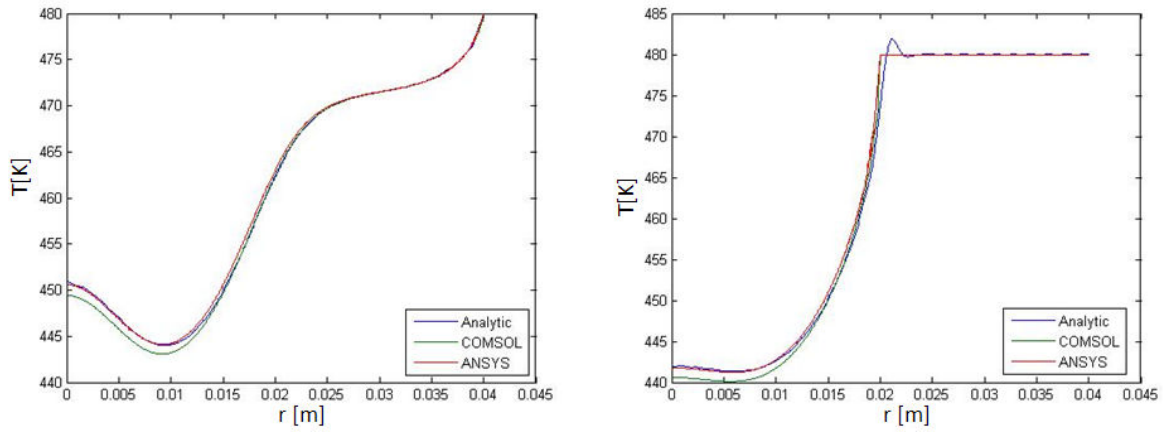

Figure 4.13: Temperature field validation for the TCS of section (4.5) - SIPHORE mirror geometry. Absorption coefficient 0.3ppm. Intracavity power 3MW. Environment temperature T_0=300K, mirror edge temperature fixed at T_1=480K, ring heater fixing the temperature of the mirror back surface between $r = 0.02$ m and $r = 0.04$ m at T_1=480K. **Left panel**: mirror surface temperature inside the optical cavity. **Right panel**: mirror surface temperature outside the optical cavity.

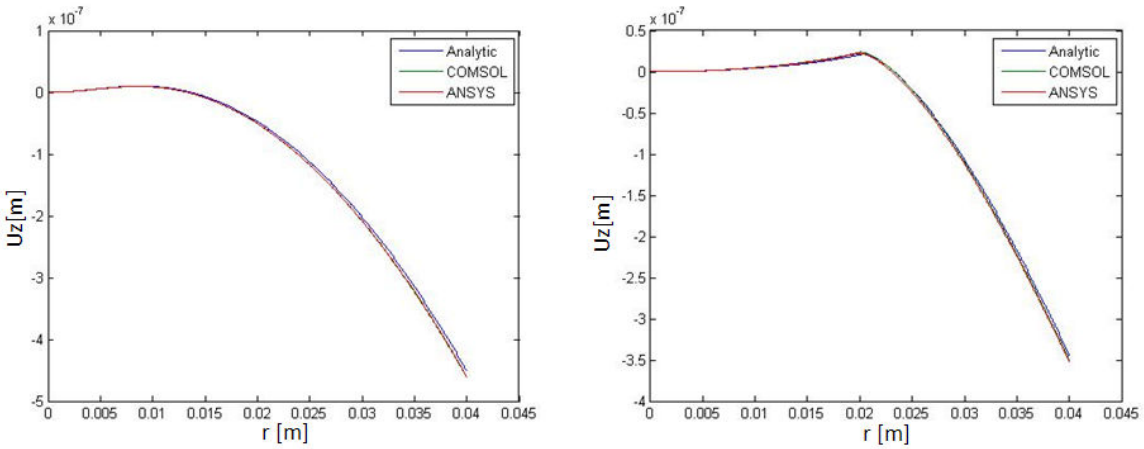

Figure 4.14: Mirror surface distortion validation for the TCS in section (4.5) - SIPHORE mirror geometry. Absorption coefficient 0.3ppm. Intracavity power 3MW. Environment temperature T_0=300K, mirror edge temperature fixed at T_1=480K, ring heater fixing the temperature of the mirror back surface between $r = 0.02$ m and $r = 0.04$ m at T_1=480K. **Left panel**: mirror surface displacement inside the optical cavity. **Right panel**: mirror surface displacement outside the optical cavity.

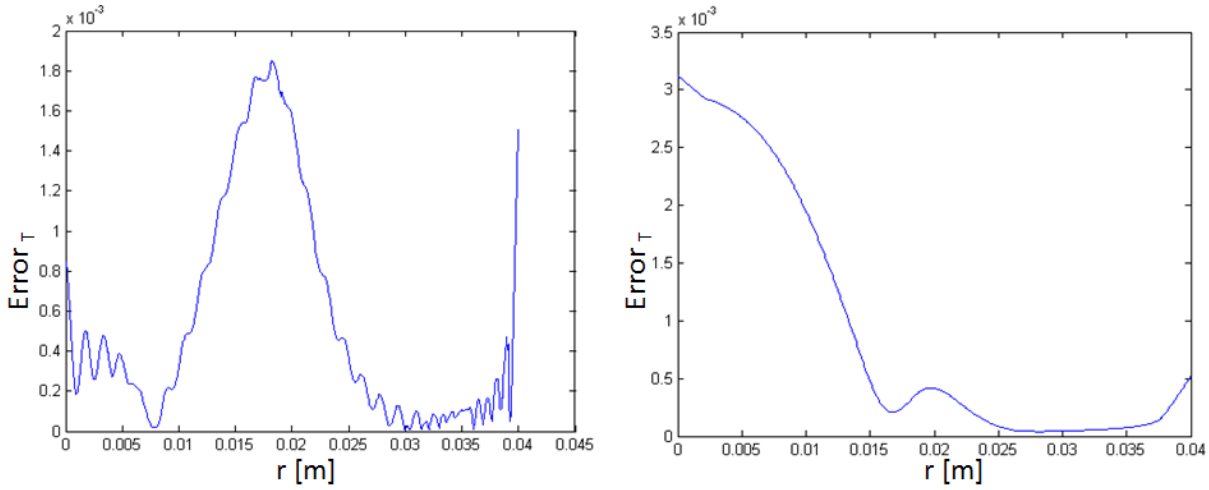

Figure 4.15: Percent error for the analytically calculated temperature field with respect to the numerically calculated one, for the TCS in section (4.5), with $T_1 = 480$K. Mirror front surface. - The reported errors are obtained through the application of equation (4.2) and they concern the data of the left panel of picture (4.13). **Left panel**: percent error of the analytical calculations with respect to the ones performed with ANSYS, as far as the mirror surface temperature inside the optical cavity is concerned. **Right panel**: percent error of the analytical calculations with respect to the ones performed with COMSOL, as far as the mirror surface temperature inside the optical cavity is concerned.

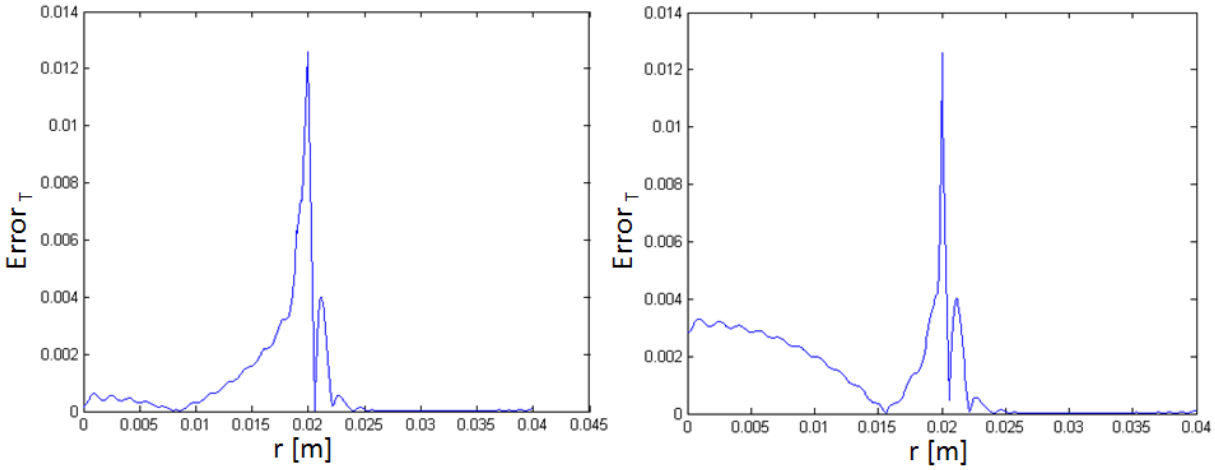

Figure 4.16: Percent error for the analytically calculated temperature field with respect to the numerically calculated one, for the TCS in section (4.5), with $T_1 = 480$K. Mirror rear surface. - The reported errors are obtained through the application of equation (4.2) and they concern the data of the right panel of picture (4.13). **Left panel**: percent error of the analytical calculations with respect to the ones performed with ANSYS, as far as the mirror surface temperature outside the optical cavity is concerned. **Right panel**: percent error of the analytical calculations with respect to the ones performed with COMSOL, as far as the mirror surface temperature outside the optical cavity is concerned.

T_1 [K]	$\tau_{max.}$ [K]	RP_L [W]	RP [W]	Err [W]	P_{abs} [W]	Err/ P_{abs}
300	33	0.16	0.17	0.01	0.9	1%
400	11	9.489	9.502	0.013	0.9	1.4 %
500	50	27.5	27.8	0.3	0.9	33%
600	100	57.3	58.9	1.6	0.9	170%

Table 4.6: Linearization effect - In the table above, τ_{max} is the maximum excess of temperature with respect to the fixed temperature T_1; RP_L is the mirror radiated power, calculated with the approximation of the linearization; RP is the effective mirror radiated power; Err is the difference between RP_L and RP; P_{abd} is the optical power absorbed by the mirror.

	Error
Mirror surface distortion inside the cavity ANSYS-analytic result comparison	3.0×10^{-2}
Mirror surface distortion inside the cavity COMSOL-analytic result comparison	4.6×10^{-2}
Mirror surface distortion outside the cavity ANSYS-analytic result comparison	1.3×10^{-2}
Mirror surface distortion outside the cavity COMSOL-analytic result comparison	1.4×10^{-2}

Table 4.7: Error estimation between analytical and numerical calculations for the TCS of section (4.5) and $T_1 = 600$ K - The values of the reported errors concern the mirror surface displacement vectors of picture (4.18) and they are evaluated by applying equation 4.1.

The quantitative analysis of the analytical solution departure from the numerical ones is performed, as usual, through the application of equation (4.1), for the mirror surface displacement vectors, and of equation (4.2), for the percent error on the analytically calculated temperature field. The results are reported in table (4.7) and in pictures (4.19), (4.20). As it is possible to see from figures (4.15), (4.16), (4.19), (4.20), the higher the fixed temperature T_1, the larger the percent error on the analytically calculated temperature field. This is due to the effect associated with the linerarization of the equations, which has been already discussed.

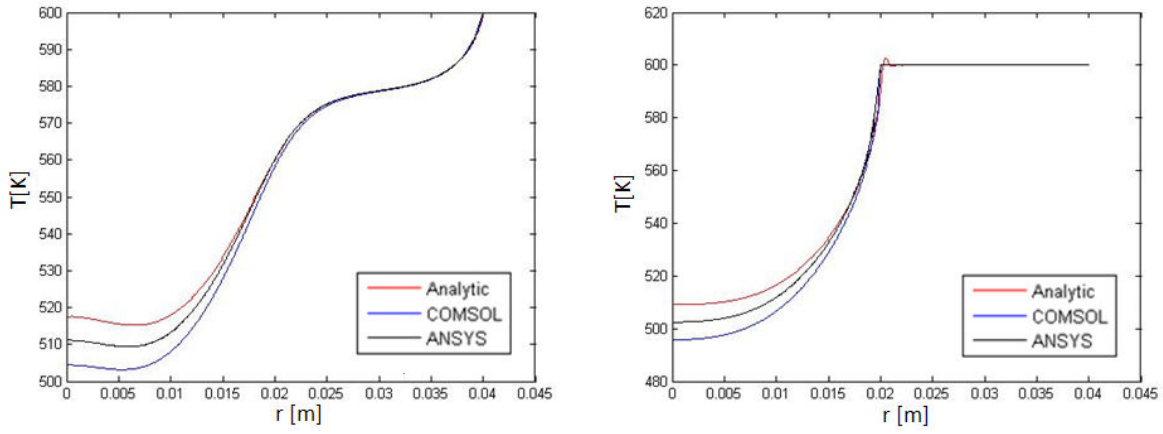

Figure 4.17: Mirror surface temperatures for the TCS of section (4.5), with $T_1 = 600$ K - SIPHORE mirror geometry. Absorption coefficient 0.3ppm. Intracavity power 3MW. Environment temperature T_0=300K, mirror edge temperature fixed at T_1=600K, ring heater fixing the temperature of the mirror back surface between $r = 0.02$ m and $r = 0.04$ m at T_1=600K. **Left panel**: mirror surface temperature inside the optical cavity. **Right panel**: mirror surface temperature outside the optical cavity.

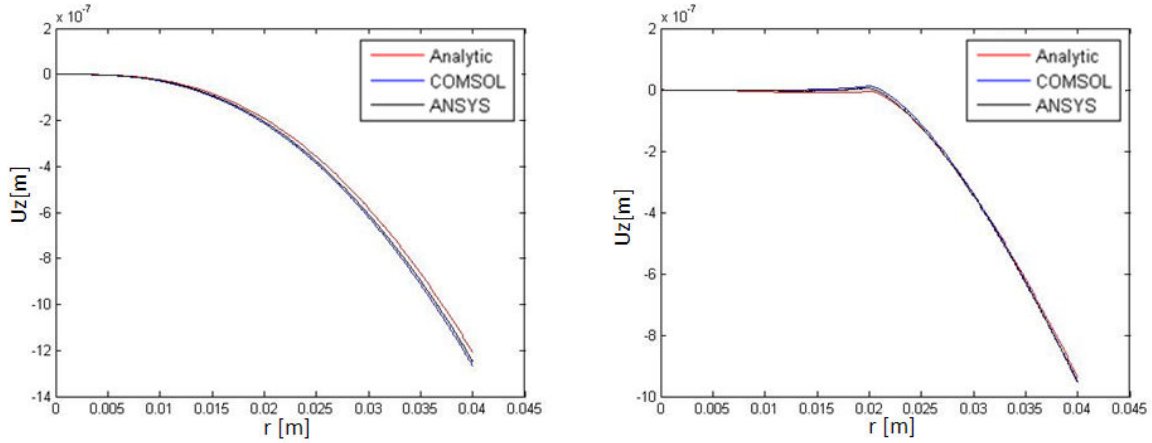

Figure 4.18: Displacements for the TCS of section (4.5), with $T_1 = 600$ K - SIPHORE mirror geometry. Absorption coefficient 0.3ppm. Intracavity power 3MW. Environment temperature T_0=300K, mirror edge temperature fixed at T_1=600K, ring heater fixing the temperature of the mirror back surface between $r = 0.02$ m and $r = 0.04$ m at T_1=600K. **Left panel**: mirror surface displacement inside the optical cavity. **Right panel**: mirror surface displacement outside the optical cavity.

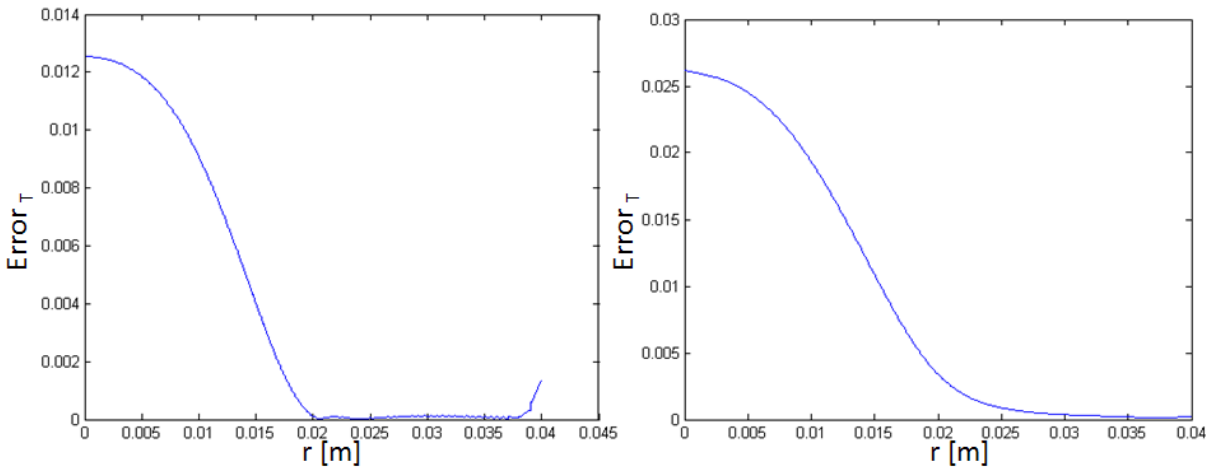

Figure 4.19: Percent error for the analytically calculated temperature field with respect to the numerically calculated one, for the TCS in section (4.5), with $T_1 = 600$K. Mirror front surface. - The reported errors are obtained through the application of equation (4.2) and they concern the data of the left panel of picture (4.17). **Left panel**: percent error of the analytical calculations with respect to the ones performed with ANSYS, as far as the mirror surface temperature inside the optical cavity is concerned. **Right panel**: percent error of the analytical calculations with respect to the ones performed with COMSOL, as far as the mirror surface temperature inside the optical cavity is concerned.

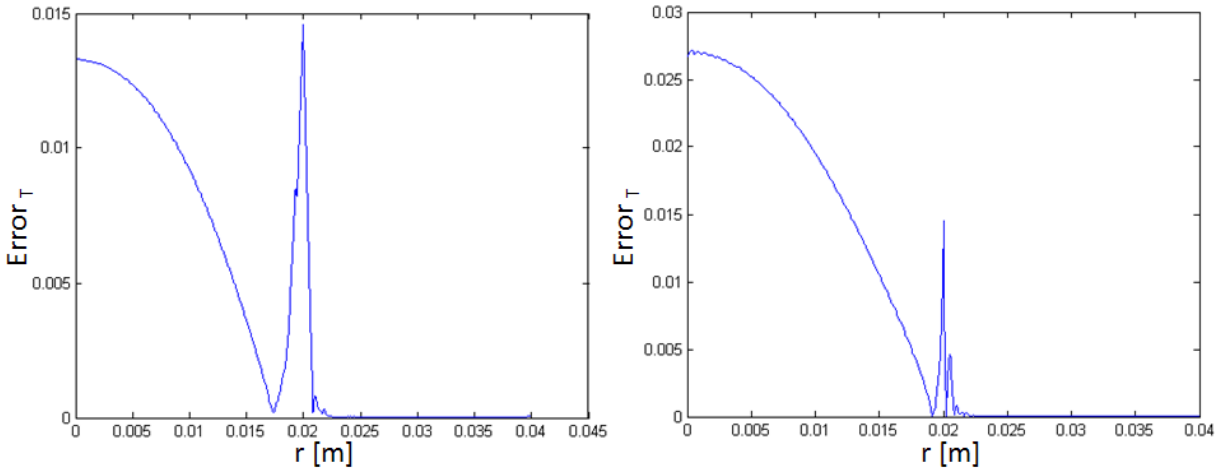

Figure 4.20: Percent error for the analytically calculated temperature field with respect to the numerically calculated one, for the TCS in section (4.5), with $T_1 = 600$K. Mirror rear surface. - The reported errors are obtained through the application of equation (4.2) and they concern the data of the right panel of picture (4.17). **Left panel**: percent error of the analytical calculations with respect to the ones performed with ANSYS, as far as the mirror surface temperature outside the optical cavity is concerned. **Right panel**: percent error of the analytical calculations with respect to the ones performed with COMSOL, as far as the mirror surface temperature outside the optical cavity is concerned.

4.6 Fixed temperature on the mirror edges, one external ring heater and a separated central disk heater

In this section, the good agreement between the analytical calculations for the TCS described in section 3.2.5 and the numerical simulations is illustrated. In this respect, in figures 4.21, 4.22, the results are showed for the configuration where a central disk heater fixes the temperature of the mirror at T_2 =320K, between $r = 0$cm and $r = 0.01$cm, an external ring heater sets the temperature of the mirror at $T_1 = 350$K, between $r = 0.03$m and $r = 0.04$m, and the edges of the mirror are kept at $T_1 = 350$K. From the pictures, it is already possible to perceive the concordance of the analytical solutions with the numerical ones. However, a more quantitative analysis is carried on with the application of equation (4.1), for evaluating the error associated with the analytical values of the mirror surface displacement vectors, and of equation (4.2), to obtain the percent errors associated with the analytically determined mirror surface temperature fields. The results are reported in table (4.8) and in pictures (4.23), (4.24). As the errors between the numerical and the analytical solutions are smaller than the software error, the MATLAB program, based on analytical calculations, is validated.

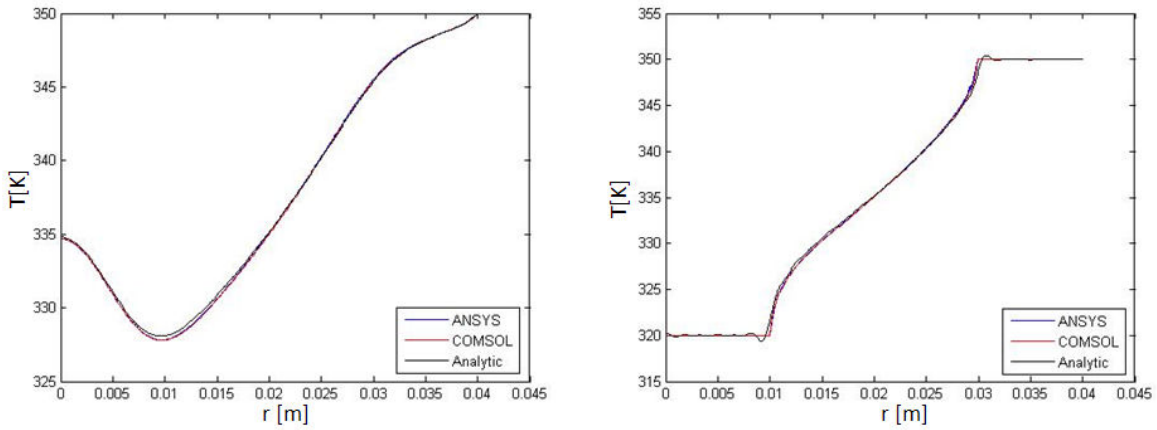

Figure 4.21: Temperature field validation for the TCS of section (4.6) - SIPHORE mirror geometry. Absorption coefficient 0.3ppm. Intracavity power 3MW. Environment temperature T_0=300K. Mirror edge temperature fixed at T_1=350K. Ring heater fixing the temperature of the mirror back surface, between $r = 0.03$ m and $r = 0.04$ m, at T_1=350K. Central disk heater fixing the temperature of the mirror back surface at T_2=320K, between $r = 0$ m and $r = 0.01$m, at T_3=320K. **Left panel**: mirror surface temperature inside the optical cavity. **Right panel**: mirror surface temperature outside the optical cavity.

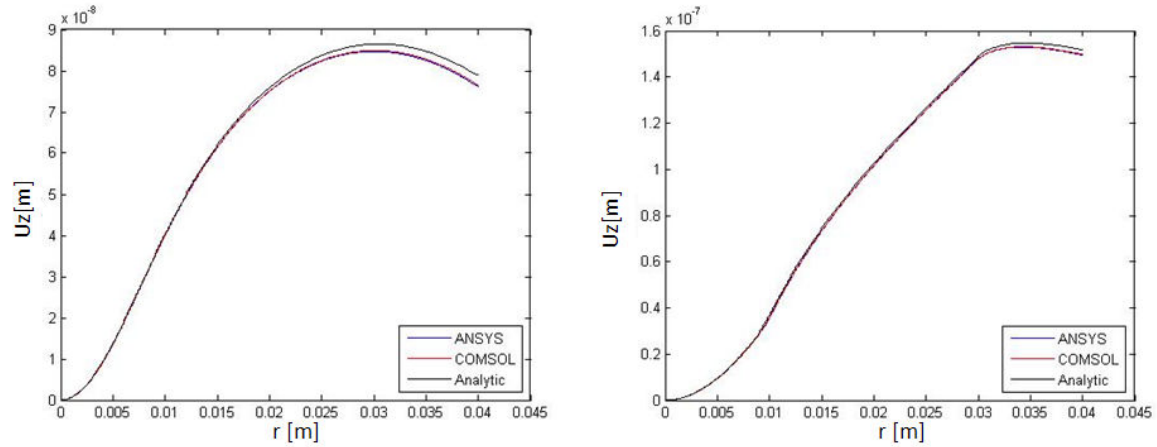

Figure 4.22: Mirror deformation validation for the TCS of section (4.6) - SIPHORE mirror geometry. Absorption coefficient 0.3ppm. Intracavity power 3MW. Environment temperature T_0=300K. Mirror edge temperature fixed at T_1=350K. Ring heater fixing the temperature of the mirror back surface, between $r = 0.03$ m and $r = 0.04$ m, at T_1=350K. Central disk heater fixing the temperature of the mirror back surface, between $r = 0$ m and $r = 0.01$m, at T_3=320K. **Left panel**: mirror surface displacement inside the optical cavity. **Right panel**: mirror surface displacement outside the optical cavity.

	Error
Mirror surface distortion inside the cavity ANSYS-analytic result comparison	2.0×10^{-2}
Mirror surface distortion inside the cavity COMSOL-analytic result comparison	2.0×10^{-2}
Mirror surface distortion outside the cavity ANSYS-analytic result comparison	1.0×10^{-2}
Mirror surface distortion outside the cavity COMSOL-analytic result comparison	1.0×10^{-2}

Table 4.8: Error estimation between analytical and numerical calculations for the TCS of section (4.6) - The values of the reported errors concern the mirror surface displacement vectors of picture (4.22) and they are evaluated by applying equation 4.1.

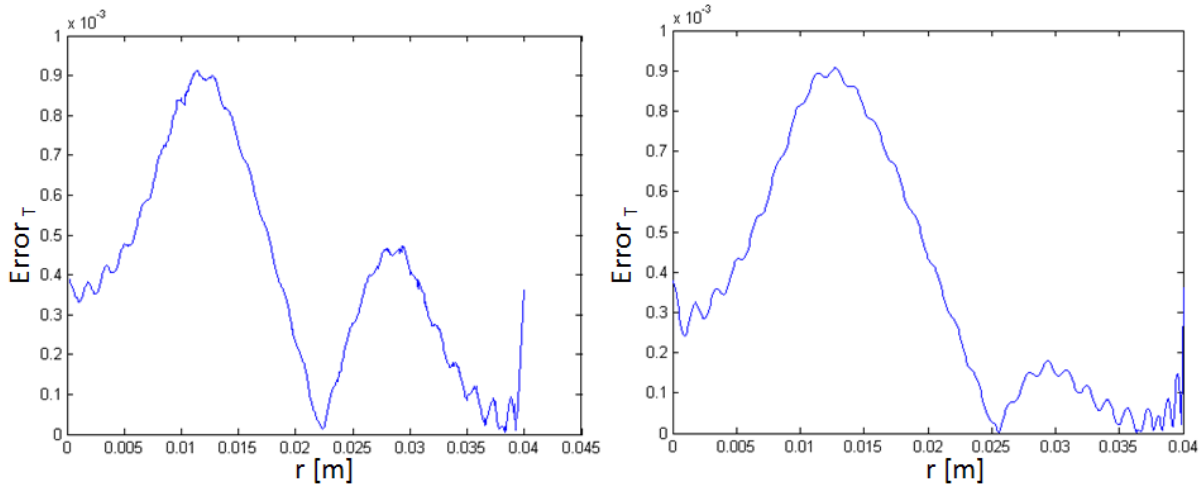

Figure 4.23: Percent error for the analytically calculated temperature field with respect to the numerically calculated one, for the TCS in section (4.6). Mirror front surface. - The reported errors are obtained through the application of equation (4.2) and they concern the data of the left panel of picture (4.21). **Left panel**: percent error of the analytical calculations with respect to the ones performed with ANSYS, as far as the mirror surface temperature inside the optical cavity is concerned. **Right panel**: percent error of the analytical calculations with respect to the ones performed with COMSOL, as far as the mirror surface temperature inside the optical cavity is concerned.

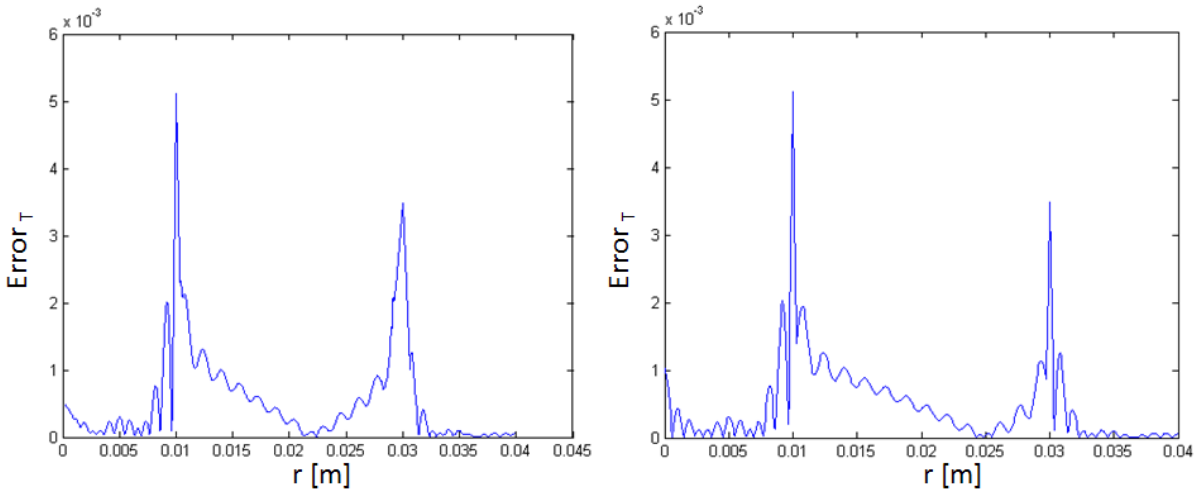

Figure 4.24: Percent error for the analytically calculated temperature field with respect to the numerically calculated one, for the TCS in section (4.6). Mirror rear surface. - The reported errors are obtained through the application of equation (4.2) and they concern the data of the right panel of picture (4.21).**Left panel**: percent error of the analytical calculations with respect to the ones performed with ANSYS, as far as the mirror surface temperature outside the optical cavity is concerned. **Right panel**: percent error of the analytical calculations with respect to the ones performed with COMSOL, as far as the mirror surface temperature outside the optical cavity is concerned.

4.7 Fixed temperature on the mirror edges, one external ring heater and a central disk heater

The TCS analytically analyzed in section (3.2.6) will be validate in the following. With this aim, in figures 4.25, 4.26, the results are reported for the configuration where a central disk fixes the temperature of the mirror at T_2 =540K, between $r = 0$m and $r = 0.01$m, an external ring heater sets the temperature of the mirror at $T_1 = 500$K, between $r = 0.01$m and $r = 0.04$m, and the edges of the mirror are kept at $T_1 = 500$K. By checking the figures, it is possible to perceive the concordance between analytical and numerical results. For a more quantitative study of the error associated with the analytically calculated mirror surface displacement vectors, equation (4.1) is used and the outcomes are given in table (4.9). As far as the percent errors on the mirror surface temperature field are concerned, they are evaluated through equation (4.2) and the results are showed in pictures (4.27), (4.28). The presented analysis allows to state the concordance between the analytical solutions and the numerical ones, for the TCS considered in this section. It is worth noticing that picture (4.28) shows a peak for the percent error on the analytically calculated mirror temperature field, in correspondence to the change of

temperature, i.e. at $r = 0.01$ m, for the considered example. This is due to the mathematical formalism used to describe the temperature field. Indeed, on the rear side of the mirror, the imposed temperature is a step function of the mirror radius and it appears that the description of such a function on a Bessel function base presents larger errors in correspondence to the step of the function. It is possible to decrease this effect, by increasing the number of terms entering the function development summation (see chapter (3)). In conclusion, for the case of the TCS taken into account in this section, the percent error on the analytically calculated temperature field is always smaller than the one of the software (COMSOL and ANSYS), hence, the error due to the function development on a Bessel function base is acceptable. It is observed that, the same feature remarked for picture (4.28) is present in pictures (4.16), (4.20) and (4.24).

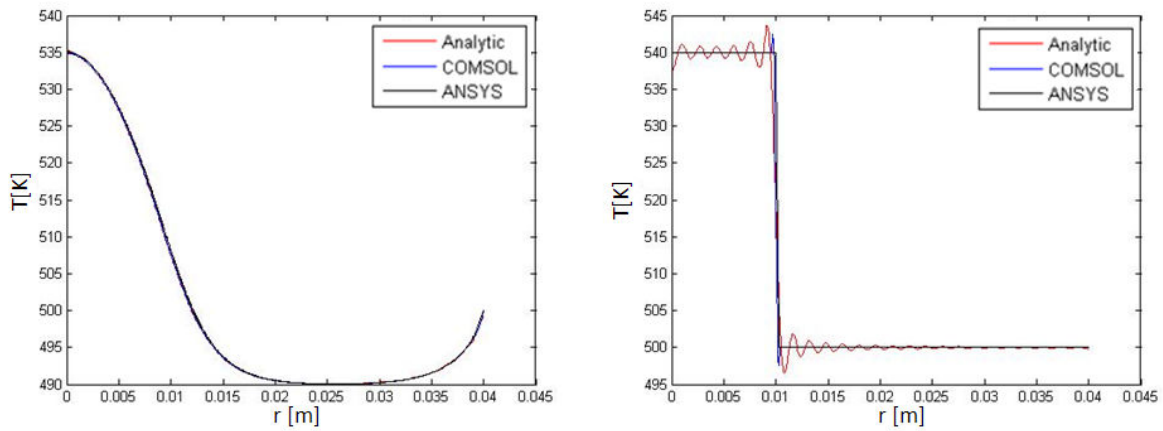

Figure 4.25: Temperature field validation for the TCS of section (4.7) - SIPHORE mirror geometry. Absorption coefficient 0.3ppm. Intracavity power 3MW. Environment temperature T_0=300K. Mirror edge temperature fixed at T_1=500K. Ring heater fixing the temperature of the mirror back surface, between $r = 0.01$m and $r = 0.04$m, at T_1=500K. Central disk heater fixing the temperature of the mirror back surface at T_2=540K, between $r = 0$ m and $r = 0.01$m. **Left panel**: mirror surface temperature inside the optical cavity. **Right panel**: mirror surface temperature outside the optical cavity.

4.8 Fixed temperature on the mirror edges, three external ring heaters and a central disk heater

This section will verify the results concerning the TCS described in section (3.2.7). To do this, the following configuration will be addressed: edge mirror temperature fixed at T_1 =400K; one ring heater fixing the mirror temperature at T_1 =400K, between $r = 0.02$m and $r = 0.04$m; one

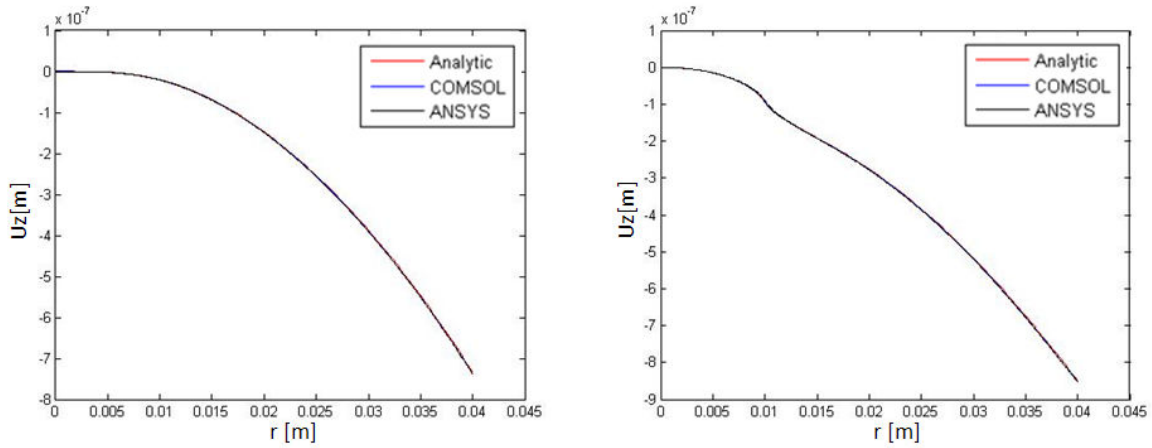

Figure 4.26: Displacement validation for the TCS of section (4.7) - SIPHORE mirror geometry. Absorption coefficient 0.3ppm. Intracavity power 3MW. Environment temperature T_0=300K. Mirror edge temperature fixed at T_1=500K. Ring heater fixing the temperature of the mirror back surface, between $r = 0.01$m and $r = 0.04$m, at T_1=500K. Central disk heater fixing the temperature of the mirror back surface at T_2=540K, between $r = 0$m and $r = 0.01$m. **Left panel**: mirror surface displacement inside the optical cavity. **Right panel**: mirror surface displacement outside the optical cavity.

	Error
Mirror surface distortion inside the cavity ANSYS-analytic result comparison	7.2×10^{-3}
Mirror surface distortion inside the cavity COMSOL-analytic result comparison	5.7×10^{-3}
Mirror surface distortion outside the cavity ANSYS-analytic result comparison	7.3×10^{-3}
Mirror surface distortion outside the cavity COMSOL-analytic result comparison	6.2×10^{-3}

Table 4.9: Error estimation between analytical and numerical calculations for the TCS of section (4.7) - The values of the reported errors concern the mirror surface displacement vectors of picture (4.26) and they are evaluated by applying equation 4.1.

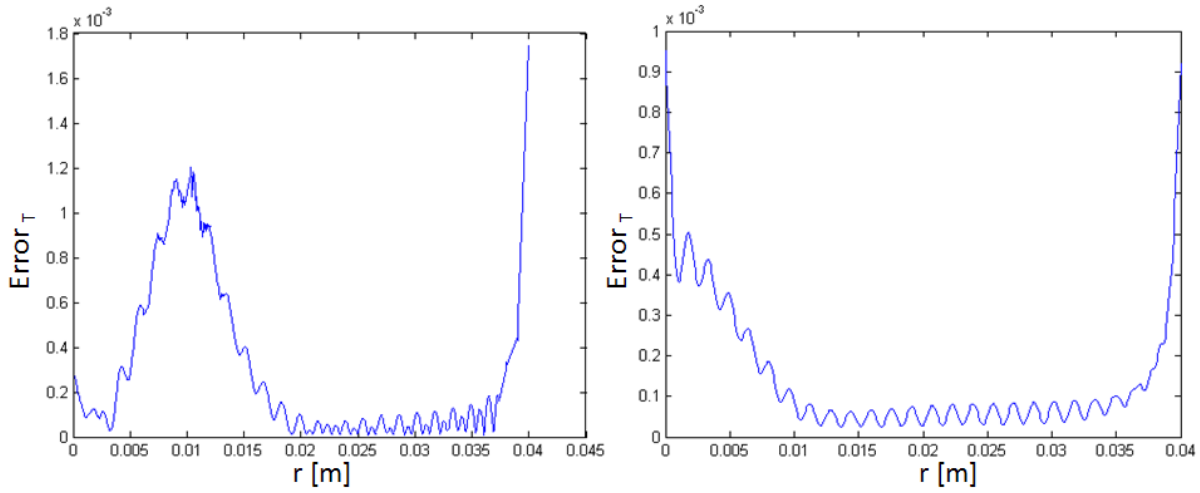

Figure 4.27: Percent error for the analytically calculated temperature field with respect to the numerically calculated one, for the TCS in section (4.7). Mirror front surface. - The reported errors are obtained through the application of equation (4.2) and they concern the data of the left panel of picture (4.25). **Left panel**: percent error of the analytical calculations with respect to the ones performed with ANSYS, as far as the mirror surface temperature inside the optical cavity is concerned. **Right panel**: percent error of the analytical calculations with respect to the ones performed with COMSOL, as far as the mirror surface temperature inside the optical cavity is concerned.

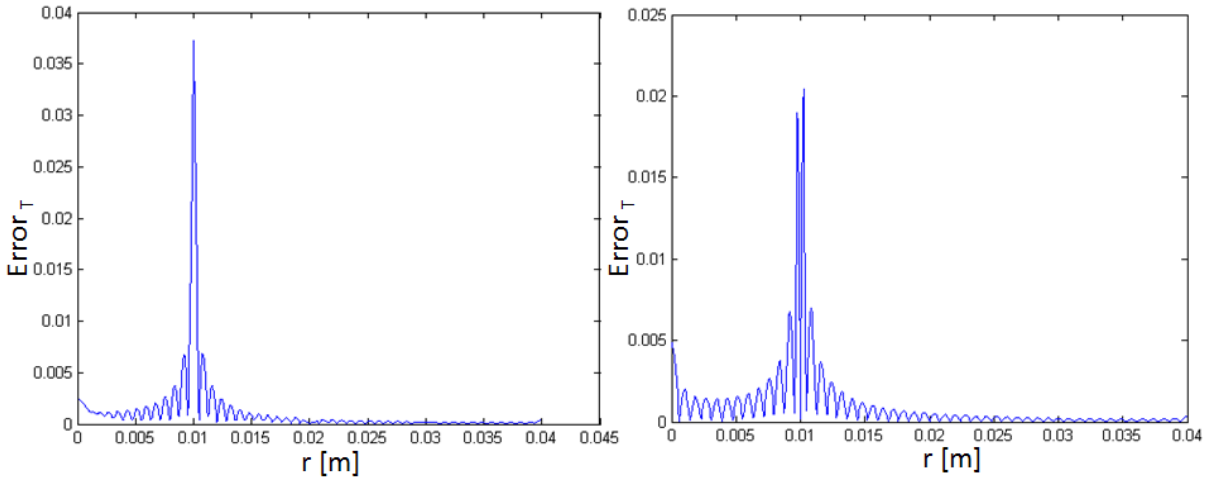

Figure 4.28: Percent error for the analytically calculated temperature field with respect to the numerically calculated one, for the TCS in section (4.7). Mirror rear surface. - The reported errors are obtained through the application of equation (4.2) and they concern the data of the right panel of picture (4.25). **Left panel**: percent error of the analytical calculations with respect to the ones performed with ANSYS, as far as the mirror surface temperature outside the optical cavity is concerned. **Right panel**: percent error of the analytical calculations with respect to the ones performed with COMSOL, as far as the mirror surface temperature outside the optical cavity is concerned.

ring heater fixing the mirror temperature at T_2 =410K between r = 0.01m and r = 0.02m; one ring heater fixing the mirror temperature at T_3 =430K, between r =0.005m and r = 0.01m; a disk heater fixing the mirror temperature at T_4 = 450K, between r =0m and r =0.005m. In figures 4.29, 4.30, the curves for both the analytical calculations and the numerical calculations are reported, as far as mirror surface temperature fields and mirror surface displacement vectors are concerned. For a quantitative analysis of the departure of the analytical solutions from the numerical ones, equation (4.1) and equation (4.2) are applied to evaluate the errors on the mirror surface displacement vectors and on the mirror surface temperature fields, respectively. The results are reported in table (4.10) and in pictures (4.31), (4.32). The obtained error values allow to state the validity of the analytical calculation for the TCS considered considered in this section.

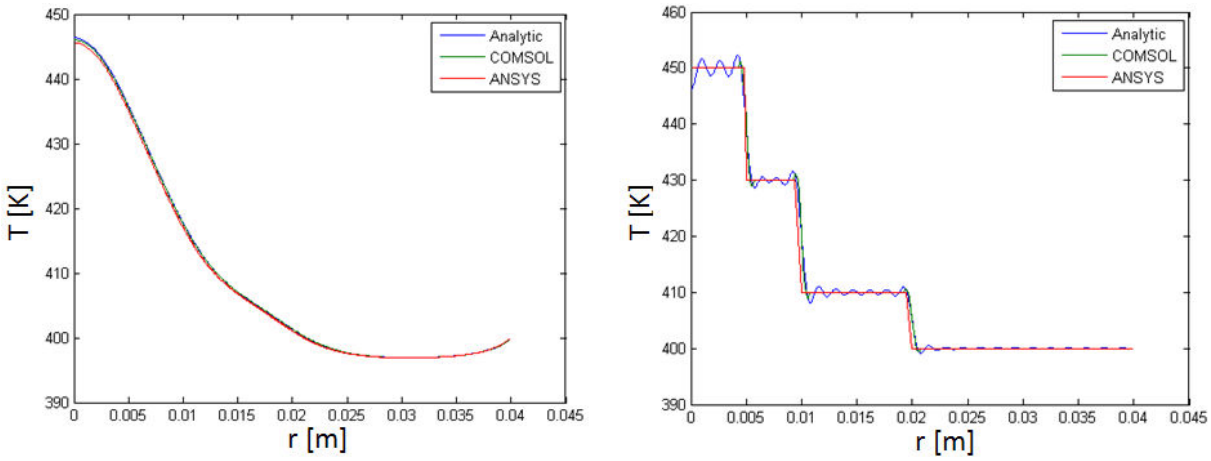

Figure 4.29: Temperature field validation for the TCS in section (4.8) - SIPHORE mirror geometry. Absorption coefficient 0.3ppm. Intracavity power 3MW. Environment temperature T_0=300K, edge mirror temperature fixed at T_1 =400K; one ring heater fixing the mirror temperature at T_1 =400K, between r = 0.02m and r = 0.04m; one ring heater fixing the mirror temperature at T_2 =410K between r = 0.01m and r = 0.02m; one ring heater fixing the mirror temperature at T_3 =430K, between r =0.005m and r = 0.01m; a disk heater fixing the mirror temperature at T_4 = 450K, between r =0 m and r =0.005m. **Left panel**: mirror surface temperature inside the optical cavity. **Right panel**: mirror surface temperature outside the optical cavity.

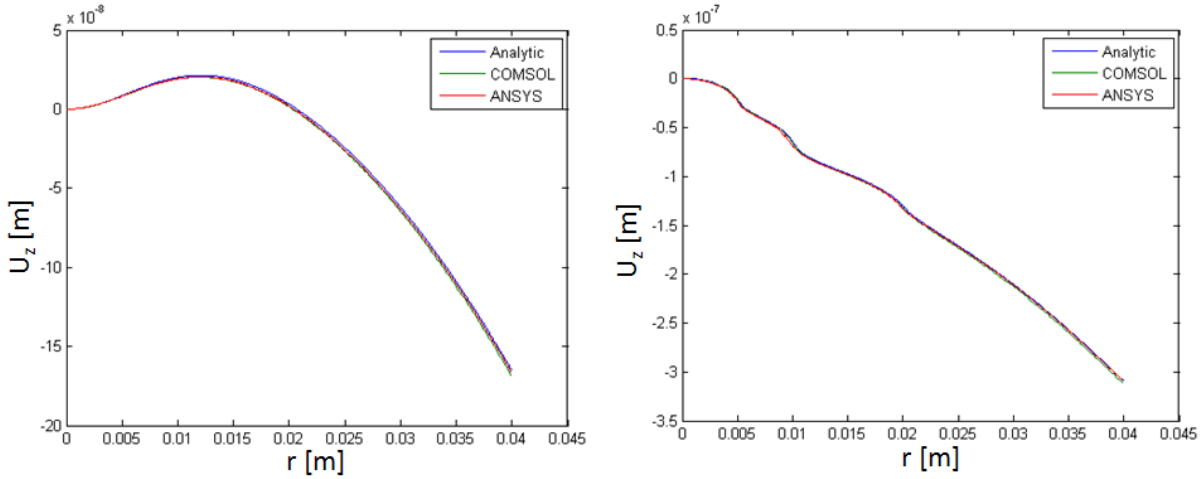

Figure 4.30: Mirror displacement validation for the TCS in section (4.8) - SIPHORE mirror geometry. Absorption coefficient 0.3ppm. Intracavity power 3MW. Environment temperature T_0=300K, edge mirror temperature fixed at T_1 =400K; one ring heater fixing the mirror temperature at T_1 =400K, between r = 0.02m and r = 0.04m; one ring heater fixing the mirror temperature at T_2 =410K between r = 0.01m and r = 0.02m; one ring heater fixing the mirror temperature at T_3 =430K, between r =0.005m and r = 0.01m; a disk heater fixing the mirror temperature at T_4 = 450K, between r =0 m and r =0.005m. **Left panel**: mirror surface displacement inside the optical cavity. **Right panel**: mirror surface displacement outside the optical cavity.

	Error
Mirror surface distortion inside the cavity ANSYS-analytic result comparison	1.0×10^{-2}
Mirror surface distortion inside the cavity COMSOL-analytic result comparison	2.0×10^{-2}
Mirror surface distortion outside the cavity ANSYS-analytic result comparison	1.0×10^{-2}
Mirror surface distortion outside the cavity COMSOL-analytic result comparison	2.0×10^{-2}

Table 4.10: Error estimation between analytical and numerical calculations for the TCS of section (4.8) - The values of the reported errors concern the mirror surface displacement vectors of picture (4.30) and they are evaluated by applying equation 4.1.

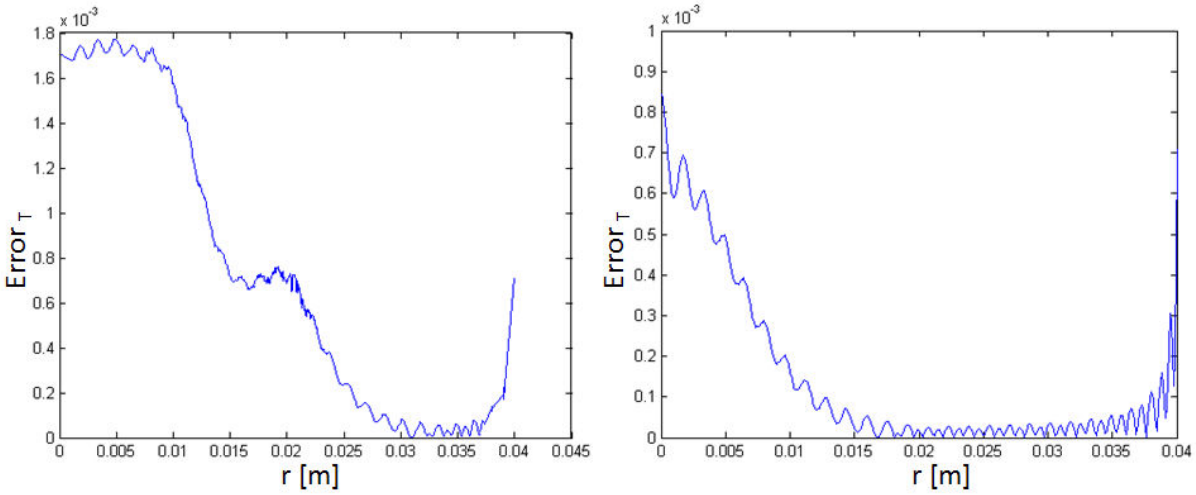

Figure 4.31: Percent error for the analytically calculated temperature field with respect to the numerically calculated one, for the TCS in section (4.8). Mirror front surface. - The reported errors are obtained through the application of equation (4.2) and they concern the data of the left panel of picture (4.29). **Left panel**: percent error of the analytical calculations with respect to the ones performed with ANSYS, as far as the mirror surface temperature inside the optical cavity is concerned. **Right panel**: percent error of the analytical calculations with respect to the ones performed with COMSOL, as far as the mirror surface temperature inside the optical cavity is concerned.

4.9 Fixed temperature on the mirror edges, one ring heaters, mechanical fixation on the mirror edges and on the mirror surface

The TCS illustrated in section (3.4.1) will be now considered, in order to validate the analytical calculations on which the results are based. In particular, the considered configuration for the analytical case is the following: mirror edge temperature fixed at T_1=330K, ring heater fixing the temperature of the mirror on the back surface at T_1=330K, between r=0.02 m and r =0.04 m, null displacement on the mirror edge, in r=0.04 cm, and null displacement vector average on the mirror surface between, r=0.039 m and r=0.04 m, both for the internal and the external face. As far as the numerical results are concerned, they are obtained by keeping exactly the same conditions of the analytical case, but the one related to the cancellation of the displacement vector average on the mirror surfaces. Indeed, for the numerical case it is assumed that the displacement vector itself is null in the same region where, in the analytical calculations, the average of the displacement vector is set to zero. The results for the numerical

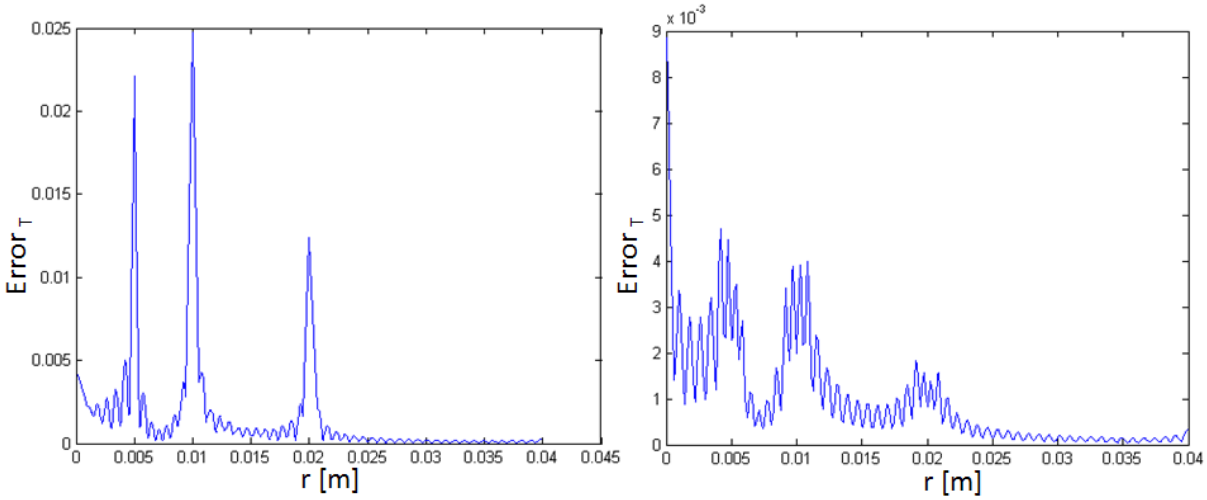

Figure 4.32: Percent error for the analytically calculated temperature field with respect to the numerically calculated one, for the TCS in section (4.8). Mirror rear surface. - The reported errors are obtained through the application of equation (4.2) and they concern the data of the right panel of picture (4.29). **Left panel**: percent error of the analytical calculations with respect to the ones performed with ANSYS, as far as the mirror surface temperature outside the optical cavity is concerned. **Right panel**: percent error of the analytical calculations with respect to the ones performed with COMSOL, as far as the mirror surface temperature outside the optical cavity is concerned.

and the analytical calculations are illustrated in figures (4.33), (4.34). The behavior of the curves analytically and numerically calculated is reasonably similar, then the differences presented by the pictures should be attributed to the different condition holding on the borders of the mirror surfaces. Indeed, it is possible to check that the disagreement between numerical and analytical results becomes more consistent when the condition of null displacement vector, for the numerical case, and the condition of null displacement vector average, for the analytical case, is imposed on a larger portion of the mirror surfaces, so that the numerical calculations become unable to validate the analytical results, see figures (4.35), (4.36). It is important to stress that the simulations performed with ANSYS pose a problem for this TCS, as their results for the mirror deformation do not agree with the COMSOL ones. For the sake of completeness, the same curves of figures (4.33), (4.34), (4.35), (4.36) are reported in figures (4.37), (4.38), (4.39), (4.40) together with the ANSYS curves. It is observed that the results concerning the temperature fields agree for ANSYS, COMSOL and the analytical method. Nevertheless, it is not necessary to quantitatively study the departure of the analytically calculated temperature fields from the numerically calculated ones. Indeed, the applied MATLAB code for the analytical calculation of

the temperature is the one which has been already validated in section (4.5). It is also noticed that the difference between numerical and analytical results for the mirror distortion increase both for ANSYS and COMSOL, when the mirror region interested by the mechanical fixation is larger. However, the validation of the analytical results through which the mirror deformation is calculated is uncertain, because of the differences between ANSYS and COMSOL solutions. In conclusion, the departure of the analytically calculated mirror surface displacement vectors from the ones numerically calculated is estimated through the application of formula (4.1), for the data concerning pictures (4.38), (4.40). The results are reported in tables (4.11), (4.12), respectively.

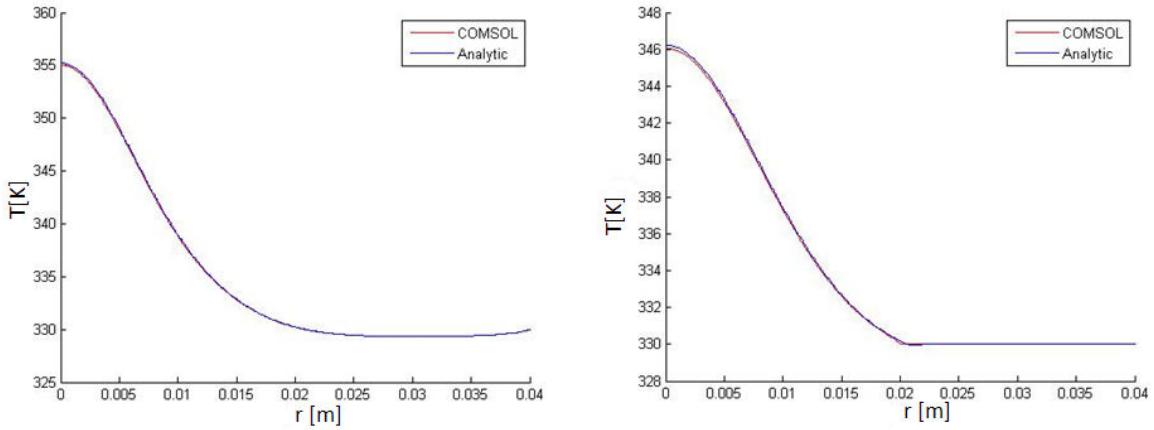

Figure 4.33: Temperature field validation for the TCS in section (4.9) - SIPHORE mirror geometry. Absorption coefficient 0.3ppm. Intracavity power 3MW. Environment temperature T_0=300K, mirror edge temperature fixed at T_1=330K, ring heater fixing the temperature of the mirror back surface between $r = 0.02$ m and $r = 0.04$ m at T_1=330K. Fixed mirror edge. Null surface displacement for both the internal and the external surface, between $r = 0.039$ m and $r = 0.04$ m. **Left panel**: mirror surface temperature inside the optical cavity. **Right panel**: mirror surface temperature outside the optical cavity.

4.10 Fixed temperature on the mirror edges, one ring heaters and mechanical fixation on the mirror edges

In this section, the comparison between the analytical calculation results for TCS introduced in section (3.4.2) and the numerical solutions will be analyzed. In particular, the considered configuration is the following: mirror edge temperature fixed at T_1=400K, ring heater fixing the temperature of the mirror on the back surface at T_1=400K, between r=0.02 m and r =0.04

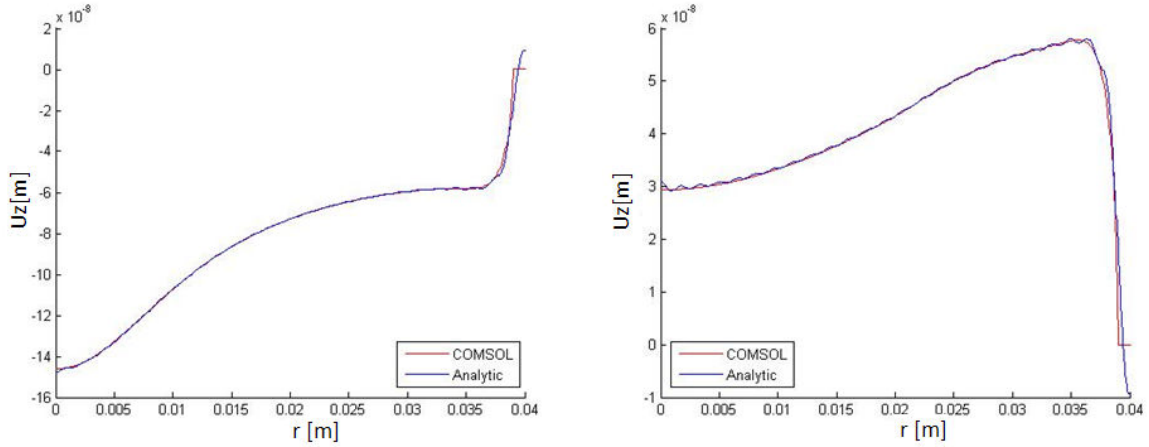

Figure 4.34: Mirror displacement validation for the TCS in section (4.9) - SIPHORE mirror geometry. Absorption coefficient 0.3ppm. Intracavity power 3MW. Environment temperature T_0=300K, mirror edge temperature fixed at T_1=330K, ring heater fixing the temperature of the mirror back surface between $r = 0.02$ cm and $r = 0.04$ m at T_1=330K. Fixed mirror edge. Null surface displacement for both the internal and the external surface, between $r = 0.039$ cm and $r = 0.04$ cm. **Left panel**: mirror surface displacement inside the optical cavity. **Right panel**: mirror surface displacement outside the optical cavity.

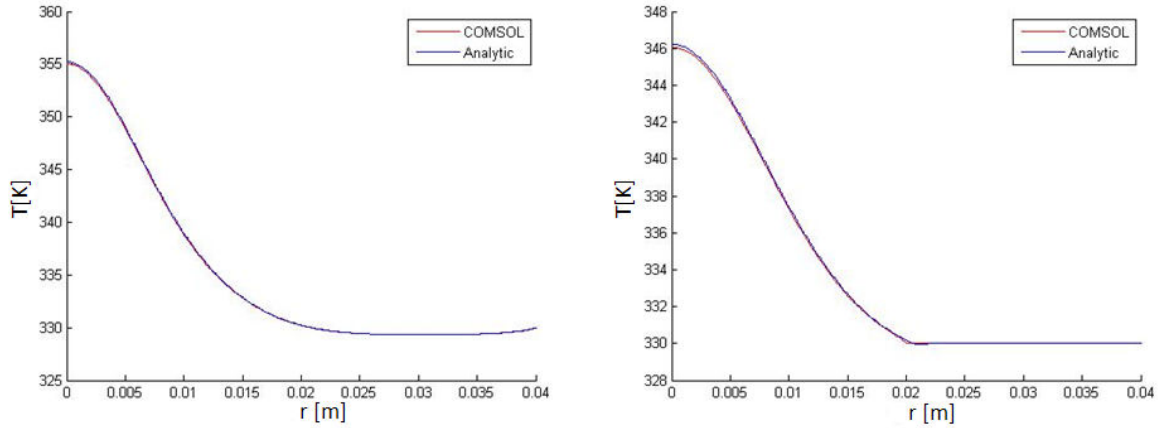

Figure 4.35: Temperature field for the TCS in section (4.9) - SIPHORE mirror geometry. Absorption coefficient 0.3ppm. Intracavity power 3MW. Environment temperature T_0=300K, mirror edge temperature fixed at T_1=330K, ring heater fixing the temperature of the mirror back surface between $r = 0.02$ cm and $r = 0.04$ m at T_1=330K. Fixed mirror edge. Null surface displacement for both the internal and the external surface, between $r = 0.03$ m and $r = 0.04$ m. **Left panel**: mirror surface temperature inside the optical cavity. **Right panel**: mirror surface temperature outside the optical cavity.

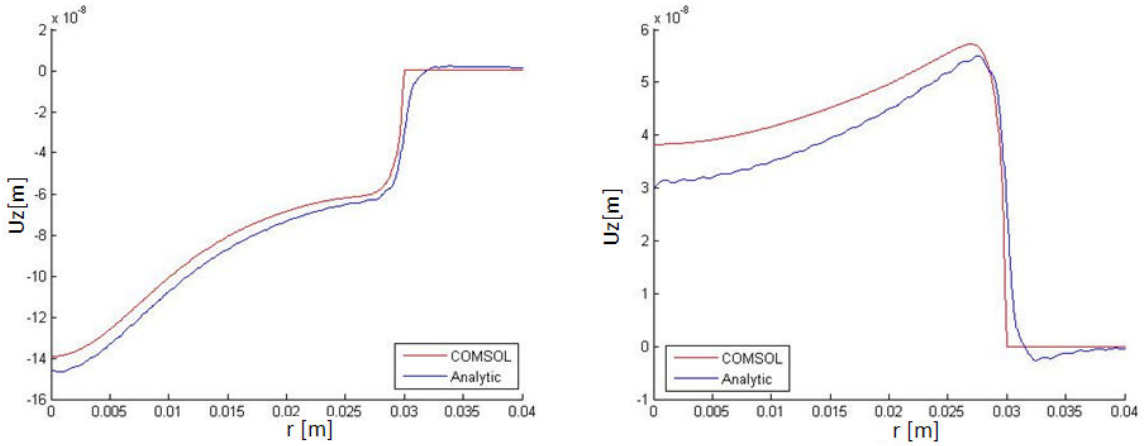

Figure 4.36: Mirror displacement for the TCS in section (4.9) - SIPHORE mirror geometry. Absorption coefficient 0.3ppm. Intracavity power 3MW. Environment temperature T_0=300K, mirror edge temperature fixed at T_1=330K, ring heater fixing the temperature of the mirror back surface between $r = 0.02$ m and $r = 0.04$ m at T_1=330K. Fixed mirror edge. Null surface displacement for both the internal and the external surface, between $r = 0.03$ m and $r = 0.04$ m. **Left panel**: mirror surface displacement inside the optical cavity. **Right panel**: mirror surface displacement outside the optical cavity.

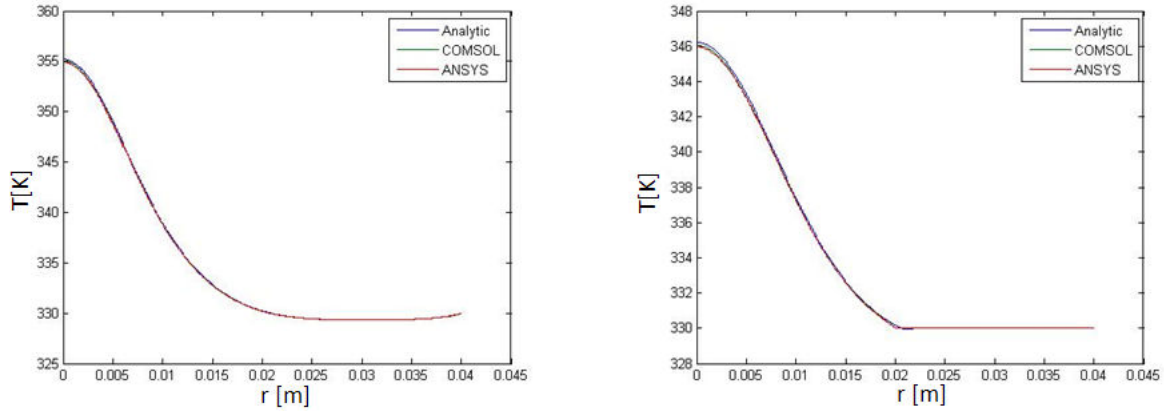

Figure 4.37: ANSYS results for the temperature field of the TCS in section (4.9) - SIPHORE mirror geometry. Absorption coefficient 0.3ppm. Intracavity power 3MW. Environment temperature T_0=300K, mirror edge temperature fixed at T_1=330K, ring heater fixing the temperature of the mirror back surface between $r = 0.02$ m and $r = 0.04$ m at T_1=330K. Fixed mirror edge. Null surface displacement for both the internal and the external surface, between $r = 0.039$ m and $r = 0.04$ m. **Left panel**: mirror surface temperature inside the optical cavity. **Right panel**: mirror surface temperature outside the optical cavity.

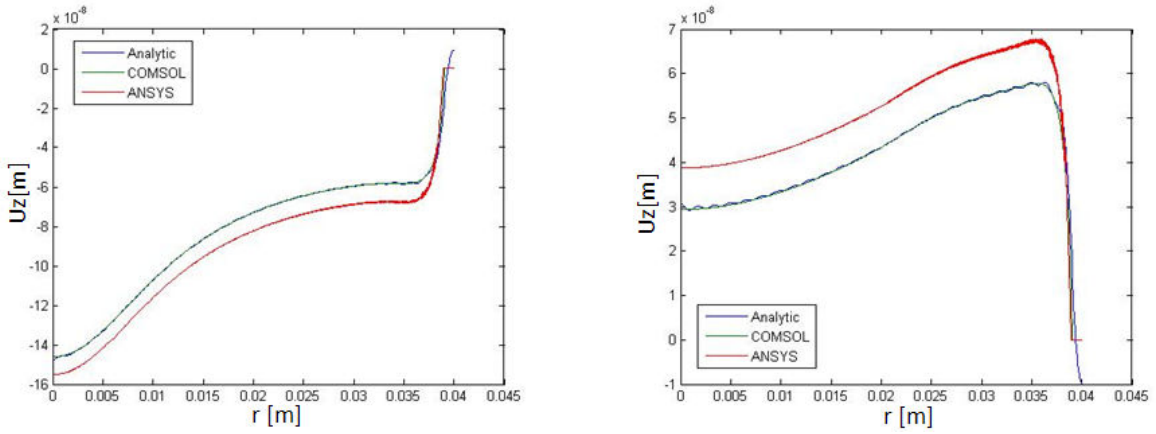

Figure 4.38: ANSYS results for the mirror displacement of the TCS in section (4.9) - SIPHORE mirror geometry. Absorption coefficient 0.3ppm. Intracavity power 3MW. Environment temperature T_0=300K, mirror edge temperature fixed at T_1=330K, ring heater fixing the temperature of the mirror back surface between $r = 0.02$ cm and $r = 0.04$ m at T_1=330K. Fixed mirror edge. Null surface displacement for both the internal and the external surface, between $r = 0.039$ cm and $r = 0.04$ cm. **Left panel**: mirror surface displacement inside the optical cavity. **Right panel**: mirror surface displacement outside the optical cavity.

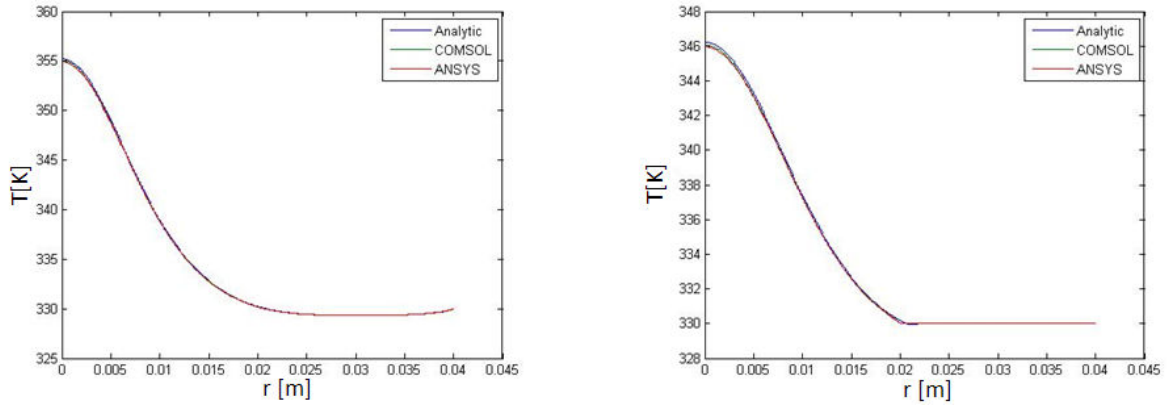

Figure 4.39: ANSYS results for the temperature field of the TCS in section (4.9) - SIPHORE mirror geometry. Absorption coefficient 0.3ppm. Intracavity power 3MW. Environment temperature T_0=300K, mirror edge temperature fixed at T_1=330K, ring heater fixing the temperature of the mirror back surface between $r = 0.02$ cm and $r = 0.04$ m at T_1=330K. Fixed mirror edge. Null surface displacement for both the internal and the external surface, between $r = 0.03$ m and $r = 0.04$ m. **Left panel**: mirror surface temperature inside the optical cavity. **Right panel**: mirror surface temperature outside the optical cavity.

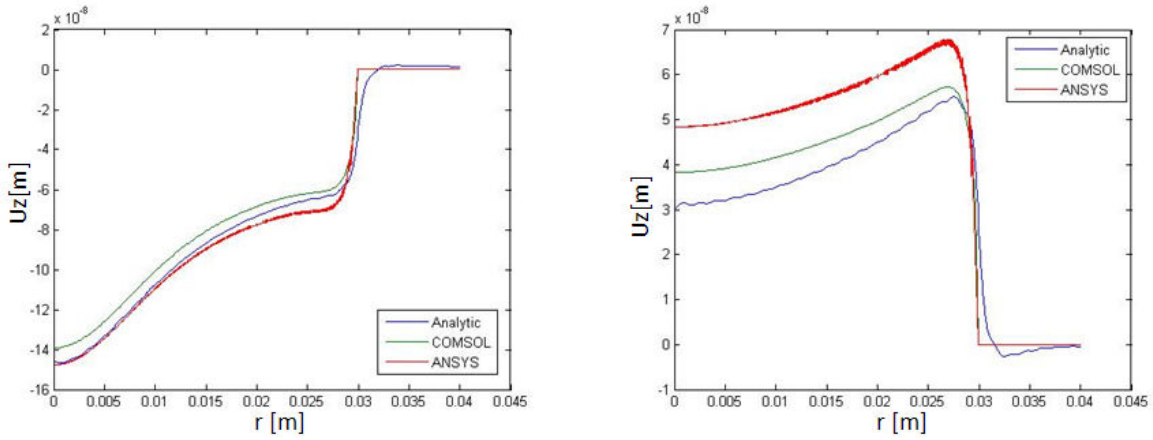

Figure 4.40: ANSYS results for the mirror displacement of the TCS in section (4.9) - SIPHORE mirror geometry. Absorption coefficient 0.3ppm. Intracavity power 3MW. Environment temperature T_0=300K, mirror edge temperature fixed at T_1=330K, ring heater fixing the temperature of the mirror back surface between $r = 0.02$ m and $r = 0.04$ m at T_1=330K. Fixed mirror edge. Null surface displacement for both the internal and the external surface, between $r = 0.03$ m and $r = 0.04$ m. **Left panel**: mirror surface displacement inside the optical cavity. **Right panel**: mirror surface displacement outside the optical cavity.

	Error
Mirror surface distortion inside the cavity ANSYS-analytic result comparison	7.0×10^{-2}
Mirror surface distortion inside the cavity COMSOL-analytic result comparison	3.3×10^{-2}
Mirror surface distortion outside the cavity ANSYS-analytic result comparison	9.6×10^{-2}
Mirror surface distortion outside the cavity COMSOL-analytic result comparison	5.0×10^{-2}

Table 4.11: Error estimation between analytical and numerical calculations for the TCS of section (4.9), and the data of picture (4.38) - The values of the reported errors concern the mirror surface displacement vectors and they are evaluated by applying equation (4.1).

	Error
Mirror surface distortion inside the cavity ANSYS-analytic result comparison	5.0×10^{-2}
Mirror surface distortion inside the cavity COMSOL-analytic result comparison	5.5×10^{-2}
Mirror surface distortion outside the cavity ANSYS-analytic result comparison	2.7×10^{-1}
Mirror surface distortion outside the cavity COMSOL-analytic result comparison	2.0×10^{-1}

Table 4.12: Error estimation between analytical and numerical calculations for the TCS of section (4.9), and the data of picture (4.40) - The values of the reported errors concern the mirror surface displacement vectors and they are evaluated by applying equation 4.1.

	Error
Mirror surface distortion inside the cavity ANSYS-analytic result comparison	9.1×10^{-3}
Mirror surface distortion inside the cavity COMSOL-analytic result comparison	7.1×10^{-3}
Mirror surface distortion outside the cavity ANSYS-analytic result comparison	2.0×10^{-2}
Mirror surface distortion outside the cavity COMSOL-analytic result comparison	1.0×10^{-2}

Table 4.13: Error estimation between analytical and numerical calculations for the TCS of section (4.10) - The values of the reported errors concern the mirror surface displacement vectors of picture (4.42) and they are evaluated by applying equation 4.1.

m, null displacement of the mirror edge in r=0.04 m. The curves for both the mirror surface displacement vectors and the mirror surface temperatures, for the numerical as well as the analytical calculations, are illustrated in figures (4.41), (4.42). From these pictures, it is already possible to understand the agreement between the numerical and the analytical solutions. Nevertheless, as customary, in order to quantify the differences between the two methods, equation (4.1) and equation (4.2) are applied and their results are reported in table (4.13) and in pictures (4.43), (4.44). By considering these last outcomes, it is possible to state the concordance between the analytical and the numerical calculations.

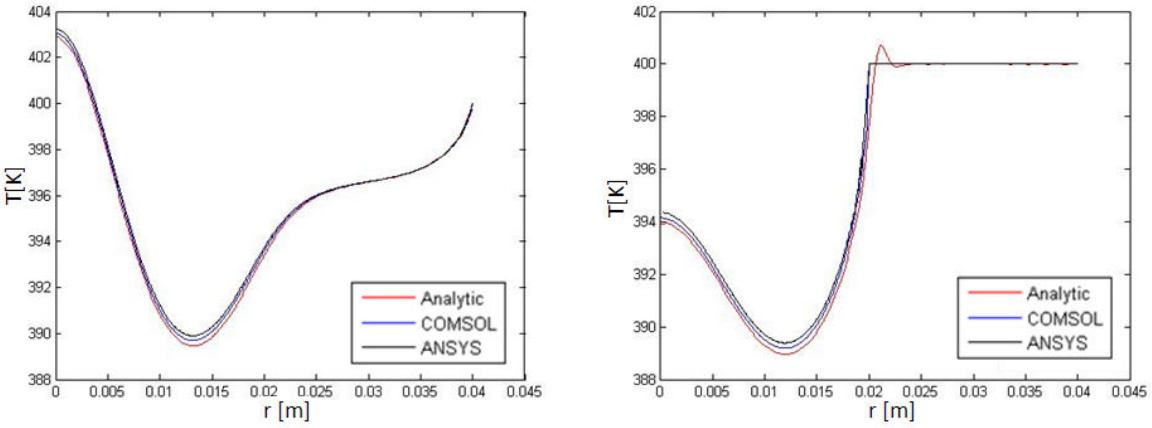

Figure 4.41: Temperature field validation for the TCS in section (4.10) - SIPHORE mirror geometry. Absorption coefficient 0.3ppm. Intracavity power 3MW. Environment temperature T_0=300K, mirror edge temperature fixed at T_1=400K, ring heater fixing the temperature of the mirror back surface between $r = 0.02$ m and $r = 0.04$ m at T_1=400K. Fixed mirror edge. **Left panel**: mirror surface temperature inside the optical cavity. **Right panel**: mirror surface temperature outside the optical cavity.

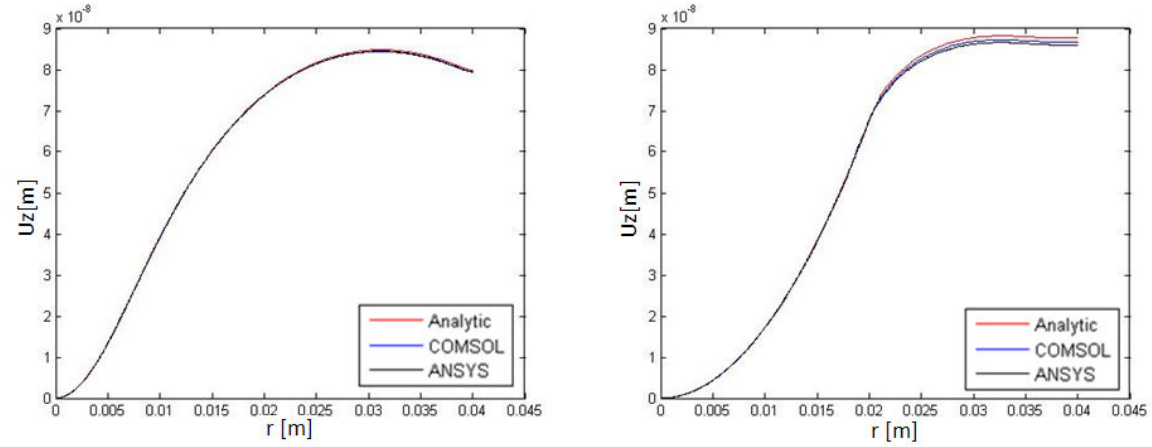

Figure 4.42: Mirror displacement validation for the TCS of section (4.10) - SIPHORE mirror geometry. Absorption coefficient 0.3ppm. Intracavity power 3MW. Environment temperature T_0=300K, mirror edge temperature fixed at T_1=400K, ring heater fixing the temperature of the mirror back surface between $r = 0.02$ m and $r = 0.04$ m at T_1=400K. Fixed mirror edge. **Left panel**: mirror surface displacement inside the optical cavity. **Right panel**: mirror surface displacement outside the optical cavity.

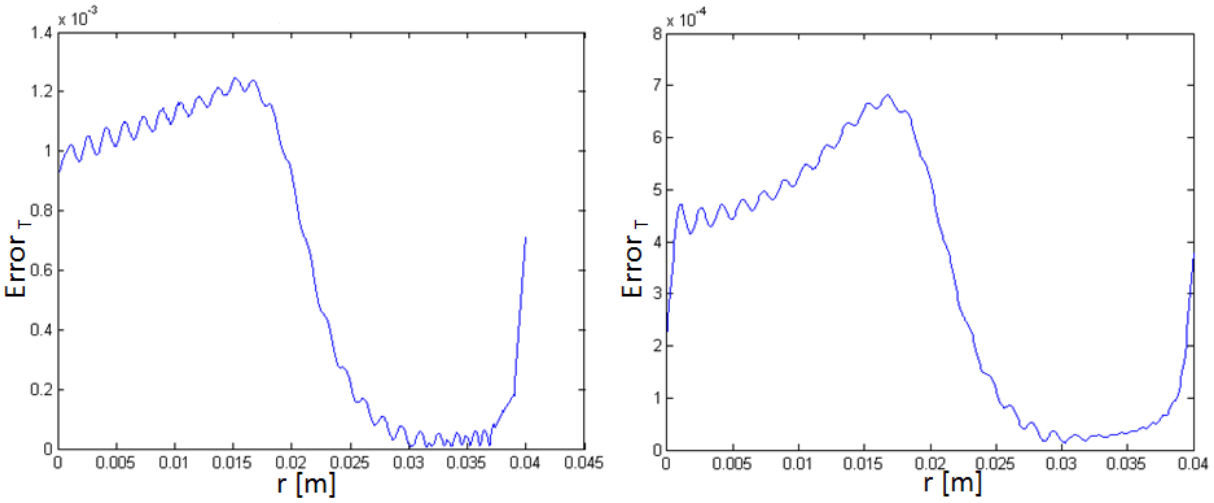

Figure 4.43: Percent error for the analytically calculated temperature field with respect to the numerically calculated one, for the TCS in section (4.10). Mirror front surface. - The reported errors are obtained through the application of equation (4.2) and they concern the data of the left panel of picture (4.41). **Left panel**: percent error of the analytical calculations with respect to the ones performed with ANSYS, as far as the mirror surface temperature inside the optical cavity is concerned. **Right panel**: percent error of the analytical calculations with respect to the ones performed with COMSOL, as far as the mirror surface temperature inside the optical cavity is concerned.

4.11 Seven external pressures applicable on the mirror rear side

The TCS considered in section (3.4.3) will now be addressed to show the good agreement of the analytical calculations with the numerical solutions. To do this, the following configuration will be fixed: mirror temperature configuration equal to the case analyzed in section (3.2.3), with the environment temperature T_0=300K, optical power absorbed by the mirror equal to 0.9W; pressure of 5000 Pa applied on the back side of the mirror on a ring between r =0.03m and r =0.04m and pressure of 1000 Pa applied on the same side of the mirror on a ring between r = 0.006m and r =0.016m. Inside the cavity, a pressure is present on a ring between r =0.038m and r =0.04m, so that the total force applied on the rear surface of the mirror has the same intensity of the one applied on the mirror surface internal to the cavity. For the other five pressures applicable on the rear side of the mirror, it has been chosen a null value. The curves obtained for both the numerical and the analytical calculations for the mirror displacements, inside and outside the optical cavity, are reported in figure (4.45). As far as the pressures applied on the mirror surfaces are concerned, the relative plots are reported in picture (4.46). It is observed that the analytical calculations for these mirror constraints are well in agreement with

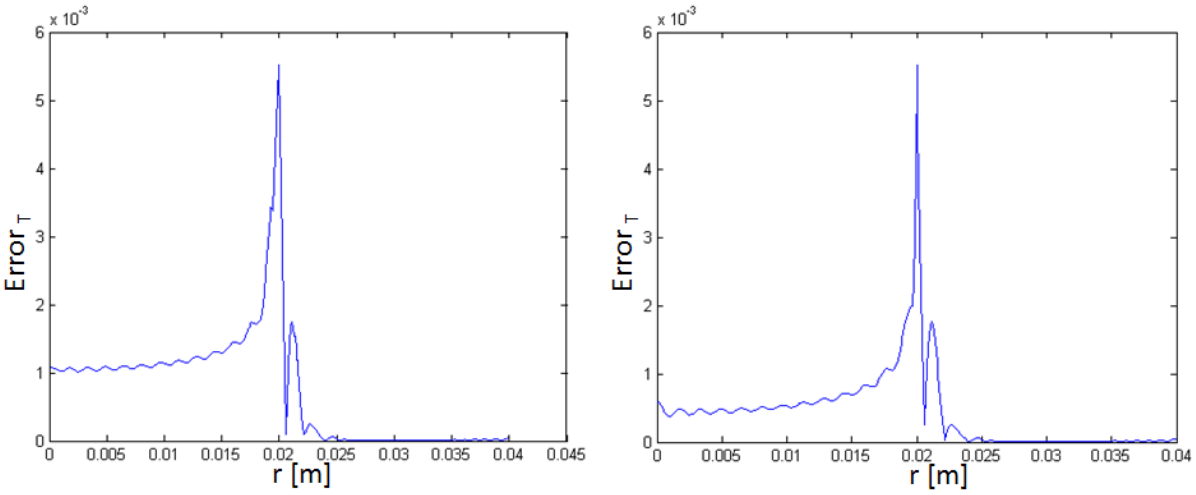

Figure 4.44: Percent error for the analytically calculated temperature field with respect to the numerically calculated one, for the TCS in section (4.10). Mirror rear surface. - The reported errors are obtained through the application of equation (4.2) and they concern the data of the right panel of picture (4.41). **Left panel**: percent error of the analytical calculations with respect to the ones performed with ANSYS, as far as the mirror surface temperature outside the optical cavity is concerned. **Right panel**: percent error of the analytical calculations with respect to the ones performed with COMSOL, as far as the mirror surface temperature outside the optical cavity is concerned.

the ANSYS ones, while the COMSOL calculations present differences both from the analytical ones and from the ANSYS ones. A quantitative estimation of the differences between the analytical and the numerical solutions for the mirror surface displacement vectors is carried on with the application of equation (4.1). The results are reported in table (4.14). As the calculated errors between analytical and numerical solutions are smaller then the numerical software error, both for ANSYS and COMSOL, it is possible to state the agreement between the analytical method and the numerical one. Nevertheless, it is observed that the errors estimated with respect to the COMSOL data are higher than the ones calculated with the ANSYS data. It is worth noticing that the analytical description of the mirror temperature field assumed for this TCS, as given in section (3.2.3), has been already verified in section (4.4). However, for the calculations of the TCS currently under study, the considered field of temperature has been written by using the zeros of the Bessel functions J_1, instead of the zeros of equation (3.33), as it is illustrated in section (3.4.3) and in appendix (C). Then, figures (4.47) is reported to show the concordance between the two analytical descriptions of the same temperature field. For a more quantitative analysis of the differences between the two calculation methods, at each value

of the mirror radius the following quantity is evaluated:

$$PE_T = \frac{|T_{zerosJ_1} - T|}{T}, \tag{4.3}$$

where PE_T indicate the percent error of the solution obtained by using the zeros of the Bessel function J_1 with respect to the solution obtained by using the zeros of equation (3.33), $T_{zerosJ1}$ is the temperature value as given by the calculations involving the zeros of the Bessel function J_1 and T is the temperature value as given by the calculations involving the zeros of equation (3.33). The results are reported in picture (4.48) and they confirme the agreement between the two methods to calculate the same temperature fields. As a consequence, the validation of the code presented in section (4.4) allows as well to validate the code based on the mathematical description of the temperature field in terms of the zeros of the Bessel function J_1.

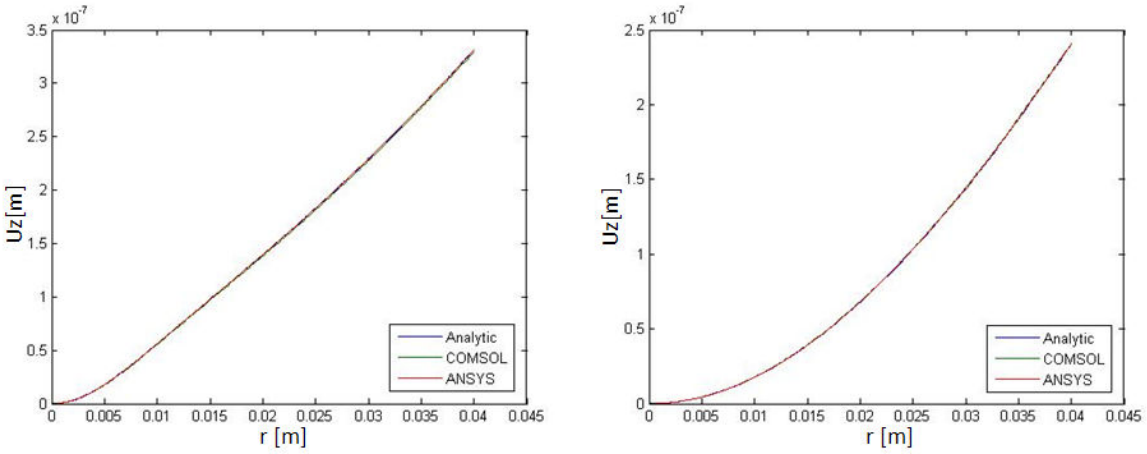

Figure 4.45: Mirror displacement validation for the TCS of section (4.11) - SIPHORE mirror geometry. Absorption coefficient 0.3ppm. Intracavity power 3MW. Environment temperature T_0=300K. Explanation within the text, in section (4.11) **Left panel**: mirror surface displacement inside the optical cavity. **Right panel**: mirror surface displacement outside the optical cavity.

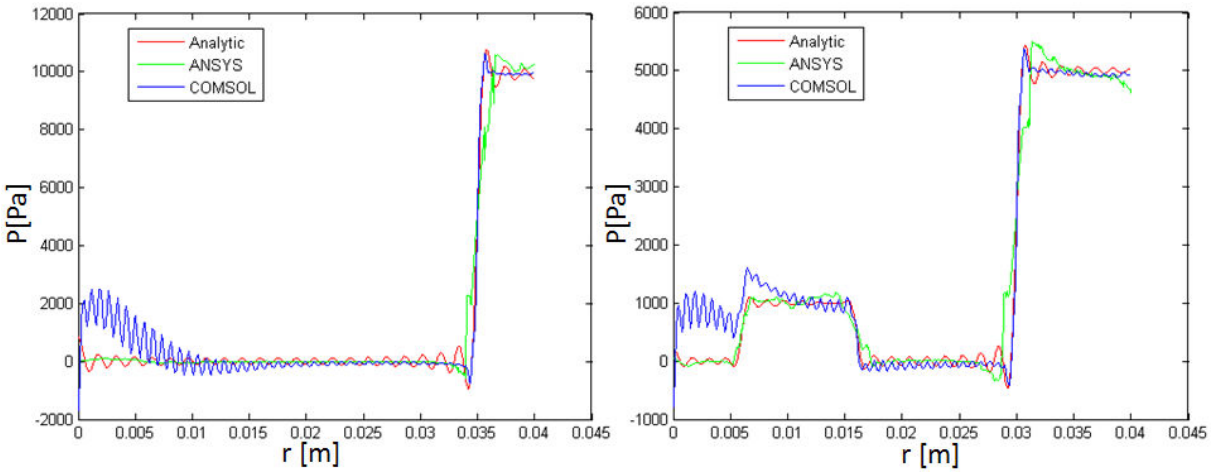

Figure 4.46: Description of the pressure applied on the mirror, for the TCS of section (4.11) - SIPHORE mirror geometry. Absorption coefficient 0.3ppm. Intracavity power 3MW. Environment temperature T_0=300K. Explanation within the text, in section (4.11) **Left panel**: pressure on the mirror surface inside the optical cavity. **Right panel**: pressure on the mirror surface outside the optical cavity.

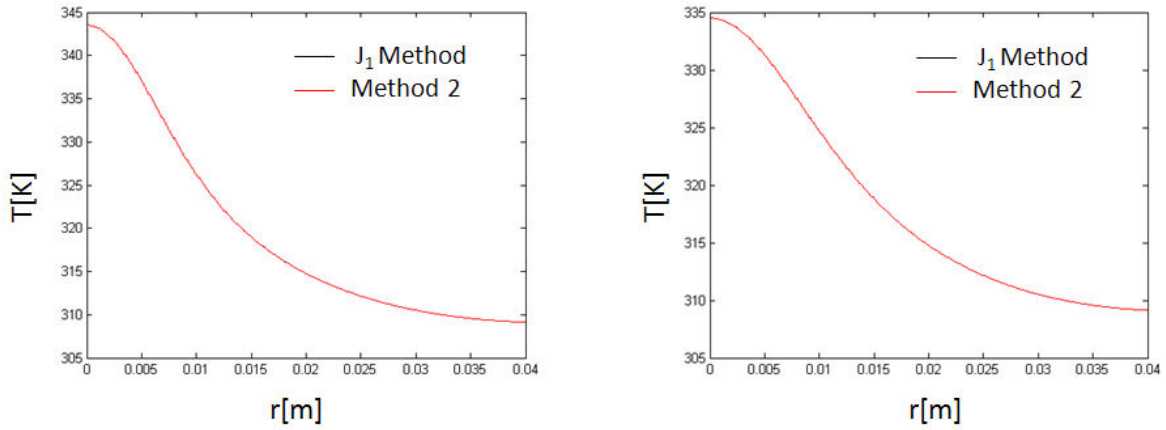

Figure 4.47: Temperature field validation for the TCS of section (4.11) - SIPHORE mirror geometry. Absorption coefficient 0.3ppm. Intracavity power 3MW. Environment temperature T_0=300K. The two panels represent the results for the surface temperatures of the mirror, as obtained when applying the method described in section (3.2.3), red line, and when applying the method described in section (3.4.3) and in appendix (C), black line. **Left panel**: mirror surface temperature inside the optical cavity. **Right panel**: mirror surface temperature outside the optical cavity.

	Error
Mirror surface distortion inside the cavity ANSYS-analytic result comparison	1.8×10^{-4}
Mirror surface distortion inside the cavity COMSOL-analytic result comparison	7.0×10^{-3}
Mirror surface distortion outside the cavity ANSYS-analytic result comparison	1.0×10^{-3}
Mirror surface distortion outside the cavity COMSOL-analytic result comparison	5.3×10^{-3}

Table 4.14: Error estimation between analytical and numerical calculations for the TCS of section (4.11) - The values of the reported errors concern the mirror surface displacement vectors for the data of picture (4.45) and they are evaluated by applying equation 4.1.

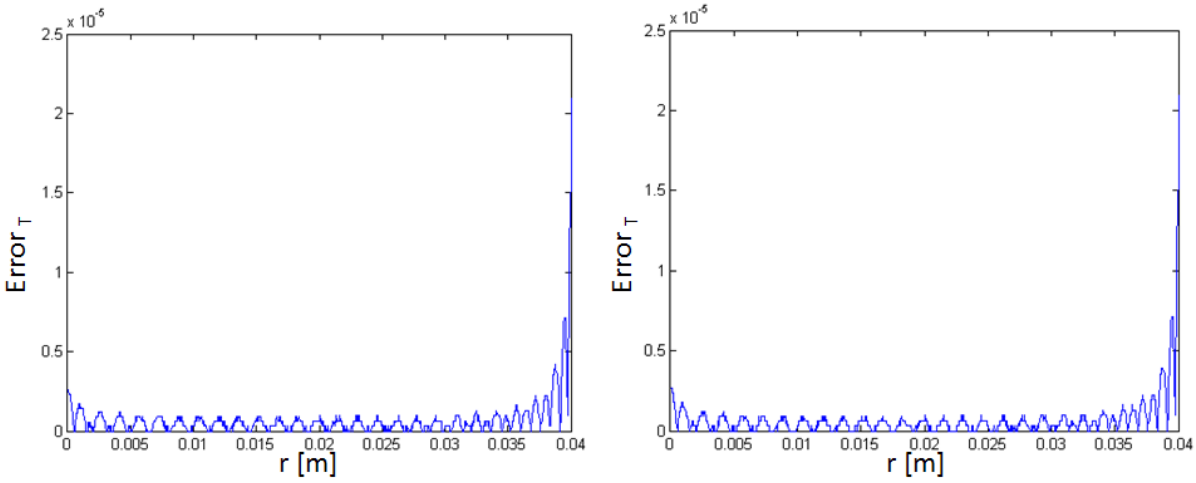

Figure 4.48: Quantitative comparison of the data of picture (4.47) - Percent error for the temperature field calculated by using the analytical method described in section (3.4.3) and in appendix (C) with respect to the one obtained through the method presented in section (3.2.3). SIPHORE mirror geometry. Absorption coefficient 0.3ppm. Intracavity power 3MW. Environment temperature T_0=300K. **Left panel**: percent error of the solution obtained by using the zeros of the Bessel function J_1 with respect to the solution obtained by using the zeros of equation (3.33), as far as the mirror surface temperature field inside the optical cavity is concerned. **Right panel**: percent error of the solution obtained by using the zeros of the Bessel function J_1 with respect to the solution obtained by using the zeros of equation (3.33, as far as the mirror surface temperature field outside the optical cavity is concerned.

Chapter 5

Optimum TCS Determination

The efficiency in correcting the cavity mirror distortions due to thermal effects, for each TCS previously described, will be evaluated in this chapter. The aim of the present analysis is the determination of an optimum system to compensate the deformations of the reflecting mirror surface, due to the optical power absorbed by the coating. Because of the thermal distortion, the effective mirror radius of curvature will be different with respect to the initial one. Furthermore, the deformed mirror will not be exactly spheric. As a consequence, part of the incident laser beam power will be diffused by the mirror reflecting surface, and this gives rise to scattering losses of the optical power. Within the context of an optical cavity, a significant change of the mirror curvature radius can lead to stability issues and with reduction of the optical power coupled on the fundamental mode of the cavity. As far as the scattering losses are concerned, they limit the total amount of power which can be stored inside an optical resonator.

The first part of this chapter is dedicated to the determination of the mathematical expression for both the thermally deformed mirror curvature and losses. Hence the implications for a simple two mirror optical cavity will be quantitatively treated. The second part of the chapter concerns the evaluation of the capability in correcting the deformed mirror curvature and losses, for each TCS introduced in chapter (3). In conclusion, the TCS which shows the optimum behavior in terms of compensations of the mirror thermal effects will be presented.

5.1 Deformed mirror curvatures and losses

The mathematical expression for the curvature of the thermally distorted mirror reflecting surface is presented in this section, together with the analytical description of the scattering losses

associated with the mirror surface departure from a perfectly parabolic profile.

The most general equation of the paraboloid which approximates better the deformed mirror surface is:

$$\tilde{Z} = cr^2 + d, \tag{5.1}$$

where c and d are found by minimizing the quantity [48]:

$$Q = \int_{R^2} \left[u_z(r) - \tilde{Z}(r) \right]^2 |\psi(r)|^2 r dr d\phi, \tag{5.2}$$

with $|\psi(r)|^2$ the normalized beam intensity:

$$|\psi(r)|^2 = \frac{2}{\pi w^2} e^{\frac{-2r^2}{w^2}}, \tag{5.3}$$

and $u_z(r)$ the displacement vector, which has been introduced in chapter 3, describing the mirror surface distortion. The least-squares formulas for c and d read:

$$c = \frac{< u_z r^2 > - < r^2 >< u_z >}{< r^4 > - < r^2 >^2}, \tag{5.4}$$

$$d =< u_z > -c < r^2 >, \tag{5.5}$$

where the notation <> indicates the weighted average performed with the normalized beam intensity of equation (5.3). It is worth noticing that the weighted average of any function $f(r)$, $< f >$, is then written as:

$$< f >= \int_{R^2} f(r) |\psi(r)|^2 r dr d\phi. \tag{5.6}$$

By considering equation (5.6), it is possible to verify that:

$$< r^4 >= \frac{w^4}{2}, \tag{5.7}$$

$$< r^2 >= \frac{w^2}{2}, \quad < r^2 >^2 = \frac{w^4}{4}, \tag{5.8}$$

then:

$$< r^4 > - < r^2 >^2 = \frac{w^4}{4}. \tag{5.9}$$

Moreover, with reference to chapter (3), if, on the reflecting mirror surface, the following dis-

placement vector form is assumed:

$$u_z(r) = \sum_{m\geq 1}^{\infty} U_m^z(-h/2)J_0(l_m r/a) + U_0^z(-h/2), \tag{5.10}$$

the relations reported below hold as well:

$$< u_z >=< u_z(r,-h/2) >= \sum_{m\geq 1}^{\infty} U_m^z(-h/2)e^{-\frac{l_m^2 w^2}{8a^2}} + U_0^z(-h/2), \tag{5.11}$$

$$< u_z r^2 >= \frac{w^2}{16a^2}\sum_{m\geq 1}^{\infty} U_m^z(-h/2)(8a^2 - l_m^2 w^2)e^{-\frac{l_m^2 w^2}{8a^2}} + \frac{w^2}{2}U_0^z. \tag{5.12}$$

As far as the Saint Venant correction (3.194) is concerned, when evaluating it in $z = -h/2$, it results:

$$\delta u_z(r,-h/2) = -\frac{\lambda}{\mu(3\lambda+2\mu)}(\omega_0(-h/2) + \omega_1(-h/2)^2/2) - \frac{\lambda+2\mu}{4\mu(3\lambda+2\mu)}\omega_1 r^2, \tag{5.13}$$

hence, if this term is taken into account to describe the mirror distortion, the following quantities have to be added to $< u_z >$ and $< u_z r^2 >$ respectively:

$$< \delta u_z >= -\frac{2\sigma}{Y}\left(\omega_0 - \frac{h}{4}\omega_1\right)\left(-\frac{h}{2}\right) - \frac{(1-\sigma)}{2Y}\omega_1\frac{w^2}{2}, \tag{5.14}$$

$$< \delta u_z r^2 >= -\frac{2\sigma}{Y}\left(\omega_0 - \frac{h}{4}\omega_1\right)\left(-\frac{h}{2}\right)\frac{w^2}{2} - \frac{(1-\sigma)}{2Y}\omega_1\frac{w^4}{2}. \tag{5.15}$$

As it is possible to see from equations (5.4) and (5.5), the best parabolic fit is now completely determined. The parameter c gives the change of the mirror radius of curvature due to the absorption of optical power by the coating, indeed $c = 1/2R_c$. The quantity d is called piston and it corresponds to a displacement of the mirror surface of the same amount for each value of the mirror radius.

As it has been already pointed out at the beginning of this section, the mirror thermal distortion is not perfectly parabolic. The consequence is that part of the laser power will be scattered, when the fundamental gaussian beam impinges on the distorted mirror. The power lost in this way defines the mirror scattering losses due to the considered thermal effects [48]. The mathematical expression for these losses can be derived by taking into account the coupling coefficient between an incoming fundamental gaussian beam, ϕ_0, reflected by the thermally

distorted mirror and matched to it, and the counter propagating gaussian beam, ϕ_c, which is the phase conjugate of ϕ_0. By considering an initially flat mirror, because of the thermal effects its operator becomes:

$$M(r) = 2ik\left[\frac{r^2}{2R_c} + d + \epsilon(r)\right], \tag{5.16}$$

where R_c and d have the same meaning introduced above, while the function $\epsilon(r)$ describes the departure of the thermally distorted mirror surface from the perfect paraboloid, defined through the quantities R_c and d. As far as ϕ_0 is concerned, this can be written as:

$$\phi_0 = \sqrt{\frac{2}{\pi}}\frac{1}{w}e^{-\frac{r^2}{w^2}}e^{-ik\frac{r^2}{2R}}. \tag{5.17}$$

Hence, the beam reflected by the distorted mirror is:

$$\phi_R = M(r) \times \phi_0, \tag{5.18}$$

and ϕ_c is:

$$\phi_c = \sqrt{\frac{2}{\pi}}\frac{1}{w}e^{-\frac{r^2}{w^2}}e^{ik\frac{r^2}{2R}}. \tag{5.19}$$

The coupling coefficient between the reflected beam, ϕ_R, and the counter propagating beam is:

$$\gamma =< \phi_c, \phi_R >= \int_0^\infty \left[\frac{2}{\pi w^2}e^{-\frac{2r^2}{w^2}}e^{i2kr^2\left(M(r)-\frac{r^2}{2R}\right)}\right]2\pi r dr. \tag{5.20}$$

The matching condition gives:

$$\frac{1}{R_c} = \frac{1}{R}, \tag{5.21}$$

therefore equation (5.20) reads:

$$\gamma =< \phi_c, \phi_R >= \int_0^\infty \left[\frac{2}{\pi w^2}e^{-\frac{2r^2}{w^2}}e^{i2kr^2(d+\epsilon(r))}\right]2\pi r dr. \tag{5.22}$$

The contribution of the piston d can be ignored since it can be compensated by changing the frequency of the laser, so that:

$$\gamma =< \phi_c, \phi_R >= \int_0^\infty \left[\frac{2}{\pi w^2}e^{-\frac{2r^2}{w^2}}e^{i2kr^2\epsilon(r)}\right]2\pi r dr. \tag{5.23}$$

Furthermore, if $\epsilon << \lambda$, where λ is the laser wavelength, the following development is possible:

$$\gamma = \int_0^\infty \left[\frac{2}{\pi w^2} e^{-\frac{2r^2}{w^2}} \left(1 + i2k\epsilon(r) - 2k^2\epsilon^2(r)\right) \right] 2\pi r dr. \tag{5.24}$$

It has to be observed that $\epsilon(r)$ is the residual function describing the difference between the actual deformed mirror surface and the best paraboloid fit, defined through equations (5.1), (5.4) and (5.5), i.e.:

$$\epsilon(r) = u_z(r, -h/2) - \frac{r^2}{2R_c}, \tag{5.25}$$

where the piston d has been set to zero and $u_z(r, -h/2)$ is the z component of the displacement vector, calculated in $z = -h/2$, which gives the effective distorted mirror surface. It can be checked that $< \epsilon(r) >$ is zero, so that:

$$i2k \int_0^\infty \left[\frac{2}{\pi w^2} e^{-\frac{2r^2}{w^2}} \epsilon(r) \right] 2\pi r dr \equiv 0. \tag{5.26}$$

As a consequence, the coupling coefficient, γ, becomes:

$$\gamma =< \phi_{out}(r), \phi_2'(r) >= 1 - \int_0^\infty \left[\frac{2}{\pi w^2} e^{-\frac{2r^2}{w^2}} \left(2k^2\epsilon^2(r)\right) \right] 2\pi r dr. \tag{5.27}$$

When $\epsilon(r) \equiv 0$, only the first term in the previous equation remains and it expresses the perfect matching between the reflected beam, ϕ_R, and the phase conjugate one, ϕ_c. Hence, for $\epsilon \neq 0$, it is possible to define the efficiency of the coupling as:

$$|\gamma|^2 = 1 - 4k^2 \int_0^\infty \left[\frac{2}{\pi w^2} e^{-\frac{2r^2}{w^2}} \epsilon^2(r) \right] 2\pi r dr. \tag{5.28}$$

Eventually, the scattering losses are given by:

$$L = 1 - |\gamma|^2 = 4k^2 \int_0^\infty \left[\frac{2}{\pi w^2} e^{-\frac{2r^2}{w^2}} \epsilon^2(r) \right] 2\pi r dr. \tag{5.29}$$

In conclusion to this section, it is worth stressing how the curvature radius of a mirror which has an initial finite radius of curvature, R_1, is modified because of the thermal effects. With this purpose, it is observed that the mirror operator for the reflection of an impinging beam, after

the thermal deformation described through a function $f(r)$, can be written as:

$$\tilde{M}(r) = 2ik\left[\frac{r^2}{2R_1} + f(r)\right], \tag{5.30}$$

with:

$$f(r) = \frac{r^2}{2R_c} + d + \epsilon(r), \tag{5.31}$$

where R_c, d and $\epsilon(r)$ have the same meaning introduced above. Hence, the radius of curvature of the thermally distorted mirror is obtained from the following relation:

$$\frac{1}{\tilde{R}_1} = \frac{1}{R_1} + \frac{1}{R_c}. \tag{5.32}$$

5.2 Thermal effect implications for an optical cavity

In order to analyze the implications of the mirror thermal distortion with respect to the properties of an optical resonator, a two mirror cavity is now considered. Firstly, the issues due to the scattering losses, as described in the previous section, will be addressed. In particular, it is assumed that the input mirror, M_1, has transmission coefficient t_1, reflection coefficient r_1 and losses p, while the end mirror, M_2, has not losses and $r_2 = 1$. The balance equation for M_1 can then be written as [48]:

$$r_1^2 + t_1^2 = 1 - p. \tag{5.33}$$

Analogously to section (2.1), it is assumed that a steady state optical signal, E_{inc}, is incident on

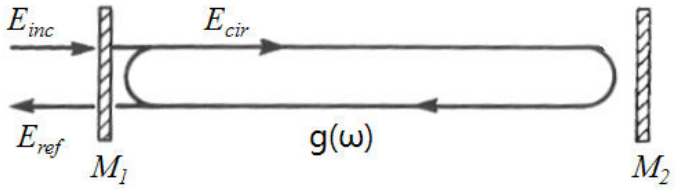

Figure 5.1: Two mirror optical cavity scheme, inspired from [49] - Scheme of the two mirror cavity, where M_1 is the mirror with reflection coefficient r_1 and M_2 is the mirror with reflection coefficient $r_2 \equiv 1$. The incident beam is indicated as E_{inc}, E_ref represents the reflected field, the circulating wave amplitude is labeled as E_{cir}, while $g(\omega)$ is the cavity gain factor for each round trip.

M_1, while the electromagnetic wave amplitude circulating within the resonator, as taken inside M_1, is denoted as E_{cir}, see picture (5.1). The latter quantity can be obtained through formula

(2.4), by imposing $r_2 \equiv 1$, hence:

$$E_{cir} = \frac{it_1 E_{inc}}{1 - r_1 e^{-i\frac{2\omega L}{c}}}, \tag{5.34}$$

and it can be checked that the power gain of the optical cavity at its resonance frequency is now:

$$|S_{max}|^2 = \frac{t_1^2}{(1 - r_1)^2}. \tag{5.35}$$

As far as the finesse of the cavity is concerned, equation (2.9), with $r_2 = 1$, gives:

$$\mathcal{F} = \frac{\pi\sqrt{r_1}}{1 - r_1}. \tag{5.36}$$

From equation (5.33), if $\mathcal{F} >> 1$, $r_2 = 1$, $p << 1$, it is possible to verify that the following relation holds [48]:

$$|S_{max}|^2 = \frac{t_1^2}{(1 - r_1)^2} = \frac{2\mathcal{F}}{\pi}\left(1 - \frac{p\mathcal{F}}{2\pi}\right). \tag{5.37}$$

The previous expression of $|S_{max}|^2$ shows a maximum for $\mathcal{F} = \pi/p$. In this case, the optical power gain of the cavity is $1/p$. It is then clear that the value of the losses determines the amount of optical power that can be stored within the resonator. In particular, to reach high levels of intracavity power, very low losses are required. However, it has to be observed that the exact value of p is not easy to determine, therefore, it is not possible to choose $\mathcal{F} = \pi/p$.

As it has been already shown, another thermal effect, in addition to the scattering losses, is the change of the cavity mirror curvature radius. This issue on one hand leads to deal with cavity stability problems, on the other hand can limit the power in the fundamental mode of the cavity because of coupling defects. In order to highlight the cavity stability issue, a simple two mirror cavity is taken into account. In the initial situation, it is assumed that the cavity is compounded of a mirror, M_2, with curvature radius R_2 and of a flat mirror, M_1. Moreover, the curved mirror is not affected by thermal effects, while the flat mirror takes a curvature radius, R_1, which depends on the thermal effects. In chapter (2), it has been introduced the stability criterion for a two mirror optical cavity, which is here reported:

$$0 < g_1 g_2 < 1, \tag{5.38}$$

where g_1 and g_2 are the g-factors of the mirrors, so that, if L is the cavity length :

$$g_1 = 1 - \frac{L}{R_1}, \tag{5.39}$$

$$g_2 = 1 - \frac{L}{R_2}. \tag{5.40}$$

If it is set $g_2 = 0.9$, $L = 100$ m, it is clear from criterion (5.38) that a significant change of the mirror radius of curvature for M_1 can lead the cavity outside the stability region. Indeed, if $R_1 \sim -1000$, $g_1 g_2 \sim 1$, then the resonator becomes marginally stable.

In order to illustrate the decrease of the cavity fundamental mode power, due to the change of the cavity mirror curvature, the optical resonator described above is considered. For the sake of clearness, its properties are recalled here: one mirror, M_2, is spherical with curvature radius R_2, the second mirror, M_1, is flat, in the unperturbed conditions, and the cavity length is $L = 100$m. The curvature radius of M_1 changes due to thermal effects, and it is denoted as R_1 in the following, while the g-factor of M_2 is fixed to $g_2 \equiv 0.9$. The unperturbed mode resonating inside the cavity can then be written as follow [49]:

$$\phi_0(z) = \sqrt{\frac{2}{\pi}} \frac{e^{-ikz + i\psi(z)}}{w(z)} e^{\frac{-r^2}{w^2} - ik\frac{r^2}{2R(z)}}, \tag{5.41}$$

where:

$$\begin{aligned} w(z) &= w_0 \sqrt{1 + \left(\tfrac{z}{z_R}\right)^2}, \quad z_R = \tfrac{\pi w_0^2}{\lambda}, \\ R(z) &= z + \tfrac{z_R^2}{z}, \quad \psi(z) = \arctan\left(\tfrac{z}{z_R}\right). \end{aligned} \tag{5.42}$$

It is worth noticing that, in the previous equations, the quantity z is the coordinate aligned with the propagation direction of the beam and it describes the position within the resonator. λ is, as usual, the laser beam wavelength. For the calculations of this chapter, it is always assumed $\lambda = 1064$ nm. Moreover, the quantity w_0 is the beam waist within the cavity, in the unperturbed condition, i.e. for $g_2 = 0.9$, $g_1 = 1$, so that:

$$w_0 = \left(\frac{L\lambda}{\pi} \sqrt{\frac{g_1 g_2 (1 - g_1 g_2)}{(g_1 + g_2 - 2 g_1 g_2)^2}} \right)^{\frac{1}{2}} = 1.0 \text{ cm}. \tag{5.43}$$

As it has been already pointed out, because of the thermal effects, the curvature of the mirror M_1 changes, then even the mode resonating inside the cavity is different. In particular, the

beam waist position changes, with respect to M_1, of a quantity Δz [49]:

$$\Delta z = \frac{g_2(1-g_1)}{g_2+g_1-2g_1g_2}L, \tag{5.44}$$

where g_1 is now the g-factor of the thermally distorted mirror, while g_2 keeps its usual value: $g_2 = 0.9$. It is observed that, in the unperturbed configuration, the beam waist is on M_1, so that $\Delta z \equiv 0$. The effective mode resonating inside the cavity, because of the thermal effects, is then:

$$\phi_{0p}(z) = \sqrt{\frac{2}{\pi}}\frac{e^{-ik(z-\Delta z)+i\psi_p(z-\Delta z)}}{w_p(z)}e^{\frac{-r^2}{w_p^2}-ik\frac{r^2}{2R_p(z)}}, \tag{5.45}$$

with:

$$\begin{aligned} &w_p(z) = w_{0p}\sqrt{1+\left(\tfrac{z-\Delta z}{z_{R_p}}\right)^2}, \quad z_{R_p} = \tfrac{\pi w_{0p}^2}{\lambda}, \\ &R_p(z) = z-\Delta z+\tfrac{z_{R_p}^2}{z-\Delta z}, \quad \psi(z) = \arctan\left(\tfrac{z}{z_{R_p}}\right), \\ &w_{0p} = \tfrac{L\lambda}{\pi}\sqrt{\tfrac{g_1g_2(1-g_1g_2)}{(g_1+g_2-g_1g_2)^2}}. \end{aligned} \tag{5.46}$$

The coupling between the unperturbed cavity mode with the mode affected by thermal effects is given by the following integration:

$$\begin{aligned} &C(z) = |2\pi\textstyle\int_0^\infty \phi_0(r,z)\phi_{0p}^*(r,z)rdr|^2 = \\ &= \frac{4}{w^2(z)w_p^2(z)\left[\left(\frac{1}{w^2(z)}+\frac{1}{w_p^2(z)}\right)^2+\left(\frac{k}{2}\left(\frac{1}{R(z)}-\frac{1}{R_p(z)}\right)\right)^2\right]}. \end{aligned} \tag{5.47}$$

The coupling defects are defined as the quantity $1-C(z)$. Since the coupling for the fundamental mode of the cavity is not perfect, a higher level of input laser power is required, in order to reach the desired value of the intracavity power, P_{int}. For example, if it is required $P_{int} = 3$ MW, the laser input power required to reach it, in the presence of coupling defects, is:

$$P_{input} = \frac{3\times 10^6 W}{|S_{max}|^2 C(z)}, \tag{5.48}$$

where the quantity $|S_{max}|^2$ has been defined, in the current section, as the maximum optical power gain of the cavity. It is important to stress that it is always $C(z) \leq 1$. Hence, if the coupling is not perfect, the factor $C(z)$, in equation (5.48), makes to increase the laser input power required to reach the desired 3MW of intracavity power.

5.3 TCS analytical results

In this section, the TCS described in the previous chapters are analyzed relatively to their efficiency in correcting mirror curvature radius changes and losses produced by thermal effects. The results in the following are obtained through the application of the analytical calculations in chapter (3), hence of the MATLAB programs based on them, to evaluate the mirror displacement vector. The values of the mirror curvature changes and of its losses, for each considered TCS, are then obtained with formulas (5.4), (5.29). It is observed that the results presented in this section and in the next ones, have been obtained by assuming the mirror geometrical characteristics already used in chapter (3). Furthermore, except for the case of the TCS in section (3.2.3), the environment temperature is always equal to 300 K. As far as the beam size is concerned, it is assumed a waist of 1 cm on the mirror reflecting surface. The absorption coefficient of the mirror is always set to 0.3 ppm. Moreover, the optical power load on the mirror reflecting surface, that can be seen as the intracavity optical power, in the context of on optical resonator, is of 3 MW. For the sake of simplicity, it is also assumed that the initial mirror, in the unperturbed condition, is flat.

It is worth giving as a reference for the results illustrated in the following, the mirror reflecting surface distortion when no TCS are applied. To this aim, in figure (5.2), the results of the MATLAB program for the TCS of section (3.2.3), with environment temperature $T_0 = 300\text{K}$, are reported. In particular, the plot shows the deformed mirror reflecting surface together with the best parabolic fit. The associated value for the change of the curvature is $c = 3.1 \times 10^{-4}$ m^{-1} and the losses are of 2518 ppm. It is worth observing the mirror reflecting surface departure from a perfect paraboloid profile, which gives rise to the scattering losses.

5.3.1 Results for the TCS with fixed temperature on the cavity mirror edges

The TCS currently under analysis is the one treated in section (3.2.1), (4.2). It is based on the application of a fixed temperature T_1, on the mirror edges, as showed in picture (3.2), in order to compensate for the mirror distortion due to the laser power absorption. As there is only one parameter that can vary, i.e. T_1, it is possible to carry on a systematic study to determine losses and curvatures of the mirror as functions of this quantity. Figure (5.3) illustrates that the losses decreases when T_1 increases. In this respect, it is observed that the highest temperature value, $T_1 = 900\text{K}$, is fixed to guarantee the feasibility of the TCS. Since the manufacturing geometrical defects of the mirror give diffusion losses of about 30 ppm [95], the losses obtained

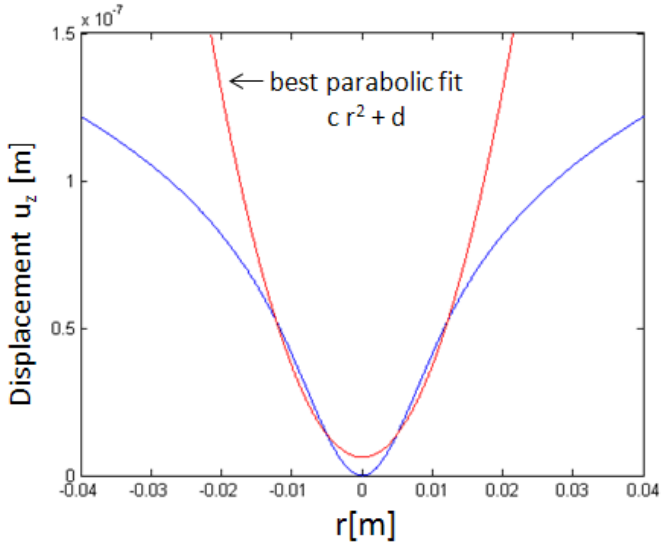

Figure 5.2: Mirror reflecting surface distortion without TCS - Distortion of the mirror reflecting surface, when there is not a TCS acting on it and the environment temperature is $T_0 = 300$ K. The red line illustrates the parabolic fit which approximates better the mirror distorted surface and the blue line is the mirror reflecting surface displacement vector. The departure of the mirror surface from the best parabolic fit gives rise to the scattering losses expressed by formula (5.29), while the parameter c, on the plot, is the change of the mirror curvature due to the thermal effects.

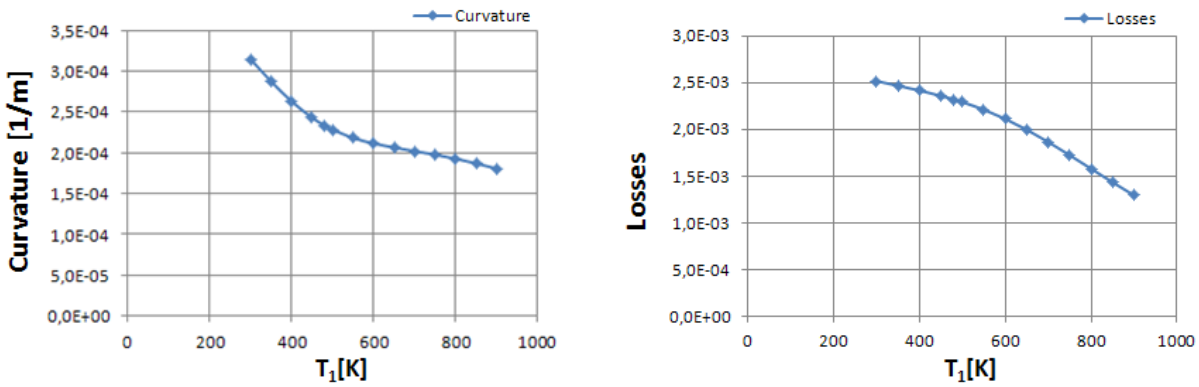

Figure 5.3: Loss and Curvature results for the TCS in section (5.3.1) - **Left panel**: the mirror curvature resulting from the combination of the thermal effect and of the application of the considered TCS is showed, when the temperature fixed at the mirror edge, T_1, changes. **Right panel**: the loss value for the mirror deformed by the combination of the thermal effect and of the application of the considered TCS is showed, when the temperature fixed at the mirror edge, T_1, changes.

through this TCS are too high. Indeed, it would be appropriated to reduce the loss value due to the thermal effects below the one due to the mirror manufacturing. Furthermore, the coupling defects, defined in section (5.2) within the context of on optical resonator, are not adequately corrected. To have an idea of this statement, it is possible to take into account the optical cavity considered in section (5.2). It is worth recalling that the g-factors of the mirrors, in the unperturbed condition, are $g_2 = 0.9$, $g_1 = 1$, and the cavity length is $L = 100$. The plot of the coupling defects as function of T_1 is reported in picture (5.4), therefore it is possible to observe that even for the value of T_1 for which the TCS works better, i.e. $T_1 = 900$K, the coupling defects, calculated by applying the formula (5.47), are of about 10%. This value is not negligible with respect to the experimental errors, which are of order of 5%. However, it must be observed that, it is always possible to adapt the properties of the input laser beam, in order to decrease the coupling defects. In conclusion, the results obtained with this TCS, for the corrections of losses and curvature radii of the distorted mirror, are not satisfactory.

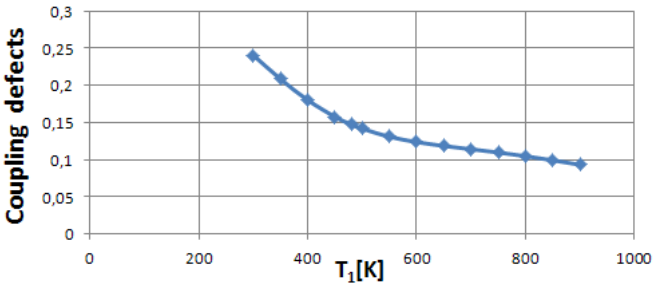

Figure 5.4: Coupling defects for the TCS in section (5.3.1) - The plot shows the coupling defects calculated through relation (5.47) for the TCS in section (5.3.1 as function of the temperature fixed at the mirror edge, T_1.

5.3.2 Results for the free cavity mirror TCS

The considered TCS is described in sections (3.2.3), (4.4). It consists in warming up the complete environment where the mirror is placed, which can freely exchanges heat with it. The temperature of the environment is fixed at T_0, and this is the only parameter that can be varied, in this configuration. Hence, a systematic study of the TCS behavior in correcting the thermal effects can be carried on. In figure (5.3.3), the results obtained for the losses of the mirror and its changes of curvature are reported, when T_0 is made to vary. As it is possible to verify from these plots both the mirror curvature changes and the losses are comparable to the ones obtained in section (5.3.1). As far as the coupling defects are concerned, their value as function

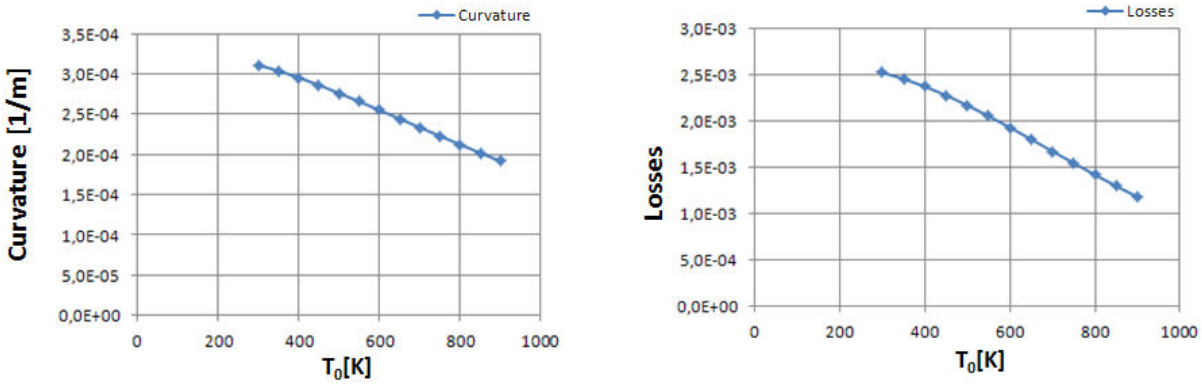

Figure 5.5: Loss and Curvature results for the TCS in section (5.3.2) - **Left panel**: the mirror curvature resulting from the combination of the thermal effects and of the application of the considered TCS is showed, when the environment temperature, T_0, is made to vary. **Right panel**: the loss value for the mirror deformed by the combination of the thermal effects and of the application of the considered TCS is showed, when the environment temperature, T_0, is made to vary.

of the temperature T_0 is reported in picture (5.6), which show that they are of the same order of greatness of the ones found in the previous section. As the mirror losses are still significantly higher than the ones due to the mirror manufacturing, even for the environment temperature value which minimizes both the curvature change and the losses, i.e. $T_0 = 900$K, this TCS could hardly be applied for correcting the mirror thermal effects.

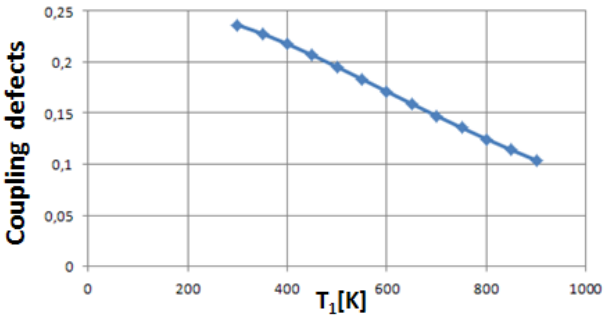

Figure 5.6: Coupling defects for the TCS in section (5.3.2) - The plot shows the coupling defects calculated through relation (5.47) for the TCS in section (5.3.2 as function of the environment temperature where the mirror is placed, T_0.

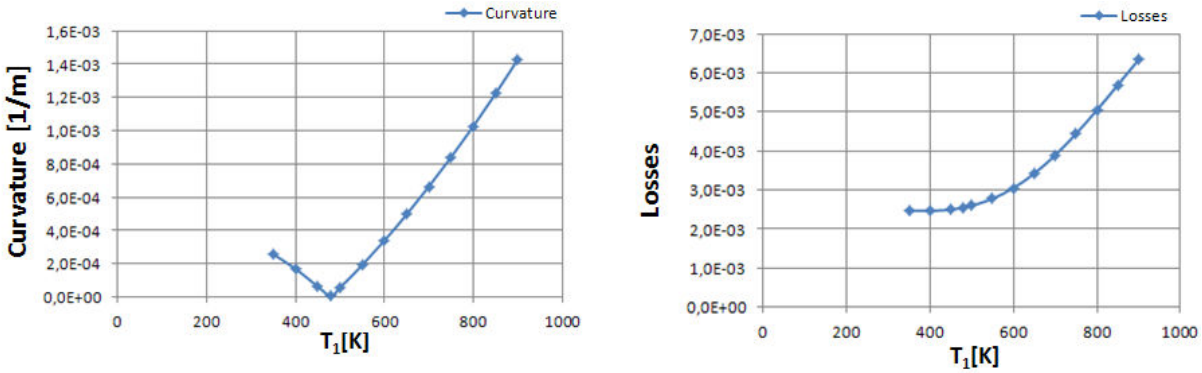

Figure 5.7: Loss and Curvature results for the TCS in section (5.3.3) - **Left panel**: the mirror curvature resulting from the combination of the thermal effects and of the application of the considered TCS is showed, when the temperature, T_1, fixed on the mirror is made to vary. **Right panel**: the loss value for the mirror deformed by the combination of the thermal effects and of the application of the considered TCS is showed, when the temperature, T_1, fixed on the mirror is made to vary.

5.3.3 Results for the TCS with fixed temperature on the cavity mirror edges and on one ring heater

The TCS discussed in secions (3.2.4) (4.5) is now studied. It is worth recalling that, in this case, the TCS consists in applying a fixed temperature, T_1, both on the mirror edges and on a circular section of the back side of the mirror, as it is shown in figure (3.4). In order to fix the internal radius of the ring heater, b, it has been observed that, as the TCS should be applied also to the input cavity mirror, it has to be $b \geq 0.02$m, not to enhance clipping losses. Moreover, by performing several simulations it has been checked that the TCS get to better results when b is smaller, and the ring occupies a larger area of the mirror back side. Hence, for the performed simulations it has been set $b = 2$ cm. The behavior of the analyzed configuration, as far as corrections of mirror losses and curvature changes are concerned, can be understood by evaluating these two quantities, when the temperature T_1 is made to vary. The plot in figure (5.7) shows the presence of an optimum T_1 value for the correction of the mirror curvature change. This value is $T_1 = 480$K, and the corresponding curvature change is $6,3 \times 10^{-6}\ m^{-1}$. With the application of relation (5.47), it is possible to realize the plot for the coupling defects as function of the temperature T_1. The results are reported in picture (5.8). It is observed that the coupling defects are reduced to $1 - C(z) = 1,2 \times 10^{-4}$, when $T_1 = 480K$. However, by taking into account the plot for the losses as function of T_1, it is easy to realize that this TCS is not able to solve the thermal effect problems. Indeed, the losses are comparable or even larger than

the ones obtained with the previously analyzed TCS. It is also worth to point out that, for the value of T_1 giving the lowest change of the mirror curvature, there are no problems due to the approximation for the linearization of the equations (see sections (3.4), (4.5)). Indeed, as it has been showed in section (4.5), this issue starts to be relevant for $T_1 \geq 600$K. So, it is possible to confirm the tendency showed in figure (5.7), for both the losses and the curvature changes of the mirror as functions of T_1.

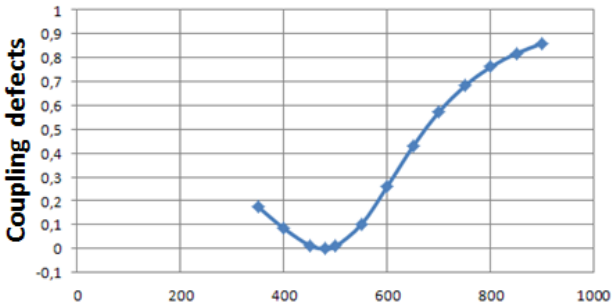

Figure 5.8: Coupling defects for the TCS in section (5.3.3) - The plot shows the coupling defects calculated through relation (5.47) for the TCS in section (5.3.3, as function of the fixed temperature, T_1.

5.3.4 Results for the TCS configurations with several temperatures fixed on the back side of the mirrors

The TCS described in sections (3.2.5), (3.2.6), (3.2.7) are now analyzed as far as the corrections of the mirror losses and curvature changes are concerned. These configurations are characterized by the presence of several parameters that can be fixed to perform the simulations. As a consequence, it is quite tricky to find the optimum parameter choice that lead to the lowest loss value and to the lowest change of the mirror curvature. For these reason, for all the TCS considered in this section, several simulations have been done. It is worth stressing that, in performing the simulations, it has to be taken into account that the linearization approximation, already discussed in sections (3.1), (3.2), can introduce errors in the results obtained through analytical calculations, when the choice of the fixed temperatures, in the rear side of the mirror, leads to deal with an excess of temperature, τ, which does not verifies the condition $\tau << T_1$. Nevertheless, there is at least one configurations, that can be seen as a limit case of the TCS of sections (3.2.6), (3.2.7), for which a systematic study for the mirror losses and curvature changes can be carried on, i.e. the configuration where a fixed temperature T_1 is set on the complete back side of the mirror and on the mirror edges. Indeed, this is also equivalent to the TCS

of section (3.2.2). The results are reported in figure (5.9). As it is possible to check from

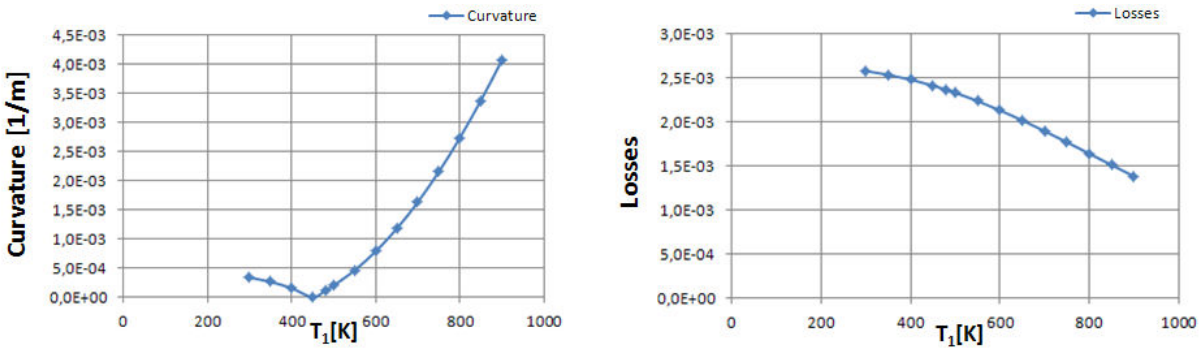

Figure 5.9: Loss and Curvature results for a particular case of the TCS configurations in section (5.3.4) - **Left panel**: the mirror curvature resulting from the combination of the thermal effects and of the application of the considered TCS is showed, when the temperature, T_1, fixed on the mirror is made to vary. **Right panel**: the loss value for the mirror deformed by the combination of the thermal effects and of the application of the considered TCS is showed, when the temperature, T_1, fixed on the mirror is made to vary.

the plots, in the particular considered case, the behavior with respect to the correction of the mirror curvature changes presents an optimum situation when $T_1 = 450$K, indeed in this case $c = 2.0 \times 10^{-6}$ m^{-1} and the coupling defects obtained, by considering formulas (5.47) and the same argumentation made in section (5.3.1), turn out to be $1 - C(z) = 1 \times 10^{-5}$. The last result is quite good, however the loss correction associated to this value of T_1 is not adequate, indeed the losses are of 2500 ppm. On the contrary, if the optimum value of the temperature with respect to the loss correction is taken into account, i.e. $T_1 = 900$ K, it is easy to see that the coupling defects become large, while the losses are not sufficiently reduced. As a consequence, this configuration as well is not completely satisfactory.

In the most general situation, as it has been already pointed out, several parameters have to be fixed, in order to start the simulations and shed light on the behavior of the TCS configurations of sections (3.2.5), (3.2.6), (3.2.7) as far as the corrections of the mirror losses and curvature changes are concerned. With reference to the obtained simulation results, it is possible to state that, for the choices of the temperatures fixed on the rear side of the mirror, for which the linearization approximation is well verified, it is not possible to obtain loss values below 8×10^2ppm. Furthermore, it is worth noticing here that the outcomes of the simulations show a reduction of the mirror losses, when the central part of the mirror rear side is kept at a higher temperature value with respect to the temperature of the other regions of the mirror. Indeed, if for the TCS of section (3.2.6), by considering picture (3.6), it is assumed: $T_1 = 350$ K, $T_2 = 380$

K, $b = 0.02$m, the losses turn out to be 2320ppm with curvature change of 2.4×10^{-4} m^{-1}. By inverting the previous temperatures, i.e. $T_1 = 380$ K, $T_2 = 350$ K, the losses become 2720ppm, while the curvature change is 2.3×10^{-4} m^{-1}. The tendency stressed here is confirmed by the TCS of section (3.2.5). Indeed, with reference to picture (3.5), by setting: $T_1 = 350$K, $T_3 = 380$K, $b = 0.03$m, $b_1 = 0.01$m, the loss value is 2400ppm, while the curvature change is 2.3×10^{-4} m^{-1}. By inverting the temperatures, i.e. $T_1 = 380$K, $T_3 = 350$K, with the same values of b and b_1, it turns out that the losses rise to 3000ppm and the curvature change rises to 2.5×10^{-4} m^{-1}. Results of order of few hundred of ppm for the mirror losses can be reach when considering higher level of the fixed temperature on the back side of the cavity mirror. In these cases, however, the linearization condition is not appropriately verified and the outcomes of the simulations based on the analytical calculations present departures with respect to the ones obtained through numerical simulations. This can be seen, for example, in figure (5.10), which concerns the TCS of section (3.2.5), for $T_1 = 700$K, $T_3 = 750$K, $b_1 = 0.005$m and $b_2 = 0.02$m. The plots represent the temperatures and the displacement vectors for both the mirror reflecting surface and the mirror rear side surface. Both the numerical and analytical results are shown, in order to make clear that the differences between the two calculation methods become significant, when the error introduced by the linearization is not negligible. For the particular case of figure (5.10), the ratio between the difference of the mirror radiated power calculated with the linearization formula and without linearization approximation to the mirror absorbed power is of 281%. A quantitative analysis of the departure of the analytical results from the numerical ones, for both the mirror surface displacement vector inside the optical cavity and the one outside the cavity, is obtained by evaluating the following expression at each radius value:

$$PE_{u_z} = \frac{|U_{z,A} - U_{z,N}|}{|U_{z,N}|}. \tag{5.49}$$

The outcomes of these calculations are reported in picture (5.11), for $r \leq 0.02$ m, indeed, the central part of the mirror is the one involved in the laser beam reflection. As it is possible to check from these plots, even if, for the surface internal to the optical cavity, equation (5.49) gives acceptable percent errors of the analytical results with respect to the numerical ones, the same thing does not hold for the rear side of the mirror. The analytical results give a loss value of 103 ppm and a curvature change of 1.4×10^{-3} m^{-1}. The corresponding values for the numerical calculations are 122 ppm and 1.4×10^{-3} m^{-1} respectively. However, it is possible to observe that these TCS can reduce the mirror losses, when considering higher values of the temperatures

fixed on the mirror rear side, but they also enhance the curvature changes, which is quite large for the example taken into account. In order to avoid problems connected with the linearization condition, discussed above, the analysis of the TCS taken into account in this section has been carried on by using only numerical simulations, but no solutions which could efficiently correct, at the same time, mirror losses and mirror curvature changes due to the thermal effects could be determined.

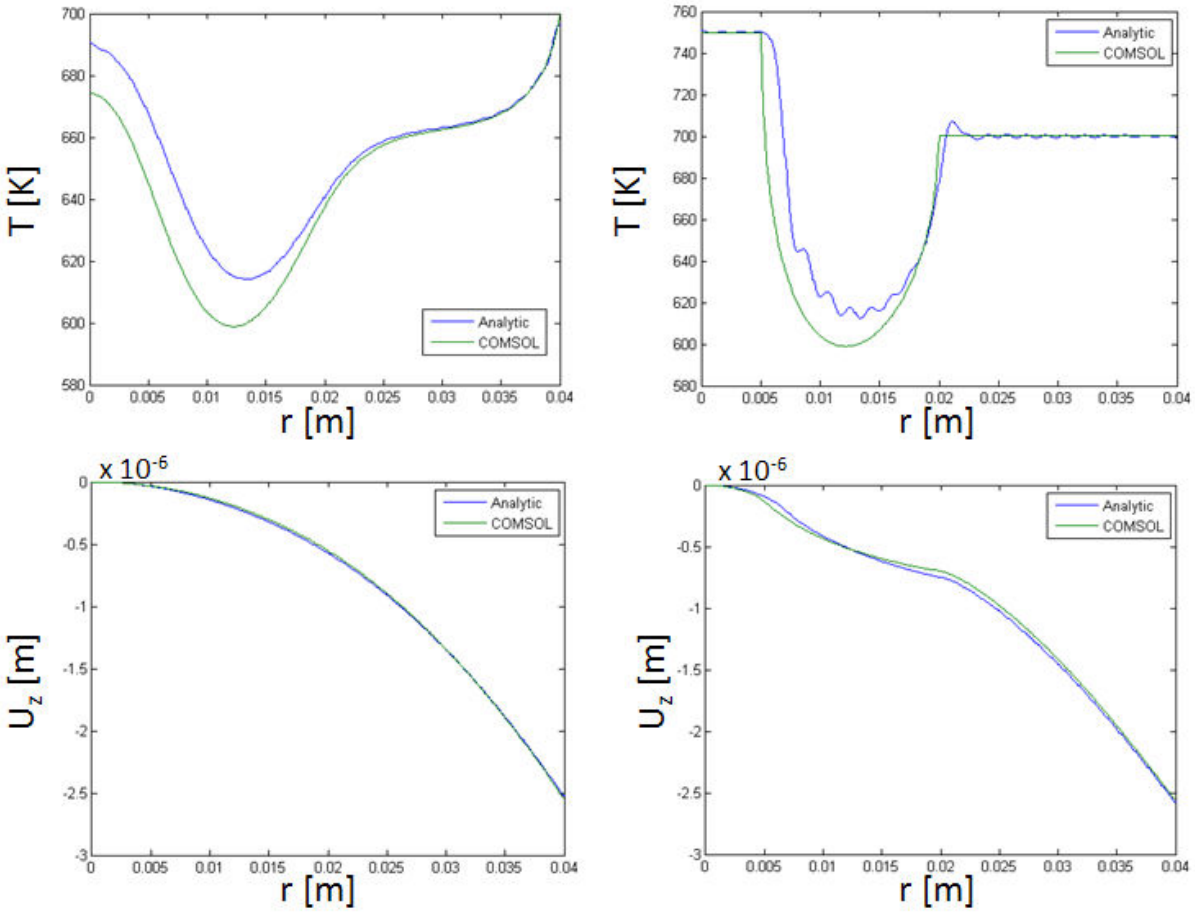

Figure 5.10: Mirror surface temperatures and distortions for a particular case of the TCS configurations in section (3.2.5) - Comparison between numerical and analytical simulations. **Top panels**: on the left, the mirror reflecting surface temperature is reported; on the right, the mirror rear side surface temperature is reported. The TCS parameter choice is described in section (5.3.4). **Bottom panels**: on the left, the displacement vector of the mirror reflection surface is reported; on the right, the displacement vector of the mirror rear side surface is reported. The TCS parameter choice is described in section (5.3.4)

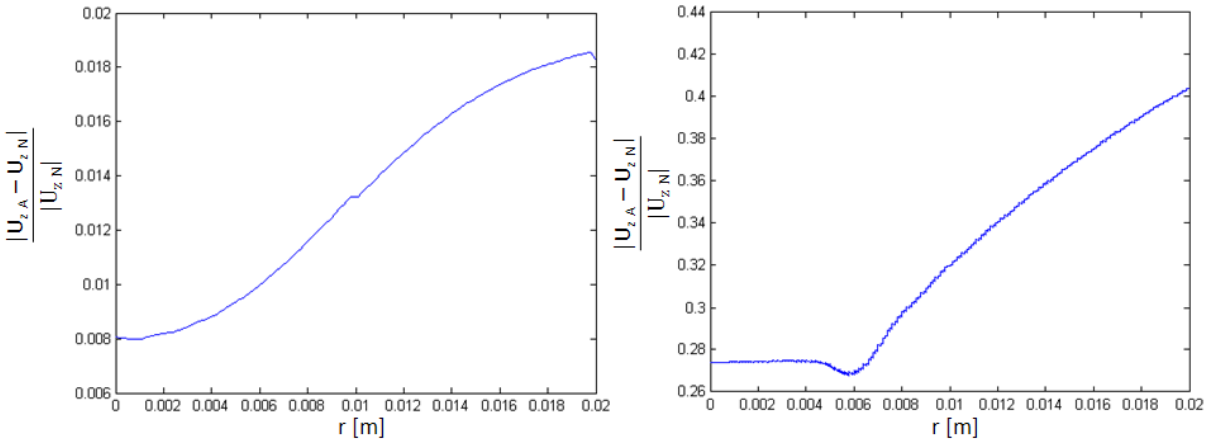

Figure 5.11: Percent errors on the mirror surface displacement vectors for a particular case of the TCS configurations in section (3.2.5) - Percent errors on the analytical calculations of the mirror surface displacement vectors with respect to the COMSOL numerical calculations, evaluated through formula (5.49). **Left panel**: percent error of the analytical calculations with respect to the ones performed with COMSOL, as far as the mirror surface displacement vector inside the optical cavity is concerned. The TCS parameter choice is described in section (5.3.4) . **Right panels**: percent error of the analytical calculations with respect to the ones performed with COMSOL, as far as the mirror surface displacement vector outside the optical cavity is concerned. The TCS parameter choice is described in section (5.3.4).

5.3.5 Results for the TCS with mechanical fixation and temperature field application on the cavity mirror

The TCS described in sections (3.4.1), (4.9) is now taken into account, in order to analyze the results concerning mirror losses and curvature changes. As it is shown is section (4.9), a good agreement between the numerical calculations performed with COMSOL and the analytical ones can be obtained only if the parameter d, illustrated in figure (3.8), is small enough. Hence, in the simulations used to determine the plots of figure (5.12), it is set $d = 1\text{mm}$. As far as the mirror temperature field is concerned, the configuration described by the TCS in section (3.2.4) is assumed, with internal radius of the ring heater fixed at $b = 0.02$ m, as it has been already done in section (5.3.3). The analysis of the TCS behavior, in correcting the cavity mirror losses and curvature changes, is then carried on by making to vary the temperature T_1. It is easy to check, from picture (5.12), that the results obtained for the corrections of both the mirror losses and curvature changes are not enough satisfactory. Indeed, on one hand, the change of the mirror curvature is quite significant for all the temperature values, on the other hand, the losses keep being sensibly larger than the ones due to the mirror manufacturing. As far as

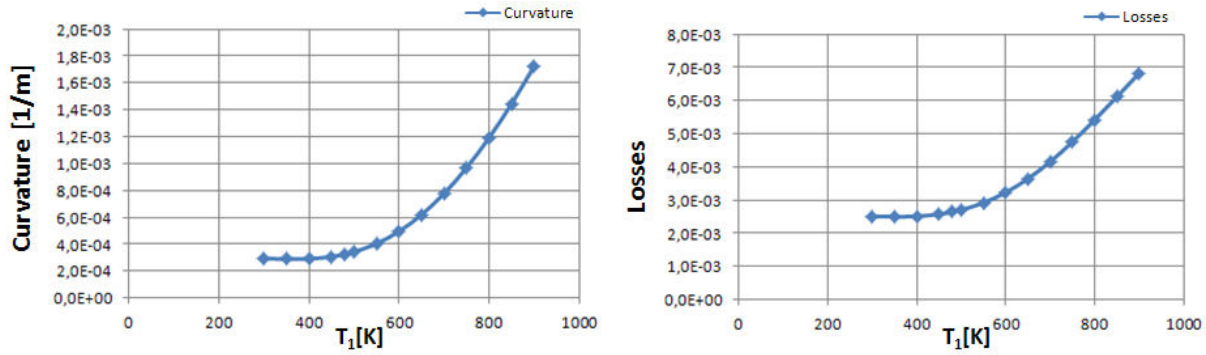

Figure 5.12: Loss and Curvature results for the TCS in section (5.3.5) - **Left panel**: the mirror curvature resulting from the combination of the thermal effects and of the application of the considered TCS is showed, when the temperature, T_1, fixed on the mirror is made to vary. **Right panel**: the loss value for the mirror deformed by the combination of the thermal effects and of the application of the considered TCS is showed, when the temperature, T_1, fixed on the mirror is made to vary.

the coupling defects are concerned, they are evaluated through formula (5.47) and the result is illustrated in picture (5.13). As it is possible to verify from this plot, the coupling defects are quite large. Indeed, for the value of the temperature which minimizes the losses, i.e. $T_1 = 300$ K corresponding to the loss value of 2510 ppm, the coupling defects turn out to be of about 20%, which is a high value with respect to the experimental errors. It is observed that, for the range of temperatures $300\text{K} \leq T_1 \leq 450\text{K}$, the values of the coupling defects are similar to each other and they are the lowest possible. Hence, the optimum value for the coupling defects is close to 20%. In conclusion, because of the analysis carried on for this TCS, it appears that the considered configuration is not appropriate to compensate the defects introduced by the thermal effects on the mirror, indeed, the losses are larger than the ones obtained for the configurations in sections (5.3.2), (5.3.3).

5.3.6 Results for the TCS with fixation of the cavity mirror edges and temperature field application

The TCS currently under analysis is the one introduced in section (3.4.2) and it consists in fixing the edges of the mirror, so that they cannot move, while applying the temperature field described in section (3.4). The idea of studying this configuration rises from the results obtained for the TCS treated in section (5.3.5), indeed, it has been introduced for checking if the mirror central deformation showed in picture (5.2) could be decreased, by leaving the mirror free to expand on its borders, while its edges are blocked. The study of this TCS behavior as far as mirror

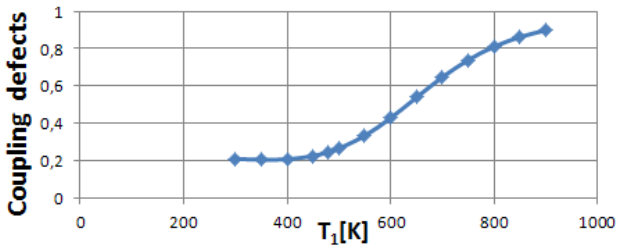

Figure 5.13: Coupling defects for the TCS in section (5.3.5) - The plot shows the coupling defects calculated through relation (5.47), for the TCS in section (5.3.5), as function of the fixed temperature, T_1, when setting $d = 1$ mm.

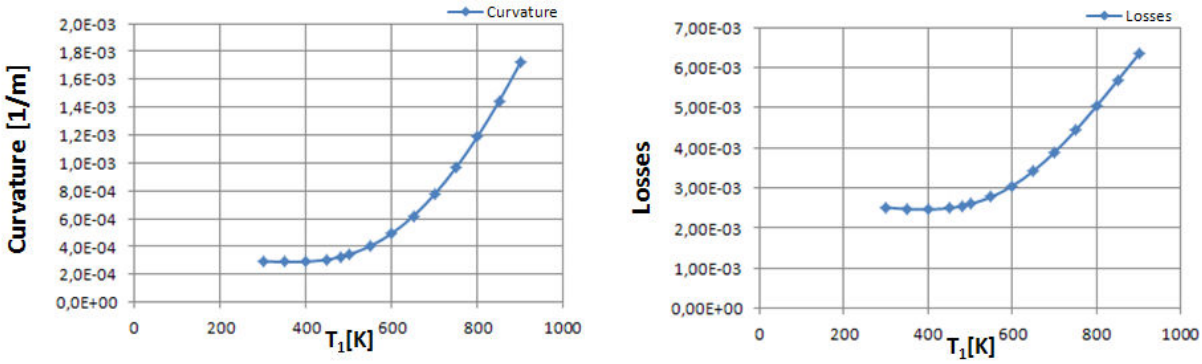

Figure 5.14: Loss and Curvature results for the TCS in section (5.3.6) - **Left pannel**: the mirror curvature resulting from the combination of the thermal effects and of the application of the considered TCS is showed, when the temperature, T_1, fixed on the mirror is made to vary. **Right pannel**: the loss value for the mirror deformed by the combination of the thermal effects and of the application of the considered TCS is showed, when the temperature, T_1, fixed on the mirror is made to vary.

losses and curvature changes are concerned, is carried on by evaluating these quantities, when the temperature T_1, fixed on the mirror rear side and on its edges, is made to vary. The obtained results are showed in figure (5.14). From the plot for the mirror losses, it is possible to see that the minimum loss value is obtained for $T_1 = 400$K. In this case, the losses are of 2460 ppm and the curvature change is of 2.9×10^{-4} m^{-1}. Additionally, the value of the curvature change does not vary significantly within the temperature range $300\text{K} \leq T_1 \leq 450\text{K}$. Thus, the optimum value for the mirror curvature is close to the one given for $T_1 = 400$K, indeed, it is 2.88×10^{-4} m^{-1}. As far as the coupling defects are concerned, they are evaluated through equation (5.47) and the results are reported in picture (5.15). The values for the coupling defects appear to be quite large. In conclusion, it is observed that, on one hand, this TCS allows to reduce the loss values below the ones obtained with the configuration of section (5.3.5), on the other hand, the curvature and loss corrections are not significantly improved. The obtained results for both losses and curvature changes are not satisfactory. In this respect, it is worth pointing out that the losses are quite high with respect to the ones due to the mirror manufacturing. Hence, this TCS cannot be applied to solve the problems introduced by the thermal effects on the mirrors.

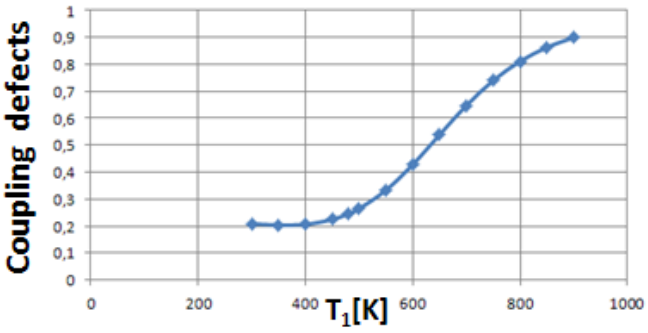

Figure 5.15: Coupling defects for the TCS in section (5.3.6) - The plot shows the coupling defects calculated through relation (5.47) for the TCS in section (5.3.6), as function of the fixed temperature, T_1.

5.3.7 Results for the TCS configurations with pressure application on the mirror

The behavior of the TCS described in section 3.4.3, in correcting the thermal effects, is now analyzed. In particular, the MATLAB program tested in section (4.11) is taken into account, hence seven different values of the pressure could be applied on the mirror rear side, at the same

time. However, the number of the parameters that have to be chosen to start the simulations is quite high. This is true even if only the application of one ring of pressure or only the central disk of pressure is considered. Indeed, there is not just the value of the pressure that has to be chosen, but the geometry of the region where it has to be applied as well. Hence, a systematic study of this TCS turns out to be quite tricky. With the aim of reducing mirror losses and curvature changes, several simulations were made, by changing the parameters of the MATLAB program. No solutions were found that could significantly lower the mirror losses and curvature changes. To give an idea of the mirror deformation dependence on the configuration of the applied pressure, it is possible to fix a value of the pressure, e.g. 5000 Pa, and to apply it on one ring, which is made to displace, on the rear side of the mirror. For each position of the pressure ring, it is possible to see how the mirror reflecting surface is deformed. It is worth noticing that, when the central part of the mirror back side is considered, a pressure disk is applied, instead of a ring. Furthermore, it is reminded that, on the mirror surface internal to the optical cavity, a ring of pressure is also present, as it is explained in section (3.4.3). For the particular case of the simulation results presented below, it has been chosen to fix the ring of pressure, on the mirror surface internal to the optical cavity, between $r = 0.038$ m and $r = 0.04$ m, while the pressure value is determined as described in section 3.4.3. In figures (5.17), (5.18), (5.19), (5.20),(5.21), (5.22), the results for the displacement vector of the mirror reflecting surface are showed together with the description of the applied pressure, on the rear side of the mirror. In the figure captions, the loss value and the curvature change are also given. The mirror reflecting surface distortion, for each considered position of the applied pressure, has to be compared with the one obtained when no pressures are applied, which is reported in figure (5.16). This last case has to be equivalent to the case of section (5.3.2), for $T_0 = 300$K. It has been checked that this is verified, indeed the losses and the curvature change for both the programs are 2518 ppm and 3.1×10^{-4} m^{-1} respectively. As it is possible to see from figures (5.16), (5.17), (5.18), (5.19), (5.20),(5.21), (5.22), for the considered value of the pressure, i.e. 5 kPa, there is not a solution that allows to invert the direction of the mirror deformation in its center, or to uniform the central deformation by enhancing the distortion of the mirror borders. However, in principle, it may be possible to find values of the pressure which allow to compensate the mirror change of curvature, when applied on appropriate regions of the mirror back side. Nevertheless, it is observed that, from the simulation results concerning different configurations of the applied pressure and of the pressure values, it seems hard to compensate both the mirror losses and the mirror changes of curvature, by applying this TCS.

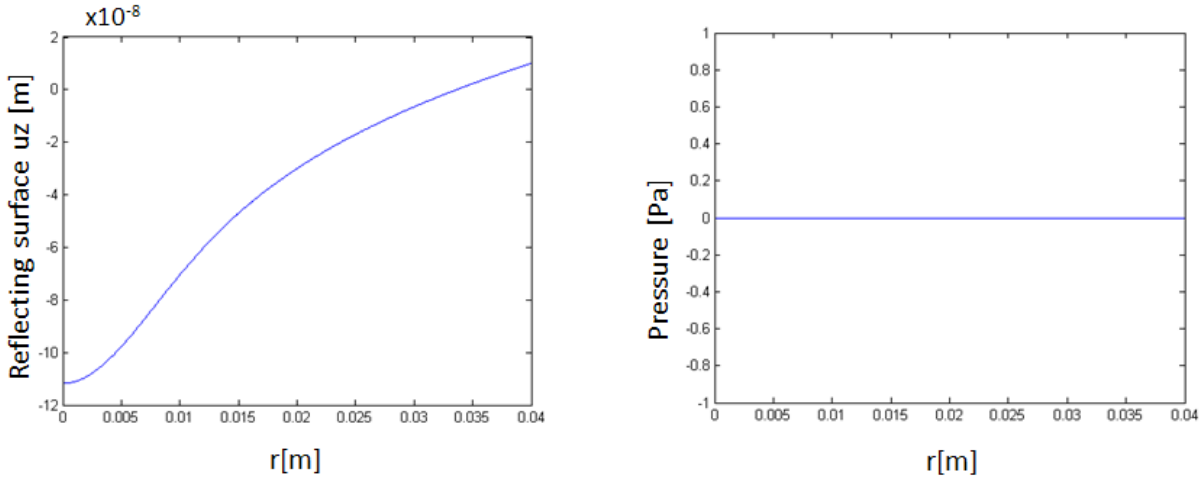

Figure 5.16: Analysis of the TCS of section (5.3.7). Configuration 1. - Mirror losses: 2518 ppm. Mirror curvature change: 3.1×10^{-4} m^{-1}. **Left panel**: Displacement vector of the mirror reflecting surface when no pressure are applied on the rear side of the mirror. **Right panel**: pressure applied on the mirror rear side as function of the mirror radius.

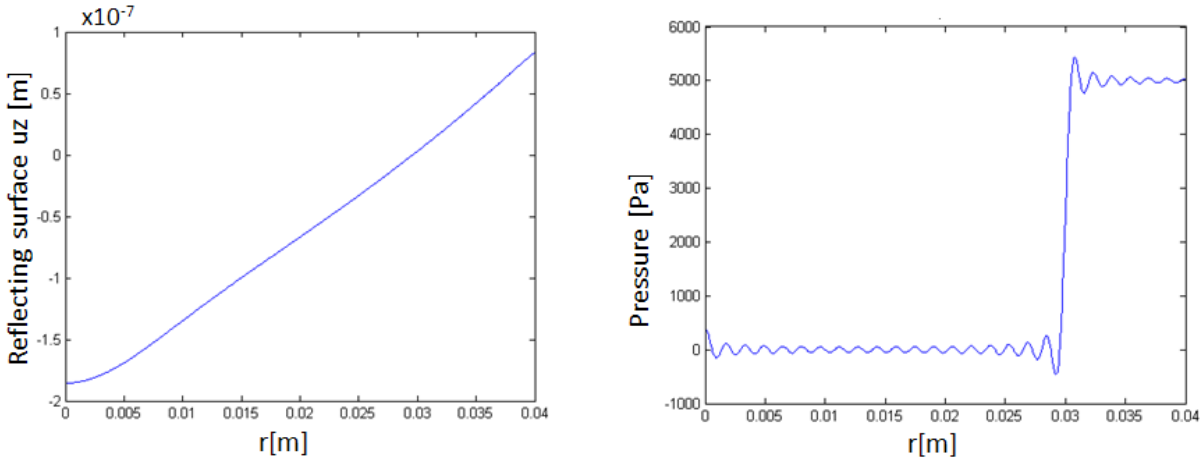

Figure 5.17: Analysis of the TCS of section (5.3.7). Configuration 2. - Mirror losses: 2518.6 ppm. Mirror curvature change: 4.0×10^{-4} m^{-1}. **Left panel**: Displacement vector of the mirror reflecting surface when a pressure of 5000 Pa is applied on the mirror back side, in the region 0.03 m$\leq r \leq$ 0.04 m. **Right panel**: pressure applied on the mirror rear side as function of the mirror radius.

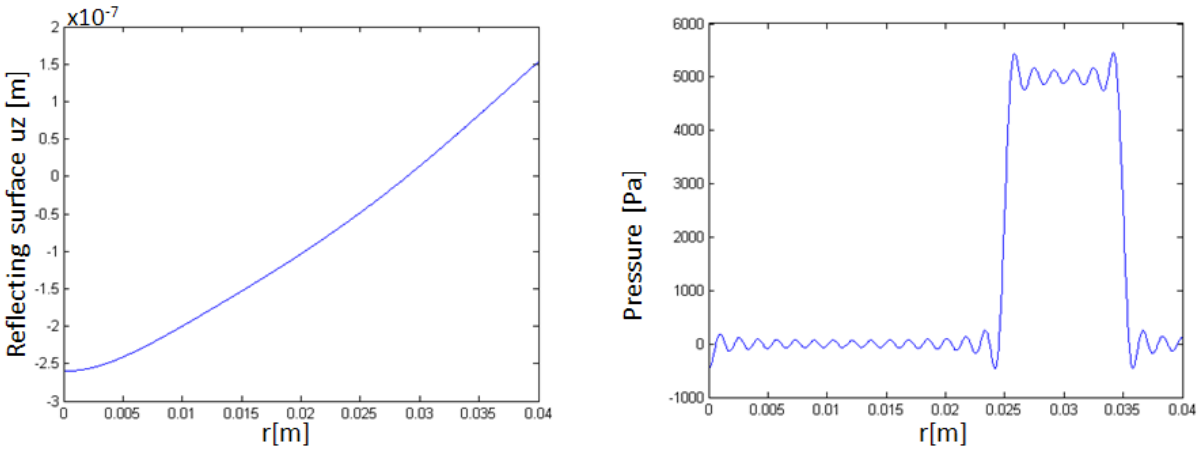

Figure 5.18: Analysis of the TCS of section (5.3.7). Configuration 3. - Mirror losses: 2518.7 ppm. Mirror curvature change: 4.9×10^{-4} m^{-1}. **Left panel**: Displacement vector of the mirror reflecting surface when a pressure of 5000 Pa is applied on the mirror back side, in the region 0.025 m $\leq r \leq$ 0.035 m. **Right panel**: pressure applied on the mirror rear side as function of the mirror radius.

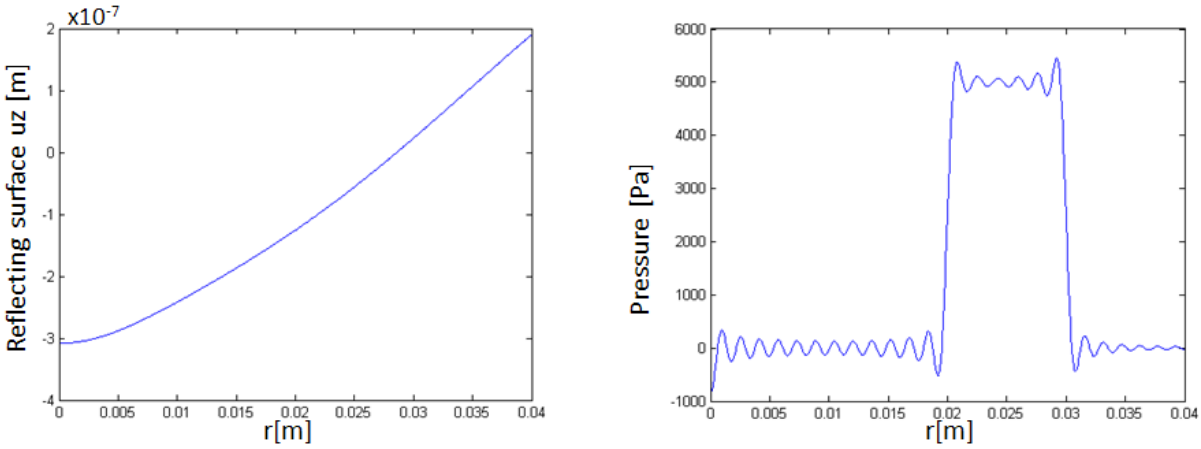

Figure 5.19: Analysis of the TCS of section (5.3.7). Configuration 4. - Mirror losses: 2518.2 ppm. Mirror curvature change: 5.6×10^{-4} m^{-1}. **Left panel**: Displacement vector of the mirror reflecting surface when a pressure of 5000 Pa is applied on the mirror back side, in the region 0.02 m $\leq r \leq$ 0.03 m. **Right panel**: pressure applied on the mirror rear side as function of the mirror radius.

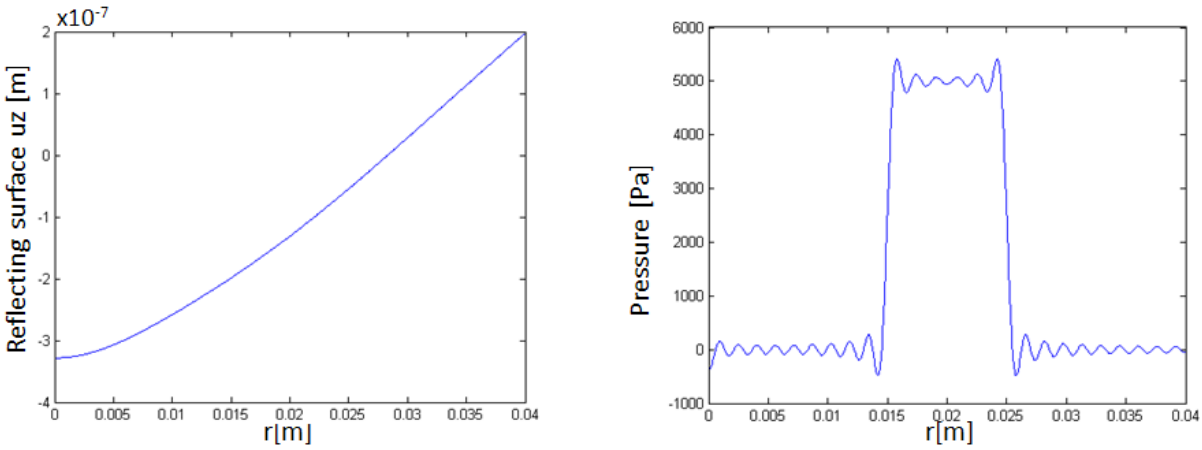

Figure 5.20: Analysis of the TCS of section (5.3.7). Configuration 5. - Mirror losses: 2511 ppm. Mirror curvature change: 5.99×10^{-4} m^{-1}. **Left panel**: Displacement vector of the mirror reflecting surface when a pressure of 5000 Pa is applied on the mirror back side, in the region 0.015m $\leq r \leq$ 0.025 m. **Right panel**: pressure applied on the mirror rear side as function of the mirror radius.

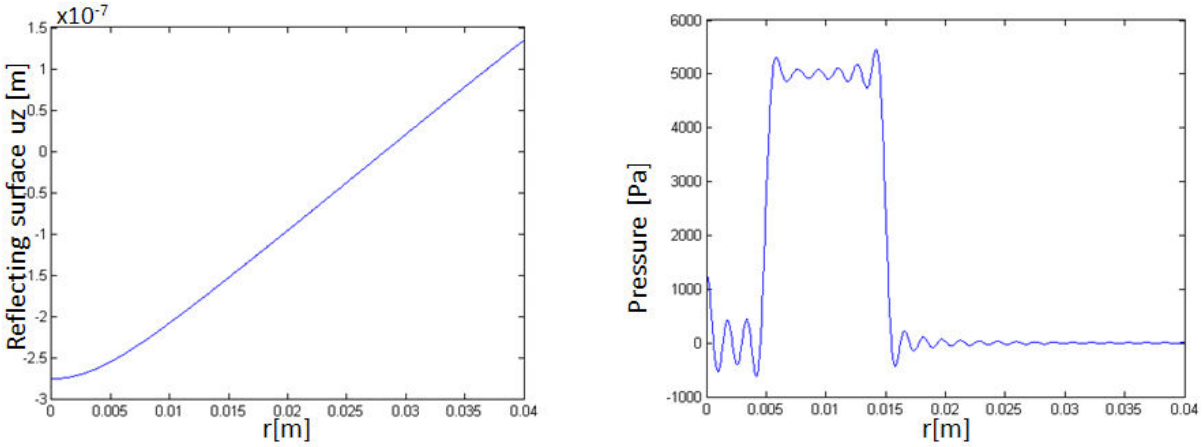

Figure 5.21: Analysis of the TCS of section (5.3.7). Configuration 6. - Mirror losses: 2784 ppm. Mirror curvature change: 5.7×10^{-4} m^{-1}. **Left panel**: Displacement vector of the mirror reflecting surface when a pressure of 5000 Pa is applied on the mirror back side, in the region 0.005 m $\leq r \leq$ 0.015 m. **Right panel**: pressure applied on the mirror rear side as function of the mirror radius.

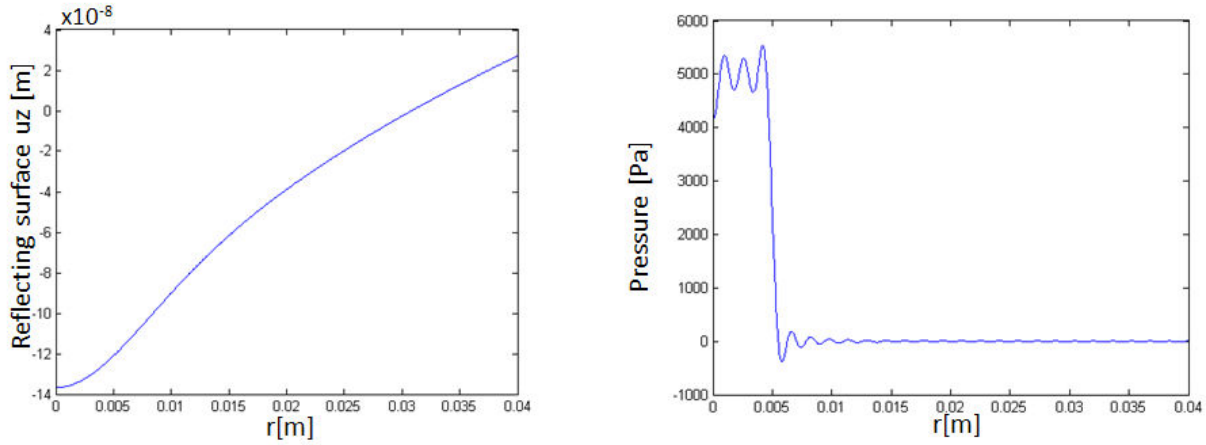

Figure 5.22: Analysis of the TCS of section (5.3.7). Configuration 7. - Mirror losses: 2836 ppm. Mirror curvature change: 3.58×10^{-4} m^{-1}. **Left panel**: Displacement vector of the mirror reflecting surface when a pressure of 5000 Pa is applied on the mirror back side, in the region 0 m $\leq r \leq$ 0.005 m. **Right panel**: pressure applied on the mirror rear side as function of the mirror radius.

5.4 Optimum TCS determination and results

The results presented in the previous sections of the current chapter show that it has been not possible to find a configuration concerning the TCS analyzed so far that could simultaneously correct the change of the mirror curvature and the mirror losses. Nevertheless, the analysis carried on in section (5.3.4) gives an important clue for a further possible TCS, based again on the application of a temperature field on the mirror rear side. Indeed, as it has been pointed out, in section (5.3.4), the mirror losses decrease when warming up the central part of the mirror. Therefore, the TCS treated in this section lies on the application of a central disk heater, on the back side of the mirror, in order to fix the temperature of the mirror region interested by the disk at the chosen value T_1. The other parts of the mirror are free to exchange heat with the environment, which is always kept at constant temperature $T_{env} = 300$ K. In section (5.3.4), it has been also noticed that, if the linearization condition is not appropriately respected, there can be significant differences between the analytical and numerical results, meaning that the errors introduced by the linearization approximation are not negligible. Therefore, in order to have the possibility of investigating this TCS on a large range of the fixed temperature, T_1, the analysis will be carried on by using the numerical calculations. Actually there is a further reason for treating this TCS through numerical simulation only. Indeed, as the mirror edges

can now exchange freely heat with the environment, the boundary equation for the heat flow on the mirror edges has to be considered, for finding the arguments of the Bessel function, entering the description of the mirror temperature field. In particular, this last quantity is written as $T_1 + \tau(r, z)$, where $\tau(r, z)$ is the excess of temperature with respect to T_1, and it has the usual form:

$$\tau(r, z) = \sum_{n=1}^{\infty} \tau_n(z) J_0(k_n \frac{r}{a}), \quad \tau_n(z) = A_n \mathrm{e}^{-k_n \frac{z}{a}} + B_n \mathrm{e}^{k_n \frac{z}{a}}, \tag{5.50}$$

where J_0 is the first kind zero order Bessel function, a solution of the Fourier equation in cylindric symmetry, with no internal source of heat [71]. As far as the coefficients A_n and B_n are concerned, they are normally obtained by solving the equations describing the boundary conditions for the heat flows on the mirror reflecting surfaces and on its rear side. Instead, the quantities k_n are found as solutions of the boundary condition equation for the heat flow on the mirror edges, and they give the arguments of the function J_0. if a is the mirror radius, the equation for the k_n reads:

$$-K\tau_{,r}|_{r=a} = \sigma \left((T_1 + \tau)^4 - {T_{env}}^4 \right), \tag{5.51}$$

with K the conductivity of the mirror material and σ the Stefan-Boltzmann constant. Thus, the left-hand side of equation (5.51) can be identified as the power lost by the substrate and its right-hand side as the power flow of thermal radiation. After the linearization of equation (5.51), assuming $T_1 >> \tau$, it results:

$$-K\tau_{,r}|_{r=a} = 4\sigma {T_1}^3 \tau + \sigma \left({T_1}^4 - {T_{env}}^4 \right). \tag{5.52}$$

The solutions of the previous equation, giving the k_n values, are not trivially found. Hence, as it has been already noticed, it is preferable to investigate this TCS with numerical analysis. Furthermore, it is assumed that the mirror is held up by a support, which prevents its edges together with a circular border 2 mm thick to expand. Therefore, the schematic illustration of the complete analyzed TCS is reported in figure (5.23). By performing simulations both with ANSYS and COMSOL, it has been observed that, when the mirror is held by a support, so that it is not free to move in the space, the simulations are faster, when they are made with COMSOL [101]. Hence, in the following, the considered TCS is analyzed, by taken into account the results obtained through the application of the software COMSOL. The validation of the TCS behavior, in correcting mirror losses and curvature change, is made by using the DarkF

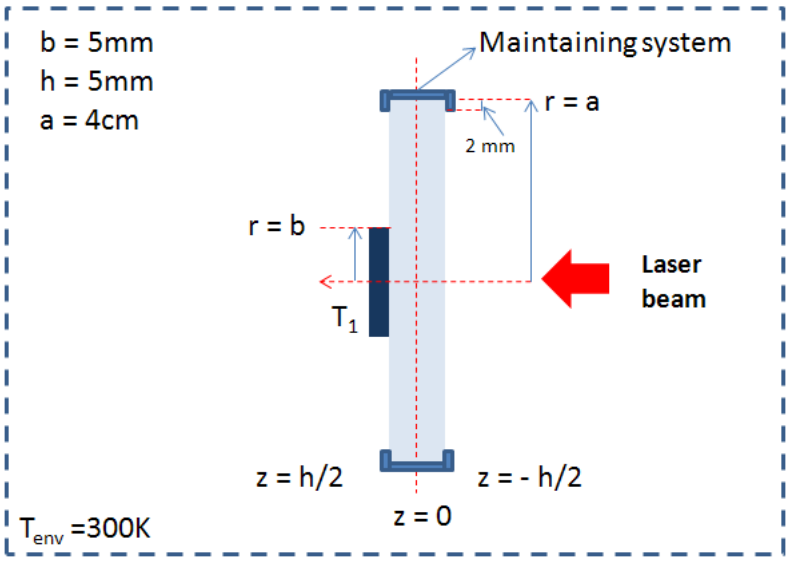

Figure 5.23: Optimum TCS schematic illustration. - Disk heater of radius b=5 mm, applied on the central part of the mirror rear side (z=h/2) to fix the temperature at the constant value T_1. Mirror radius equal to $a = 0.04$m, mirror width equal to $h = 0.005$m. Environment temperature $T_{env} = 300K$. Maintaining system which prevents the mirror edges and a circular border region, 2 mm thick, to expand.

code, which is a software based on the numerical calculation of optical field propagation, through Fourier transform application [102], [103], [104]. It is worth remarking that the COMSOL values for the losses and for the curvature change are obtained by using the COMSOL data for the displacement vector of the mirror surface internal to the optical cavity and the formulas given in section (5.1), i.e. equations (5.4), (5.5) and 5.29. Particularly, as far as the loss value is concerned, the function $\epsilon(r)$, entering equation (5.29), in the most general case, has the following expression:

$$\epsilon = u_z(r) - cr^2 - d, \tag{5.53}$$

with u_z the displacement vector of the mirror reflecting surface and cr^2+d the function describing the paraboloid which fits better the deformed reflecting mirror surface. The parameter c gives the change of the mirror curvature and its value is calculated through equation (5.4). As far as the DarkF results are concerned, they are obtained by applying the mirror deformation maps, calculated by COMSOL simulations, on an initially flat mirror. The resulting mirror profile is used in the DarkF simulations, which compute the properties of the reflected beam, when the impinging beam is the fundamental gaussian beam, of waist 1 cm, on the reflecting mirror surface. Hence, the DarkF software is able to derive the curvature of the mirror, which is

distorted by the deformation map, and its associated losses due to the mirror surface departure from a perfect paraboloid profile (see appendix (D)). It is important to observe that the radius of the disk heater applied on the rear side of the mirror, it is always assumed equal to 5 mm, in the following treatment. In figure (5.24), the mirror curvature changes and losses, as functions of T_1, are reported both for the results obtained with COMSOL and for the ones obtained with DarkF. The tables (5.1), (5.2) show the values used for realizing the plots of figure (5.24). The first thing that can be observed, when looking to the plots, is that for the curvature change as well as for the losses there is an optimum value of the fixed temperature, T_1, for which the two quantities have a minimum. Nevertheless, the T_1 value giving the lowest mirror curvature change is not equal to the T_1 value giving the lowest losses. In spite of this, when T_1 is such that it minimizes the losses, i.e. $T_1 = 690$K, the value of the curvature change is not too high. The same consideration holds for the coupling defects, as calculated by applying formula (5.47), which are of the order of 2%. The main feature of this TCS is that it can reduce the mirror losses below the ones due to the mirror manufacturing defects. Indeed, for $T_1 = 690$ K, the loss value is of about 5 ppm.

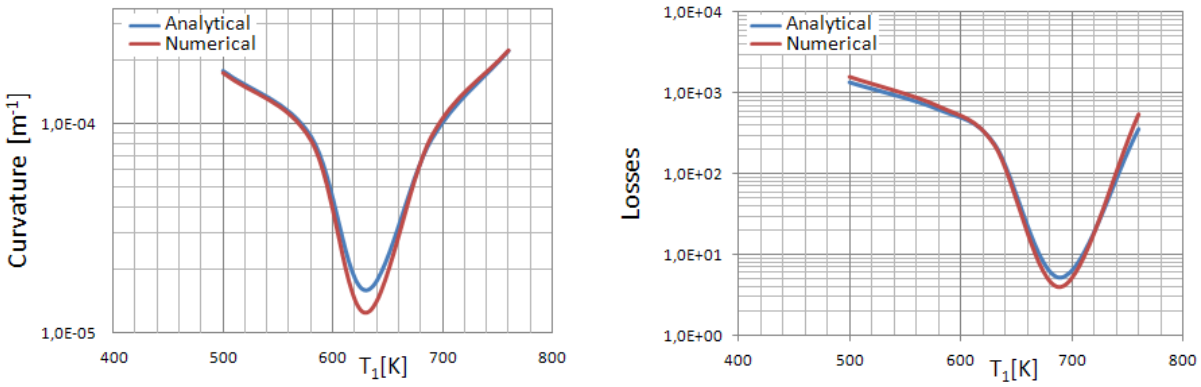

Figure 5.24: Optimum TCS results - Left panel: curvature change as a funtion of the temperature T_1 fixed on a central disk of radius 0.005 m, on the rear side of the mirror. Calculations performed by using the deformed mirror map numerically calculated with COMSOL and the analytical formula (5.4), blue line, and the same mirror map together with the DarkF calculation for the curvature changes, red line. **Right panel**: mirror losses as a funtion of the temperature T_1 fixed on a central disk of radius 0.005 m, on the rear side of the mirror. Calculations performed by using the deformed mirror map numerically calculated with COMSOL and the analytical formula 5.29, blue line, and the same mirror map together with the DarkF calculation for the losses, red line.

For a deeper comprehension of the TCS under study, it is worth comparing it with the case where no temperature field is applied on the mirror, even if the same maintaining system is

COMSOL plus DarkF	
T_1 [K]	Losses [ppm]
500	1585
580	684
630	230
690	4
760	545

COMSOL plus analytic formulas	
T_1 [K]	Losses [ppm]
500	1353
580	624
630	237
690	5
760	358

Table 5.1: Mirror loss results for the TCS in section (5.4). Comparison of the mirror losses as calculated with the application of the formulas in section (5.1) and with the DarkF method, by using the numerical data for the mirror deformation computed by COMSOL.

COMSOL plus DarkF	
T_1 [K]	Curvature [m^{-1}]
500	1.7×10^{-4}
580	8.3×10^{-5}
630	1.2×10^{-5}
690	8.7×10^{-5}
760	2.2×10^{-4}

COMSOL plus analytic formulas	
T_1 [K]	Curvature [m^{-1}]
500	1.8×10^{-4}
580	8.7×10^{-5}
630	1.6×10^{-5}
690	8.4×10^{-5}
760	2.2×10^{-4}

Table 5.2: Absolute values of the mirror curvature change for the TCS in section (5.4). Comparison of the mirror curvature changes as calculated with the application of the formulas in section (5.1) and with the DarkF method, by using the numerical data for the mirror deformation computed by COMSOL.

used. In particular, in figure (5.25), the results concerning the mirror temperature field, its distortion and the best parabolic fit are given both for the mirror without TCS, and for the mirror with the considered TCS, when $T_1 = 690$K. It is worth stressing that the environment temperature is always considered equal to 300K. The main feature to be highlighted, on figure (5.25), is that the warming up of the central part of the mirror rear side leads to invert the longitudinal temperature gradient. Furthermore, by paying attention on the deformation of the mirror for the case with the application of the TCS and for the case without TCS, it is evident that the inversion of the longitudinal temperature gradient also pushes the deformation to invert its direction. Thus, the mirror central bulging, for the case with TCS, turns out to be inverted with respect to the one present in the case without TCS. The consequence of this effect is the compensation of the mirror reflecting surface deformation showed when no TCS is applied. Indeed, as it is possible to check from the plot of the best paraboloid fit on the bottom of figure (5.25), the parabolic fit approximates quite well the surface of the mirror, and it is for this reason that the mirror losses result so low. In order to clarify this point, picture (5.26) is reported, where the difference between the best paraboloid fit and the real deformed mirror surface is plotted, for both the case with TCS and for the one without TCS, for the mirror region involved in the beam reflection, i.e. $r \lesssim 0.01$ m. With reference to figure (5.26), by approximating the integration in equation (5.29) with the difference pick-to-valley, σ, for each of the plotted curves, a mirror loss estimation, for both the configurations, can be expressed as follows:

$$\tilde{L} = 4\left(\frac{2\pi}{\lambda}\right)^2 \sigma^2, \tag{5.54}$$

where λ is the laser wavelength. In picture (5.26), the difference pick-to-valley for the case without TCS is indicated as σ_{Free} and the one for the case with TCS is labeled as σ_{TCS}, the ratio between the two is:

$$\frac{\sigma_{Free}}{\sigma_{TCS}} \approx 20, \tag{5.55}$$

therefore, from equation (5.54), the loss reduction factor, when the TCS considered in this section is applied, with respect to the case without TCS is:

$$\frac{\tilde{L}_{Free}}{\tilde{L}_{TCS}} \approx 400. \tag{5.56}$$

In conclusion, the TCS considered in this section is a possible solution for the control of the mirror thermal effects.

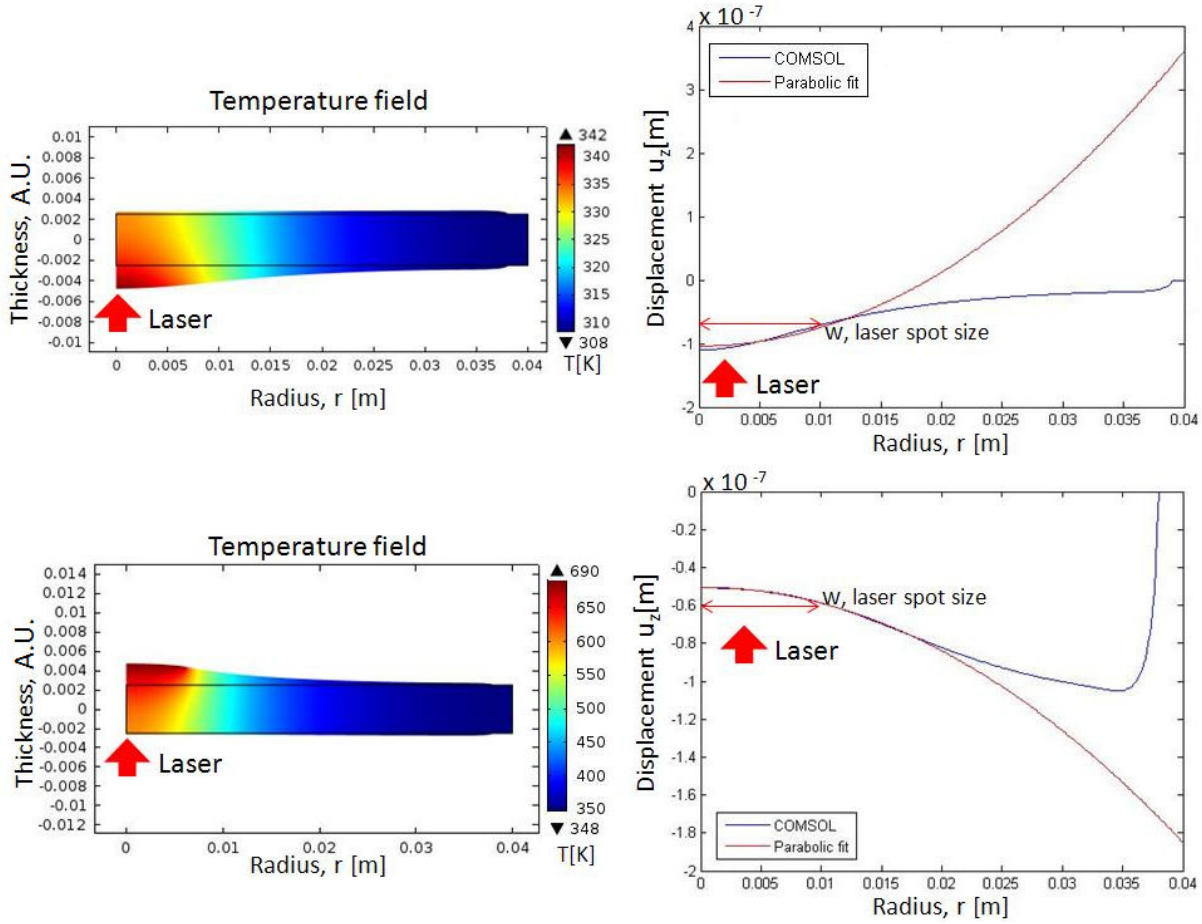

Figure 5.25: Mirror thermal effects correction by the Optimum TCS. - comparison between the case where the best configuration for the optimum TCS is applied on the mirror and the case without TCS. The environment temperature is 300 K **top panels**: on the left side, the temperature fields and the volumetric deformation of the mirror is showed, when the TCS is not applied. The plot on the right illustrates the paraboloid which fits better the distorted reflecting surface of the mirror without TCS. **bottom panels**: on the left side, the temperature field and the volumetric deformation of the mirror is showed, when the optimum TCS for $T_1 = 690$K is applied. The plot on the right illustrates the paraboloid which fits better the distorted reflecting surface of the mirror when the optimum TCS, for $t_1 = 690$K is applied.

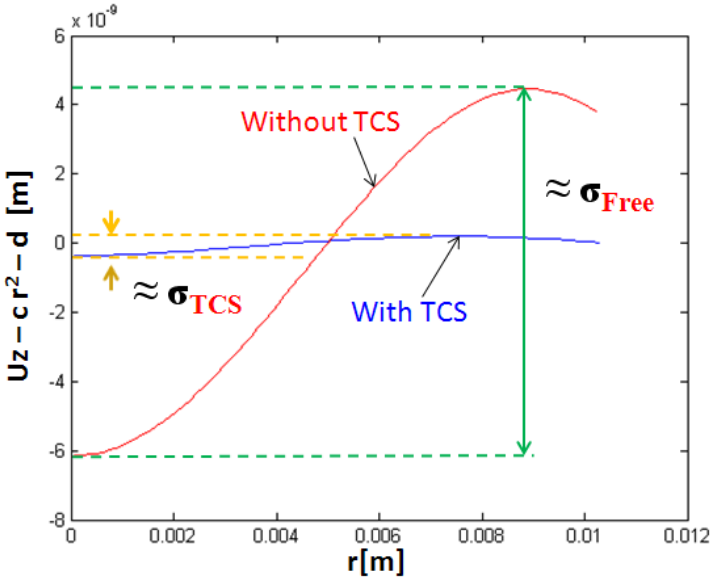

Figure 5.26: Difference between the best paraboloid fit and the real deformed mirror surface, for the mirror region involved in the beam reflection. - The blue line describes the difference between the best paraboloid fit and the real deformed mirror surface, when assuming to apply the best configuration for the considered TCS, on the mirror, i.e. a temperature $T_1 = 690$K is fixed on the rear side of the mirror, on a central disk of radius 0.005 m. The red line describes the difference between the best paraboloid fit and the real deformed mirror surface, for the case without TCS detailed in section (5.4). Furthermore, σ_{TCS} and σ_{Free} indicate the difference pick-to-valley for the curve concerning the case with TCS and the one without TCS, respectively.

Chapter 6

Test on Large Mode Area (LMA) Leaky 0ptical Fiber

It has been already pointed out that a laser source of about 1 kW should feeds the optical cavity used for NBI system applications, in order to reach an intracavity power of few MW, which is required for a suitable neutralization efficiency of the negative ion beam. Currently, it is not a trivial issue to realize so powerful laser sources. In this respect, several methods are under study, such as the coherent superposition of laser beam [105], [106] and their amplification through fiber amplifiers. Particularly, in the present chapter, it is reported on the experimental tests concerning a new concept of optical fibers, which have been carried on, in order to verify the possibility of applying this new fiber design for realizing fiber amplifiers. Indeed, by starting from a feasible laser source, laser beam amplifiers could then be used to get to the optical power required for NBI system applications. The fibers under analysis are known as Large Mode Area (LMA) Leaky fibers, a modification of the LMA fibers which have been developed for allowing single mode operation without enhancements of nonlinear effects, either due to the optical intensity dependence of refractive index of the medium or due to inelastic-scattering phenomenon [107] [108]. Indeed, the mentioned nonlinear effects are usually present in ordinary single mode fiber, as the light beam is confined in a smaller transverse region with respect to the one of the LMA fibers, hence a lower optical power is required for reaching high optical intensity and, as a consequence, for the nonlinear effect to show up [109]. The main issue concerning the ordinary LMA fibers is that the techniques used to obtain their single mode operation lead often to significant power losses of the transmitted beam [110]. This is the reason to look for new single mode fiber design. In the first part of the chapter, general notions about optical fibers

will be presented, which are useful for the comprehension of the following sections. The second part of the chapter aims to describe the working principles on which the LMA Leaky optical fibers are based, their difference with respect to the ordinary LMA fiber and the particular structure of the LMA Leaky fiber which have been analyzed in this work. In the last section, the experimental tests on the considered optical fiber are described and the relative results are reported.

6.1 Generalities on optical fibers

Optical fibers are waveguide for electromagnetic wave transmission realized with low-loss material, such as silica glass. Their working principles can be examined both from the point of view of the electromagnetic theory and from the one of the geometric optics. In the former case, the electric and magnetic fields of the guided waves, which solve the Maxwell equations together with the boundary conditions defined by the fiber optical and geometric properties, are determined. In the latter case, the light guiding is explained through the total internal reflection phenomenon that can take place when a light ray impinges a boundary surface to a medium with lower refractive index, at an appropriate incidence angle. [52], [111].
Within the context of the geometric optics treatment, it is worth reminding the mathematical expression for the critical angle. To this aim, we consider a light ray passing from a medium with higher refractive index, n_B, to another with lower refractive index, n_A, and we label with α the incidence angle and with β the refractive angle. The *Snell's law of refraction* reads:

$$\frac{\sin\alpha}{\sin\beta} = \frac{n_A}{n_B}, \tag{6.1}$$

if $\beta = 90°$, no light is transmitted in the medium characterized by n_A. The incidence angle for which this happens is called critical angle:

$$\sin\alpha_{critic} = \frac{n_A}{n_B} < 1. \tag{6.2}$$

For incidence angles larger than α_{critic}, the total internal reflection phenomenon takes place and the light ray is reflected back into the medium with higher refractive index.

The first fibers were realized in 1920s and they were simple one-layer structure of glass. However, the fiber optics was born only in 1950s, after the introduction of a cladding layer of slightly lower refractive index. Indeed, because of the two-layer structure, the region outside

the fiber and the electromagnetic wave guiding region are not anymore in contact. Hence, the fiber function of light transmission is not compromised by contacts with other glass structures or because of the presence of impurities on the fiber surface, which would lead to high loss levels. These two-layer structure fibers are known as *step index fiber*. The internal structure has a circular cross-section and is known as fiber core. The external structure has a ring shape and it is called fiber cladding. Hence, from the point of view of the geometric optics, light rays incident on the core-cladding boundary at greater angle with respect to the critic one experience total internal reflection and are guided within the core. Rays incident on the core-cladding boundary at smaller angle than the critical one lose part of their power in the cladding, at each reflection, hence they are not guided. It is now appropriate to introduce three parameters which characterize the fibers, i.e. the core cladding index difference, Δ, the numerical aperture, NA, and the so called V parameter. The former quantity is defined as:

$$\Delta = \frac{n_1^2 - n_2^2}{2n_1^2}, \tag{6.3}$$

where n_1 and n_2 are the refractive indexes of the two media used for the core and the cladding respectively, hence $n_1 > n_2$. However, usually $n_1 \sim n_2$, with Δ of few tenths of 1%, hence:

$$\Delta \sim \frac{n_1 - n_2}{n_1}. \tag{6.4}$$

The numerical aperture is:

$$NA = \sqrt{n_1^2 - n_2^2}, \tag{6.5}$$

in terms of Δ, it becomes:

$$NA = n_1\sqrt{2\Delta}. \tag{6.6}$$

The V-parameter is:

$$V = ka(n_1^2 - n_2^2)^{1/2}, \tag{6.7}$$

where a is the core radius, $k = 2\pi/\lambda$ and λ is the wavelength of light. It is worth noticing that this quantity is introduced within the context of the electromagnetic theory treatment for the wave propagation within an optical fiber. It is possible to express V in terms of the numerical aperture, so that:

$$V = kaNA. \tag{6.8}$$

The V parameter determines the number of modes supported by an optical fiber. Furthermore,

from relation 6.8, it appears that the number of modes guided by a fiber also depends on the numerical aperture. It is observed that a step index fiber supports only one mode if $V < 2.405$. Optical fibers with this characteristic are addressed as single-mode fibers. The main difference between single-mode and multimode fibers concerns the core size. Particularly, for multimode fibers the core radius is customary of 25-30 μm, instead fibers with $\Delta \sim 0.003$, core refractive index, $n_1 = 1.46$, $\lambda = 1.55\mu$m, need a core radius smaller than 5 μm to operate as a single-mode fiber.

Another step ahead in the improvement of fiber capability in transmitting electromagnetic waves has been made in 1970s, when methods were determined to decrease the fiber losses from the original value of about 1000 dB/km to the value of 20 dB/km in silica fibers, see [112], [113]. This has led to deal with the issues of nonlinear effects in optical fibers, due to the increased level of electromagnetic field intensity within the fibers, e.g. stimulated Raman scattering and stimulated Brillouin scattering, which are briefly discussed in the next section. In particular, stimulated Raman scattering is efficient when considering pulsed operation laser, while stimulated Brillouin scattering is mainly due to the small effective area of the mode supported by a given mono-mode fiber and to the long propagation distance. In the present context, only Brillouin scattering could be involved. It is relevant to observe that nonlinear effects are mostly present in single mode fibers due to their smaller core diameter which leads to higher levels of electromagnetic field intensities inside the fiber. To conclude this section, it is worth mentioning that in 1990s the doping of optical fiber core with rare earth elements has opened the field of fiber amplifiers and fiber lasers [108].

6.2 Fiber Nonlinearities

In the optical fiber context, nonlinearities indicate the non linear response of the fiber medium to the light, which becomes important for electromagnetic fields of high intensity. Indeed, in this condition, the total polarization, $\overrightarrow{P}$, of the fiber medium responds nonlinearly to the electric field of the electromagnetic wave propagating inside the fiber, i.e.:

$$P_i = \epsilon_0 \left(\sum_j \chi_{ij}^{(1)} E_j + \sum_{j,k} \chi_{i,j,k}^{(2)} E_j E_k + \sum_{j,k,l} \chi_{i,j,k,l}^{(3)} E_j E_k E_l + ... \right), \tag{6.9}$$

where i is the i-th Cartesian coordinate of the polarization, ϵ_0 is the free space permittivity and $\chi^{(n)}$ is the n-th order susceptibility of the considered medium. In particular, $\chi^{(n)}$ is a tensor

of rank $n+1$. The linear susceptibility $\chi^{(1)}$ gives rise to effects included in the definition of the refractive index and attenuation coefficient of the medium. As far as $\chi^{(2)}$ is concerned, it is normally zero for media compounded by symmetric molecules, such as the silica glasses. It has to be noticed that second-order nonlinear effects could be introduced by the electric quadrupole and magnetic-dipole moments, but they are weak, so that, customary, optical fibers do not show second order non linear effects. In optical fiber, the nonlinear effects associated to $\chi^{(3)}$ are represented by the dependence of the refractive index on the intensity of the electromagnetic field and by stimulated inelastic scattering, i.e. the stimulated Raman scattering and the stimulated Brillouin scattering [114].
As far as the effects associated with the refractive index dependence on the electric field intensity, it is worth noticing that the following relation holds:

$$n(\omega, |E|^2) = n_N(\omega) + n_{NL}|E|^2 \tag{6.10}$$

where $|E|^2$ is the electric field intensity, $n_N(\omega)$ is the linear part of the refractive index depending on the light frequency, ω, and n_{NL} is the nonlinear part depending on $\chi^{(3)}$. Indeed:

$$n_{NL} = \frac{3}{8n_N} Re(\chi^{(3)}), \tag{6.11}$$

with Re indicating the real part. The dependence of the refractive index on the electric field intensity leads to several nonlinear effects the main ones are the self-phase modulation (SPM) and the cross-phase modulation (XPM), described in reference [108]. Shortly, SPM is the phase shift induced by the optical field itself while propagating within a fiber, instead, XPM is the phase shift of an optical field introduced by another optical field with different wavelength, propagation direction or polarization.
As far as the Raman and Brillouin inelastic scatterings are concerned, in both the cases the electromagnetic field transfer part of its energy to the medium where it is propagating. The main difference between the two scatterings is that optical phonon, i.e. out of phase movements of the atom in the lattice of the considered medium, participate to the first one and acoustic phonon, i.e. coherent movements of the atom in the lattice of the considered medium, participate to the second. For a simplified description of both the inelastic scatterings, it is possible to imagine that a photon of the incident field is annihilated by generating a photon of lower energy, with respect to the initial one, and a phonon (optical or acoustic depending on the considered process) with the suitable energy and momentum required by the conservation laws of momentum and

energy. It is worth noticing that the presence of optical phonon, for the Raman scattering, and of acoustic phonon, for the Brillouin scattering, implies different dispersion relations which in turn lead to differences between the two scattering. For example, stimulated Brillouin scattering in fiber occurs only in the backward direction, with scattered photons of lower frequency with respect to the one of the incident field, because of the energy conservation requirement, while the stimulated Raman scattering can occurs in both the directions. The initial growth of the Stoke wave, which is the wave produced by the photons resulting from both the scattering processes, can be described with an analogue formula for both the Raman and Brillouin case [108], i.e.:

$$\frac{dI_s}{dz} = g_{R/B} I_p I_S, \tag{6.12}$$

where I_s is the intensity of the Stokes wave, I_p is the intensity of the incident optical field and g_R, g_B indicate the gain coefficient for the Raman scattering and for the Brillouin scattering respectively. It is important to note that both g_R, g_B depend linearly on the third order susceptibility $\chi^{(3)}$ [108]. Another important characteristic of both the Raman and Brillouin scattering is that they are threshold process. Indeed a significant conversion of the incident optical intensity is converted into the Stokes wave intensity only if the incident intensity exceeds a given threshold level. It is also observed that, as the Brillouin gain coefficient is larger than the Raman gain coefficient, the threshold for the incident intensity is lower in the case of the Brillouin scattering [108].

6.3 Large Mode Area (LMA) Fiber and LMA Leaky Fiber

As it has been already pointed out in section (6.1), nonlinear effects are mostly present in single mode fiber, where light is confined in a small transverse region, so that its intensity can reach high level. Nevertheless, single mode guidance has many important applications, e.g. in fiber lasers and in fiber amplifiers for obtaining high beam quality at output of the fiber and in optical communications, for an appropriate transmission of the input signals at the receiver [110]. In this respect, it is noticed, that single mode optical fiber present a high beam quality, which is the fundamental properties for the applications mentioned above. Hence, the issue of determining a single mode fiber structure, which does not enhance nonlinear effects, had to be faced. Indeed, nonlinear effects, on one hand, can limit the optical power transmitted by the fibers, on the other hand, they can spoil the beam quality. A first step ahead toward the problem solution, has been done with the introduction of Large Mode Area fibers, i.e. optical fibers which support

only one mode, while having a quite large core radius (few tens of μm). Due to the larger area where light is confined, the intensity of the light in such fibers is reduced with respect to the one in ordinary single mode fibers, hence they present lower nonlinearities and a damage threshold at higher optical powers. There are several techniques for realizing LMA fiber. A possibility is the fiber bending which leads to important power losses for higher order modes. The problem concerning this method is that the losses are large even for the fundamental mode.
With the aim of finding an optimal solution for limiting nonlinearities in single mode fibers, a new concept of LMA fiber has been introduced, i.e. the LMA Leaky fiber. This kind of optical fiber is based on the concept of large differential leakage losses between the fiber higher order modes and the fundamental one. The consequence is a substantial single mode (SM) operation of the fibers, which then result to guide the fundamental mode only. It is stressed that these fibers still present a large core radius, but they structure is studied for allowing significant higher leakage losses for the fiber higher order modes with respect to the ones of the lowest order mode [115], [116], [117], [118]. Several methods have been determined to get to this fiber behavior:

- fiber structure with uniform refractive index in the core and segmented cladding through alternate regions at high and low refractive index on the cladding angular direction, e.g. [119];

- fiber structure consisting in a cladding refractive index which increases monotonically in the radial direction, e.g. [116];

- fiber structure with uniform core refractive index and a cladding made up of trenches at low refractive index, with different values, alternated to high refractive index trenches, with same value of the core refractive index, e.g. [120].

Particularly, the fibers taken into account in this analysis have the structure based on the third technique described above. A core of high refractive index is surrounded by a cladding made up of periodical trenches at low refractive index, while the other cladding regions have the same refractive index value of the core. An appropriate choice of the parameters, for this kind of fiber structure, leads to the resonant coupling of the higher order mode power from the core to the external fiber region with the same refractive index of the core. The complete structure is then made highly leaky, by adding a last layer with the same core refractive index. In this way, the differential leakage loss between the fundamental mode and the higher order modes increases considerably, so that, after a suitable propagation length, the fiber results in an effective single

mode operation. It is worth noticing that the suppression of the fiber higher order modes, with respect to the fundamental one, has to be effective within a propagation length inside the fiber, which is suitable for the foreseen applications of the fiber itself.

6.4 Analysis of LMA Leaky fiber properties

The study presented in this chapter has the aim of validating the working principles of LMA leaky fiber whose structure is based on the presence of a core with uniform refractive index and a cladding configuration where regions at lower refractive index values are alternated to regions with the same core refractive index value. As already said, this cladding design acts as modal filter, which allows the single mode operation of the fiber, by suppressing all the higher order modes, after a certain propagation length within the fiber. The presented fiber description is based on the previous work of Ref. [109]. For the sake of simplicity, a cladding structure with only two trenches at lower refractive index values, with respect to the one of the core, is taken into account. The considered fiber refractive index profile structure is reported in figure (6.1). The core fiber and the other regions with the same refractive index value, n_1, are made with pure

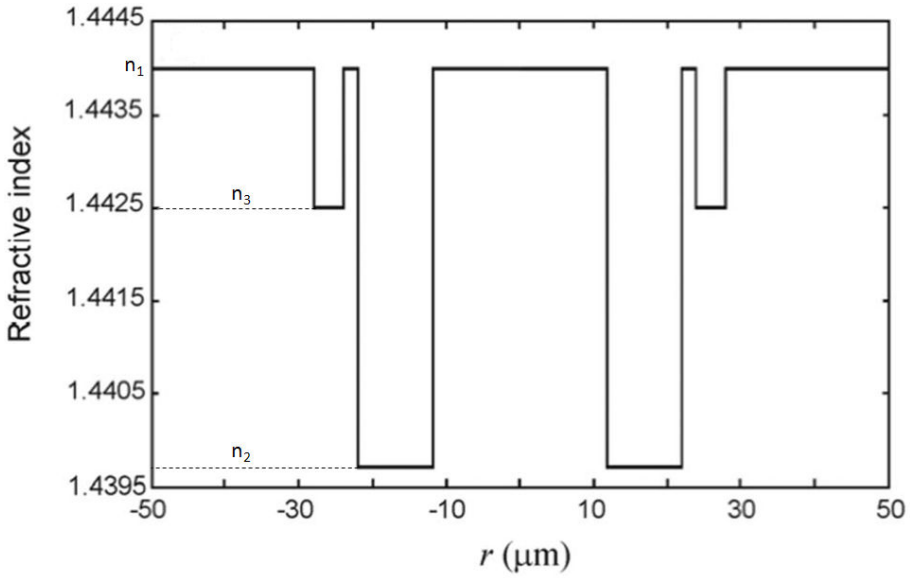

Figure 6.1: Theoretical refractive index profile - Theoretical refractive index profile as function of the fiber radius, for the analyzed LMA leaky fiber. In the picture, the refractive indexes of the different regions are indicated as n_1, n_2 and n_3.

silica. The region with lowest refractive index value, n_2, is obtained by doping the pure silica

with fluorine (F). By decreasing the quantity of fluorine, the refractive index value increases and it is possible to realize a region at refractive index value n_3, where $n_3 > n_2$. Numerical studies conducted through the transfer matrix method (TMM) [121] show that, for the proposed fiber structure, the leakage losses of the modes increases with the mode number. As a consequence, for determining the single mode operation condition for the analyzed fiber, it will be enough to check the differential leakage losses between the fundamental mode of the fiber and the first higher order mode. Numerical calculations give a value of 0.35 dB/m for the leakage loss of the fiber fundamental mode and a value of 8.3 dB/m for the first higher order mode. Furthermore, simulation results indicate that the fiber should be single mode, after a propagation length inside the fiber of 2.4 m [109]. The numerical calculations also give a mode field diameter at the fiber exit of 26 μm. The considered fiber has been realized by starting from a preform of diameter 11.4 ± 0.2mm, which has been fabricated with the modified chemical vapor deposition (MCVD) technique [122]. The preform has then been drawn into a fiber with total diameter of $110.0 \pm 0.2\mu$m. The refractive index profile of the realized fiber has been measured with the optical fiber analyzer NetTest S14 and it is reported in picture (6.2). The relative refractive

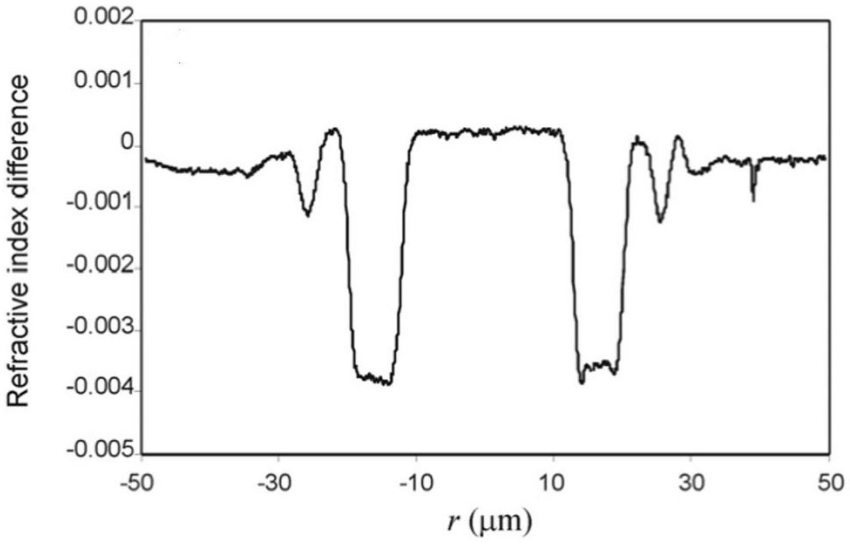

Figure 6.2: Refractive index profile of the fabricated fiber - Refractive index profile as function of the fiber radius, for the realized LMA leaky fiber

index difference concerning the core and its adjacent region is $\Delta \sim n_1 - n_2/n_1 = 0.28\%$, the numerical aperture, calculated for the same two regions, is $NA = 0.11 \pm 6\%$, and the diameter of the core is $25.4 \pm 0.3\mu$m. It is worth noticing that the numerical aperture of the fiber is

quite large for a single mode fiber. Indeed, with these properties and for $\lambda = 1.55\mu$m, a V parameter of about 5.6 results, so that several modes would be guided by a conventional fiber. The second low refractive index trench is 25 μm far from the fiber center and it has a width of 3 μm. Moreover, the associated relative refractive index difference is $\Delta \sim n_1 - n_3/n_1 = 0.1\%$. By considering the real refractive index profile, the TMM method gives a fundamental mode diameter, at $1/e^2$ of maximum intensity, of 26μm. Furthermore, as the fiber structure presents a certain ellipticity, the calculated propagation losses on both the axes for the fundamental mode and for the first higher order mode are 3.25 dB/m and 1.63 dB/m, for the lowest order mode, and 56 dB/m and 37 dB/m, for the first higher order mode. Hence, the first higher order mode, as well as the other higher order modes, should be suppressed after a short propagation length within the fiber. Experimental studies for the fiber characterization were conducted by injecting into the fiber a laser of wavelength $\lambda = 1.55\mu$m. The measured $1/e^2$-mode diameter after 4 m propagation turned out to be $22 \pm 2\mu$m, in a quite good agreement with the numerical simulations. Hence, this last result will be taken into account to start the experimental tests on the considered fibers.

6.5 Experimental tests on LMA Leaky fibers

In this section, the experimental results concerning the optical fiber previously described are presented. In particular, a laser beam of wavelength $\lambda = 1064$ nm is injected inside the fiber and the output beam is analyzed as far as its shape and power are concerned, for different lengths of the optical fiber. To efficiently inject the laser beam inside the fiber, the fiber itself and the laser beam have to be correctly aligned. With this purpose, a dedicated stage with three degrees of freedom (vertical translation, horizontal translation and translation along the direction of the fiber optical axis) is used to fine position the fiber with respect to the laser beam, and the beam direction is also controlled by using the pitch and yaw degrees of freedom guaranteed by the mirrors used to inject the laser beam into the fiber. Furthermore, the waist of the laser beam has to be on the starting point of the fiber and it has to be equal to the radius of the fiber output mode, hence the three degrees of freedom stage is placed on a translation plate which allows larger displacements along the direction of the fiber optical axis with respect to the one permitted, along the same direction, by the three degrees of freedom stage. As it has already been said, theoretical studies carried on with the TMM method indicate, for the fiber output mode, a diameter, at $1/e^2$ of maximum intensity, of 26 μm. Nevertheless, experimental analyses

to characterize the fiber show a $1/e^2$ mode diameter of 22±2 μm, after 4 m propagation [109]. For the experimental tests, whose results are reported in this section, it is firstly assumed a fiber output mode radius of 11 μm. Hence, the waist of the laser beam has to be adapted in order to be of 11μm, at the starting point of the fiber. To this aim, an optical system compounded of three lenses is applied. Indeed, as it has been already pointed out in precedent chapters, measurements performed with the Beam Scan and the dedicated software indicate a waist of 650 μm ± 5 %, for the laser beam produced by the fiber laser utilized, after passing through the collimator. Through the software *GaussianBeam*, a three lens optical system to reduce the laser beam waist to 11 μm, at a suitable distance for the fiber positioning, has been found. In order to verify experimentally the results concerning the described optical system, the value of the laser beam diameter was measured at several distances from a mirror placed at 12.5 cm from the last lens of the system, through the Beam Scan and a dedicated software. It turned out that the laser beam waist was actually of 15 μm at 137.5 cm from the collimator, hence it has been necessary to change the position of the lenses until finding a configuration giving the required beam width. To verify that the laser beam waist, after passing through the new optical system, was of 11 μm, the laser beam diameter has been measured again at several distances from a mirror placed at 127.5 cm from the laser collimator, by using the Beam Scan and the dedicated software. The obtained values have been used to make fits, with the software *GaussianBeam*, in order to determine the waist and its position, after the optical system. In picture (6.3), it is reported on the fit results concerning the measurements of the beam horizontal diameter. Regarding to picture (6.3), it is worth noticing that the distance values are referred to the mirror placed at 127.5cm from the laser collimator, and that an error of 5% can be associated with the beam diameter measures. The accuracy of the fit results is not high, as the errors on the measurements are large and the fit does not take into account them. Nevertheless, the outcomes of the fit both for the beam horizontal diameter, presented in picture (6.3), and for the vertical one indicate the same values for the beam waist and its position, thus it is assumed that the determined optical system gives the required beam waist and the fiber experimental analysis is begun.

The fiber behavior, with respect to the electromagnetic wave transmission, can be analyzed for different lengths of the fiber itself. In particular, the test is started by taking into account the 1 m long optical fiber. Once the optical system to adapt the laser beam waist is determined, it is necessary to properly set the beginning of the optical fiber at the waist position of the laser beam and to align the laser beam with the fiber. Firstly, the initial part of the fiber is

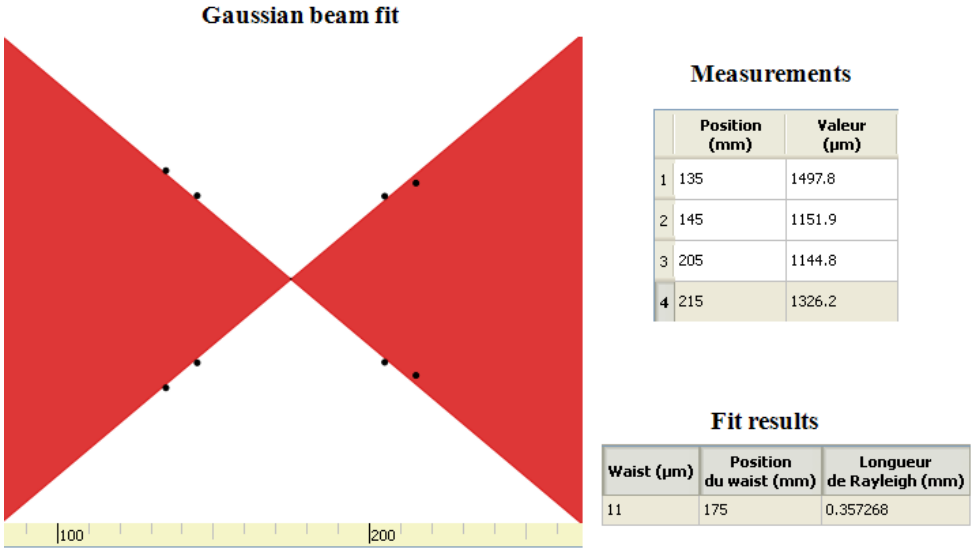

Figure 6.3: Fit performed with the software *GaussianBeam*, giving the beam waist and its position. - **Right panels:** on the top, the values of the beam diameter as measured with the Beam Scan and the dedicated software, at different distance from a mirror at 127.5 cm from the laser beam collimator, are reported; on the bottom, the fit results for the beam waist and its position are showed. **Left panel:** fit performed with the software *GaussianBeam*.

set close to the laser beam waist position. Then, the fine alignment between fiber and beam is obtained, by using the mirror mounts, which allow to control the laser beam direction, and the three degrees of freedom of the fiber stage. The latter one, in turn, is placed on a mobile support which allows the fiber translation to put its starting point exactly on the waist of the laser beam. The optimum match between fiber and laser beam has to maximizes the fiber output power. In this condition, the ration between the power at the fiber exit and the power injected into the fiber is 0.41, i.e. the 41 % of the input power can be found at the fiber exit. This result is not satisfactory with respect to the applications foreseen for this kind of fibers. Hence, it is checked if the radius of the mode supported by the fiber is different from 11 μm. To do this, the diameter of the beam at the exit of the fiber is measured, for several distances from the ending point of the fiber. The measured values of the beam diameter are used to make a fit and to find the waist of the beam, at the exit of the fiber. It is worth noticing that the procedure utilized is analogue to the one applied to experimentally verified that the realized optical system was giving an output beam with waist 11 μm. Thus, the Beam Scan and the dedicated software are used to measure the laser beam diameter at the exit of the fiber for different positions. The results are reported in table (6.1). The fit performed with the *GaussianBeam* software, by considering

Distance [cm]	$Width_x$ [μm]	$Width_y$ [μm]	$Error_x$ [μm]	$Error_y$ [μm]
1.7	578.9	658	29	33
3.4	1127.3	1302.2	56	65
4.4	1717.1	2010	86	100
5.6	2223	2604	111	130
6	2467	2914.4	123	146
7.3	3073	3544	154	177

Table 6.1: Measurements of the laser beam diameter at several distances from the end point of the optical fiber 1 m long. It is observed that the distances are taken from the fiber end point, which is set to zero. Furthermore, the coordinate x indicates the horizontal diameter and the coordinate y indicate the vertical diameter. The errors are assumed equal to the 5 % of the measured diameter value, i.e. the effective accuracy possible for laser beam diameter measurements.

	Position [cm]	Focal length [mm]
L_1	10.5	50
L_2	21.5	750
L_3	115.1	200

Table 6.2: Optical system for getting to a waist of 8 μm. It is observed that the distance are taken from the starting point of the laser beam, i.e. from the laser beam collimator.

the measured values of the laser beam horizontal diameter, reported in table (6.1), gives a waist dimension of 8.8 μm at distance 6.3 mm from the end of the fiber. Moreover, the fit concerning the measured values of the vertical laser beam diameter of table (6.1) gives a laser beam waist of 7.5 μm at distance 6.4 mm, from the end point of the fiber. Hence, the mode diameter that can be supported by the fiber should be of about 16 μm. It is then worth changing the position of the three lenses compounding the optical system used to reduce the laser beam waist to 11 μm, in order to get to a laser beam with waist 8 μm at the beginning of the fiber. In this way, it is possible to check if the ratio between the fiber output power and the fiber input power increases. By using the software *GaussianBeam*, several lens configurations were determined to get to a waist of 8 μm. The adopted setup is reported in table (6.2). Indeed, for this case, the values of the laser beam diameter were measured, with the Beam Scan and the dedicated software, at different distances from the mirror placed at 11.5 cm from the last lens (L_3, in table (6.2)). The measures concerning the laser beam diameter and the corresponding positions are showed in table (6.3). The fits realized with the software *GaussianBeam* and made by taking into account these data, for both the horizontal and vertical beam diameter, give the results of a waist of 8 μm at distance 24.2 cm and 24.3 cm, respectively, from the mirror at distance 11.5

Distance [cm]	$Width_x$ [μm]	$Width_y$ [μm]	$Error_x$ [μm]	$Error_y$ [μm]
16.5	3854	4055	193	203
18.9	2620	2701	131	135
29.5	2601	2484	130	124
31.1	3416	3341	171	167

Table 6.3: Measurement of the laser beam diameters at several distances from the mirror at distance 11.5 cm from the last lens, L_3, of table (6.2). The coordinate x indicates the horizontal diameter and the coordinate y indicate the vertical diameter. The errors are assumed equal to the 5 % of the measured diameter value, i.e. the effective accuracy possible for laser beam diameter measurements

cm from the last lens. Hence, the optical system described in table (6.2) is chosen. The analysis of the optical fiber behavior in transporting the electromagnetic waves, when the injected laser beam has a waist of 8 μm at the starting point of the fiber, is carried on by measuring the fiber output power and by comparing it with the fiber input power. For the configuration of optimum alignment between fiber and laser beam, it is observed a ratio between fiber output and input power of 27%. It is worth noticing that the optimum alignment configuration corresponds also to the configuration for which the ratio between fiber output and input power is higher. Hence, from the obtained result, it is clear that the reduction of the laser beam waist to 8 μm does not allow to reach an improvement of the fiber capability in transmitting the input power. The departure of the obtained results with respect to the expected behavior can be explained by the fact that, as the wavelength of the laser beam and the waist of the mode supported by the fiber are comparable, the paraxial approximation, on which the Gaussian optics is based, is at its margin of validity. Hence the laser beam behavior might present differences with respect to the description given in the context of the Gaussian optics.

By remembering the physical principles on which the tested fibers are based, when the fiber length increases, the higher order modes should be better suppressed. Hence, the 6 m long fiber is considered in order to obtain the waist value of the beam coming out from this fiber, as a further estimation of the waist of the beam supported by these fibers. Measurements of the ratio between the fiber output and input power are then performed, when the waist of the injected laser beam is adjusted to the value determined at the exit of the 6 m long fiber. The measurements are made by initially keeping the waist of the input beam equal to 8 μm. For the optimum alignment between fiber and input laser beam, which is found by maximizing the output power, the beam diameter is measured at several distance from the end point of the fiber,

Distance [mm]	$Width_x$ [μm]	$Width_y$ [μm]	$Error_x$ [μm]	$Error_y$ [μm]
32.5	4277.8	3306.2	214	165
32.5	4695.6	3402.1	235	170
27.5	4400	2907	220	145
22.5	3453	2311	173	116
6	1875	1819	94	91

Table 6.4: Measurement of the laser beam diameter at several distances from the ending point of the fiber 6 m long. The coordinate x indicates the horizontal diameter and the coordinate y indicates the vertical diameter. The errors are assumed equal to the 5 % of the measured diameter value. Furthermore, it is noticed that two sets of measurements are taken for the distance 32.5 mm

with the camera (WinCamD^{TM} Series Cameras [64]). The results are given in table (6.4). As it is possible to check from the reported data, two measurements are taken for the distance 32.5 mm. Hence, two different fits are made, with the software *GaussianBeam*, for each diameter direction (horizontal and vertical). The fit for the horizontal diameter measurements, obtained by considering the first row of table (6.4), together with the third one, the fourth one and the fifth one, gives a waist of 6.9 μm. Instead, if the fit is made by considering the data from the second to the fifth row of table (6.4), a waist of 6.2 μm is found. As far as the fits for the measures of the laser beam vertical diameter are concerned, when considering the first row of table (6.4), together with the third row, the fourth one and the fifth one, a waist of 12.5 μm is found, instead, when the data from the second to the fifth row are taken into account, a waist of 12 μm results. Thus, there is not a clear definition of the fiber output beam radius. The difficulty in determining this quantity could still be due to the fact that the Gaussian optics is at its margin of validity, as it has been already pointed out. However, the fiber 1 m long is again taken into account to verify if the ratio between the fiber output and input power increases, when a laser beam with waist 12 μm is injected into the fiber. Indeed, the results for the beam waist at the exit of the 6 m long fiber give a clue of the fact that the considered fibers could actually support a mode of radius 12 μm. To carry on the analysis of the optical fiber behavior, the three lenses compounding the optical system applied to reduce the laser beam waist are displaced in order to get to a waist of 12 μm at the starting point of the 1 m long fiber. The determined setup of the three lenses is reported in table (6.5). The laser beam diameter, after the optical system, has been measured with the Beam Scan and the dedicated software at different distances from the reference point, i.e. the mirror at 11.5 cm from the last lens, L_3, of table (6.5). The aim was to verify if the laser beam waist was 12 μm and to obtain its position. The measures are

	Position [cm]	Focal length [mm]
L_1	10.5	50
L_2	21.7	750
L_3	88.3	200

Table 6.5: Optical system for getting to a laser beam waist of 12 μm. It is observed that the distance are taken from the starting point of the laser beam, i.e. from the laser beam collimator.

Distance [mm]	$Width_x$ [μm]	$Width_y$ [μm]	$Error_x$ [μm]	$Error_y$ [μm]
105	5340	5409	276	165
140	4195	4276	210	170
410	4793	4554	240	145
429	5336.8	5095.6	267	255

Table 6.6: Measurement of the laser beam diameter at several distances from the mirror at 11.5 cm from the last lens of the optical system described in table (6.5). The coordinate x indicates the horizontal diameter and the coordinate y indicate the vertical diameter. The errors are assumed equal to the 5 % of the measured diameter value.

given in table (6.6). From the fits performed with *GaussianBeam*, when considering the vertical beam diameter measurements, the waist turns out to be of 12 μm, at a distance of 27.1 cm from the reference point, while, when considering the horizontal beam diameter measurements, the beam waist keeps the same value, but its position results at 26.6 cm. To perform the next test, the starting point of the 1 m long fiber is firstly set at distance 26.6 from the reference point (the mirror at 11.5 cm of distance from L_3). Hence, the position of the fiber beginning and its alignment with respect to the injected laser beam are optimized, by maximizing the fiber output power. It is observed that fiber movements are allowed thanks to its mobile supports. In the position corresponding to the optimum alignment, the ratio between the fiber output power and the fiber input power is evaluated and it turns out to be of 18 %. This value is even lower than the one found when a laser beam with a waist of 8 μm was injected inside the fiber 1 meter long. The same procedure described for this fiber length has been carried on also for a fiber 3 meters long and for a fiber 6 meters long. The maximum value for the ratio between the power coming out from the fiber and the power injected inside the fiber is of 13 % for the 3 meters long fiber and of 29 % for the 6 meters long fiber.

Analysis of the mode profile at the output of the tested fibers

The analysis of the shape of the mode at the output of the optical fiber is now carried on, in order to verify if there is the possibility of coupling among the different fiber modes, which would indicate that the fibers do not work as monomode fiber and also could partially account for the low transmission of power, because of mode coupling losses. This analysis is conducted for all the considered fiber lengths, i.e. 1 meter, 3 meters and 6 meters. In particular, for each fiber of different length, its disposition on the optical table is made to vary and pictures of the output mode are taken, by using the camera (WinCamD^{TM} Series Cameras [64]), for each fiber configuration on the table. In figure (6.4), the pictures for the output modes, concerning three different bending configurations on the table for the 1 meter long fiber, are reported. Picture (6.5) and picture (6.6) represent the output modes for three different fiber bending dispositions on the table, for the 3 meter long fiber and the 6 meter long fiber, respectively. As it is easy to verify from the pictures, these fibers are highly sensitive to bending conditions, indeed, the shape of the fiber output mode strongly depends on the fiber bending. This is due to the coupling between the modes supported by the analyzed fibers, which then do not result suitable for laser signal amplification. It is also interesting to compare the mode shapes of figures (6.4), (6.5), (6.6) with the mode profiles of picture (6.7), which are obtained when no extra bending configurations are applied. This means that, the fiber 1 m long completely lead down on the optical table, while the fiber 3 meters long and the one 6 meters long are disposed on the table with the configurations used to make the analysis discussed previously in this section. As it is possible to check from the images, the fiber output modes present departures from a perfect Gaussian profile even when no bending configurations are introduced, e.g. this is particularly evident for the fiber three meters long.

In conclusion, it is important to note that the studied fibers were realized for applications concerning laser beam with wavelength $\lambda = 1.55\mu$m. We have been told by the fiber constructor that they should work for the laser wavelength $\lambda = 1064$ nm as well, however the numerical simulations have been carried on for $\lambda = 1.55\mu$m, it is not possible then to exclude that the analyzed fiber structure does not allow a single mode operation for $\lambda = 1064$ nm. Nevertheless, it has to be pointed out that the laser beam wavelength used in the experimental tests presented in this section has been chosen in order to be suitable for NBI system applications. Hence, it may be confirmed that this fiber structure can hardly be a solution for obtaining the high power laser source required by NBI systems.

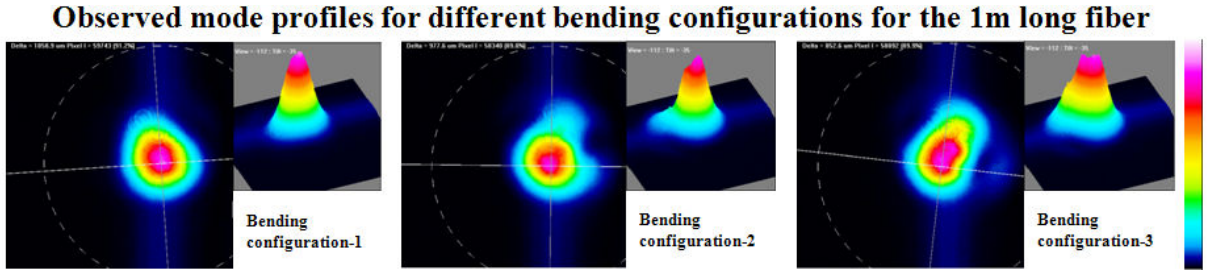

Figure 6.4: Output modes for 1 meter long fiber for different bending conditions - The pictures show that the fiber output mode is sensitive to the disposition of the fiber on the optical table. Indeed, for different fiber bending configurations the fiber output mode present different shapes. It is worth noticing that the color bar, on the right side of the picture, represents the intensity scale of the beam, the white for the beam regions with higher intensity and the blue for the beam regions with lower intensity.

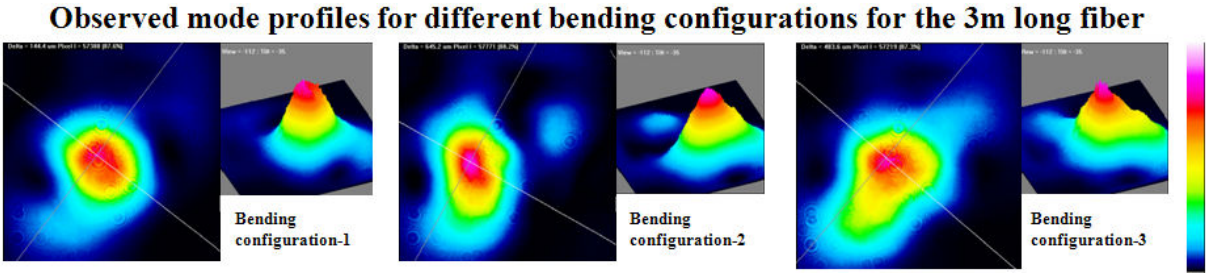

Figure 6.5: Output modes for 3 meter long fiber for different bending conditions - The pictures show that the fiber output mode is sensitive to the disposition of the fiber on the optical table. Indeed, for different fiber bending configurations the fiber output mode present different shapes. It is worth noticing that the color bar, on the right side of the picture, represent the intensity scale of the beam, the white for the beam regions with higher intensity and the blue for the beam regions with lower intensity.

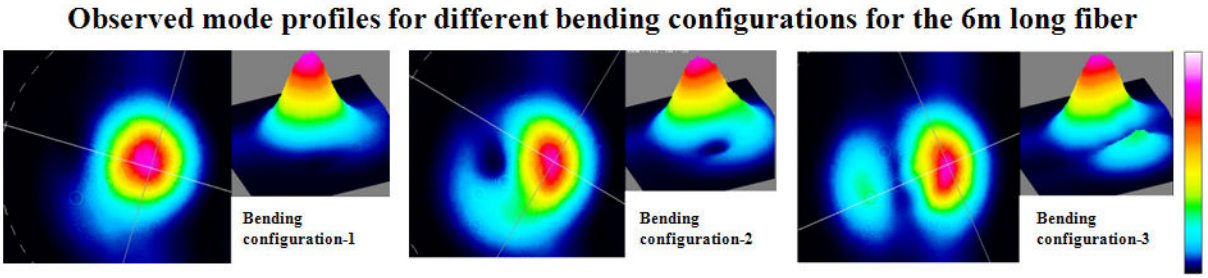

Figure 6.6: Output modes for 6 meter long fiber for different bending conditions - The pictures show that the fiber output mode is sensitive to the disposition of the fiber on the optical table. Indeed, for different fiber bending configurations the fiber output mode present different shapes. It is worth noticing that the color bar, on the right side of the picture, represent the intensity scale of the beam, the white for the beam regions with higher intensity and the blue for the beam regions with lower intensity.

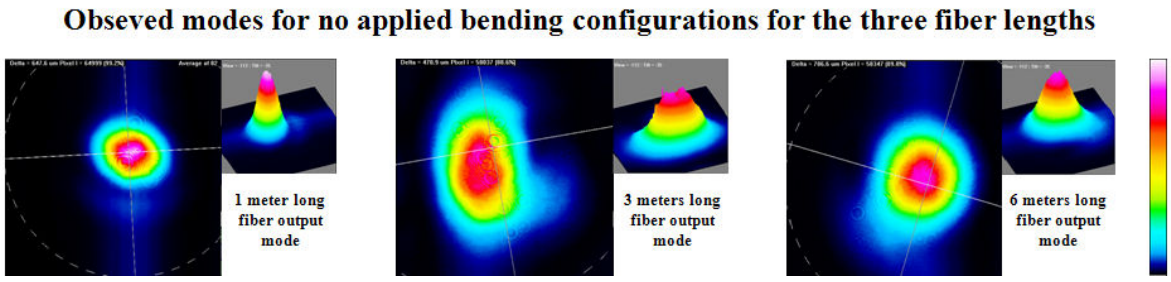

Figure 6.7: Output modes for no applied bending configurations for the three fiber lengths - The pictures show the fiber output mode for each considered fiber length. Departure of the output mode from a perfect Gaussian beam are observable. This is particularly evident for the fiber 3 meter long. It is worth noticing that the color bar, on the right side of the picture, represent the intensity scale of the beam, white for the beam regions with higher intensity and blue for the beam regions with lower intensity.

Conclusions and Perspectives

The work I have carried on during the PhD thesis has the aim of analyzing the feasibility of an optical cavity whose properties would allow the application of the photo-detachment process in NBI systems of nuclear fusion reactors of the next generation (such as DEMO). In this respect, different issues connected to the implementation of an optical resonator in a NBI system environment, at the purpose of reaching high neutralization efficiency of the high energetic D^- beam, have been taken into account. Particularly, the following aspects have been explored:

- Determination of an optical cavity design which, on one hand, accommodates all the requirements for applications in NBI systems, e.g. stability, constance of the intracavity laser beam radius (percent variations up to 5% are allowed), beam waist of 1 cm; and, on the other hand, consents to solve possible encumbrance problems;
- Study of the thermal effects on the cavity mirrors due to the mirror coating absorption of the intracavity power ($\sim$ 3 MW), at the rate of $\simeq$ 0.3 ppm, and analysis of compensation systems to correct the cavity mirror reflecting surface deformations;
- Research for techniques which can allow to obtain high powerful laser beam, as a laser beam of $\sim$ 1kW must feed the optical cavity, for the requirements of NBI system applications.

As far as the first point of the list reported above is considered, in chapter (2), it has been showed that an easy solution for the design of an optical cavity for NBI systems applications is possible, if there is enough space, within the environment of a nuclear fusion reactor, so that a resonator length of 100 m is allowed. In this case, indeed, the cavity would be effectively equivalent to a simple two mirror resonator compounded of a flat mirror and of a curved mirror with a curvature radius $R = 1$km, separated by a distance of 100 m. Nevertheless, the resonator would have four refoldings, obtained through the application of other three flat mirrors, at the aim of guaranteeing the complete overlap between the laser beam and the D^- ion beam. On

the contrary, if a smaller space is available for the optical cavity, it has been demonstrated, in chapter (2), that a three mirror optical cavity, with the geometrical design reported in picture (2.3), where two of the mirrors compound a telescope, would accommodate all the NBI system application requirements on a L_2 length equal to 31 m.

As far as the study of the thermal effects on the cavity mirrors and of the compensation systems to correct the mirror reflecting surface distortions are concerned, it is recalled that this has been carried on in an analytical way, and the results have been verified with ANSYS and COMSOL, softwares which allow numerical simulations based on the finite elements method. Mostly, analytical and numerical results show to be in agreement, but when slightly different boundary conditions are considered and for choices of analytical calculation parameters for which the approximations imposed to simplify the equations to solve are not anymore valid or hold only marginally. In our analysis, only thin mirrors are considered (5mm of thickness), so that the mirror bulk absorption can be neglected with respect to the one of the coating. The mathematical framework settled to analytically calculate the thermal effects on the mirrors, due to the coating absorption, and also the effects of thermal compensation systems (TCS) is based on harmonic functions for the temperature field and bi-harmonic functions for the displacement vector, involving Bessel functions. In particular, the temperature field is determined by solving the steady state Fourier equation with no internal source of heat, and this solution is used to write the equations for the displacement vector components, which describe the mirror deformation. It is worth noticing that compared to finite elements simulations, analytic calculations have the advantages to be computationally lighter (up to 20 times faster). However, they also show limitations due to approximation introduced in order to solve the involved equations. The simulation results show that among the considered TCS methods, the ones based on the applications of temperature fields are the most appropriate. Particularly, the best result is obtained when a fixed temperature of T_c=690K is applied on the central part of the back side of the mirror, through a disk heater with radius 5 mm. To give an idea of the gain factor in term of mirror losses reduction, without applying the mentioned TCS, the mirror losses due to the coating absorption of optical power are of 2500 ppm and the mirror curvature change is of 2.9×10^{-4} m^{-1}, when starting from an initially flat mirror. If the described TCS is applied, the mirror losses are reduced to 5 ppm and the mirror curvature change is now of 8.7×10^{-5} m^{-1}. It must be observed that the presented solution is only valid for totally reflective mirrors since the TCS acts on the central part of the mirror rear side. Further investigations have to be conducted for the case of the input mirror for which the central part of its back side must be kept free (CO_2

laser heating is an interesting alternative) and on the cavity mode behavior when all effective mirror curvatures are taken into account. Finally, one has to notice that the scattering losses we have estimated represent an upper limit to the losses within the cavity. Indeed, scattered light from one mirror can be re-coupled to the cavity mode, when reflected on another mirror.

The last point to be considered concerns the research for techniques which could allow the realization of high power laser beam. Indeed, as it as been pointed out in chapter (2), an input laser beam of $\sim$1kW must feed the optical cavity for applications in NBI systems. Within this context, we have experimentally tested a new concept of Large Mode Area (LMA) fiber, said LMA Leaky optical fiber, which has been developed for allowing single mode operation without enhancements of nonlinear effects. Hence they should be particularly indicated as laser amplifiers. Their single mode operation is guaranteed by an appropriate refractive index profile which should allow high power losses for higher order modes of the fiber and significantly lower losses for the fundamental mode. The experimental tests have demonstrated that these fibers are quite sensitive to fiber bending: as the fiber is bent, the outcoming mode sees his shape changing. The analyzed fibers can then hardly be used for monomode amplification of laser beam. Further researches aiming to find appropriate optical fiber amplifiers could be conduced, however, the possibility of the coherent superposition of laser beams must be explored, as, from the results obtained so far, it seems to be the more interesting solution for getting to high powerful laser beam.

Conclusions et Perspectives

Le travail que j'ai réalisé au cours de la thèse de doctorat a pour but d'analyser la faisabilité d'une cavité optique dont les propriétés permettrait l'application du processus du photo-détachement aux systèmes d'injection de neutres des réacteurs de fusion nucléaire de la prochaine génération (tel que DEMO). À cet égard, différentes questions liées à la mise en œuvre d'un résonateur optique dans lenvironnement de systèmes d'injection de neutres ont été prises en compte, ceci afin d'atteindre une grande efficacité de neutralisation du faisceau dions D^- très énergétiques, ont été prises en compte. En particulier, les aspects suivants ont été éxaminés :

- Détermination d'une cavité optique qui, d'une part, accueille toutes les exigences pour les applications aux systèmes d'injection de neutres, on peut citer la stabilité et la constance du rayon du faisceau laser dans la cavité (pourcentage des variations allant jusqu'à 5% sont autorisées), la taille de faisceau de 1 cm; et, d'autre part, consent à résoudre les possibles problèmes d'encombrement;

- Étude des effets thermiques sur les miroirs de la cavité en raison de l'absorption de puissance intra-cavité ($\sim$ 3 MW) du revêtement des miroirs, au taux de $\simeq$ 0.3 ppm. Analyse des systèmes de compensation pour corriger les déformations de la surface réfléchissante des miroirs de la cavité;

- Recherche de techniques permettant d'obtenir des faisceaux laser à haute puissance, car nécessité d'un faisceau laser de 1kW pour alimenter la cavité optique, pour les besoins des applications aux systèmes IDN.

Concernant le premier aspect, dans le chapitre (2), nous avons montré dans le chapitre (2) qu'une solution simple pour concevoir une cavité optique pour les systèmes IDN est possible s'il y a suffisamment d'espace dans le réacteur de fusion nucléaire, de sorte qu'un résonateur dune longueur de 100 m puisse rentrer. Dans ce cas, la cavité serait effectivement équivalente à un

simple résonateur de deux miroirs, composé d'un miroir plat et d'un miroir courbe avec un rayon de courbure $R = 1$ km, séparés par une distance de 100 m. Néanmoins, le résonateur aurait quatre repliements, obtenus par l'application de trois autres miroirs plats, en vue de garantir le chevauchement complet entre le faisceau laser et le faisceau d'ions D^-. Au contraire, si un plus petit espace est disponible pour la cavité optique, il a été démontré, dans le chapitre (2), qu'une cavité optique à trois miroirs, avec la conception géométrique de la figure (2.3) où deux des miroirs forment un télescope, accueillerait tous les besoins pour l'application aux systèmes IDN sur une longueur L_2 égale à 31 m.

En ce qui concerne l'étude des effets thermiques sur les miroirs et des systèmes de compensation pour corriger les distorsions de la surface réfléchissante des miroirs, nous rappelons que cette analyse a été réalisée de manière analytique, et les résultats ont été vérifiés avec ANSYS et COMSOL, logiciels permettant des simulations numériques basées sur la méthode des éléments finis. Les résultats analytiques et numériques sont en accord, sauf quand les conditions aux bords sont légèrement différentes et pour les choix des paramètres des calculs analytiques pour lesquels les approximations imposées pour simplifier les équations à résoudre ne sont plus valables ou que marginalement. Dans notre analyse, seulement des miroirs fins (5 mm d'épaisseur) sont considérés, de sorte que l'absorption de l'intérieur du miroir peut être négligée par rapport à celle de son revêtement. Le cadre mathématique utilisé pour calculer analytiquement les effets thermiques sur les miroirs à cause de l'absorption due au revêtement, ansi que les effets des Systèmes de Compensation Thermique (SCT) est basée sur des fonctions harmoniques pour le champ de température et sur des fonctions bi-harmoniques pour le vecteur de déplacement, impliquant les fonctions de Bessel. En particulier, le champ de température est déterminé par la résolution de l'équation de Fourier, en régime stationnaire, avec aucune source de chaleur interne. Cette solution est utilisée afin d' écrire les équations pour les composantes du vecteur de déplacement décrivant la déformation du miroir. Il est intéressant de remarquer que, comparativement aux simulations aux éléments finis, les calculs analytiques présentent l'avantage d'être plus légers en termes de temps de calcul (jusqu' à 20 fois plus rapides). Cependant, ils montrent aussi des limitations dues aux approximations introduites dans le but de résoudre les équations concernées. Les résultats des simulations montrent que, parmi les méthodes SCT considérées, celles basées sur lapplication des champs de température sont les plus appropriées. En particulier, le meilleur résultat est obtenu lorsqu'une température fixe $T_c = 690$ K est appliquée sur la partie centrale de la face arrière du miroir, avec un dispositif de chauffage à forme de disque, avec un rayon de 5 mm. Pour donner une idée du facteur de gain en termes de

réduction des pertes des miroirs, sans appliquer le SCT mentionné, les pertes des miroirs en raison de l'absorption de puissance optique par le revêtement des miroirs sont de 2500 ppm et le changement de courbure est de 2.9 10^{-4} m^{-1}, avec un miroir initialement plat. Si le SCT décrit est appliquée, les pertes du miroir sont réduites à 5 ppm et le changement de courbure est maintenant de 8.7 10^{-5} m^{-1}. Il faut observer que la solution présentée est uniquement valable pour les miroirs totalement réfléchissants, étant donné que le SCT agit sur la partie centrale. D'autres investigations doivent être conduites pour le cas du miroir d'entrée pour laquelle la partie centrale doit être libre (le chauffage par un laser CO_2 est une possibilité intéressante) et sur le comportement du mode de la cavité lorsque toutes les courbures effectives des miroirs sont prises en compte. Enfin, il faut remarquer que les pertes de diffusion que nous avons estimées représentent une limite supérieure des pertes au sein de la cavité. En effet, la lumière diffusée par un miroir peut être couplée à nouveau au mode de la cavité, , lorsqu'elle est réfléchie sur un autre miroir. Le dernier point à considérer concerne la recherche de techniques qui pourraient permettre la réalisation d'un faisceau laser à haute puissance. En effet, comme il a été souligné dans le chapitre (2), un faisceau laser d'entrée de $\sim$ 1kW doit alimenter la cavité optique pour les applications aux systèmes d'injection de neutres. Dans ce contexte, nous avons testé expérimentalement un nouveau concept des fibres LMA (Large Mode Area), appelées fibres *LMA Leaky*, développé pour permettre un fonctionnement monomode sans augmentation des effets effets non-linéaires. Par conséquent, ces fibres devraient être particulièrement indiquées comme amplificateurs laser. Leur fonctionnement monomode est garanti par un profil d'indice de réfraction approprié qui devrait permettre des pertes de puissance élevées pour les modes supérieurs de la fibre et des pertes beaucoup plus basses pour le mode fondamental. Les tests expérimentaux ont démontré que ces fibres sont très sensibles aux flexions : lorsque la fibre est pliée, le mode sortant voit sa forme changer. Les fibres analysées peuvent alors difficilement être utilisées pour l'amplification monomode d'un faisceau laser. Des analyses complémentaires visant à trouver des amplificateurs à fibre optique appropriés pourraient être conduites. Toutefois, au regard des résultats obtenus jusqu'ici, la superposition cohérente des faisceaux laser semble être la solution la plus intéressante pour obtenir un faisceau à haute puissance, et doit donc ètre explorée.

Appendices

Appendix A

Mathematical description of Laser beams

The free space propagation of an electromagnetic field, $E(\vec{r},t)$, is governed by the wave equation:

$$\left(\nabla^2 - \frac{1}{c^2}\frac{\partial^2}{\partial t^2}\right) E(\vec{r},t) = 0, \tag{A.1}$$

with c the speed of the light and:

$$\nabla^2 = \frac{\partial^2}{\partial x^2} + \frac{\partial^2}{\partial y^2} + \frac{\partial^2}{\partial z^2}, \tag{A.2}$$

in rectangular coordinates. As the purpose of this section is to find a mathematical description of laser beams, assumed monochromatic, it is possible to look for a solution of the previous equation of the kind:

$$E(\vec{r},t) = u(\vec{r})e^{i\omega t}, \quad \omega = \frac{2\pi c}{\lambda}, \tag{A.3}$$

with λ the wavelength of the laser. By substituting this solution in equation (A.1), it is found that $u(\vec{r})$ must satisfies the Helmholtz equation:

$$\left(\nabla^2 + k^2\right) u(\vec{r}) = 0, \tag{A.4}$$

where $k = 2\pi/\lambda = \omega/c$ is the propagation constant. It is observed that a laser beam, analogously to a plane wave, propagate primarily along one direction, which is chosen as the z coordinate direction in what follows. Furthermore, the amplitude and phase of a laser beam has a dependence on the x and y coordinate directions which defines the transverse profile of the beam. Due to the propagations effects, the transverse profile of the beam also shows dependences on the z

coordinate. It is then possible to look for a solution of the Helmholtz equation of the form:

$$u(x,y,z) \equiv \tilde{u}(x,y,z)e^{-ikz}, \tag{A.5}$$

where $\tilde{u}$ is a complex scalar wave amplitude describing the transverse profile of the beam, namely its nonuniform intensity distribution, the expansion with the propagation distance and its wavefront curvature. By inserting solution A.5 in equation (A.4), it is found:

$$\frac{\partial^2\tilde{u}}{\partial x^2} + \frac{\partial^2\tilde{u}}{\partial y^2} + \frac{\partial^2\tilde{u}}{\partial z^2} - 2ik\frac{\partial\tilde{u}}{\partial z} = 0. \tag{A.6}$$

As the term e^{-ikz} has been factored out from the previous equation, the only remaining dependence on z is the one given by the function $\tilde{u}$. In this respect, it is observed that the laser beam expansion with the propagation distance, which is described by $\tilde{u}$, is slow on a wavelength scale, along the z direction, and laser beams are in general well collimated, with finite beam width. Hence, it is possible to solve equation (A.6) in the context of the paraxial approximation, which indeed states that the laser beam propagates at small angle with respect to the z direction [36]. Mathematically, the paraxial approximation reads:

$$\left|\frac{\partial^2\tilde{u}}{\partial z^2}\right| << \left|\frac{2k\partial\tilde{u}}{\partial z}\right|, \quad \left|\frac{\partial^2\tilde{u}}{\partial z^2}\right| << \left|\frac{\partial^2\tilde{u}}{\partial x^2}\right|, \quad \left|\frac{\partial^2\tilde{u}}{\partial z^2}\right| << \left|\frac{\partial^2\tilde{u}}{\partial y^2}\right|. \tag{A.7}$$

Consequently, the second derivative $\frac{\partial^2\tilde{u}}{\partial z^2}$ can be neglected in equation (A.6) which then reduces to the paraxial wave equation:

$$\frac{\partial^2\tilde{u}}{\partial x^2} + \frac{\partial^2\tilde{u}}{\partial y^2} - 2ik\frac{\partial\tilde{u}}{\partial z} = 0. \tag{A.8}$$

A possible solution of the previous equation is a gaussian beam with the following form:

$$\tilde{u}(x,y,z) = \left(\frac{2}{\pi}\right)^{\frac{1}{2}} \frac{\exp\left[-ikz + i\phi(z)\right]}{w(z)} \exp\left[-\frac{x^2+y^2}{w^2(z)} - ik\frac{x^2+y^2}{2R(z)}\right], \tag{A.9}$$

which satisfies:

$$\int_{-\infty}^{\infty}\int_{-\infty}^{\infty} |\tilde{u}|^2 dxdy = 1. \tag{A.10}$$

As far as the parameters appearing in equation (A.9) are concerned, it is observed that $R(z)$ is the curvature of the beam wavefront, while $w(z)$ is known as *spot radius* or *beam half width*, and it gives the distance from the z axis at which the beam amplitude decreases to $1/e$ of its

maximum [37]. The beam diameter at a given z coordinate is $2w(z)$. The minimum value assumed by $w(z)$ is denominated *beam waist*, and it is indicated as w_0. At the z value, z_0, for which $w(z_0) \equiv w_0$, the phase front is plane. For the sake of simplicity, it is assumed $z_0 = 0$, and z is measured from the waist position. The $R(z)$ dependence on z is:

$$R(z) = z\left[1 + \left(\frac{\pi w_0^2}{\lambda z}\right)^2\right], \tag{A.11}$$

while for $w(z)$, it is:

$$w(z) = w_0\sqrt{1 + \left(\frac{z\lambda}{\pi w_0^2}\right)^2}. \tag{A.12}$$

The spot size and the wavefront curvature enter the definition of the *q-parameter*, a quantity characterizing the beam and its propagation, which reads:

$$\frac{1}{q} = \frac{1}{R(z)} - i\frac{\lambda}{\pi w^2(z)}, \tag{A.13}$$

with λ the laser wavelength. By using equations (A.11), (A.12) and (A.13), it is also:

$$q(z) = z + i\frac{\pi w_0^2}{\lambda}, \tag{A.14}$$

where z is the distance from the beam waist. Furthermore, as it is already pointed out, at the beam waist $R(z = 0) = \infty$ and the q-parameter is purely imaginary:

$$q(z = 0) = q_0 = i\frac{\pi w_0^2}{\lambda}. \tag{A.15}$$

The quantity $\pi w_0^2/\lambda$ is know as Rayleigh length, z_R, and it defines the propagation distance from the waist position after which the beam radius increases of a factor $\sqrt{2}$. Therefore, it can be seen as an approximate separation line between the so called *near-field*, i.e. $z << z_R$, and the *far-field*, i.e. $z >> z_R$, for a gaussian beam propagating from its waist. In the far-field regime, $w(z)$ increases linearly with z and it is possible to define the *beam divergence* angle as:

$$\theta = \lim_{z\to\infty} \frac{w(z)}{z} = \frac{\lambda}{\pi w_0}. \tag{A.16}$$

It is worth noticing that θ has a constant value. In picture (A.1), $R(z)$, $w(z)$, w_0 and $\theta(z)$ are schematically represented. The quantity $\phi(z)$ in equation (A.9) is referred to as *Gouy phase* and it represents an additional longitudinal phase shift a gaussian beam goes through when

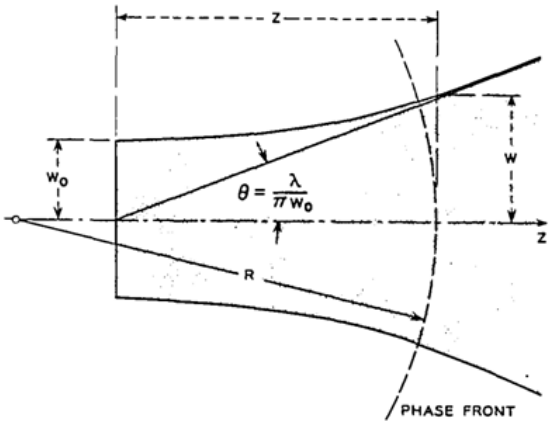

Figure A.1: Scheme of the gaussian beam parameters. - Gaussian beam parameters representation, from Ref. [37].

propagating, with respect to the term e^{-ikz} which is present for plane waves as well. It gives then the difference between the gaussian beam axial phase shift with respect to the one of a plane wave during the propagation. By assuming to measure the Gouy phase from the beam waist, its dependence on the z coordinate is:

$$\phi(z) = \arctan\left(\frac{z}{z_R}\right). \tag{A.17}$$

The effect of this additional term, for a beam described by equation (A.9), is a phase shift of 180° when the beam propagate from $z = -\infty$ to $z = +\infty$, with most of the phase shift accumulated within one or two z_R on both sides of the waist, see picture (A.2). It is then the phase shift due to the passing of the gaussian beam through its focal region, accordingly to the *Gouy effect* (see Ref [38]-[42]).

Higher-order gaussian modes

So far, only a particular solution of equation (A.8) have been discussed, namely beams whose transverse profile is described by a gaussian. However, there are other solutions of equation (A.8) with similar properties. These solutions are referred to as *propagation modes* and they form a complete and orthonormal family of functions, so that any monochromatic light beam can be expressed in terms of these modes. In rectangular coordinates (x,y,z), these solutions

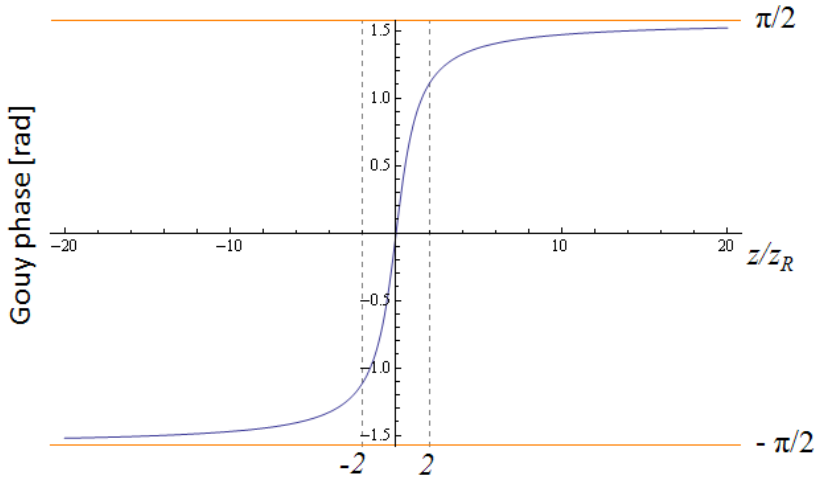

Figure A.2: Gouy phase. - Dependences of the Gouy phase on the quantity z/z_R.

take the following form:

$$\tilde{u}_{m,n}(x,y,z) = \left(\frac{2}{\pi}\right)^{\frac{1}{2}} \left(\frac{\exp[i(m+n+1)\phi(z)]}{2^{n+m}n!m!}\right)^{\frac{1}{2}} \times H_m\left(\frac{\sqrt{2}x}{w(z)}\right) \times H_n\left(\frac{\sqrt{2}y}{w(z)}\right) \times \exp\left[-ikz - ik\frac{x^2+y^2}{2R(z)} - \frac{x^2+y^2}{w(z)^2}\right] \tag{A.18}$$

where H_m and H_n are Hermite polynomials of degree m and n, respectively. Furthermore, the quantity $N = m + n$ is the order of the mode, while m and n are the transverse mode numbers. The parameters $R(z)$, $w(z)$ and $\phi(z)$ are still defined through equations (A.11), (A.12), (A.17) and they are the same for all the mode. However, as the term $\phi(z)$ appears in solution (A.18) with an additional factor $(m+n+1)$, the gouy phase shift depends on the order of the considered mode. It is observed that the solution (A.9) is obtained for $m = n = N \equiv 0$, and this is the reason why it is called the *fundamental propagation mode* or the *lowest order mode*, with reference to the other modes, for which $N > 0$, and which are then denominated as *higher order propagation modes*. The solutions described by relation (A.18) are known as *Hermite-Gauss* modes, whose transverse intensity profile, for the first order modes, is reported in picture (A.3).

An alternative family of solutions of the paraxial wave equation (A.8) is the one obtained when using cylindrical coordinates instead of the rectangular ones. In this respect, the coordinate

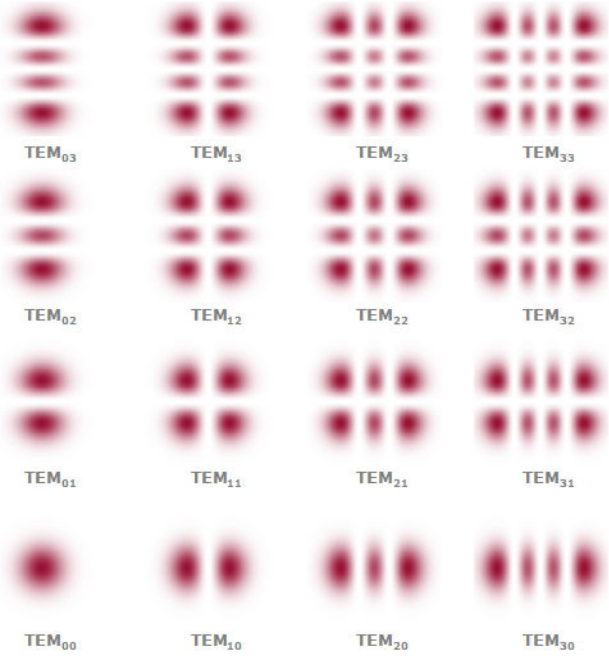

Figure A.3: Lowest order Hermite-Gaussian modes. - Illustration of the Hermite-Gauss transverse electromagnetic modes of propagation (TEM) for the first higher order modes, from [43].

transformation is:

$$\begin{aligned} r &= \sqrt{x^2+y^2} \\ \theta &= \tan^{-1}\left(\tfrac{y}{x}\right) \\ z &= z \end{aligned} \tag{A.19}$$

and solutions of equation (A.8) read:

$$\begin{aligned} \tilde{u}_{p,m}(r,\theta,z) &= \sqrt{\tfrac{4p!}{\pi(1+\delta_{m,0})(m+p)!}}\,\tfrac{\exp i(2p+m+1)\phi(z)}{w(z)} \\ &\times \left(\tfrac{\sqrt{2}r}{w(z)}\right)^m L_p^m\left(\tfrac{2r^2}{w(z)^2}\right)\binom{\cos(m\theta)}{\sin(m\theta)}\exp\left[-ik\tfrac{r^2}{2}\left(\tfrac{1}{R(z)}-i\tfrac{\lambda}{\pi w^2(z)}\right)\right]. \end{aligned} \tag{A.20}$$

In the previous expression, the integers $p \geq 0$ and m are the radial and the azimuthal mode indexes, respectively; the order of the mode is $N = 2p+|m|$ (Ref. [44], [45], [46]) and the quantity L_p^m indicates the generalized Laguerre polynomials. As solution (A.20) includes generalized Laguerre polynomials, the modes it describes are said *Laguerre-Gauss* modes and their transverse intensity distributions, for the first modes, is reported in picture (A.4). Analogously to the case of solution (A.18), the parameters $R(z)$ and $w(z)$ which enter equation (A.20) are the same for all the modes and they are expressed through equation (A.11), (A.12), hence spot size and

beam curvature radius also vary in the same way for all the orders. As far as the Gouy phase is concerned, $\phi(z)$ is still given by equation (A.17), nevertheless it enters solution (A.20) together with the additional factor $2p + m + 1$ which indicates that the gouy phase shift depends on the order of the considered mode. In conclusion, it is stressed that the fundamental gaussian mode of equation (A.9) is obtained for $p = m = 0$.

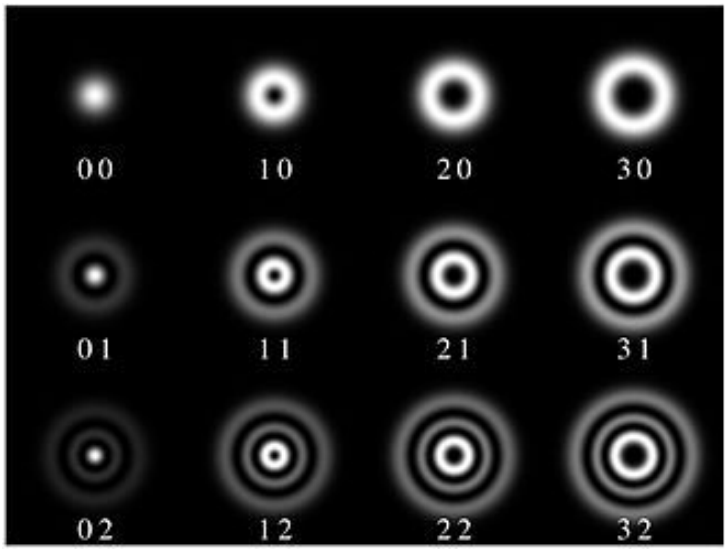

Figure A.4: Lowest order Laguerre-Gaussian modes. - Illustration of the axisymmetric Laguerre-Gauss transverse electromagnetic modes of propagation for the first higher order modes, from [47].

Appendix B

Any real function $f(x, y, z)$ with continuous second partial derivatives which satisfies the following equation in rectangular coordinates:

$$\frac{\partial^2 f(x,y,z)}{\partial x^2} + \frac{\partial^2 f(x,y,z)}{\partial y^2} + \frac{\partial^2 f(x,y,z)}{\partial z^2} = 0, \tag{B.1}$$

is called *harmonic function* [82], [83], [84]. The operator:

$$\Delta = \frac{\partial^2}{\partial x^2} + \frac{\partial^2}{\partial y^2} + \frac{\partial^2}{\partial z^2}, \tag{B.2}$$

is known as *Laplace operator*. When passing to a cylindrical coordinate system, Δ takes the following form:

$$\Delta = \frac{1}{r}\frac{\partial}{\partial r}\left(r\frac{\partial}{\partial r}\right) + \frac{1}{r^2}\frac{\partial^2}{\partial \phi^2} + \frac{\partial^2}{\partial z^2}, \tag{B.3}$$

with (see picture (B.1)):

$$\begin{aligned} r &= \sqrt{x^2 + y^2}, \\ \phi &= \tan^{-1}\left(\tfrac{y}{x}\right), \\ z &= z. \end{aligned} \tag{B.4}$$

If the considered function has cylindrical symmetry, its values will not depend on the coordinate ϕ. As a consequence, equation (B.1), in a cylindrical coordinate system, reads:

$$\frac{1}{r}\frac{\partial}{\partial r}\left(r\frac{\partial f(r,z)}{\partial r}\right) + \frac{\partial^2 f(r,z)}{\partial z^2} = 0. \tag{B.5}$$

The solution of the previous equation is then a harmonic function with cylindrical symmetry.

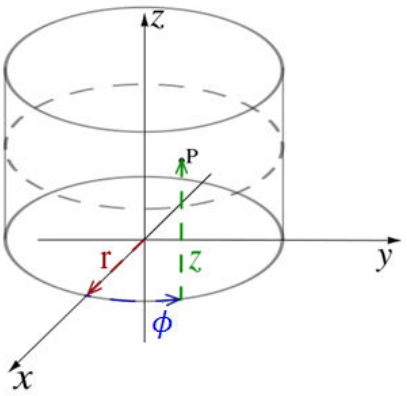

Figure B.1: Scheme of the cylindrical coordinate system with respect to the rectangular one - Representation of the relation between cylindrical and rectangular coordinate system.

Appendix C

in what follows the agreement between the two analytical methods of sections (3.3.1) and (3.3.2) for the calculation of the displacement vector for the TCS described in section (3.2.3) is presented. In particular, in order to use the displacement vector, $\vec{u}$, solutions reported in sections (3.3.1), it is necessary to develop the field of temperature introduced in section (3.2.3) in terms of zeros of the Bessel functions J_1. This has been already done in section (3.4.3), where it has been showed that the excess of temperature of equation (3.39), which is the quantity entering the Navier-Cauchy equations (3.159), in terms of zeros of the Bessel functions J_1, l_m, becomes:

$$\tilde{\tau} = \sum_{m\geq 0}^{\infty} \tilde{\tau}_m(z) J_0\left(l_m \frac{r}{a}\right) \tag{C.1}$$

$$\tilde{\tau}_m(z) = \frac{2}{a^2 J_0^2(l_m)} \int_0^a J_0(l_m r/a)\tau(r,z) r dr. \tag{C.2}$$

It is stressed that $\tau(r,z)$ has the form given in equation (3.39). Hence, it is possible to write equation (C.2) as:

$$\begin{aligned} &\tilde{\tau}_m(z) = \tfrac{2}{a^2 J_0^2(l_m)} \textstyle\int_0^a J_0(l_m r/a) \sum_{n=1}^{\infty} J_0(k_n r/a) \left(A_n \mathrm{e}^{-k_n \frac{z}{a}} + B_n \mathrm{e}^{k_n \frac{z}{a}}\right) r dr = \\ &= \textstyle\sum_{n=1}^{\infty} \left(A_n \mathrm{e}^{-k_n \frac{z}{a}} + B_n \mathrm{e}^{k_n \frac{z}{a}}\right) D_{m,n} \end{aligned} \tag{C.3}$$

with k_n zeros of the equation (3.33), and $D_{m,n}$ the same integration as given in (3.168). Particularly, it is interesting noticing that, for $m = 0$, it is:

$$\tilde{\tau}_{m=0} = \frac{2}{a^2 J_0^2(l_0)} \int_0^a \tau(r,z) r \mathrm{d}r = 2 \sum_{n=1}^{\infty} (A_n e^{-k_n \frac{z}{a}} + B_n e^{k_n \frac{z}{a}}) \frac{J_1(k_n)}{k_n}. \tag{C.4}$$

The two expressions for the temperature excess, i.e. equation (3.39) and equation (C.1), lead to the same total mirror temperature field. In this respect, picture (C.1) is reported, which show the mirror surface temperature fields, inside and outside the optical cavity, when the temperature of the environment where the mirror is placed is set to $T_0 = 900\text{K}$. Hence, the field of temperature reported on the picture is given by the sum of the constant environment temperature T_0 and of the temperature excess. It is worth remarking that, in picture (C.1), the label J_1 *Method* and *Method 2* refer to the solutions given in equation (C.1) and in section (3.2.3), respectively. As it is possible to perceive, there is agreement between the results. In order to quantitatively illustrate this last statement, at each radius value, and for both the mirror surface internal to the optical cavity and for the one outside the cavity, the following function is evaluated:

$$PE_T = \frac{|T_{zerosJ_1} - T|}{T}, \tag{C.5}$$

where PE_T indicate the percent error of the solution obtained by using the zeros of the Bessel function J_1 with respect to the solution obtained by using the zeros of equation (3.33), $T_{zerosJ1}$ is the temperature value as given by the calculations involving the zeros of the Bessel function J_1 and T is the temperature value as given by the calculations involving the zeros of equation (3.33). The results are reported in picture (C.2) and they confirm the agreement between the two methods to calculate the same temperature fields. It is also interesting to point out that the temperature field data obtained with formula (C.1) give the same percent errors than the ones obtained in section (4.4), when comparing them to the ANSYS and COMSOL data, through the application of equation (4.2). To illustrate this last assertion, pictures (C.3) and (C.4) are reported.

As far as the mirror surface distortion for the TCS described in section (3.2.3) is concerned, the comparison of the results obtained by applying the $\vec{u}$ solution given in section (3.3.1) and the one given in section (3.3.2) is reported in picture (C.5). The presented plots show the displacement vector for the mirror surface internal to the optical cavity as well as for the one outside the cavity, for both the solution in section (3.3.1) and the one in section (3.3.2). The reported curves let us perceive the agreement between the two analytical calculation methods. For a more quantitative analysis of the differences between the two methods, the following quantity is evaluated:

$$Error = \frac{\sqrt{\int_0^a (U^z - U^z_{J_1})^2 r dr}}{\sqrt{\int_0^a (U^z - \text{Min}\,[U^z])^2 r dr}}, \tag{C.6}$$

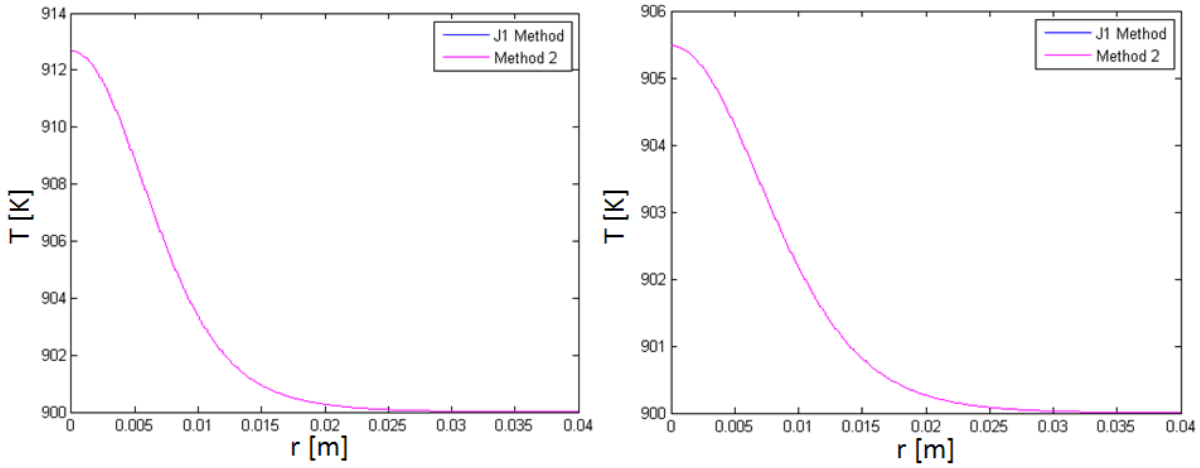

Figure C.1: Concordance between two analytical descriptions of the temperature field for the TCS in section (3.2.3) - SIPHORE mirror geometry. Absorption coefficient 0.3ppm. Intracavity power 3MW. Environment temperature T_0=900K. The two panels represent the results for the surface temperatures of the mirror, as obtained while applying the method described in section (3.2.3), *Method 2*, and when applying the development involving the zeros of the Bessel function J_1, J_1 *Method*. **Left panel**: mirror surface temperature inside the optical cavity. **Right panel**: mirror surface temperature outside the optical cavity.

where U^z and $U^z_{J_1}$ indicate the z component of the mirror surface displacement vector calculated by applying the solution in section (3.3.2) and the one in section (3.3.1), respectively, and $\mathrm{Min}\,[U^z]$ is the minimum value of U^z. The result of equation (C.6), for the mirror surface internal to the optical cavity, is 2.6×10^{-6}, the one for the rear mirror surface is 5.6×10^{-6}. Furthermore, it is possible to use the ANSYS and COMSOL data of section (4.4), to compare them to the corresponding $\vec{u}$ solution obtained by applying the formulas of section (3.3.1). The results are reported in table (7). As it is possible to see, the obtained values are equal to the ones of table (4.4).

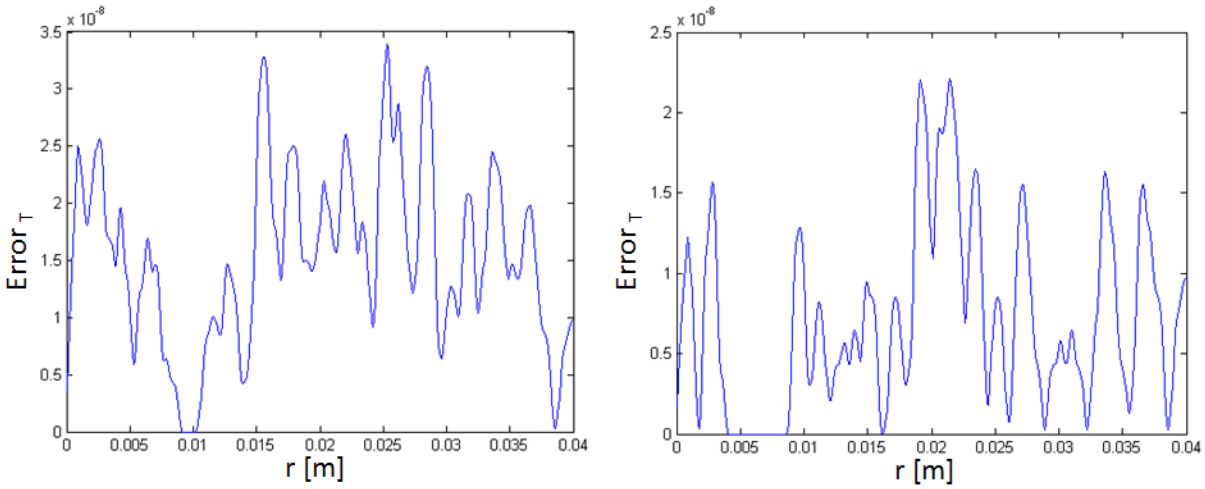

Figure C.2: Percent error for the temperature field of the TCS introduced in section (3.2.3), when calculated by using the analytical method involving the zeros of the Bessel function J_1 with respect to the one obtained when using the zeros of equation (3.33) - SIPHORE mirror geometry. Absorption coefficient 0.3ppm. Intracavity power 3MW. Environment temperature T_0=900K. **Left panel**: percent error of the solution obtained by using the zeros of the Bessel function J_1 with respect to the solution obtained by using the zeros of equation (3.33), as far as the mirror surface temperature field inside the optical cavity is concerned . **Right panel**: percent error of the solution obtained by using the zeros of the Bessel function J_1 with respect to the solution obtained by using the zeros of equation (3.33, as far as the mirror surface temperature field outside the optical cavity is concerned

	Error
Mirror surface distortion inside the cavity ANSYS-analytic result comparison	5.8×10^{-3}
Mirror surface distortion inside the cavity COMSOL-analytic result comparison	5.5×10^{-3}
Mirror surface distortion outside the cavity ANSYS-analytic result comparison	3.8×10^{-3}
Mirror surface distortion outside the cavity COMSOL-analytic result comparison	2.6×10^{-3}

Table 7: error on the analytical calculations performed by using the formulas of section (3.3.1), for TCS described in section (4.4), by considering the ANSYS and COMSOL data applied in table (4.4) - The values of the reported errors concern the mirror surface displacement vectors, inside and outside the optical cavity, and they are evaluated by applying equation 4.1.

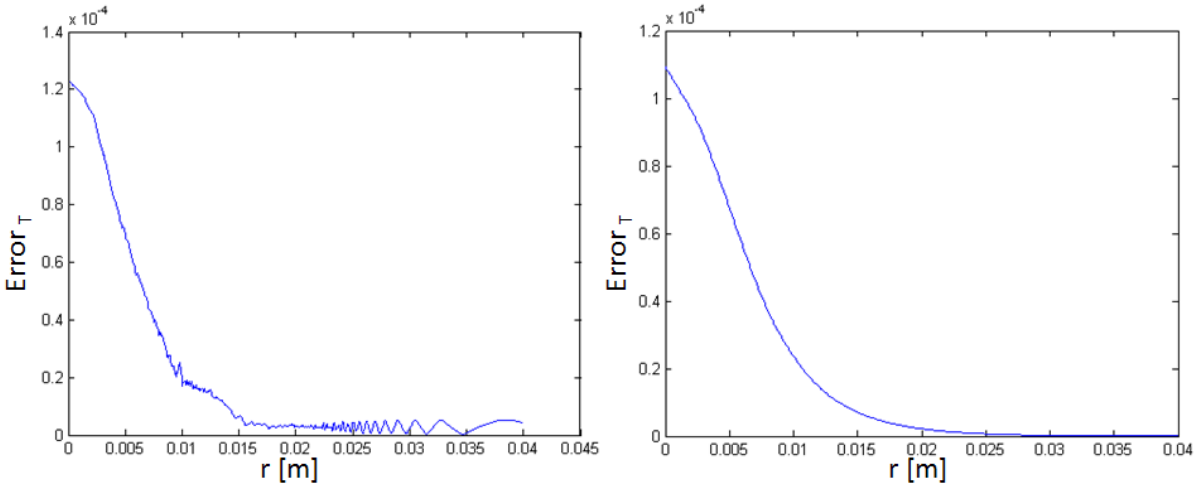

Figure C.3: Percent errors for the temperature field calculated through the analytical method involving the zeros of the bessel function J_1 with respect to the numerically calculated one, for the TCS in section (3.2.3). Mirror front surface. - SIPHORE mirror geometry. Absorption coefficient 0.3ppm. Intracavity power 3MW. Environment temperature T_0=900K. The reported errors are obtained through the application of equation (4.2) and they concern the numerical data of picture (4.11) and the corresponding analytical data obtained with the calculation method involving the zeros of the Bessel function J_1. **Left panel**: percent error of the analytical calculations with respect to the ones performed with ANSYS, as far as the mirror surface temperature inside the optical cavity is concerned. **Right panel**: percent error of the analytical calculations with respect to the ones performed with COMSOL, as far as the mirror surface temperature inside the optical cavity is concerned.

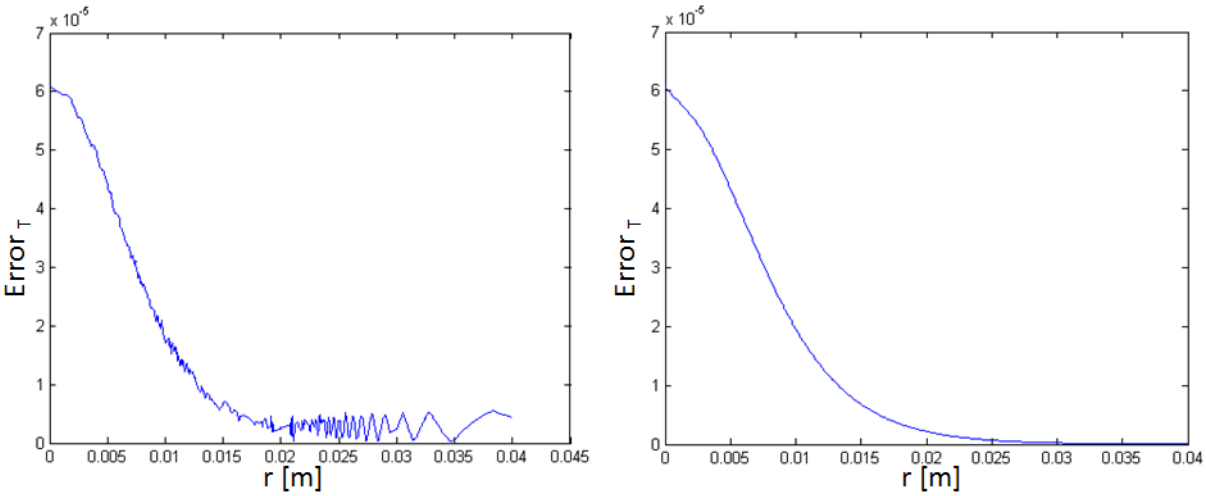

Figure C.4: Percent errors for the temperature field calculated through the analytical method involving the zeros of the bessel function J_1 with respect to the numerically calculated one, for the TCS in section (3.2.3). Mirror rear surface. - SIPHORE mirror geometry. Absorption coefficient 0.3ppm. Intracavity power 3MW. Environment temperature T_0=900K. The reported errors are obtained through the application of equation (4.2) and they concern the numerical data of picture (4.12) and the corresponding analytical data obtained with the calculation method involving the zeros of the Bessel function J_1. **Left panel**: percent error of the analytical calculations with respect to the ones performed with ANSYS, as far as the mirror surface temperature outside the optical cavity is concerned. **Right panel**: percent error of the analytical calculations with respect to the ones performed with COMSOL, as far as the mirror surface temperature outside the optical cavity is concerned.

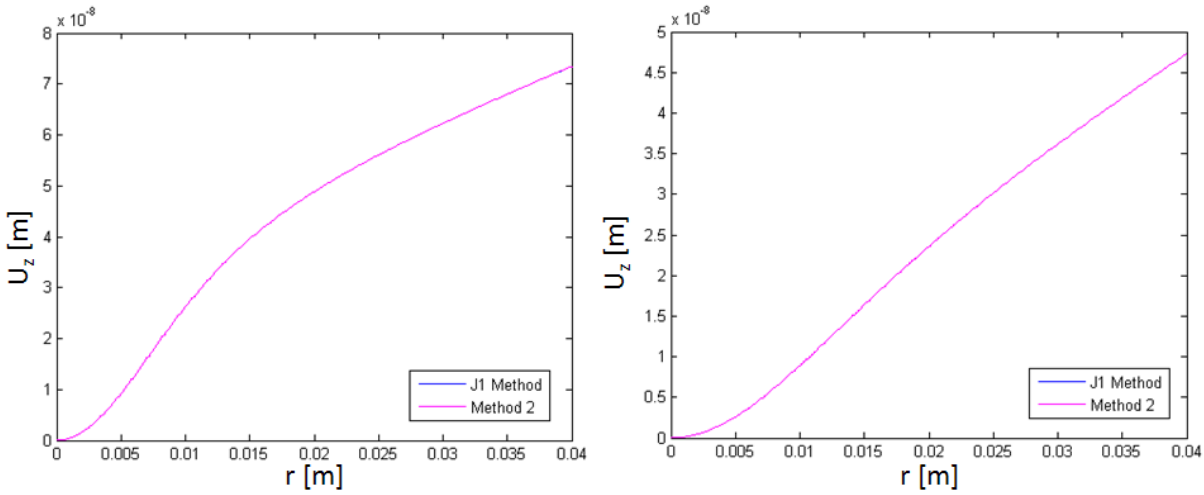

Figure C.5: Concordance between two analytical descriptions of the mirror surface distortion, for the TCS in section (3.2.3) - SIPHORE mirror geometry. Absorption coefficient 0.3ppm. Intracavity power 3MW. Environment temperature T_0=900K. The two panels represent the results for the mirror surface displacement vectors, as obtained when applying the method described in section (3.3.2), *Method 2*, and when applying the development involving the zeros of the Bessel function J_1, J_1 *Method*. **Left panel**: mirror surface displacement inside the optical cavity. **Right panel**: mirror surface displacement outside the optical cavity.

Appendix D

More details on the calculations performed by the DarkF software to obtain mirror curvature changes and losses, for the TCS analyzed in section (5.4), will be given in the following. As it has been already pointed out in section 5.4, the DarkF simulations are made by applying the mirror deformation maps, numerically calculated by COMSOL, on an initially flat mirror. The resulting mirror profile is used in the DarkF simulations, which compute the properties of the reflected beam, when the impinging beam is the fundamental gaussian beam, of waist 1 cm, on the reflecting mirror surface. In particular, a map of the reflected electromagnetic field is calculated at the level of the mirror reflecting surface. The curvature change of the mirror is determined by using the map of the reflected field phase, indeed, a fit for calculating the paraboloid which approximates better the curvature of the beam can be performed and through it the value of the mirror curvature radius is obtained [123]. In order to verify if the curvature radius given by DarkF was exactly the curvature radius of the distorted mirror, the $ABCD$ matix law has been applied. Indeed, DarkF provides the waist and the waist position of the beam after the reflexion on the mirror, by performing a gaussian fit, so that, knowing the q-parameter of the impinging beam, the following relation can be used to calculate the mirror curvature radius:

$$q_1 = \frac{Aq + B}{Cq + D}, \tag{D.1}$$

where the coefficients of the previous relation A, B, C, D are the components of the $ABCD$ matrix for the mirror, i.e:

$$\begin{pmatrix} 1 & 0 \\ -\frac{2}{R_c} & 1 \end{pmatrix}, \tag{D.2}$$

with R_c the mirror curvature radius and q_1 and q are the q-parameter of the reflected and of the incident beam, respectively. It is observed that:

$$q = 0 + \jmath z_R \qquad\qquad z_R = \frac{k w_0^2}{2}, \tag{D.3}$$

where w_0 is the waist of the laser beam impinging on the mirror and $k = 2\pi/\lambda$, with λ the laser wavelength. Furthermore:

$$q_1 = z_1 + \jmath z_{R,1} \qquad\qquad z_{R,1} = \frac{k w_1^2}{2}, \tag{D.4}$$

is the q-parameter of the beam reflected by the mirror, where w_1 is beam waist and z_1 is the position along the beam propagation direction. From relations (D.1), (D.2), (D.3), (D.4), by equating the imaginary parts of the right-hand side and of the left-hand side of equation (D.1), it is possible to obtain the expression for the curvature radius of the deformed mirror:

$$R_c = \frac{2 z_R \sqrt{z_{R,1}}}{\sqrt{z_R - z_{R,1}}}. \tag{D.5}$$

The previous relation is applied together with the value of the reflected beam waist, given by DarkF, for a given mirror map obtained through COMSOL, in order to obtain the curvature radius of the deformed mirror. In this way, it is possible to verify the concordance of this result with the one obtained by DarkF, when using the calculation method involving the map of the reflected beam phase. To show this point, the TCS of section (5.4) for $T_1 = 760$ K is considered. The map of the displacement vector for the reflecting mirror surface calculated by COMSOL is applied on a flat mirror and the resulting mirror map is used in the DarkF simulation, whose result for the reflected beam waist is:

$$w_1 = 9.67 \times 10^{-3}\text{m}. \tag{D.6}$$

By remembering that for the incident beam it is $w_0 = 0.01$ m, relation (D.5) gives $R_c = 2.2413 \times 10^3$ m. The value determined with the DarkF algorithm involving the map of the reflected beam phase is $R_c = 2.2408 \times 10^3$ m. The last result shows that the DarkF formula, which uses the map of the reflected beam phase, gives exactly the curvature radius of the deformed mirror and it is applied to determine the values reported in the first column of table (5.2).

As far as the DarkF calculation of the losses for a fundamental gaussian beam, L, is concerned, this is performed by using a formula which involves the coupling between the electromagnetic field of the incident beam on the deformed mirror, $\vec{E_0}$, and the electromagnetic field of the beam reflected by the mirror, $\vec{E}$. Therefore, the expression of the losses is written as

follows:

$$L = \text{coupling}(\vec{E_0}, \vec{E}) \times P(\vec{E}), \tag{D.7}$$

where $P(\vec{E})$ is the power of the electromagnetic field $\vec{E}$ and the coupling between $\vec{E_0}$ and $\vec{E}$ is defined through the following scalar product:

$$SP = \sum (\vec{E_0}, \vec{E}) dxdy, \tag{D.8}$$

with $dxdy$ the dimension of one element of the grid which the electromagnetic fields and mirrors are sampled on (see Ref. [102], [103], [104]). In terms of the scalar product SP, the coupling is evaluates as follow:

$$\text{coupling}(\vec{E_0}, \vec{E}) = \frac{\text{Re}[SP]^2 + \text{Im}[SP]^2}{P(\vec{E_0}) \times P(\vec{E})}, \tag{D.9}$$

with $P(\vec{E_0})$ the power of the electromagnetic field $\vec{E_0}$.

Bibliography

[1] J. Ongena and G. Van Oost. **Energy For Future Centuries**. Laboratorium voor Plasmafysica - Laboratoire de Physique des Plasmas. 19, 27, 33

[2] John Wesson. **Tokamaks**. Forth edition, *Oxford University Press.* 2011. 37

[3] C.M. Braams,P.E.Stott. **Nuclear Fusion: Half a Century of Magnetic Confinement Research**. *Institute of Physics Publishing.* 2002.

[4] T.J. Dolan. **Fusion research : principles, experiments and technology**. *New York: Pergamon Press,* 1982.

[5] J. Raeder et al. **Controlled Nuclear Fusion.** *John Wiley & Sons.* 2000.

[6] C. Leloup. **Aspects techiques d'un reacteur thermonucleaire à confinement magnetique** *Journal de Physique*, **N.8**, Tome 38, 1977.

[7] Commissariat à l'nergie atomique et aux énergies alternatives (CEA). **La fusion par confinement magnetique** *CLEFS CEA*, **N.49**. 2004. 37

[8] K. Nishikawa and M. Wakatani. **Plasma Physics**. Third Edition *Springer-Verlag.* 2000. 38

[9] S. Glasstone and R. H. Loveberg. **Controlled Thermonuclear Reactions**. *Robert E. Krieger Publishing Company, Huntington, NY.* 1975. 38

[10] A. Vieira Da Rosa. **Fundamentals of Renewable Energy Processes**. Third edition, *Elsevier Inc.* 2013. 38

[11] European Atomic Energy Community(EURATOM)-Commissariat à l'nergie atomique et aux énergies alternatives(CEA). **Magnetic Fusion**. *EURATOM and CEA*. 2006. 40, 41, 51

[12] J. Johner. **Optimized monomial approximations with integer exponents of the deuterium-tritium thermonuclear reaction rate**. *INIS.* **Vol. 18**, **N. 23**, 1987. 41

[13] J. D. Lawson. **Some Criteria for a Power Producing Thermonuclear Reactor**. *Proceedings of the Physical Society*, Section B, **Volume 70**, Issue 1, pp. 6-10. 1957. 41

[14] International Atomic Energy Agency. **Twelfth International Conference on plasma Physics and Controlled Nuclear Fusion Research**. *IAEA-CN-50.* October, 1988. 41, 51

[15] Commissariat à l'nergie atomique et aux énergies alternatives (CEA). **Fusion thermonuclaire : Le projet WEST au CEA de Cadarache, banc dessai pour ITER**. *Dossier de presse*, septembre, 2013. 42

[16] ulham Centre for Fusion Energy. **how fusion works**. *EPSRC and EURATOM*, 2012. 42

[17] Iter Website . https://www.iter.org/fr/mach/heating. 11, 43

[18] J. Pamela. **The physics of production, acceleration and neutralization of large negative ion beams**. *Plasma Phys. Control. Fusion.* 37, 1995. 44

[19] A. Simonin. **Towards an efficient Neutral Beam Injection system for a thermonuclear Fusion reactor**. *Mémoire de HDR.* 09 August 2012. 11, 44, 45, 47, 48, 50, 51, 52, 53, 54, 55

[20] K. R. Lykke, K.K. Murray, W. C. Lineberger . **Threshold photodetachment of H^-**. *Physical Review A.* **41**, **N.11**, (1991). 45

[21] L. M. Branscomb, S. J.Smith. **Experimental Cross Section for Photodetachment of Electrons from H^- and D^-**. *Physical Review.* **98**, **N.4**, (1955). 45

[22] S. J.Smith, D. S. Burch. **Photodetachment cross section of the negative hydrogen ion**. *Physical Review Letters.* **2**, **N.4**, (1959). 45, 46

[23] T. Ohmura and H.Ohmura. **Electron-Hydrogen Scattering at Low Energies**. *Physical Review.* **118**, **N.1**, (1960). 45

[24] W. Chaibi, C.Blondel, L.Cabaret, C.Delsart, C.Drag, A.Simonin. **Photo-neutralization of Negative Ion Beam for Future Fusion Reactor**. **CP1097**, *Negative Ions, Beams and Sources: 1st International Symposium*,(2009). 45, 46, 48

[25] M. Vandevraye, P.Babilotte, C.Drag, C.Blondel. **Laser measurement of the photodetachment cross section of H^- at the wavelength 1064 nm**. *Physical Review A*. **90**, **013411**, (2014). 46

[26] M.Génévriez, X.Urbain. **Animated-beam measurement of the photodetachment cross section of H^-**. *Physical Review A*. **91**, **033403**, (2015). 46

[27] J. Wesson. **The science of JET**. JET Report, JET-R(99)13. (1999). 51

[28] T.T.C. Jones. **Tritium operation of the JET NBI system**. *Fusion engineering and design*, **Vol. 47**, pp.205-231. (1999). 51

[29] ITER Organization. **The way to new energy**, (2015) *http://www.iter.org/*. 52

[30] H. Zohm, C. Angioni, E. Fable, G. Federici, G. Gantenbein,T. Hartmann, K. Lackner, E. Poli, L. Porte, O. Sauter, G. Tardini, D. Ward and M. Wischmeier. **On the physics guidelines for a tokamak DEMO**. *Nucl. Fusion*. **53**. (2013). 52

[31] J.Pamela et al. **Efficiency and availability driven R&D isues for DEMO**. *Fusion Eng. And design*, **Vol. 84**, pp. 194-204, 2009. 52

[32] ITER Technical Basis. **Neutral beam heating & current drive (NB H&CD) system, Detailed Design Document**. section 5.3 DDD5.3, 2002. 52

[33] R.S. Hemsworth. **Status of the ITER neutral beam injection system**. *Review of scientific instrument*. **Vol. 79**, Issue 2, pp02C109-02C109-5, 2008. 52

[34] A. Simonin, L.Christin, H.de Esch, P. Garibaldi, C.Grand, F. Villecroze, C. Blondel, C. Delsart, C. Drag, M. Vandervraye, A.Brillet and W. Chaibi. **SIPHORE: Conceptual Study of a High Efficiency Neutral Beam Injector Based on Photodetachment for Future Fusion Reactors**. *AIP Conference Proceedings* **1390**, 494, 2011. 52

[35] D. Fiorucci, J. Feng, M. Pichot, W. Chaibi. **Thermal effects in high power cavities for photoneutralization of D^- beams in future neutral beam injectors**. *NIBS conference*, 2014. 22, 25, 55, 61

[36] O. Svelto. **Principles of Laser**. *Springer*, Fifth Edition, 2010. 264

[37] H. Kogelnik and T. Li. **Laser Beams and Resonators**. *APPLIED OPTICS*, Vol. 5, No. 10, 1966. 265, 266

[38] L. G. Gouy. **Sur une propriete nouvelle des ondes lumineuses**. *C. R. Acad. Sci. Paris* 110, 1890. 266

[39] L. G. Gouy. **Sur la propagation anomale des ondes**. *C. R. Acad. Sci. Paris* 111, 1890.

[40] A. Rubinowicz. **On the anomalous propagation of phase in the focus**. *Phys. Rev.* **54**, 1938.

[41] W. H. Carter. **Anomalies in the field of a gaussian beam near focus**. *Optics. Commun.* **7**, March, 1983.

[42] R. W.Boyd. **Intuitive explanation of the phase anomaly of focused light beams**. *J. Opt. Soc. Am.* **70**, July, 1980. 266

[43] RP Photonics: http://www.rp-photonics.com/hermite_gaussian_modes.html?s=ak. 268

[44] C. Bond, P. Fulda, L. Carbone, K. Kokeyama and A.Freise. **Higher order Laguerre-Gauss mode degeneracy in realistic, high finesse cavities**. *PHYSICAL REVIEW D*, 84, 2011. 268

[45] E. Nagali and F.Sciarrino. **Manipulation of Photonic Orbital Angular Momentum for Quantum Information Processing**. *InTech*, ISBN: 978-953-51-0153-6, 2012. 268

[46] J. ARLT, K. DHOLAKIA, L. ALLEN and M. J. PADGETT. **The production of multiringed Laguerre-Gaussian modes by computer-generated holograms**. *Journal of Modern Optics*, Vol. 45, No. 6, 1998. 268

[47] Wikipedia website: **http://en.wikipedia.org/wiki/Gaussian_beam**. 269

[48] The Virgo collaboration. **Optics and related Topics**. *The VIRGO Physics Book, Vol.II*. April 21, 2006. 55, 200, 201, 204, 205

[49] A. E. Siegman. **LASER**. *University Science Books*, 1986. 11, 14, 56, 59, 61, 66, 67, 68, 72, 204, 206, 207

[50] F. Träger. **Handbook of Lasers and Optics**. *Springer*, 2012. 57

[51] Yehuda B. Band. **Light and Matter**. *John Wiley & Sons, Inc.*, 2006. 57

[52] Bahaa E. A. Saleh, Malvin Carl Teich. **Fundamentals of Photonics**. *John Wiley & Sons, Inc.*, 1991. 57, 60, 234

[53] R. Menze. **Photonics: Linear and Nonlinear Interactions of Laser Light and Matter**. *Springer*, 2007. 57

[54] D.Kleckner, W.Marshall, M. J. A. de Dood, K. N. Dinyari, B.-J. Pors. **High Finesse Opto-Mechanical Cavity with a Movable Thirty-Micron-Size Mirror**. *Physical Review Letters*, **PRL 96**, 173901, 2006. 57

[55] M. Granata. **Optical Development for Second- and Third-Generation Gravitational-Wave Detectors: Stable Recycling Cavities for Advanced Virgo and Higher-Order Laguerre-Gauss Modes**. *PhD thesis*, 2011. 60, 61, 77

[56] A. M. Gretarsson, E. D'Ambrosio, V. Frolov, B. OReilly and P. K. Fritschel. **Effects of mode degeneracy in the LIGO Livingston Observatory recycling cavity**. *J. Opt. Soc. Am. B,* **24** ,2821, 2007. 60

[57] P. Hello and C. N. Man. **Design of a low-loss off-axis beam expander**. *Applied Optics*, Vol. **35**, No. 15, 1996. 62

[58] H. Heitmann. **Design of a three-lens mode matching telescope**. *VIRGO notes*, IP IJ IT 19 14 10 1318, 1994. 62

[59] M. A. Arain and G. Mueller. **Design of the Advanced LIGO recycling cavities**. *Optical Society of America*, Vol. **16**, No. 14, 2008. 62

[60] G. A. Massey and A. E. Siegman. **Reflection and Refraction of Gaussian Light Beams at Tilted Ellipsoidal Surfaces**. *Applied Optics*, Vol. **8**, No.5, 1969. 65, 77

[61] N. Hodgson and H. Weber. **Optical resonators: fundamentals, advanced concepts and applications**. *Springer*, Berlin, 1997. 66

[62] Laser KOHERAS ADJUSTIK^{TM}, Model:TRAdY10PztSPm. 80, 86, 90

[63] **CVI MELLES GRIOT**, Capabilities Brochure. 83, 99

[64] IHS Engineering360. **WinCamD[TM] Series Cameras CCD/CMOS Beam Imagers User Manual**. 2007. 84, 247, 249

[65] CVI. Mirror manufacturing capabilities: http://cvilaseroptics.com/products/Mirrors. 84

[66] G. N. Watson. **Theory of Bessel functions**. *CAMBRIDGE AT THE UNIVERSITY PRESS*, *Second Edition*, 1958. 108, 137

[67] F Bowman. **Introduction to Bessel Functions**. *Dover*, 1958. 108, 137

[68] F. W. J. Olver. **Asymptotics and special functions**. *ACADEMIC PRESS*, *New York, San Francisco, London*, 1974. 137

[69] Milton Abramowitz and Irene A. Stegun. **Handbook of Mathematical Functions with Formulas, Graphs, and Mathematical Tables**. *Dover*, 1964. 108, 138

[70] R. S. Esfandiari. **Numerical Methods for Engineers and Scientists Using MATLAB**. *CRC Press*, 2013. 121

[71] J-Y Vinet. **On Special Optical Model and Thermal Issues in Advanced Gravitational Wave Interferometric Detector**. *Living Reviews in Relativity*, 17 July 2009. 103, 104, 111, 136, 142, 144, 226

[72] P. Hello and J-Y Vinet. **Analytical models of thermal aberrations in massive mirrors heated by high power laser beams**. *J. Phys. France*, **51**, 1267-1282, (1990). 104

[73] P. Hello and J-Y Vinet. **Analytical models of transient thermoelastic deformations of mirrors heated by high power cw laser beams**. *J. Phys. France*, **51**, 2243-2261, (1990).

[74] C. J. Myers and R. C. Allen. **Development of an analytical mirror model addressing the problem of thermoelastic deformation**. *Appl. Opt.*, **24**, 1933-1939, (1985).

[75] N. Tankovsky, D. Ivanov and J. Burov. **Surface thermoelastic deformations caused by a laser**. *Rev. Phys. Appl.*, **19**, 631-634, (1984).

[76] A.Cutolo, P. Gay and S. Solimeno. **Mirror deformations and wavefront aberrations caused by c.w. high power laser beams,**. *Opt. Acta*, **27**, 1105-1116, (1980). 103

[77] V. Fafone. **AdV Thermal Compensation System**. *VIR-0115A-10*, (2010). 103

[78] A. Rocchi, E. Coccia, V. Fafone, V. Malvezzi, Y. Minenkov, L. Sperandio. **Thermal effects and their compensation in Advanced Virgo**. *Journal of Physics: Conference Series*. **363**, 012016, (2012).

[79] T. Accadia et al. **Central heating radius of curvature correction (CHRoCC) for use in large scale gravitational wave interferometers**. *Class. Quantum Grav.* **30**, 055017, (2013).

[80] The Virgo Collaboration. **Advanced Virgo Technical Design Report**. *VIR0128A12*, (2012).

[81] The LIGO Collaboration. **Instrument Science White paper**. *LIGO-T1400316v4*, (2014). 103

[82] S. Axler, P. Bouron and W. Ramey. **Harmonic function theory**. *Springer-Verlag*, (1992). 104, 271

[83] Lawrence C. Evans. **Partial Differential Equations**. *American Mathematical Society*, (1998). 104, 271

[84] W. E. Byerly. **Harmonic functions**. *John Wiley & Sons*, (1906). 104, 271

[85] Landau & Lifshitz. **Theory of Elasticity**. *Vol. 7 of course of theoretical physics. PERGAMON PRESS*. 1959. 135

[86] S. P. Timoshenko. **Theory of Elasticity**. *Third Edition. McGRAW-HILL INTERNATIONAL EDITIONS*. 1970. 135, 140

[87] A. J. C. B. de Saint-Venant. **Mémoire sur la torsion des prismes**. *Mémoires présentes pars divers Savants á l Académie des Sciences de l Institut Impérial de France. read to the Academy.* Jun 13, 1853.

[88] A. J. C. B. de Venant. **Mémoire sur la flexion des prismes**. *J Math Pures Appl,* **1**, (Ser.2), pp. 89-189. (1855).

[89] R. Mises. **On Saint-Venant Principle**. *Bull Amer Math Soc,* **51**, (Ser.2), pp. 555-562. (1945).

[90] E. Sternberg. **On Saint-Venant Principle**. *Quart Appl Math,* **11**, pp. 393-402. (1954).

[91] O. Zanaboni. **Dimostrazione generale del principio del De Saint-Venant**. *Atti Acad. Naz. dei Lincei, Rendiconti,* **25**, pp. 117-121. (1937).

[92] R. A. Toupin. **Saint-Venants Principle**. *Archive for Rational Mech and Anal,* **18**, pp. 83-96, (1965).

[93] V. L. Berdichevskii . **On the proof of the Saint-Venants Principle for bodies of arbitrary shape.** *Prikl. Mat. Mekh,* **38**, pp. 851-864, (1974).

[94] C. O. Horgan and J. K. Knowles. **Recent developments concerning SaintVenants principle**. *In Adv in Appl Mech. Wu TY and Hutchinson JW ed., Vol.* **23**, pp. 179-269, (1983). 140

[95] Laboratoire des Matriaux Avancs, LMA, Lyon. Private discussion. 2014. 208

[96] ANSYS website: **http://www.ansys.com** 157

[97] COMSOL **COMSOL Multiphysics Users Guide**. Version COMSOL 4.3, 2012. 157

[98] COMSOL website: **http://www.comsol.com** 157

[99] CATIA website: **http://www.3ds.com/products-services/catia** 157

[100] AutoCAD website: **http://www.autodesk.com/products/autocad/overview** 157

[101] Feng Jiatai. **Master degree thesis work.** 2014. 159, 226

[102] Mikhael Pichot. **DarkF user's guide**. 2014. 227, 283

[103] Jean-Yves Vinet, M.Laval. **DarkF User's Guide**. *Virgo internal note: VIR-007A-08*. 2008. Unpublished. 227, 283

[104] The Virgo collaboration. *App. Opt.* **46**. *pp. 3466*. 2007. 227, 283

[105] T. Y. Fan. **Laser Beam Combining for High-Power, High-Radiance Sources**. *IEEE Journal of selected topics in quantum electronics*, Vol. **11**, No. 3, 2005. 233

[106] D. Pabuf, F. Emaury, S. De Rossi, R. Mercier, G. L. Leclin, P. Georges. **Coherent beam superposition of ten diode lasers with a Dammann grating**. *Optics Letters, Optical Society of America*, Vol. **35**, No. 10, 2010. 233

[107] S. P. Singh and N. Singh. **Nonlinear effects in optical fibers: origin, management and applications**. *PIER* , VOL. **73**, 2007. 233

[108] Govind P. Agrawal. **Nonlinear Fiber Optics**. *Academic Press*, third edition 2001. 233, 236, 237, 238

[109] Bernard Dussardier, Vipul Rastogi, A. Kumar and G. Monnom. **Large-mode-area leaky optical fiber fabricated by MCVD**. *App. Opt. Vol.* **50** *No.* **19**. *pp. 3118*. 1 July 2011. 233, 240, 241, 243

[110] R. Paschotta. **Encyclopedia of Laser Physics and Technology**. *Wiley-VCH*, 2008. 233, 238

[111] Fedor Mitschke. **Fiber Optics**. *Springer-Verlag Berlin Heidelberg*, 2009. 234

[112] K. C. Kao G. A. Hockham. *IEE Proc.* **113**, (1966). 236

[113] F. P. Kapron, D. B. Keck and R. D. Mauer. *Appl. Phys. Lett.* **17**, 423, (1970). 236

[114] Luc Thévenaz. **Advanced Fiber Optics: Concepts and Technology**. *EPFL Press*,First edition, 2011. 237

[115] A. Yeung, K. S. Chiang, V. Rastogi, P. L. Chu, and G.D. Peng. **Experimental demonstration of single-mode operation of large-core segmented cladding fiber**. *Proc. Optical Fiber Communication Conf. (Los Angeles)*, Paper ThI4, Feb. 2004. 239

[116] K. S. Chiang, V. Rastogi. **Leaky optical fiber for large mode area single mode operation**. *Electron. Lett.*, Vol. **39**, 2003. 239

[117] K. S. Chiang, V. Rastogi. **Analysis of segmented-cladding fiber by the radial effective index method**. *J. Opt. Soc. Am B*, Vol. **21**, 2004. 239

[118] K. S. Chiang, V. Rastogi. **Holey optical fiber with circularly distributed holes analyzed by the radial effective-index method**. *Opt. Lett.*, Vol. **28**, 2003. 239

[119] Vipul Rastogi and Kin Seng Chiang. **Propagation characteristics of a segmented cladding fiber**. *OPTICS LETTERS*. Vol.**26**, No. 8, April 15, 2001. 239

[120] Vipul Rastogi and Ajeet Kumar. **Design and analysis of a multilayer cladding large-mode-area optical fibre**. *J. Opt. A: Pure Appl. Opt.* **10 015303**, 12 December 2007. 239

[121] K.Thyagarajan, S. Diggavi ,A. Taneja, A.K. Ghatak . **Simple numerical technique for the analysis of cylindrically symmetric refractive-index profile optical fibers**. *Appl. Opt.* **30**, 3877-9, (1991). 241

[122] S. Nagel *et al.* **An overview of the modified chemical vapor deposition (MCVD) process and performance**. *IEEE J. Quantum Electron.* Vol. **18**, No. 4, (1982). 241

[123] Laboratoire ARTEMIS, Nice. Private discussion. 2014. 281